IKS
Instituut voor Kern- en Stralingsfysica
Departement Natuurkunde en Sterrenkunde
Faculteit Wetenschappen

1425
KATHOLIEKE UNIVERSITEIT
LEUVEN

Precision moments of the ^{11}Li halo nucleus

Promotor:
Prof. Dr. G. Neyens

Proefschrift ingediend tot
het behalen van de graad van
doctor in de wetenschappen
door

Dana Borremans

2004

Contents

Introduction

One of the actual key topics in nuclear physics is the study of exotic nuclei, i.e. nuclei with extreme properties, such as an extreme ratio of the number of neutrons and protons, excitation energy or total nuclear spin. The interest for exotic nuclei has increased enormously since the recent progress in nuclear accelerators. This made it possible to produce exotic nuclei with sufficient rates. The study of neutron rich[1] nuclei revealed unexpected phenomena such as weakening of closed shells and the formation of neutron halos[2] [Tan85, Thi75, Tan96]. These phenomena indicated that the interaction between the nucleons - the strong force - was not well enough understood. In particular the influence of extreme conditions on the spin-orbit term, which had given rise to the magic numbers in the shell model [May49], was not understood. As a consequence, the parametrization of existing nuclear models such as the shell model [May49] had to be adapted and new models were developed.

The magnetic and quadrupole moment of exotic nuclei are stringent tests for these new developed nuclear models. They contain a lot of information about the structure of the nuclear state: the magnetic dipole moment is sensitive to the orbitals of nucleons that are not paired off to zero spin. The electric quadrupole moment gives information on the deformation of the charge distribution of the nucleus.

Of particular interest are the quadrupole moments of the ground states of the neutron rich ^{9}Li and ^{11}Li. ^{11}Li is a drip line nucleus with a magic number of neutrons (eight) and is a textbook example of a halo nucleus. It consists of a ^{9}Li core and two loosely bound neutrons. The influence of these two neutrons on the charge distribution of the core can be determined by $\frac{Q(^{11}Li)}{Q(^{9}Li)}$. The expected influence is small. Therefore precision measurements are needed. In order to determine the quadrupole moments precisely via multiple-rf-NQR, first an accurate knowledge of the magnetic moments is needed.

---

[1] This means that the ratio of the number of neutrons and protons is much larger than for nuclei in the valley of stability.

[2] A neutron halo nucleus is a nucleus with some very loosely bound neutrons. This results in a long tail of the neutron density distribution and a very extended matter radius.

These magnetic and quadrupole moments were studied using the β-NMR/ NQR (Nuclear Magnetic Resonance/ Nuclear Quadrupole Resonance) technique [Mat71] at the ISOLDE facilities in CERN[3]. For the production of the required spin-orientation, the technique of optical pumping [Kas50, Kas57, Coh66] was used. The measurements were performed in collaboration with the COLLAPS group of Mainz (Germany) lead by Prof. Dr. R. Neugart. This group had already measured these moments [Arn92] at the ISOLDE facilities in CERN, using optical pumping to create nuclear spin-orientation. But the obtained accuracy was not good enough to be conclusive about the influence of the two loosely bound neutrons. Therefore a precision measurement was performed with an improved version of the same set-up. Like this the present know-how was optimally used. For the optimization of the parameters of the set-up and the calibration of the magnetic field, the well produced ^{8}Li isotopes were used. Both the parameters for the optical pumping set-up and those for the β-NMR/NQR set-up were optimized. My main contributions concerned the optimization of the β-NMR/NQR.

---

[3] Conseil Européen pour la Recherche Nucléaire, European Council for Nuclear Research [CERN]

Chapter 2

Motivation

In an attempt to understand the interaction between nucleons, nuclear models have been being developed since the fifties. The most famous of these, the nuclear shell model [May49], works quite well close to the valley of stability. In this model nuclear structure is dominated by the shell structure, originating from an harmonic oscillator potential with spin-orbit coupling. Large energy gaps in between two shells favor configurations in which the nucleons fill completely a shell. The numbers of nucleons that give rise to closed shells are called "magic numbers". Going towards the drip lines [1], however, unexpected phenomena appeared, such as disappearing shell closures and the formation of neutron- and proton-halos [Thi75, Tan85, Tan96, Han87]. To understand and model these new phenomena it is important to study experimentally the properties of exotic nuclei. Of particular interest is ^{11}Li as a halo-nucleus and a nucleus with a magic neutron number (N=8).

2.1 ^{11}Li as a halo nucleus

A nucleus with a neutron halo is one with some very loosely bound neutrons[2]. The neutron density distribution in such loosely bound nuclei shows an extremely long tail, called the neutron halo. As a consequence the radius of such a nucleus is much larger than expected. Although the density of a halo is very low, it strongly affects the reaction cross section and leads to new properties in such nuclei, e.g. a very narrow momentum distribution. This reflects the Heisenberg uncertainty principle

$$\Delta x \Delta p_x \geq \frac{\hbar}{2} \tag{2.1}$$

---

[1] Proton and neutron drip lines are the borders of the region of bound nuclei on the nuclear chart.

[2] The one or two neutron separation energy $S_{n(2n)} < 1$MeV, compared to the common $S_n \approx 6 - 8$MeV for nuclei in the valley of stability.

Since the matter radius is very extended, there is a large uncertainty in the position and thus a small uncertainty in the linear momentum.

In a halo nucleus the three basic ”rules” of nuclear density for nuclei close to the valley of stability are broken. These three rules are [Tan96]

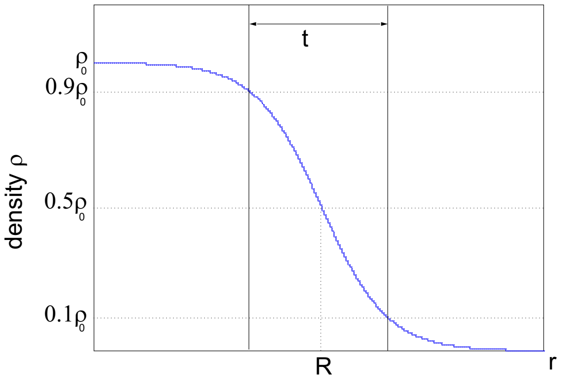

Figure 2.1: *Schematic view of the nuclear density as a function of distance with the definition of the half density radius R and the surface thickness t.*

1. The radius where the nuclear density is reduced to half of the maximal density is expressed as $R = r_0 A^{1/3}$. $r_0 \approx 1.2$fm is the radius constant (fig. 2.1)
2. Protons and neutrons are homogenously mixed in the nucleus, i.e. $\rho_p(r) \approx \rho_n(r)$. In halo nuclei this is only true for the core.
3. The distance from where the nuclear density drops from 90% of the maximal value to 10% of its maximal value, called the surface thickness t, is constant and is about $t \approx 2.3$fm (fig. 2.1). This feature is true for nuclei in the valley of stability because of the nearly-constant nucleon separation energy (6-8MeV) for stable nuclei. In general the surface thickness, or the surface diffuseness is expected to depend on the nucleon separation energy. The neutron halo is the most pronounced case for a small separation energy ($<$ 1MeV).

The most prominent and most studied example is ^{11}Li with a ^{9}Li core and two loosely bound neutrons (fig. 2.2). As early as 1975, C. Thibault et al. [Thi75] found a very small two-neutron separation energy $S_{2n}(^{11}\text{Li}) = 170 \pm 80$keV, but they didn’t attribute this to a neutron halo. In 1985 Tanihata et al. [Tan85] discovered the large interaction cross section of ^{11}Li and attributed it to a halo property. In the fragmentation of ^{11}Li, narrow momentum distributions were

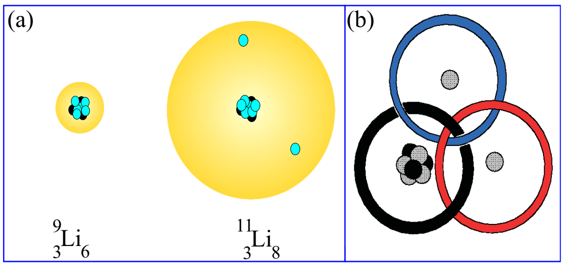

Figure 2.2: *(a) Schematic view of ^{11}Li as ^{9}Li core and two loosely bound neutrons. (b) Visualization of the three-body system in ^{11}Li.*

found for the ^{9}Li fragments, but not for the other fragments such as ^{8}Li or ^{8}He, indicating that only the two neutrons in the last orbital contribute to the formation of a neutron halo [Tan96]. ^{11}Li was found to be a three-body system, in which none of the internal two-body subsystems (dineutron and ^{10}Li) were bound, giving it the name "Borromean[3] halo nucleus" [Han87, Zhuk93]. Three-body interactions are necessary for a full description of the nucleus. A lot of interest was shown in this Borromean nucleus [Sch00, Ann90, Rii92, Neu00], but nevertheless a lot of questions concerning the structure of this nucleus remain unanswered. One such question is the polarizability of the core by the two loosely bound neutrons: do the two loosely bound neutrons influence the proton distribution in the core?

The existing experimental data point towards an almost decoupled core and two neutrons.
An example of the experimental data consists of the almost equal charge-changing cross sections σ_{cc} of ^{8}Li, ^{9}Li and ^{11}Li (fig. 2.3) [Bla92, Tan96]. The charge-changing cross section σ_{cc} is the cross section for all processes which result in a change of the atomic number of the projectile, i.e. the removal or pick-up of proton(s). The reaction cross section[4] σ_R is a measure of the nuclear matter radius [Tan96]. Therefore the reaction cross sections in fig. 2.3 increase with increasing mass. Analogously the charge-changing cross section is a measure of the proton-radius [Bla92, Chu00]. The fact that the charge-changing cross sections for the Li-isotopes are nearly constant with increasing mass, indicates a nearly constant proton radius. This is an indication that the influence of the neutrons on the proton distribution is small. However, the uncertainty on the charge-changing cross section of ^{11}Li is about 8%. Within this uncertainty the neutrons might influence the proton radius.
Another important measurement is that of the quadrupole moments of ^{9,11}Li by E. Arnold et al. [Arn92]. The two quadrupole moments were found to be

---

[3] This name is given by the analogy of the three subsystems to the three rings of the coat of arms of the Italian Borromean family

[4] The reaction cross section is the sum of the cross sections for all possible reaction channels.

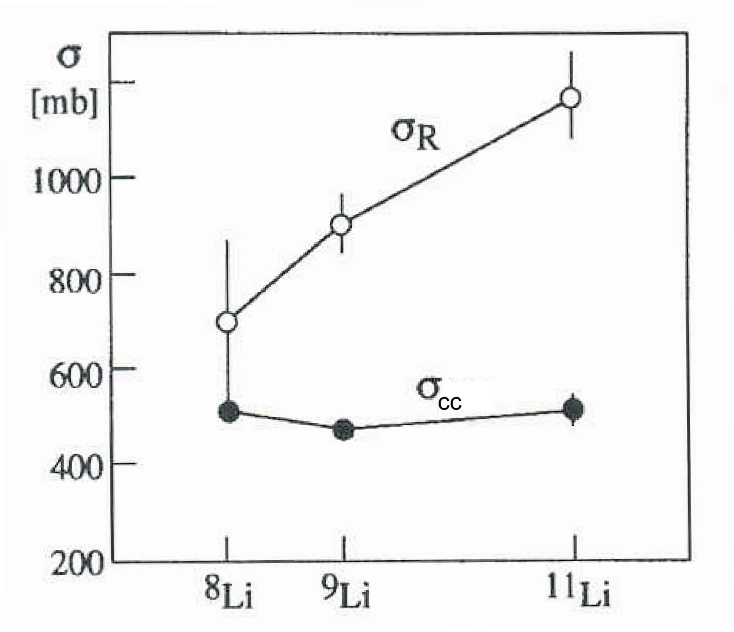

Figure 2.3: *Reaction cross sections σ_R and charge-changing cross sections σ_{cc} as a function of neutron number for some Li isotopes. Picture taken from [Tan96].*

equal within the experimental uncertainty of 10%, which also suggests a minor influence of the halo neutrons on the ^{9}Li core.
On the other hand, T. Misu et al. [Mis97] predicted that in the limit of zero binding energy the total deformation of a two-body halo system with a core part and a valence part is totally determined by the spatial structure of the valence state wave function, independently of the shape of the core. The deformed core merely establishes the quantization axis of the system, important for determining Λ, the projection of the angular momentum of the valence state wave function. In these calculations a halo state is defined as a state with an infinite root mean square radius in the asymptotic case of zero binding energy. T. Misu showed that this is only the case for positive parity states ($s_{1/2}$) with $\Lambda = 0$ and for negative parity states ($p_{1/2}$) with $\Lambda = 0, 1$. However, this does not mean that other orbitals cannot form very extended structures when their binding energy becomes very small. In figure 2.4 some examples of calculated

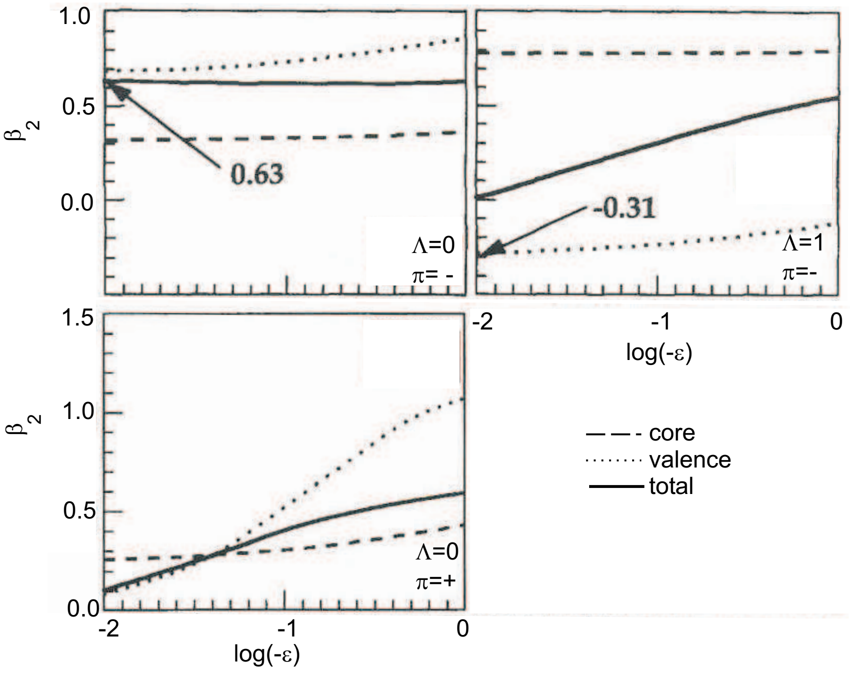

Figure 2.4: *Deformation β_2 as a function of log$(-\epsilon)$ with ϵ the binding energy of the halo neutrons. The binding energy itself is negative. In the limit of zero binding energy the logarithm becomes $-\infty$. Picture taken from [Mis97].*

deformations[5] β_2 for superdeformed shapes with $\delta = (\frac{R_\parallel}{R_\perp})^{\frac{2}{3}} - 1 = 0.6$ are given. Here $R_{\parallel(\perp)}$ denotes the major (minor) axis of the ellipsoid that represents the nucleus. When the binding energy goes to zero, or the logarithm goes to $-\infty$, the total deformation of the total system converges to that of the valence state. For positive parity halos with $\Lambda = 0$ the deformation goes to 0 while for negative parity halos the deformation goes to 0.63 for $\Lambda = 0$ and to -0.31 for $\Lambda = 1$. The calculations of T. Misu et al. [Mis97] are made for two-body halos: a core state and a valence state. This makes the generalization towards ^{11}Li, a three-body system with a core and two interacting valence particles, difficult. Nevertheless it is an indication that it might be possible that the extra neutrons influence the core. If only the valence neutrons determine the quadrupole moment of ^{11}Li, only a contribution of a configuration in which one (or the two) neutron(s) is (are) in the $0d_{5/2}$ orbital will enhance the ^{11}Li quadrupole moment because of the spherical shape of the $1s_{1/2}$ orbital and the necessary coupling to spin 0 for the configurations $p^2_{1/2}$ and $s^2_{1/2}$.
To verify whether the two loosely bound neutrons in ^{11}Li influence the proton distribution of the core ^{9}Li, a very accurate measurement of the quadrupole moments of ^{9,11}Li is necessary. If the quadrupole moment of ^{11}Li turns out to be different from that of ^{9}Li, the two loosely bound neutrons polarized the proton distribution of the core.

2.2 Shell closure around $N = 8$ approaching the neutron drip line

The first indications for weakening of shell closures far from stability were found around the $N = 20$ shell with mass measurements on the $^{26-31}$Na isotopes by C. Thibault et al. [Thi75]. The observed binding energies were much smaller than expected for closed shell nuclei.

The region around the $N = 8$ shell closures far from the valley of stability at the neutron-rich side consists of very light nuclei. The shell model assumes that all nucleons feel a mean field from the other nucleons. The question raises if this assumption is still valid for such light nuclei and in particular for halo nuclei with loosely bound neutrons. Nevertheless, because of its simplicity, the picture of the shell model is often used to extract from the experimental data the contribution of different orbitals to the total wave function. When configurations with some nucleons in the orbitals of the sd-shell (fig. 2.5) are necessary to explain the experimental data of the ground state of such light nuclei with $N \leq 8$, one speaks about a disappearing $N = 8$ shell gap.

---

[5] The deformation β_2 is defined as

$$\beta_2 \equiv \frac{4\pi}{5} \frac{\langle r^2 Y_2^0 \rangle}{\langle r^2 \rangle} \tag{2.2}$$

The disappearance of the $N = 8$ shell closure (fig. 2.5) was first suggested in the $_4$Be-isotopes. The $_4$Be-isotopes have proton configurations with a full

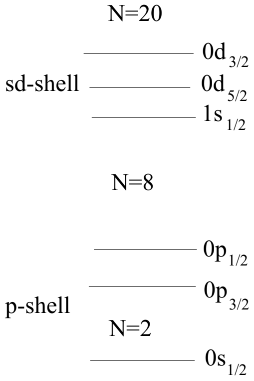

Figure 2.5: *Schematic view of the p- and sd-shell single particle levels for light neutron-rich nuclei [Ots03] (section 7.2.2) .*

$0s_{1/2}$ orbital and two protons and two holes in the $0p_{3/2}$ orbital. $^{11}_{4}\mathrm{Be}_7$ consists of a $^{10}_{4}\mathrm{Be}_6$ core and a loosely bound neutron. Since the ground state of the core ^{10}Be has spin zero, the spin of the ground state of ^{11}Be is expected to be determined by the orbital $0p_{1/2}$ of the unpaired neutron. This gives a spin/parity $1/2^-$. However, this spin/parity was measured to be $1/2^+$ [Mil83]. This can mean that the unpaired neutron is situated in the $1s_{1/2}$ orbital or that the core is in its first excited state 2^+ and couples to the unpaired neutron in the $0d_{5/2}$ orbital, giving the $|(^{10}Be)^{2+} \otimes \nu 0d_{5/2}, I^\pi = 1/2^+\rangle$ configuration. In any case it means that configurations with neutrons in orbitals of the sd-shell, across the $N = 8$ shell gap play a role in the wave function of the ground state of ^{11}Be. The later measurement of its magnetic moment [Gei99] together with shell model calculations by Millener with a free neutron g_s factor, suggested a large contribution ($\approx$ 82%) of the intruder $|0^+ \otimes \nu 1s_{1/2}\rangle$ configuration in the total configuration [Gei99]. This was confirmed by the ^{11}Be(p,d)^{10}Be transfer reaction in which the $|\nu 0d_{5/2}\rangle$ component was found to represent 16% of the ground state of this nucleus [For99, Win01]. Extra confirmation came from the study of the one-neutron knockout reaction ^{9}Be(^{11}Be,^{10}Be + γ) at 60 MeV/nucleon. The comparison of the experimental cross sections to calculated spectroscopic factors, indicates a dominant 1s single-particle character of the ^{11}Be ground state and a small contribution of core excitation $|(^{10}Be)^{2^+} \otimes \nu 0d_{5/2}\rangle$ in the wave function [Aum00].
In $^{12}_{4}\mathrm{Be}_8$, a low lying 1^- state was observed at 2.68(3)MeV [Iwa00] (fig. 2.6). The lowering of this state is explained by a quenching of the energy gap between the $0p_{1/2}$ and $1s_{1/2}$ orbitals. This quenching is explained by Otsuka et al. [Ots03] by a reduced strength of the attractive interaction between spin-orbit partners when the number of nucleons in one of the partner orbitals is decreas-

ing (section 7.2.2). Recently also a low lying 0_2^+ isomeric state at 2.24(2)MeV

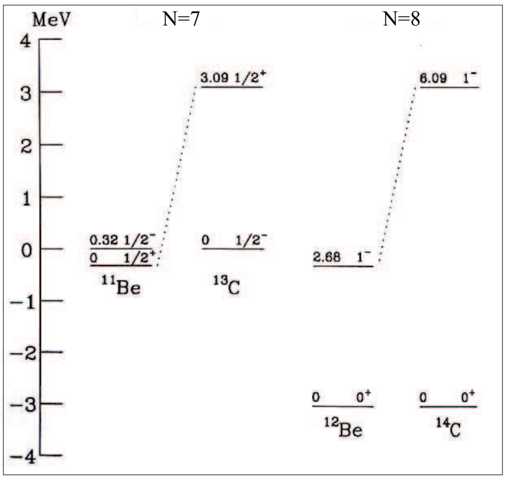

Figure 2.6: *Comparison of the* $1/2^+$ *excited states of the N=7 and the* 1^- *excited states of the N=8 isotones of Be and C [Iwa00, Tal60]. Picture taken from [Iwa00].*

was observed with a lifetime 50ns$< \tau <$ 11μs [Shi03]. This can also be understood in the picture of the quenching of the gap between the $0p_{1/2}$ and the $1s_{1/2}$ orbitals. In this picture the wave function of both the ground state and that of the 0_2^+ isomer is an admixture of $\nu(0p_{1/2})^2$ and $\nu(1s_{1/2})^2$ configurations. In addition, the cross section for obtaining the first excited 2^+ state of ^{12}Be via inelastic proton scattering on the 0_1^+ ground state was measured [Iwa00b]. Via comparison with theoretical calculations this gives an indication of a large deformation length $\delta = 2.00(23) fm$ of the $^{12}_{4}$Be$_8$ ground state [Iwa00b], while a closed shell nucleus (N=8) is expected to be almost spherical. The comparison of the spectroscopic factors and the experimental cross sections in the one neutron knockout reaction ^{9}Be(^{12}Be,^{11}Be+γ)X show a significant occupancy of the $1s_{1/2}$ state in ^{12}Be as well as an admixture of the $0d_{5/2}$ state [Nav00, Zwie79]. Finally a large breaking of the p-shell closure in ^{12}Be was suggested by the theoretical study based on the shell model to explain the observed anomalously large $logft(^{12}\mathrm{Be}^{0+} \rightarrow ^{12}\mathrm{B}^{1+}_{g.s.}) = 3.834(17)$ value [Suz97]. Such a large $logft$ value corresponds to a retarding of the Gamow-Teller transitions, i.e. of the decay.

Recently an indication was found of a large admixture of $\nu 1s^2_{1/2}$ in the ground state wave function of the two-neutron halo ^{14}Be [Lab01] by comparison of the measured two-neutron removal cross sections and neutron angular distributions with the three-body model calculations of Thompson et al. [Tho96].

For the $_5$B-isotopes a weakening of the shell closure is found by spectroscopy [Aoi97]. The main configuration of the 2^- ground state of $^{14}_{5}\mathrm{B}_9$ with nine neutrons is considered to be $\pi(0p^3_{3/2})\nu(0p^2_{1/2}1s^1_{1/2})$ in a single particle picture (fig. 2.5) [Aoi97]. The lowest 1^+ state of ^{14}B is in the same picture a $\pi(0p^3_{3/2})\nu(0p^1_{1/2}0p^{-1}_{1/2}1s^2_{1/2})$ [Aoi97]. In this case the 1^+ state corresponds to the excitation of one $0p_{1/2}$ neutron to the $1s_{1/2}$ orbital. Thus the energy difference $\Delta\epsilon$ between the $1s_{1/2}$ and $0p_{1/2}$ orbitals could be determined. Similar analysis for N=7 and N=9 isotones lead to the picture of a decreasing $\Delta\epsilon$ for Z decreasing from 6 to 4, independent of the neutron number [Aoi97] (fig. 2.7). The reduced shell gap $\Delta\epsilon$ is also observed in the quadrupole moments of the B-isotopes. The quadrupole moments of the odd-even $_5$B-isotopes decrease towards $N = 8$, as expected for a normal shell-closure (fig. 2.9b). However, the effect is very reduced. Often a reduction of $20 - 30\%$ is observed if $2 - 4$ nucleons are removed. Two examples are given in figure 2.8. In figure 2.8a the quadrupole moments of the isomeric states in the Pb-region are compared to the quadrupole moment of corresponding isomers in the doubly magic $^{208}_{82}\mathrm{Pb}_{126}$ [Ney03]. When two neutrons are removed (N=124), the quadrupole moment rises by more than 30%. In figure 2.8b an example in the region of the doubly magic $Z = 8$, $N = 8$ is given. The quadrupole moment of the ground state of $^{19}_{8}\mathrm{O}_{11}$ is about 30% higher than that of $^{17}_{8}\mathrm{O}_9$ with nine neutrons, approaching the doubly magic nucleus $^{16}_{8}\mathrm{O}_8$.

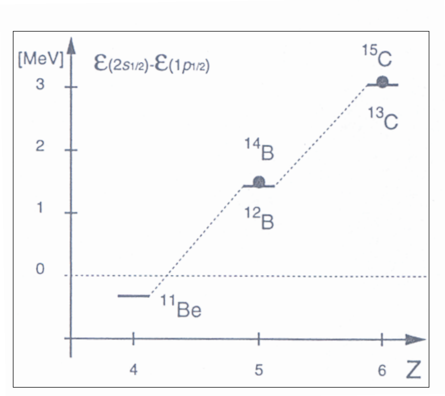

Figure 2.7: *Energy difference between the $\nu 1s_{1/2}$ and $\nu 0p_{1/2}$ orbitals for the nuclei with 7 (horizontal bars) and 9 (filled circles) neutrons as a function of atomic number Z. Picture taken from [Aoi97].*

The magnetic moments of the odd-even B isotopes, which are sensitive to the structure of the unpaired valence particles, increase towards the Schmidt value when the $\nu 0$p-shell is being filled (fig. 2.9a). Their spins are known to be $3/2^-$. This indicates a pure $\pi 0p^3_{3/2}$ configuration. The magnetic moment of the odd-

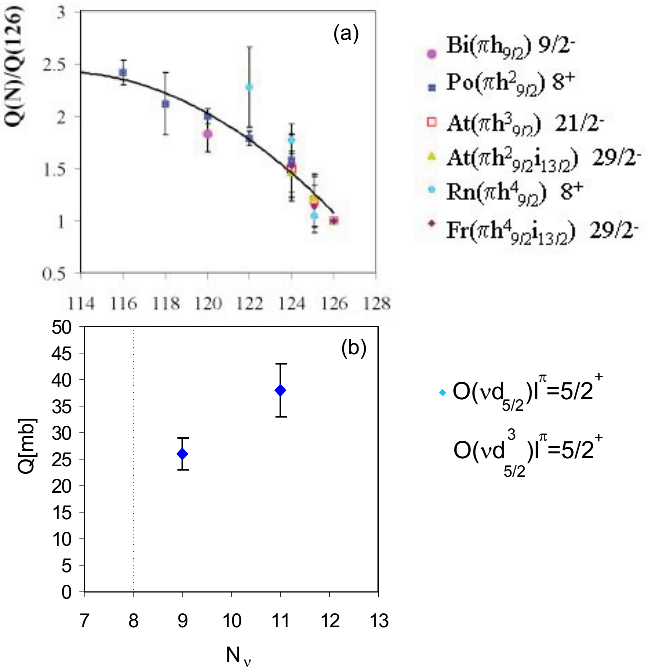

Figure 2.8: *(a) Quadrupole moments of isomers in the Pb-region compared to that of the corresponding isomer in the doubly magic* $^{208}_{82}Pb_{126}$*. Picture taken from [Ney03]. (b) Quadrupole moment of the ground state of the* $^{17}_{8}O_9$ *and* $^{19}_{8}O_{11}$ *isotopes as a function of the neutron number.*

odd ${}^{14}_{5}\mathrm{B}_9$ isotope $\mu({}^{14}_{5}\mathrm{B}_9) = 1.185(5)\mu_N$ [Oku95] can only be explained in the frame of shell model calculations if the $\nu 1s_{1/2}$ orbit is lowered and the gap between the $\nu 1s_{1/2}$ orbit and the $\nu 0d_{5/2}$ orbit becomes larger [Oku95].

For the ${}_3$Li-isotopes the situation is less clear. The spins of ${}^{9,11}_{3}\mathrm{Li}_{6,8}$ are known to be $I^\pi = 3/2^-$ and the magnetic moments of the Li-isotope chain increase towards the Schmidt-value (fig. 2.9a), indicating a pure $\pi 0p_{3/2}$ configuration. This doesn't indicate any disappearance of the $N = 8$ shell gap. However, as demonstrated also in the odd-even B-chain, the magnetic moment is not very sensitive to deformation. The quadrupole moment of ^{11}Li has an error which is too large to allow conclusions about the shell closure to be drawn (fig. 2.9b). Some experimental indications of weakening of the $N = 8$ shell closure in the Li-chain were found in the past. An indirect indication of admixture of the intruder $\nu 1s^2_{1/2}$ configuration in the ground-state of ^{11}Li was given several times by the anomalously large logft values in the β-decay of ^{11}Li [Suz94, Bor97, Aoi97, Ots95, Roe74, Bjo81]. This corresponds to a retarding of the β-decay and can be explained by two effects. If the initial state of the β-decay is loosely bound as in a halo and the final state is deeply bound, the overlap of the single-particle wave functions of the two states of the β-decay becomes small, which retards the β-decay ("halo effect"). A second effect is the possible contribution of the sd-shell to the wave function of the ground state. Because of the absence of sd-shell components in the configuration of the protons, the neutrons that are excited into the sd-shell do not contribute to the β-decay. To describe the experimental data, Otsuka et al. needed the two effects [Ots95]. Another indirect indication came from the study of the unstable ^{10}Li [Zin95]. A low lying s- [Kry93, Zin95] and p-state [You94, Boh93] in the spectrum of ^{10}Li were found. Thompson et al. [Tho94] found that a neutron s state at low energy in the spectrum of ^{10}Li would lead to an ^{11}Li halo with about equal admixtures of $1s^2_{1/2}$ and $0p^2_{1/2}$. A direct interpretation of the experimental results by M. Zinser et al. confirmed an appreciable amount of $1s^2_{1/2}$

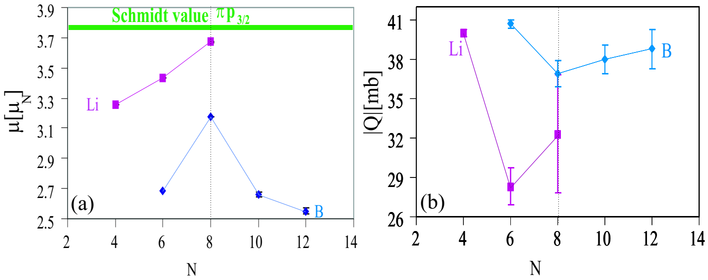

Figure 2.9: *Experimental (a) magnetic moments and (b) quadrupole moments of the odd-even Li and B isotopes measured before this work [Arn87, Arn88, Arn92, Oga03, Oku95, Izu96].*

in the ^{11}Li halo wave function [Zin95].
Recently a direct experimental indication of admixtures in the sd-shell was found [Sim99]. After the fragmentation of ^{11}Li incident on a carbon target, the momentum distribution of the ^{10}Li fragments was studied, which gives access to the momentum distribution of the removed neutron in ^{11}Li. From the shape of the distribution, the $\nu 1s^2_{1/2}$ contribution to the mixture of $\nu 1s^2_{1/2}$ (positive parity) and $\nu 0p^2_{1/2}$ (negative parity) components in the ground state wave function was determined to be $45 \pm 10\%$. In the calculation the $0d_{5/2}$ orbital was not taken into account. Precise values of the quadrupole moments of ^{9,11}Li can indicate an extra mixing of normal and intruder states with at least one neutron in the $0d_{5/2}$ orbital in the total wave function of the ^{11}Li ground state. The two halo neutrons in the configurations $\nu(0d^2_{5/2})$ and $\nu(1s_{1/2}0d_{5/2})$ can couple to 2^+. These neutrons can couple with the proton in the $0p_{3/2}$ orbital, giving the total $((\nu 0d_{5/2})^2_{2+} \otimes (\pi 0p_{3/2})_{3/2-})_{3/2-}$ or $((\nu 1s_{1/2}0d_{5/2})_{2+} \otimes (\pi 0p_{3/2})_{3/2-})_{3/2-}$ configuration. This coupling can enhance the quadrupole moment, while coupling to the $\nu(1s^2_{1/2})_{0+}$ or $\nu(0p^2_{1/2})_{0+}$ configurations would not enhance the quadrupole moment.

Summary

In this thesis the ratio of the quadrupole moments of ^{11}Li and ^{9}Li is determined. There exist two different approaches to describe a possible change of the ^{11}Li quadrupole moment with respect to that of its core ^{9}Li.

1. If the $N = 8$ shell closure is strong enough for the neutron rich ^{9,11}Li nuclei, we will observe a smaller quadrupole moment for the ground state of ^{11}Li than for the ground state of ^{9}Li. If not, as indicated by the observed admixture of $\nu(s_{1/2})^2$ and $\nu(p_{1/2})^2$ configurations in the ground state of ^{11}Li [Sim99], the two quadrupole moments can be equal. Only an admixture of a configuration with at least one neutron in the $0d_{5/2}$ orbital, in the ground state wave function will enhance the quadrupole moment.

2. If the two loosely bound neutrons of the halo nucleus ^{11}Li polarize the proton distribution of the core, the quadrupole moment of ^{11}Li will be different from that of ^{9}Li. When the wave function of the two loosely bound neutrons have only contributions from the $1s_{1/2}$ and $0p_{1/2}$ orbitals, both neutrons will couple to 0^+ and the quadrupole moment of ^{11}Li could become smaller than that of ^{9}Li. When one of the two loosely bound neutrons is in the $0d_{5/2}$ orbital, both neutrons can couple to 2^+. This could give rise to a quadrupole moment of ^{11}Li, being larger than that of ^{9}Li. If the core and the two loosely bound neutrons are fully decoupled, the quadrupole moments of ^{9}Li and ^{11}Li will be equal.

In the two theories, an admixture of the configuration with two neutrons coupled to 2^+ in the wave function of the ^{11}Li ground state will enlarge its quadrupole moment.

Because of the almost constant charge-changing cross sections of $^{8-11}$Li [Bla92] and the similar quadrupole moments of ^{9,11}Li [Arn92], the expected effect is small ($< 10\%$) and a high-precision measurement of the ^{9,11}Li quadrupole moments is needed.

2.3 Test of new theoretical models

The newly discovered phenomena as halos and disappearing shell closures could not be explained by simple shell model calculations. Therefore new models were developed. Some models have already calculated the nuclear moments of the Li isotopes [Nav98, Var95, Var02, Ots99, Des97, Kan01]. Other models, such as microscopic models using hyperspherical coordinates and functions, are working at the limits of computational power [Tim02]. They are not yet able to calculate the nuclear moments of ^{11}Li. Our new precise experimental results will provide now or in future a stringent test of these models.

2.4 Structure of this work

After the physics motivation in this first chapter, the second chapter describes the production of spin-oriented Li-isotopes. The technique of optical pumping is explained in this chapter.

A third chapter explains some level mixing techniques to measure nuclear moments via a resonant destruction of the created spin-orientation.

The fourth chapter handles about calibration- and test measurements in order to optimize some parameters of the β-NMR (Nuclear Magnetic Resonance) set-up.

In the next chapter we come to the experimental results with a section about magnetic moments and one about quadrupole moments behind the section on error propagation. The nuclear moments of ^{9,11}Li were measured relative to those of ^{8}Li, which are known up to an accuracy of 0.001% for the g-factor and 2% for the quadrupole moment [Rag89]. For the earlier measurements of $Q(^{8,9}\mathrm{Li})$, the quadrupole moment of ^{7}Li was used as a reference. Recently this quadrupole moment has been revised [Pyy01]. The presently adopted value is $Q(^{7}\mathrm{Li}) = -40.0(3)$mb [Voe91, Pyy01]. This makes a revision of the earlier published values of $Q(^{8,9}\mathrm{Li})$ necessary.

The precision on the ratio $\frac{Q(^{11}Li)}{Q(^{9}Li)}$ is obtained from the precision on the ratio of the observed quadrupole frequencies. This doesn't depend on the precision of the absolute values of the quadrupole moments and can, in principle, be better than 2%.

The last chapter is devoted to the interpretation of the experimental results within the nuclear shell model. This model is not able to answer all our questions, and more accurate models are under development. Therefore an overview of the present status of these more accurate models is also presented.

The expected difference between the quadrupole moments of ^{9}Li and ^{11}Li is small. To improve the experimental accuracy, some experimental parameters were optimized with less exotic Li isotopes such as ^{8,9}Li. In each section the optimization of the parameters explained in that section is given. Here I give a short overview of the different optimized parameters: an attempt was made to optimize the production rate by using different targets. The power and frequency of the laser light were adjusted to create maximal polarization. Several implantation crystals have been investigated to find the host with the best implantation properties and a suitable electric field gradient. In addition, the homogeneity of the static magnetic field was tested and measurements for different rf-powers were performed.

Chapter 3

Production of spin-oriented Li-isotopes

In this chapter, the production of the Li-isotopes at ISOLDE is described first. Afterwards, the creation of atomic and nuclear spin-orientation via the technique of optical pumping is explained.

3.1 Production of Li-ions

The experiments are performed at the ISOLDE[1] experimental facility at CERN. A schematic view of the ISOLDE hall is given in figure 3.1.
The ISOLDE facility uses the PSB booster of the large proton synchrotron PS to accelerate the pulsed proton beam to 1.4GeV. The proton pulses (2.4μs wide) consist of about 3.10^{13}protons. They are separated by 1.2s and distributed to several facilities. In most of the performed experiments we got about 7 pulses out of the 14 pulses that form a "super cycle" of 16.8s.

These protons irradiate a target material which is situated in a heated tube, kept at a temperature of about 1800°C. For the choice of the target material one can be lead by [iso, Let97]. Both Ta and UC_2 were used as target material. The fragmented isotopes evaporate from the target material and diffuse via a drift tube to a connected ion source [Kug93, Kug00]. For the Li alkali-metals with a low work function a surface ion source made of a hot W wire is used. The ion source and the whole target vacuum-chamber are kept at high voltage ($HV_{ISOLDE} \approx +60$kV) to accelerate the ions up to 60keV.
Once extracted, the ions are mass separated. There are two mass separators at ISOLDE, called GPS (General Purpose Separator) and HRS (High Resolution Separator). The GPS consists of one dipole magnet and has a resolution of $\frac{m}{\Delta m} = 2400$. The HRS consists of two dipole magnets and has a higher resolution of $\frac{m}{\Delta m} = 5000$. For the very light Li isotopes the resolution of the GPS

---

[1] Ion Separator On Line DEvice [Isolde, Kug93, Kug00]

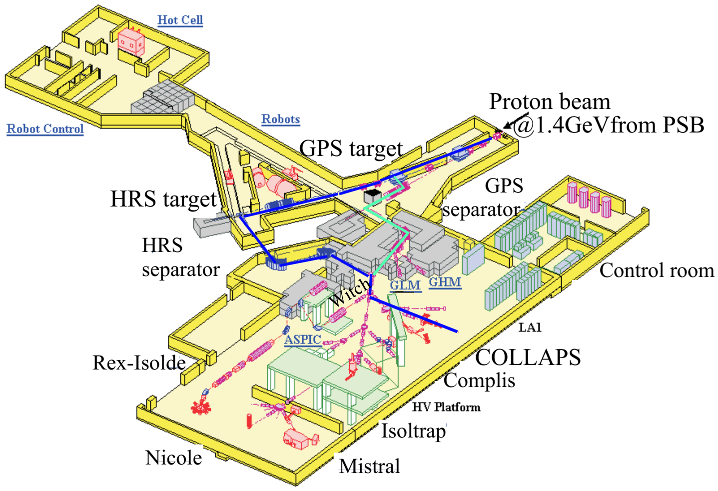

Figure 3.1: *Schematic view of ISOLDE at CERN. Figure taken from [Isolde].*

is good enough because there are almost no isobaric contaminants in this mass region. In the experiments of 2003 the GPS was used. In October 2001 the HRS was used. In June 2002, two different targets, which were each installed at the front-end of a different separator, were used. In that experiment, the GPS was used for the separation of ^{8,9}Li. The HRS was used for the separation of ^{11}Li. After separation, the ions are guided to the experimental COLLAPS set-up.

The time between a proton pulse impinging onto a target and the arrival of Li-ions in the COLLAPS set-up is of the order of 100ms. The main contribution is the release time out of the target ($\approx$ 100ms) [Ben02, Kos00]. The time needed for the transport towards the set-up ($\approx 10^{-5}$s) is negligible compared to this release time.
The release time is small compared to the half life of ^{8}Li ($T_{1/2}(^{8}\mathrm{Li}) = 838(6)$ms). So most of the produced ^{8}Li-ions arrive at the set-up, leading to a high observed count-rate of $> 10^{6}\frac{\beta}{pulse}$. The release time is of the same order as the half life of ^{9}Li ($T_{1/2}(^{9}\mathrm{Li}) = 178.3(4)$ms). The observed count rate stays sufficiently high ($> 10^{5}\frac{\beta}{pulse}$). The β-decay of the Li-isotopes was detected via two plastic scintillator telescopes at the end of the COLLAPS set-up.
The half life of ^{11}Li ($T_{1/2}(^{11}\mathrm{Li}) = 8.5(2)$ms) is one order of magnitude shorter than the release time. This reduces enormously the observed amount of Li-isotopes. In addition, the large neutron excess of ^{11}Li ($Z = 3$, $N = 8$) causes a low production rate. To increase the observed amount of Li-isotopes, it is important to use the optimal target which minimizes the release time and maximizes the production rate.
We used a UC_2 foil and two different Ta targets (table 3.1). The first Ta target

(in the table: "thick") consists of a rack of roled Ta foils. The foils themselves have a thickness of about 20μm. The total thickness of the roled foils is $122\frac{g}{cm^2}$. The second Ta target (in the table: "thin") consists of different thin Ta foils of about 2μ m (added to a total thickness of $13\frac{g}{cm^2}$) thickness, which is designed for short-lived isotopes [Ben02].

Table 3.1: *(a) β-counts/pulse in one of the detectors of the scintillator telescopes at the end of the COLLAPS set-up with a typical current of 2μA. (b) Deduced ^{A}Li-rates after correction for the efficiency of one of the detectors and the loss due to beam-transport and normalized for a current of 1μA. (c)Tabulated ion-rate coming out of the ion source(per pulse) normalized for a current of 1μA [Let97, iso].*

		^{8}Li	^{9}Li	^{11}Li
(a)	**UC$_2$ target**			
	1990		$9*10^4$	200
	October 2001	10^6	10^5	200
	Ta target thick			
	1990min. ISOLDE2	$8*10^6$	$4*10^5$	40
	1990max. ISOLDE2			150
	June 2002	$2*10^6$	$3*10^5$	180
	Ta target thin			
	June 2002 beginning		$9*10^5$	260
	June 2002 averaged over one night			140
	June 2002 end		$4*10^5$	50
(b)	**UC$_2$ target**			
	1990 ISOLDE2		$9*10^5$	2000
	October 2001	$1*10^7$	$1*10^6$	2000
	Ta target thick			
	1990min. ISOLDE2	$8*10^7$	$4*10^6$	400
	1990max. ISOLDE2			1500
	June 2002	$2*10^7$	$3*10^6$	1800
	Ta target thin			
	June 2002 beginning		$9*10^6$	2600
	June 2002 averaged over one night		$4*10^6$	1400
	June 2002 end			500
(c)	**UC$_2$ target**	$5.8*10^7$	$3.9*10^6$	1400
	Ta target thick	$8*10^8$	$7*10^7$	
	Ta target thin	$5.8*10^8$	$1.7*10^7$	7000

In table 3.1, the different count rates in one of the scintillator telescopes (a) are shown, together with the expected number of ions per pulse coming out of the ion source (c). We have to correct for the loss in beam transport of about 50% and the efficiency of the scintillator-telescope of about 10%. After this correction, the count-rate is normalized to a pulse of 1μA. Note that the corrected production rates (b) are smaller than the expected numbers for ^{8,9}Li. The production rate of ^{11}Li ions using a UC$_2$ target is more or less as expected by the tabulated value. The thin Ta target produces less ^{11}Li isotopes than expected. In addition, the yield drops very fast as a function of time[2]. On the other hand, most ^{11}Li atoms were produced with this target. This fact and the promise of having a better "thin Ta target" for the experiment with the optimal set-up in May 2003 and June 2003, lead to the conclusion of using the "thin Ta target" for the production of ^{11}Li. To spare this target, we chose a different target for the production of ^{8,9}Li, i.e. the "thick Ta target".

3.2 Creation of nuclear spin-orientation

3.2.1 Spin-orientation

An ensemble of nuclei (atoms) with spin I is spin-oriented if the nuclear (atomic) spins have a preferential direction in space. Choosing a quantization axis Z allows the description of this spin-orientation in terms of the probability $P(m)$ that the nuclear spin has a projection $|m\rangle$ onto this axis. If the quantization axis is an axial symmetry axis of the oriented ensemble, the orientation is fully determined by these probabilities $P(m)$. For a non-axially symmetric oriented ensemble, the density matrix $\rho_{mm'} = \langle m|\rho|m'\rangle$ is necessary for the description of the spin-orientation. The diagonal elements $\rho_{mm} = P(m)$ describe the population of the different spin-projections. The non-diagonal elements describe the coherence between different m-states. The density matrix is related to the density tensor ρ_k^n [Stef75]:

$$\rho_k^n = \sqrt{2k+1}\sum_{mm'}(-1)^{I+m}\begin{pmatrix} I & I & k \\ -m & m' & n \end{pmatrix}\langle m|\rho|m'\rangle \tag{3.1}$$

and to the orientation tensor

$$B_k^n = \sqrt{2I+1}\rho_k^{n*} \tag{3.2}$$

If there exists axial symmetry, but the reflection symmetry is broken, i.e. $P(m) \neq P(-m)$, the ensemble is spin-polarized (fig. 3.2).

The normalized polarization is defined such that for maximal positive polarization, with all spins parallel to the quantization axis, $P(I) = +1$ and for maximal negative polarization, with all spins anti-parallel to the quantization axis, $P(I) = -1$ [Ney03]

$$P(I) \equiv \frac{\sum_m mP(m)}{I} \tag{3.3}$$

The polarization is related to the first order orientation tensor [Kra86]

$$P(I) = -\sqrt{\frac{I+1}{3I}}B_1^0(I) \tag{3.4}$$

---

[2] After the experiment, sintered foils were observed. This can explain the enormous drop in the yield.

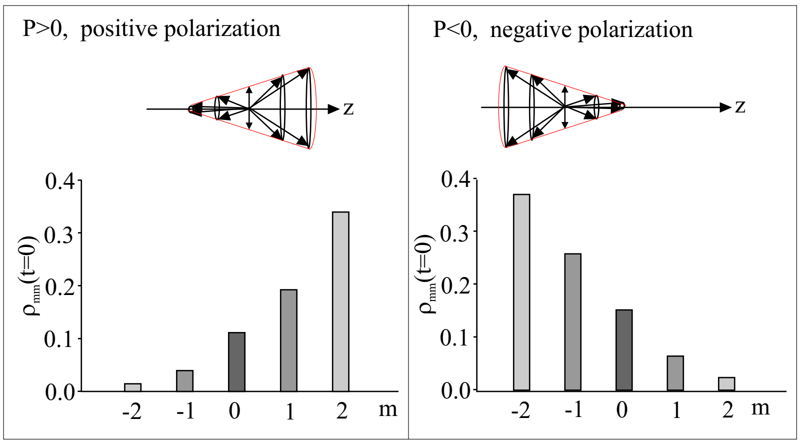

Figure 3.2: *Spins and population of the m-levels for a polarized ensemble of nuclei.*

3.2.2 Creation of nuclear spin-orientation

In figure 3.3 a schematic overview of the COLLAPS set-up is given. Laser light (fig. 3.3a) is produced with a continuous wave (CW) dye laser [3] focussed with lenses and guided towards the set-up. After the focussing, the laser beam has a diameter of about 7mm. A prism of calcite (fig. 3.3b) polarizes the laser light linearly. A $\frac{\lambda}{4}$ wave plate (fig. 3.3c), consisting of a quartz plate, is placed where the laser light enters the set-up. This plate introduces a phase shift $\delta = \frac{\pi}{2}$ between the orthogonal polarization components of the electric field $\vec{E} = E_0 cos(\omega t)\vec{i} + E_0 cos(\omega t + \delta)\vec{j}$ when the incoming wave of the laser light makes an angle of $\frac{\pi}{4}$ with the optical axis of the quartz plate. Thus the laser light becomes circularly polarized. This plate will be turned by 90^o to change the sign of the polarization.

The beam of laser light and the ion beam (fig. 3.3d) are made collinear by two vertical deflection plates (fig. 3.3e) at about 2kV which deflect the ions at 60keV by 10^o. Then the ions are accelerated (or decelerated) by a voltage V_{acc} (fig. 3.3f), which can be varied from about -10kV to about $+10$kV.

The accelerated ions are guided to the charge exchange cell (CEC)(fig. 3.3g) full of Na vapor, which neutralizes the Li$^+$ ions [4]. Solid Na is heated to vaporized

---

[3] A dye is a chemical molecule in a liquid solvent. The used dye is DCM(LC6501), which is $C_{19}H_{17}N_3$ (4-Dicyanmethylene-2-methyl-6-(p-dimethylaminostyryl)-4H-pyran). The used solvent is a mixture of 95% ethylene glycol and 5% benzyl alcohol. This laser is pumped by an Argonion ArII laser.

[4] The used reaction is $Li^+ + Na \rightarrow Li + Na^+ + \Delta E$. Here ΔE is the difference in ionization energies of Na ($E_{ion}(Na)$ = 5.14eV) and Li ($E_{ion}(Li)$ = 5.39eV). Other properties of Na are its solid density of $\rho = 968\frac{mg}{cm^3}$, its melting temperature $T_{melting}$ = 370.87K and boiling temperature T_{boil} = 1156K [CRC77]. The electronic configuration of Na is $1S^2 2P^6 3S$ and that of Li is $1S^2 2S$.

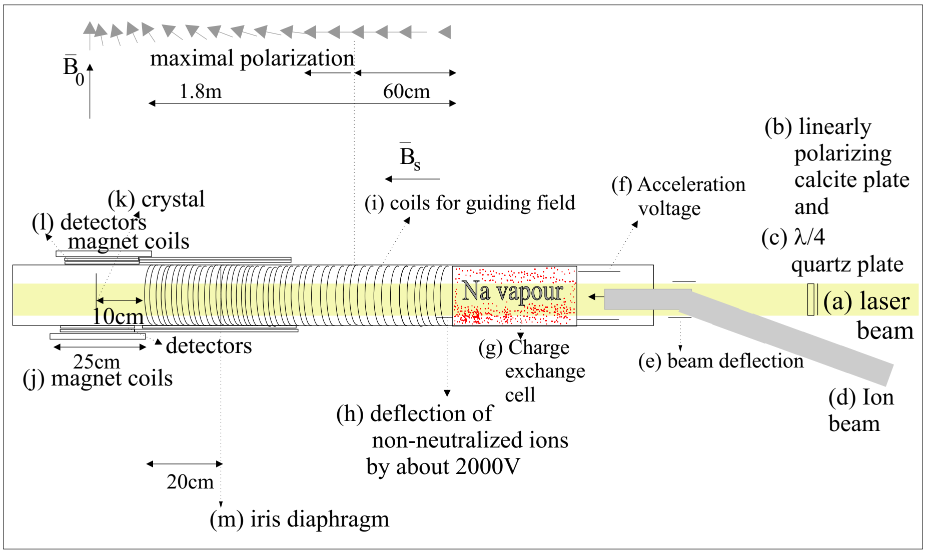

Figure 3.3: *Schematic view of the experimental COLLAPS set-up.*

Na by a coaxial thermo cable at 40V and about 1.2A around the tube filled with Na. The reached temperature is about 560K, giving a Na vapor pressure of about 10^{-2}mbar [Vee03, Gei02] and a neutralization efficiency of about 50%. The non-neutralized ions are deflected out of the beam by a deflection plate on a high voltage (e.g. 2000V) (fig. 3.3h), while the neutral atoms continue their way.

Once the atoms are neutralized, the optical pumping process can start [Kas50, Kas57, Coh66, Ber65, Kei96, Kop69]. This means the atoms are "pumped" to one m_F-state via laser light ("optical").

In figure 3.4 the concept of optical pumping is visualized for ^{8}Li atoms with three electrons and nuclear spin $I = 2$. The ground state of the valence electron is the $2S$ orbital with an orbital angular momentum $l = 0$. The energy gap with the first exited state $2P$ ($l = 1$) is $\Delta E = 1.848$eV[5]. The coupling of the intrinsic electron spin $s = 1/2$ with its orbital angular momentum l, to the total spin of the electron J, results in the fine splitting of the atomic levels [Sob79]. This splitting is 10^5 times smaller than the splitting between the atomic ground state and the first atomic excited state. The total electron spin J couples with the nuclear spin I to the total atomic spin F due to the hyperfine interaction [Sob79, Cot02]. This hyperfine splitting is 10^3 times smaller than the fine splitting.

Each of these hyperfine levels F has $2F+1$ degenerated sublevels $|F, m_F\rangle$, named

---

[5] To excite free ^{8}Li atoms at rest we need an electromagnetic wave, e.g. laser light, with a frequency $\nu_{laser} = \frac{\Delta E}{h} = 0.447\ 10^{15}$Hz. This corresponds to a wavelength $\lambda = \frac{c}{\nu} = 670.976$nm (red light) and a wave number $k = \frac{1}{\lambda} = 14903.67cm^{-1}$.

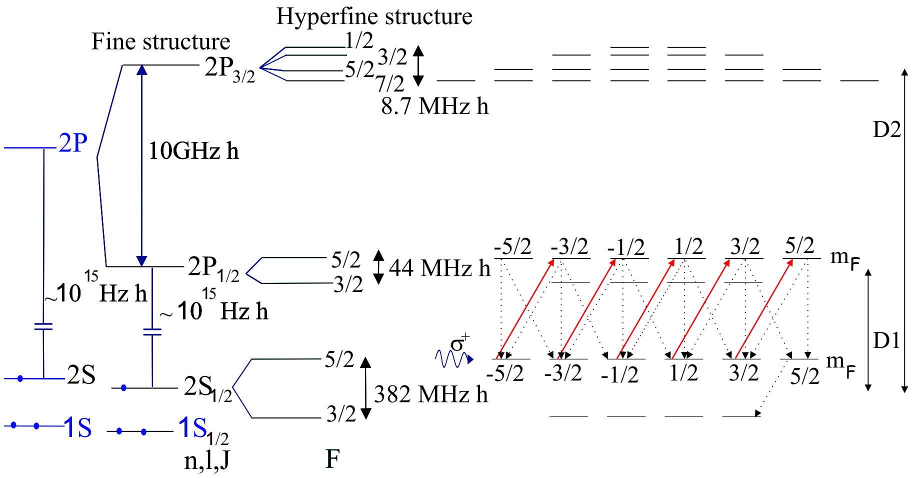

Figure 3.4: *Principle of optical pumping on the atomic m_F levels of ^8Li with $I = 2$. The drawn energy gaps are not in scale.*

by their projection m_F on the quantization axis. While m_F is a good quantum number, the spin projections of the nuclear spin m_I and electron spin m_J are not good eigenstates of the free atom. It are the m_F sublevels that are involved in the optical pumping process. Right σ^+ (left σ^-) circularly polarized laser light induces transitions from the ground state to an excited state[6], obeying the selection rule $\Delta m_F = +(-)1$ [Coh66]. The subsequent spontaneous emission obeys the selection rules $\Delta m_F = \pm 1, 0$. The continuous process of excitation and decay continues until the level $m_F = F(-F)$ is reached, which can not be excited by the σ^+ (σ^-) laser light. After some pumping cycles, typically of the order of 0.5μs [Kei96], most atoms end up in the $m_F = F(-F)$ level. A high amount of atomic spin-polarization is created. The symmetry axis of the polarized atomic ensemble is along the laser beam direction.

Over the whole optical pumping region, the atoms are subjected to a small "guiding" magnetic field (fig. 3.3i). This field B_s is induced by a DC current through coils, shielded with μ-metal, around the beam-line over a length of 1.8m. With a velocity of $v = 1.2\ 10^6 \frac{m}{s}$ the atoms will pass during 1.5μs in the optical pumping section. In the first 60cm maximal spin-polarization is created [Kei96]. Behind the optical pumping region, the atoms are subjected to an additional high static magnetic field of about $B_0 \approx 3000$G (fig. 3.3j), perpendicular to the guiding field. The atomic spins, precessing around the total field, rotate

---

[6] The transition from $2S_{1/2}$ to $2P_{1/2}$ is called a D1-transition. The transition from $2S_{1/2}$ to $2P_{3/2}$ is called a D2-transition.

from the direction of the guiding field $\vec{B}_s$ to the direction of the high static magnetic field $\vec{B}_0$. This rotation of the atomic spins should go slow enough, i.e. adiabatically, in order to keep the spin-orientation [Kei96]. Therefore the guiding field was increased towards the large magnetic field from about 10G to 20G. Combined with the stray field of the static magnetic field B_0 this causes a slightly increasing field in the direction of the field $\vec{B}_0$ and thus an adiabatic rotation of the atomic spins.

Atomic spin polarization implies an indirect spin polarization of the nuclei via the hyperfine interaction. In a high magnetic field, the hyperfine interaction becomes negligible compared to the Zeemann-interactions (fig.3.5) for a free atom [Kei96, Ney93b]. The electron Zeemann-interaction dominates the nuclear Zeemann-interaction because the Bohr-magneton is 1836 times larger than the nuclear magneton[7]. The guiding field is small enough to keep the coupling of the electron- and nuclear spin and thus to allow the creation of atomic spin orientation. The large static magnetic field B_0 at the end of the set-up decouples the electron- and nuclear spins. Like this an oriented ensemble of nuclear spins is created just before the implantation of the Li-isotopes into a single crystal (fig. 3.3k). This is important because the electron spins will loose very quick their orientation due to the interaction with the electrons of the crystal lattice. The nuclear spin-relaxation time due to the interaction of the electrons in the

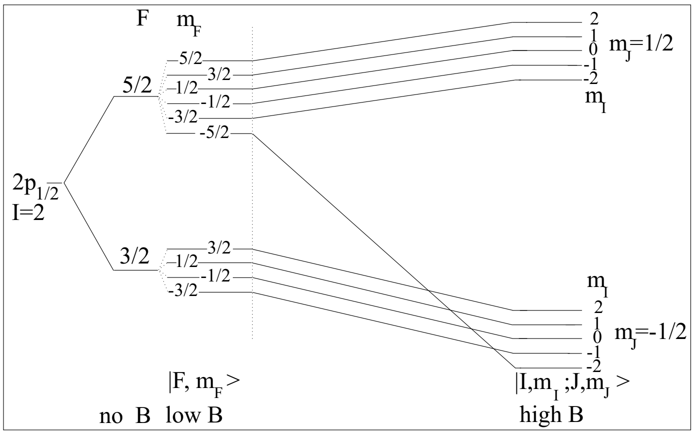

Figure 3.5: *Decoupling of the electron spin J and nuclear spin I in the presence of a static magnetic field, higher than some hundreds of Gauss (Breit-Rabi diagram). At high B, the eigenstates of the system approach the eigenstates $|Im_I; Jm_J\rangle$ of the Zeemann-interaction. At low field we get $|(IJ)Fm_F\rangle$ states which are linear combinations of the $|Im_i; Jm_J\rangle$ states [Ney93b].*

---

[7] The precession frequency of the electrons $\nu_{L,e} = \frac{g_e \mu_B B_0}{h}$ while that of the nuclei $\nu_{L,n} = \frac{g_n \mu_N B_0}{h}$

crystal lattice with the nuclei, is much longer than the electronic spin-relaxation time. It varies from 0.5ms up to several seconds or minutes, depending on the host. So the decoupling of nuclear- and electron spins allows a slower relaxation of the nuclear spin-orientation.

The spin-orientation is monitored via the β-asymmetry by two plastic (NE102A) scintillator telescopes (fig. 3.3l). Each detector is biased with a voltage of -2.150kV. Each telescope consists of two thin ΔE detectors of 1mm, placed at respectively 0^o and 180^o with respect to the axis of the static magnetic field $\vec{B}_0$. In each of the detectors the electrons loose about 300keV. The β-asymmetry is then defined as $\frac{N(0^\circ)-N(180^\circ)}{N(0^\circ)+N(180^\circ)}$ with $N(0^\circ)$ and $N(180^\circ)$ the number of counts in the detector placed at respectively 0^o and 180^o with respect to $\vec{B}_0$. To eliminate noise in the β-spectra, coincidences between the two detectors of one telescope were taken. The individual and coincidence counts were stored in the data acquisition.

About 20cm before the coils that induce the large static magnetic field B_0, an "iris" diaphragm (fig. 3.3m) is placed. This is a kind of variable collimator to be able to cut the halo around the beam spot (typically about 7mm diameter). The diameter of the iris is variable between 3mm and 9mm. This diaphragm can be used for the tests of the collinearity of the laser beam with the ion beam. If the amount of created polarization doesn't decrease by opening the iris diaphragm, the two beams are collinear.

This "optical pumping" technique creates rather high polarization ($P \leq 30\%$ [Kei96]), but it is not universally applicable. In general, the atomic level scheme needs to be studied case by case to check the feasibility of the technique. For all alkali-atoms the atomic level scheme is simple and similar. Singly ionized alkali-metals have a closed shell configuration like the noble gasses. E.g. for Li^+, the energy gap between the ground state $1s^2$ and the first exited state $1s^12s^1$ is $\Delta E = 59$eV, corresponding to a needed wavelength $\lambda = 21$nm. Laser light with this wavelength is experimentally hard to create[8]. For neutral alkali metals the needed laser light to excite the atoms has a wavelength in the range of the electromagnetic spectrum of visible light. In addition the atomic excitation scheme is such that there are no major orientation losses. So this technique is very suitable for neutral atoms of alkali-metals or ions of alkaline earth metals. For other elements the atomic excitation scheme is often more complicated such that it is more difficult (if not impossible) to create sufficient amount of spin-orientation.

---

[8] The electromagnetic spectrum of visible light goes from about $\lambda = 400$nm until $\lambda = 700$nm.

3.3 Doppler shifted laser frequency

3.3.1 Calculation of the Doppler shifted frequency

To resonantly excite the accelerated Li atoms with the laser light, the Doppler shifted laser frequency needs to be applied. When the total acceleration voltage V_{tot} is known, one can calculate this frequency [Kei96, Gei02, Arn86]:

$$\nu_{L,D} = \nu_0 + \delta\nu_D = \nu_0 \frac{1+\beta}{\sqrt{1-\beta^2}} \tag{3.5}$$

with ν_0 the resonant laser frequency to excite atoms in rest and

$$\begin{aligned} \beta &= \frac{v}{c} = \sqrt{1 - \frac{m^2c^4}{(eV_{tot}+mc^2)^2}} \\ &\approx \sqrt{\frac{2eV_{tot}}{mc^2}} \end{aligned}$$

with e the charge of an electron, m the mass of the isotope and $v(c)$ the speed of the ions (light). In the approximation on the second line eV_{tot} is assumed to be small in comparison with mc^2. Applying this approximation once more gives

$$\nu_{L,D} \approx \nu_0(1 + \sqrt{\frac{2eV_{tot}}{mc^2}}) \tag{3.6}$$

In principle it is possible to excite individual hyperfine levels, which can enhance the amount of produced spin-polarization. The produced polarization is different for each resonant hyperfine transition.
To find the correct ν_0 for a particular transition, one needs to know the hyperfine splitting and thus the magnetic and electric coupling constants for the ground state (and/or excited state of the hyperfine structure), respectively A and B [Ott89, Sob79, Cot02] (fig. 3.6). In first order the energy splitting is given by

$$\Delta E(F) = \frac{AK}{2} + B\frac{3/4K(K+1) - I(I+1)J(J+1)}{2(2I-1)(2J-1)IJ} \tag{3.7}$$

with

$$\begin{aligned} K &= F(F+1) - I(I+1) - J(J+1) \\ A &= \frac{\mu_I B(0)}{IJ} \\ B &= eQV_{zz}(0) \end{aligned}$$

with B(0) the magnetic field induced by the atomic electrons at the place of the nucleus, μ_I the nuclear magnetic moment, Q the spectroscopic nuclear quadrupole moment and $V_{zz}(0)$ the electric field gradient induced by the atomic electrons at the place of the nucleus. The magnetic coupling constant A will be the largest for s-electrons. For $J = 1/2$ electron states, such as $P_{1/2}, S_{1/2}$ electron states, the quadrupole coupling constant $B = 0$ because they do not induce an electric field gradient. In addition the quadrupole moments of the Li-isotopes are small. Therefore the hyperfine splitting of the ground-state of Li($2S_{1/2}$) will be fully determined by the magnetic coupling constant A.

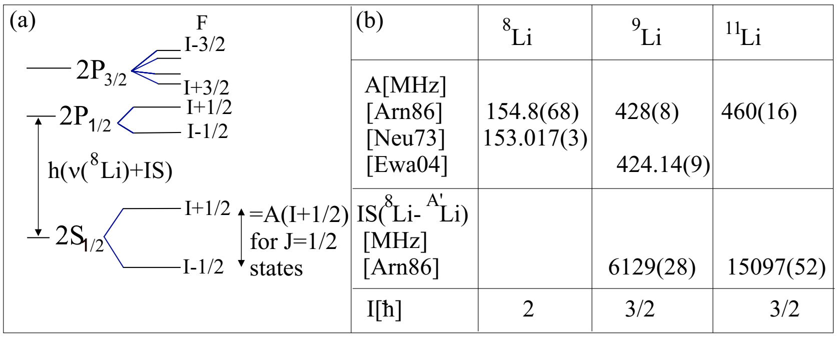

(b)	^{8}Li	^{9}Li	^{11}Li
A[MHz]			
[Arn86]	154.8(68)	428(8)	460(16)
[Neu73]	153.017(3)		
[Ewa04]		424.14(9)	
IS(^{8}Li- $^{A'}$Li) [MHz] [Arn86]		6129(28)	15097(52)
I[ħ]	2	3/2	3/2

Figure 3.6: *(a) Hyperfine structure for* $^{A'}$*Li. (b) The total isotope shift and the magnetic coupling constant for some Li-isotopes.*

The resonance frequency ν_0 for exciting an electron from the $2S_{1/2}$ to $2P_{1/2}$ level, is dependent on the isotope. The isotope shift IS [Gei02, Lie91, Ott89, Sob79, Kin84] has two causes: the change in mass between the isotopes (mass shift) and the change in volume and deformation between isotopes, leading to a change of the electrostatic potential (field shift or volume shift). For light atoms as Li, the field shift is 10^4 times smaller than the mass shift. In figure 3.6 we tabulated the measured isotope shifts [Arn86]

$$IS = K_{MS}\frac{m_{A'} - m_A}{m_{A'}m_A} + F_{el}\delta\langle r^2\rangle^{AA'} \tag{3.8}$$

with K_{MS} the mass factor and F_{el} the electronic factor, which are each element dependent constants [Kin84, Gei02]. m_A and m'_A are the masses of the isotopes and $\delta\langle r^2\rangle^{AA'}$ is the difference in the mean square charge radii between isotope A' and the reference isotope A.

3.3.2 Tuning the resonance wavelength for doppler shifted atoms

The total uncertainty on the exact resonance frequency to apply is rather high, due to systematic errors on the total acceleration voltage V_{tot} ($\Delta V = 5 - 10V$), on the read-out of the used frequency of the laser light ($\Delta\nu_{read} = 300$MHz) and the uncertainties on the isotope shifts (fig. 3.6). Therefore we have to verify experimentally which frequency creates atomic spin-polarization, by scanning

the Doppler shifted frequency. By monitoring the β-asymmetry during such "hyperfine scan" the resonance where polarization is created can be found.
The easiest way to vary the Doppler shifted laser frequency is to modify the beam velocity with a varying voltage V_{acc} and to keep the frequency of the laser light constant. This voltage V_{acc} will accelerate the positively charged ions when this voltage is negative. It will decelerate the ions when it is positive. The total voltage V_{tot} is then the difference between the ISOLDE high voltage and the voltage V_{acc}.

$$\begin{aligned} V_{tot} &= HV_{ISOLDE} - V_{acc} && (3.9) \\ &= HV_{ISOLDE} - (V_{fluke} + 50V_{scan}) && (3.10) \end{aligned}$$

consists of the ISOLDE high voltage of about $HV_{ISOLDE} \approx 60kV$ and the additional voltage V_{acc}. On its turn, V_{acc} consists of a fixed voltage $-10kV \leq V_{fluke} \leq 10kV$ provided by a Fluke power supply and a varying voltage $-10V \leq V_{scan} \leq 10V$ which is amplified by a factor of 50. The read-out of the additional voltage V_{acc} is done with a high precision digital PREMA voltage meter and is stored in the acquisition. The minimal reading time of this precision meter is 2s. During the experiment in October 2001 and a part of the experiments in June 2002, May 2003 and June 2003, this reading time was accidentally put too short. Therefore only the set-value of the V_{fluke} is available, which has a large systematic error ($\approx$ 20V). The accuracy on the read voltage with the PREMA meter is 10^{-4}.
Once the right Doppler shifted frequency is found, V_{scan} will be fixed. The created polarization will allow β-NMR-NQR measurements for the determination of the nuclear moments.

In figure 3.7 an example of a "hyperfine scan" is given [9]. The hyperfine structure of the $2S_{1/2}$ and $2P_{1/2}$ levels in ^{8}Li is scanned. In this scan four transitions are possible.

Due to the high power of the laser light (more than $50\frac{mW}{cm^2}$), the linewidth of the power broadened resonances is larger than the hyperfine splitting of the $2P_{1/2}$ level ($FWHM \approx$ 100MHz $\approx$ 0.14V) [Cit77]. The two overlapping resonances form one broader resonance with a linewidth of about 150MHz ($FWHM = 0.22(1)$V). So only two resonances are visible in the measured β-asymmetry shown in figure 3.7b. Out of the distance of the two resonances[10]

---

[9] A program HFSSIM is made by the COLLAPS group to simulate a "hyperfine scan". It calculates the needed voltage for a given hyperfine structure and Doppler-shifted wavelength. As an input it needs the used wave number $[\frac{1}{cm}]$ and linewidth [MHz] of the laser light, the needed total voltage [V] for a reference nucleus. From this reference nucleus, the mass[u], total electronic spin[$\hbar$] of the ground state and excited state has to be given. Afterwards you can give as an input of different isotopes with its mass[u], nuclear spin[$\hbar$], isotope shift [MHz] with respect to the reference nucleus, A_{ground} [MHz], B_{ground} [MHz], $A_{excited}$ [MHz] and $B_{excited}$ [MHz].

[10] To find the positions of the resonances in such "hyperfine scans" the spectra are fitted with Lorentzian curves. This is only an approximation of the real line shape. But it is a sufficient approximation for our purposes.

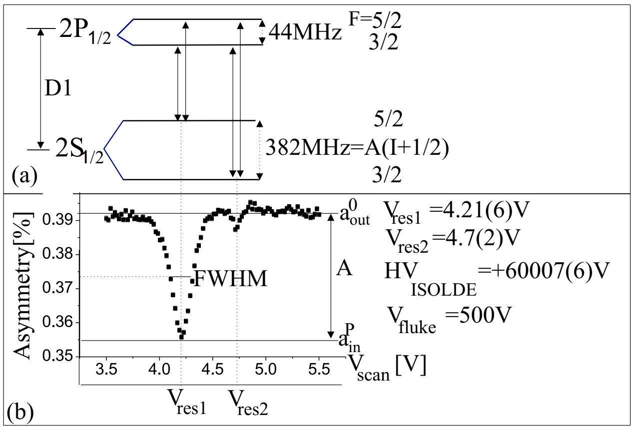

Figure 3.7: *(a) Scanned transitions for* ^{8}*Li in a "hyperfine scan" for the D1-line. (b) Example of a "hyperfine scan" of* ^{8}*Li in Si with as power of the laser light* $W = 75mW$*.* $A = 3.8(1)\%$*,* $FWHM = 0.22(1)\,V$*.*

and equation 3.6, we can get a rough determination of the hyperfine splitting of the ground $2S_{1/2}$ level:

$$\begin{aligned}&\frac{\Delta E(2S_{1/2}(F=5/2)-2S_{1/2}(F=3/2))}{h}\\&= A(I+1/2) = \nu_{Doppler1} - \nu_{Doppler2}\\&= \frac{\nu_0}{c}\sqrt{\frac{2e}{m(^8Li)}}(\sqrt{|V_{tot1}|}-\sqrt{|V_{tot2}|})\end{aligned}$$

The mass of ^{8}Li is 8.0224867(5)u [Aud95], $e = 1.602176462(63)\,10^{-19}$C and $c = 2.99792458\,10^8\,\frac{m}{s}$ [NIST99]. In this example the total acceleration voltage applied at the position of the first peak is $V_{tot1} = +59296(6)$V and $V_{tot2} = +59271(7)$V. This gives us an energy splitting of the $2S_{1/2}$ level $\Delta E = 388(20)$MHz or $A = 155(8)$MHz ([11]). This is in agreement with the known coupling constant A (fig. 3.6). This allows also a rough determination of the magnetic moment if the magnetic field induced by the electrons at the place of the nucleus is known. In this example we scanned a range of $V_{scan} = 3.2$V to $V_{scan} = 5.5$V, corresponding to a range of $\Delta\nu = 1726$MHz, in 100 channels with a step of $\Delta V = 0.025$V, corresponding to $\Delta\nu = 19$MHz.

In resonance, spin-polarization is created. The asymmetry in resonance is called a^P_{in}. Out of resonance, there is no polarization and the instrumental asymmetry is called a^0_{out}.

---

[11] In this calculation only the difference in voltage is important. So the systematic error on V_{fluke} cancels out.

The amplitudes $A = a^0_{out} - a^P_{in}$ of the resonances are proportional to the detected polarization (section 3.4).

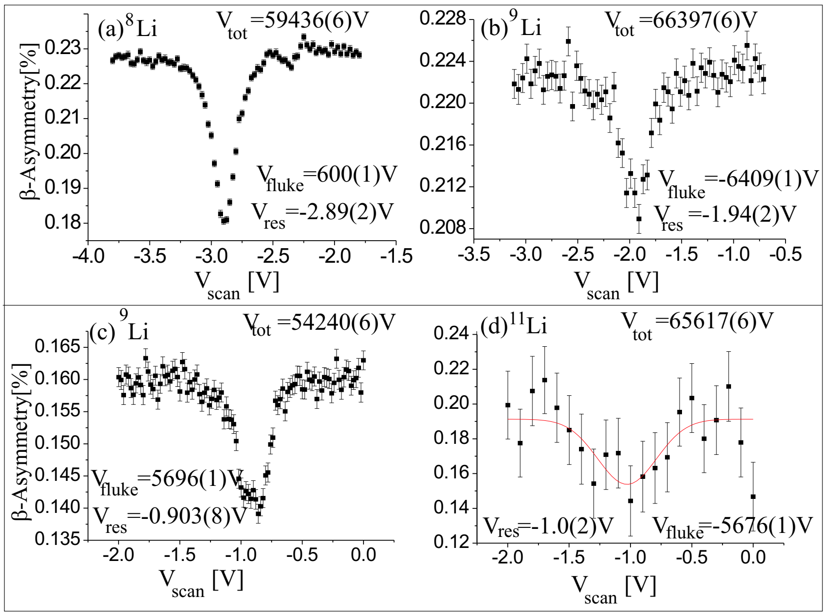

Figure 3.8: *Hyperfine scans for different isotopes and different frequencies of the laser light. The high voltage of ISOLDE was* $HV_{ISOLDE} = +59891(6)\,V$. *(a-b)* ^{8}*Li and* ^{9}*Li with as wave number of the laser light* $k_D = 14963.46cm^{-1}$. *(c-d)* ^{9}*Li and* ^{11}*Li with as wave number of the laser light* $k_D = 14957.72cm^{-1}$.

In figure 3.8 a "hyperfine scan" for different isotopes is shown. The shift in the total needed acceleration voltage V_{tot} for the resonances in the different isotopes gives the isotope shift ΔIS. For ^{8}Li and ^{9}Li this gives

$$\nu_L = \nu_0(^8Li)(1 + \sqrt{\frac{2eV_{tot}(^8Li)}{m(^8Li)c^2}}) \tag{3.11}$$

$$= \nu_0(^9Li)(1 + \sqrt{\frac{2eV_{tot}(^9Li)}{m(^9Li)c^2}}) \tag{3.12}$$

taking into account that the frequency ν_L of the laser light was the same during the "hyperfine scans" of the two isotopes. Replacing $\nu_0(^9Li) = \nu_0(^8Li) + \Delta IS$

gives an isotope shift

$$\Delta IS = \nu(^8Li)\frac{(\sqrt{\frac{2eV_{tot}(^8Li)}{m(^8Li)c^2}} - \sqrt{\frac{2eV_{tot}(^9Li)}{m(^9Li)c^2}})}{1+\sqrt{\frac{2eV_{tot}(^9Li)}{m(^9Li)c^2}}} \tag{3.13}$$

Because of the large systematic error on V_{fluke}, we don't calculate the number here.

Because of the large mass difference between the isotopes ^{8}Li and ^{11}Li, for ^{11}Li the additional voltage V_{acc} needs to be $\Delta V_{acc} \approx 21.\ 10^3$V. The limits of the used Fluke power supplies do not allow us to keep the frequency of the laser light constant for all Li isotopes. Therefore the measurements were performed in two steps. First the measurements on ^{8,9}Li were performed with one setting of the frequency of the laser light. Afterwards the frequency of the laser light was changed and the measurements on ^{11}Li were performed with a reference measurement on ^{9}Li. In table 3.2 an overview of the different settings is given.

Table 3.2: *Overview of the settings of the frequency of the laser light and applied voltages for the D1-line. "k_D[cm^{-1}]" is the wave number of the laser light we used in the mentioned experiment. The uncertainty on the ISOLDE high voltage is* 10^{-4}. *The uncertainty on the fluke voltages is* 1 *V. The uncertainties on* $V_{scan,res}$ *is given by the statistical fit error.* * *These fluke voltages are only the set-values and not the values read by the PREMA voltage meter.*

	Oct. 2001	Jun. 2002	May 2003	Jun. 2003
HV_{ISOLDE}	+60007(6)	+59891(6)	+60009(6)	+60008(6)
k_D(^{8,9}Li)[cm^{-1}]	14963.536	14963.46	14963.64	14963.63
power laser [mW]	130	120	115	300
$V_{fluke,8Li}$[V]	500*	600*	400*	500*
$V_{fluke,9Li}$[V]		−6409*	−6700*	−6400*
$V_{scan,res}$(^{8}Li)[V]	4.22(3)	−2.83(1)	−3.51(3)	−5.939(4)
$V_{scan,res}$(^{9}Li)[V]		−1.94(1)	−2.03(2)	−7.208(4)
k_D(^{9,11}Li)[cm^{-1}]		14957.72		14957.45
$V_{fluke,9Li}$		5696(1)		6368.3(10)
$V_{fluke,11Li}$		−5676(1)		−5003.4(10)
$V_{scan,res}$(^{9}Li)[V]		−0.90(1)		−1.86(2)
$V_{scan,res}$(^{11}Li)[V]		−1.03(2)		−0.04(1)

3.4 Determining the created spin-polarization

The time integrated angular distribution of β-decay is given by [Pos86]:

$$W(\theta,\phi,\tau)=\sqrt{4\pi}.\frac{v}{c}\sum_{k,n}A_kQ_k^nB_k^n(I)Y_k^n(\theta,\phi) \tag{3.14}$$

with θ,ϕ the angles defining the detector position with respect to the chosen reference frame (fig. 3.9 and 3.3). A_k are the radiation parameters determined by the type of radiation [Van86]. $B_k^n(I)$ is the orientation tensor. Q_k^n represent the experimental losses of orientation between the time of production and detection. v is the velocity of the β-particles and c denotes the constant speed of light.

For allowed β-decay $A_k \neq 0$ for $k=1$. $A_k \neq 0$ for odd k only due to the parity violation of the β-decay. Because $L=0$ for the $\beta^{+/-}$ particles, the maximum k-value for which $A_k \neq 0$ is $k=1$ [Sev89]. So we can restrict expression (3.14) to $k=1$. In our experimental set-up (fig. 3.3), $\phi=0$ for all detectors. Therefore only $n=0$ terms contribute to the final angular distribution:

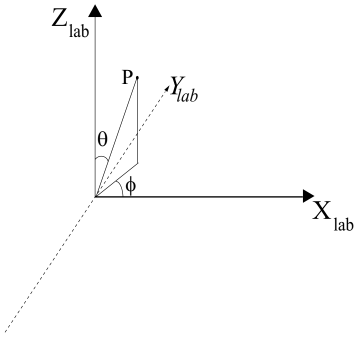

Figure 3.9: *Definition of the angles θ,ϕ for a point P.*

$$W(\theta,\tau)=1+\frac{v}{c}A_1Q_1B_1^0(I)\cos\theta \tag{3.15}$$

with $\theta=0°$ and $\theta=180°$.
The experimental asymmetry is

$$\begin{aligned} a &= \frac{N(0°)-N(180°)}{N(0°)+N(180°)} \\ &= \frac{\epsilon_0W(0°)-\epsilon_{180}W(180°)}{\epsilon_0W(0°)+\epsilon_{180}W(180°)} \end{aligned} \tag{3.16}$$

$\frac{\epsilon_0-\epsilon_{180}}{\epsilon_0+\epsilon_{180}}$ represents an experimental correction factor, the experimental asymmetry due to the possible different efficiencies of the detectors, the position of the beam with respect to the crystal, etc. To extract out of these data the polarization, independent of this experimental asymmetry $\frac{\epsilon_0-\epsilon_{180}}{\epsilon_0+\epsilon_{180}}$, the asymmetry in resonance (a_{in}^P) which is sensitive to P, is compared to the asymmetry out of resonance (a_{out}^0) which is sensitive to the experimental asymmetry of the detection set-up

$$\begin{aligned} a_{out}^0 &= \frac{\epsilon_0-\epsilon_{180}}{\epsilon_0+\epsilon_{180}} \\ a_{in}^P &= \frac{\epsilon_0(1+M)-\epsilon_{180}(1-M)}{\epsilon_0(1+M)+\epsilon_{180}(1-M)} \end{aligned} \tag{3.17}$$

with

$$M = \frac{v}{c}A_1Q_1B_1^0(I) \tag{3.18}$$

The experimental asymmetry cancels when we take the normalized asymmetry

$$a_n = \frac{a_{in}^P - a_{out}^0}{1-a_{in}^P a_{out}^0} \tag{3.19}$$

This normalized asymmetry is proportional to the created polarization P

$$\begin{aligned} a_n &= \frac{v}{c}A_1Q_1B_1^0(I) \\ &= -\sqrt{\frac{3I}{I+1}}\frac{v}{c}A_1Q_1P \end{aligned} \tag{3.20}$$

The factors $\frac{v}{c}$, A_1 (12) and Q_1 determine how much of the created polarization can be detected.
Because of the high $Q_\beta(^A\mathrm{Li}) > 13\mathrm{MeV}$ [Fir96, Ajz88], $\frac{v}{c} = 1$ is assumed.
The radiation parameter A_1 is related to the spins of the initial and final states of the β-decay and depends on the kind of transition, Gamow-Teller or Fermi, β^+ or β^- [End90]. For pure Gamow-Teller transitions we have [Pos86]

$$A_1(\beta^\pm) = \pm\frac{v}{c}\sqrt{\frac{I_i}{3(I_i+1)}} \quad for\ \ I_f = I_i+1 \tag{3.21}$$

$$A_1(\beta^\pm) = \mp\frac{v}{c}\sqrt{\frac{I_i+1}{3I_i}} \quad for\ \ I_f = I_i-1 \tag{3.22}$$

with $I_{i,f}$ the initial and final spin of the transition respectively. When the initial and final spins are equal, a mixture of Gamow-Teller and Fermi transitions can occur, giving

$$A_1(\beta^\pm) = \frac{v}{c}\frac{1}{1+y^2}\left(\frac{\mp 1}{\sqrt{3I_i(I_i+1)}} + \frac{2}{\sqrt{3}}y\right) \tag{3.23}$$

---

[12] In literature very often another definition of the asymmetry parameter A [Jac57] is used, corresponding to an angular distribution of $W(\theta) = 1 + \frac{v}{c}AQPcos\theta$. The two asymmetry parameters are related by $A_1 = -\sqrt{\frac{I_i+1}{3I_i}}A$.

with y the relative strength of the Gamow-Teller axial vector matrix elements $C_A(GT)$ and Fermi vector matrix elements $C_V(F)$:

$$y = \frac{C_V(F)}{C_A(GT)} \tag{3.24}$$

Based on the observed decay schemes (fig. 3.10) [Fir96], the radiation parameters of ^{8,9}Li are calculated to be $A_1(^8\mathrm{Li}) = 0.24$ $(A = -0.3)$ and $A_1(^9\mathrm{Li}) = 0.08(A = -0.098)$. For ^{11}Li the asymmetry parameter was deduced in the past

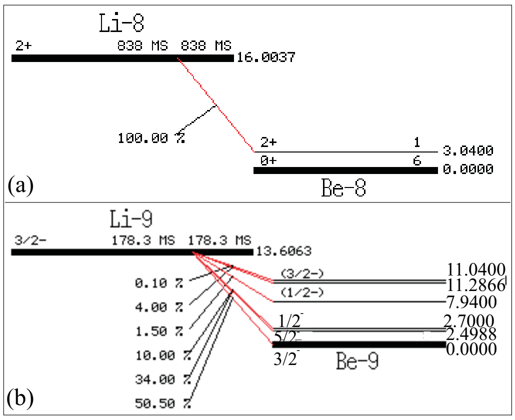

Figure 3.10: *Decay scheme of (a)^{8}Li and (b)^{9}Li [Ajz88]. Figures taken from [bnl].*

from the measured β-asymmetry by E. Arnold et al.: $A_1(^{11}\mathrm{Li}) = 0.24$ (A=-0.3) [Arn92]. The ratio of the amplitudes $\frac{A(^{11}Li)}{A(^{9}Li)}$ and $\frac{A(^{11}Li)}{A(^{8}Li)}$ in the spectra of this work are similar as in [Arn92, Arn88].
Q_1 represents the experimental losses of the created orientation. In the ideal case, the detected polarization equals the created polarization, sensitive to the power of the laser light and the kind of transition. In reality there are losses of spin-orientation. Since the creation of spin-orientation happens at the end of the beam line, losses in spin-orientation before the adiabatic rotation of the atomic spins are minimal. The main loss of orientation will happen due to the implantation of the nuclei in the stopper crystal. The spin-lattice relaxation which causes this loss of spin-orientation is dependent on the crystal. So the amplitudes of the resonances depend on the crystal and the power and frequency of the laser light. The optimization of these parameters is discussed in next section.

3.5 Optimizing the laser set -up and the crystal.

3.5.1 Frequency of the laser light and sign of polarization

The doppler shifted frequency is adjusted to the hyperfine structure-transition that induces the largest polarization. The sign of the circular polarization of the laser light (σ^+ or σ^-) determines together with the asymmetry parameter A_1 the direction of the resonances and which m_F level will be most populated. To scan the different possibilities for ^{8}Li, the frequency of the laser light is fixed on $k_{laser} = 14963.536cm^{-1}$, corresponding to a wavelength of $\lambda = 668.291$nm. The additional voltage $V_{fluke} + 50V_{scan}$ on top of the ISOLDE High Voltage HV_{ISOLDE} is varied. Each of the visible resonances in figure 3.11c(d) consists of 2(4) non resolved resonances.

Most polarization is created in the D1-transition with right circularly polarized light. This is in agreement with the experiments of E. Arnold [Arn86].

3.5.2 Power of the laser light

The power of the laser light is proportional to the number of laser photons. More photons means a larger probability to interact with the atoms and to create polarization. Once we have enough photons to have several excitations (typical 10-20) in the optical pumping region, adding more photons will have no effect on the amount of created polarization. We are interested in the needed power of the laser light to saturate the polarization. The power of the laser light is measured at the entrance of the laser beam into the apparatus. This power will be a bit lower at the optical pumping section.

In figure 3.12 the saturation curves are shown for ^{8}Li implanted into three cubic crystals LiF, Au and Si. On the left we see the amplitude of the resonances, i.e. the asymmetry. On the right the spin-polarization is plotted. The spin-polarization is calculated as in section 3.4. The power needed to saturate the polarization is of course independent on the crystal and is $\approx 75mW$. Therefore in the rest of the experiments a power of the laser light of 75mW or more is used unless explicitly mentioned.

Figure 3.12 learns us also that the amount of polarization in saturation is dependent on the crystal. The crystal for which the spin-orientation is the best conserved, is LiF. This will be discussed in section 5.2.1.

3.5.3 Stability of the laser light in time

Instabilities of the frequency of the laser light or of the ISOLDE high voltage, show up in a shift of the resonance position of the ”hyperfine scan”. To adjust for possible instabilities of the laser light, ”hyperfine scans” were performed regularly, i.e. every two hours throughout the experiment. If the position of the resonance was drifted, the additional voltage V_{scan} was adapted in the NMR scan. Like this the fixed voltage V_{scan} caused maximal nuclear polarization.

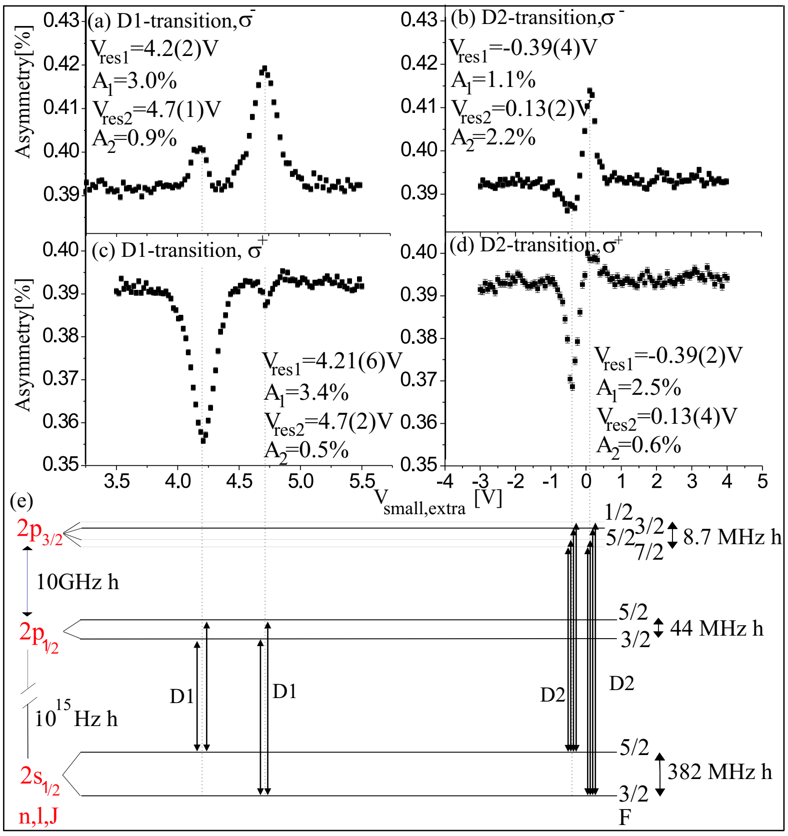

Figure 3.11: *(a-d) Hyperfine scans of ^8Li in Au with different fixed voltages, with a common baseline. The high voltage of ISOLDE was* $HV_{ISOLDE} = +60007(6)\,V$

(a-c) D1-transitions from $2S_{1/2}$ *to* $2P_{1/2}$. $U_{fluke} = 500(1)V$

(b-d) D2-transitions from $2S_{1/2}$ *to* $2P_{3/2}$. $U_{fluke} = 1400(1)V$

(a-b) Left circularly polarized σ^- *light.*

(c-d) Right circularly polarized σ^+ *light.*

(e) Level scheme corresponding to the different resonances.

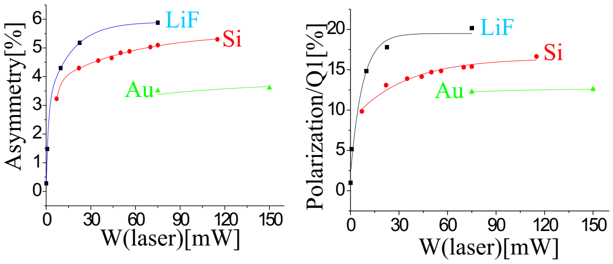

Figure 3.12: *Created polarization as a function of the power of the laser light for different crystals.*

3.5.4 Adjusting the measuring time t_{meas}

In the sweep of V_{scan}, each voltage is applied for a time t_{meas}. For the start of a measurement, the acquisition program waits for the trigger of the proton-pulse. When triggered, the beam gate is opened for a time t_{meas}. In this time, the counters connected to the signals of the β-telescopes are working. After closing the beam gate, the counting is stopped and the variable parameter is changed to its next value. The program waits for a new trigger [13] to restart (see figure 3.13).

For the measurement of decay curves the beam gate [14] is opened very shortly [15] when the acquisition program is triggered by a proton pulse. Then the counters count for a time t_{meas} in the first channel. Then the second channel is started and the counters start again, without waiting for a new trigger[16]. So during the whole measurement of the decay curve, the beam gate is closed, except for the very beginning.

The measuring time t_{meas} is chosen as a function of the half life of the isotopes. In general, the measuring time is limited to $t_{meas} \approx 3T_{1/2}$ such that most atoms are decayed and the activity of longer-lived daughter decay is not measured.

In the case of ^{8}Li with $T_{1/2} = 838(6)$ms, we chose $t_{meas} = 2$s.
For ^{9}Li with $T_{1/2} = 178.3(4)(6)$ms, we have used $t_{meas} = 1s$. As ^{9}Li decays to

---

[13] This mode of triggering is called "trigger step" in the acquisition program "MCP". It is used for scans, such as a hyperfine scan. The MCP (Measuring and Control Program) program was developed for the COLLAPS experiments at ISOLDE by Michael Neuroth and later improved and implemented for windows by Stephan Kappertz.

[14] The beam gate is an electrostatic deflector which prevents the ion beam from passing through the beam line if the voltage (≈ 4.5kV) is turned on. When the voltage is turned on, one says the beam gate is closed. When the voltage is turned off, one says the beam gate is open.

[15] The beam gate is opened during ≈ 20ms for ^{8}Li, ≈ 10ms for ^{9}Li and ≈ 1ms for ^{11}Li.

[16] This mode of triggering is called "trigger sweep" in the acquisition program MCP.

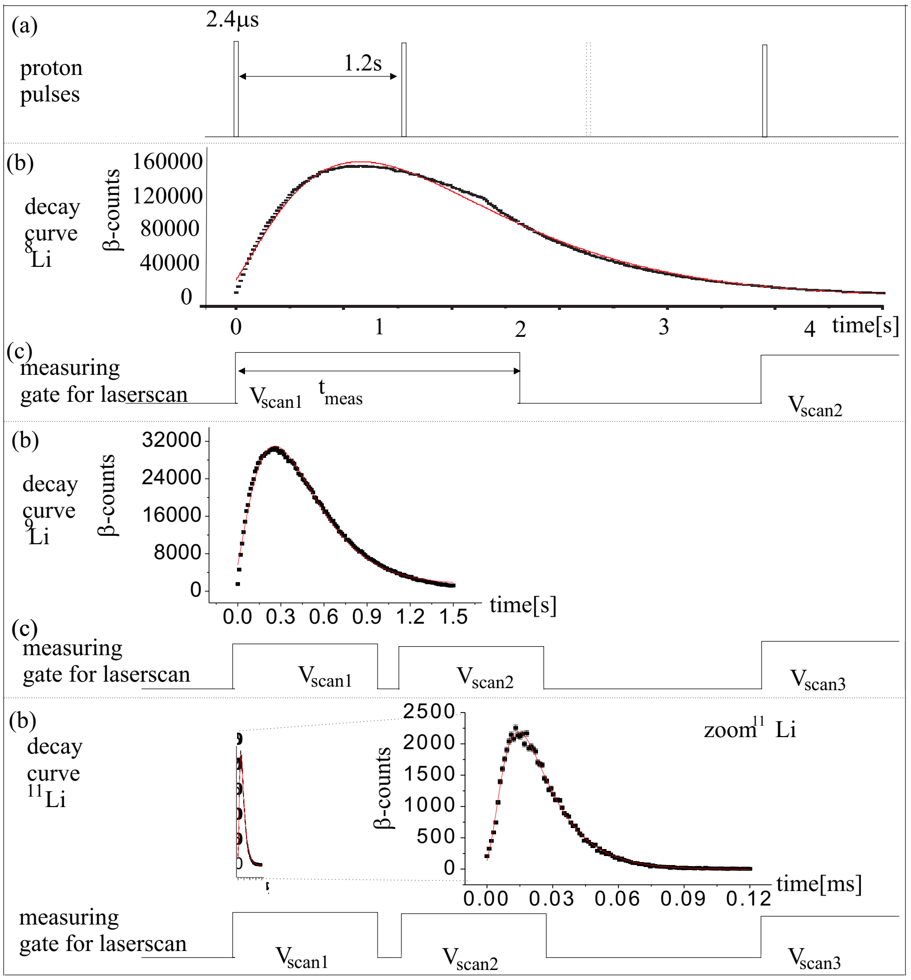

Figure 3.13: *(a)Example of the structure of the proton pulses. The dotted pulse is one that was distributed to another facility in CERN than ISOLDE. The sequence of pulses for ISOLDE was not regular, so this is an example. (b) Decay curve for different Li-isotopes. This curve has nothing to do with the measuring time during a "hyperfine scan". It is just shown to watch the amount of remaining ions at the end of one measuring channel. (c) Measuring gate during a "hyperfine scan". A proton pulse hitting the target triggers the acquisition program. Then the acquisition measures and the beam gate is opened for a time* t_{meas}. *Then the measuring gate is closed, the variable parameter is changed to the next value and the acquisition program waits for a new trigger .*

^{9}Be, which is stable, the setting of the measuring time is not so important.
^{11}Li decays to ^{11}Be which has a half life of 13.8s. After one second 0.2% of the ^{11}Be isotopes has decayed to the stable ^{11}B isotope. So if the measuring time for ^{11}Li is put lower than 1s, a maximal background of 0.2% due to daughter activity is present. The best setting for the measuring time for ^{11}Li is $t_{meas} = 0.1$s. In that case the background due to daughter activity is about 0.03%. In most experiments the ^{11}Li measuring time was set equal to that for ^{9}Li.

In figure 3.13 the proton pulses and the measuring gates are schematically shown for the different isotopes. In addition the decay curves, measured with a different trigger mode, are shown. This curve is added on the picture to show that the lifetime of the selected isotope corresponds to that of the wanted isotope and to show the remaining activity at the end of one measuring channel.

Chapter 4

Measuring nuclear moments with level mixing techniques

4.1 Experimental set-up

In figure 4.1 the part of the experimental set-up, used for level mixing techniques, is shown.
About 30cm behind the iris, the atoms are implanted in a 1mm thick crystal. The implantation depth depends on the crystal, going from $d = 0.2\mu$m to $d = 0.5\mu$m for the used crystals. Thus the surface of the crystals needs to be carefully polished and treated.
Around the crystal in the vertical direction, perpendicular to $\vec{B}_0$ and $\vec{B}_s$, a radio-frequency (rf)-coil, connected with a variable capacity (section 5.1.1) is placed. An AC current produced by a Rode Schwarz rf-generator is amplified and sent through the LRC-circuit. This induces a rf-field $\vec{B}_{rf}$ to destroy the polarization in the β-Nuclear Magnetic or Quadrupole Resonance (NMR/NQR) measurements.

The β-asymmetry is monitored by the two plastic (NE102A) scintillator telescopes used in the "hyperfine scans" (section 3.2.2). The total efficiency of the β-detection is about 10%.

4.2 Some Level Mixing Techniques

In this section we start from a nuclear ensemble with spin-polarization. This means the acceleration voltage V_{acc} is fixed to resonance, producing the maximum amount of atomic and nuclear polarization. The nuclear spin-polarization will be resonantly destroyed via level mixing techniques.

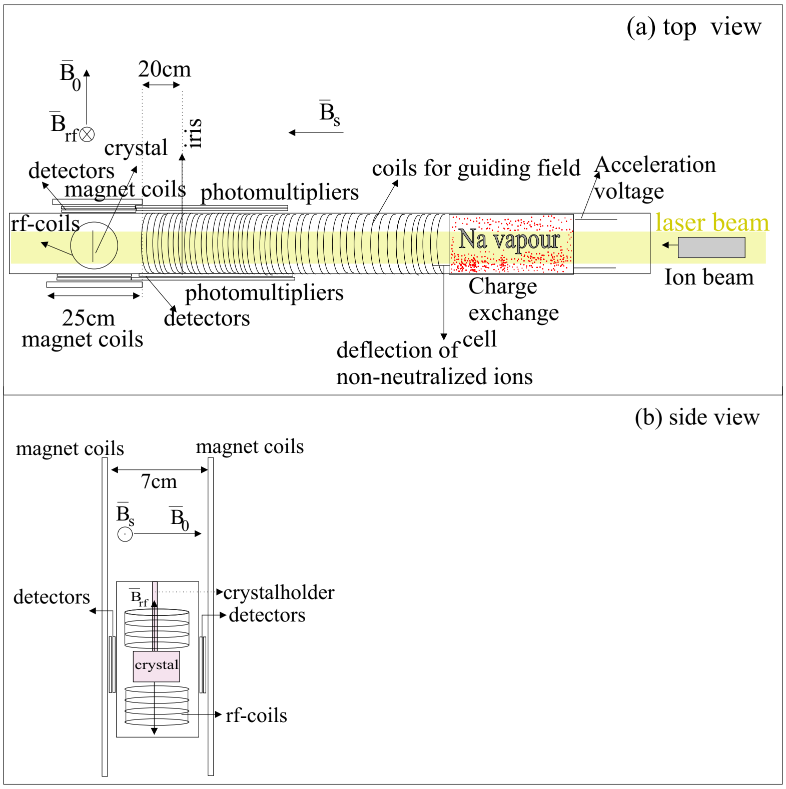

Figure 4.1: *Schematic view of the experimental COLLAPS set-up.*

4.2.1 β-NMR (Nuclear Magnetic Resonance)

The atoms are subjected to two perpendicular dipole interactions, induced respectively by a static field $\vec{B}_0$ and a radio-frequent field $\vec{B}_{rf}$ (with amplitude B_1). The radio-frequent field $\vec{B}_{rf}(t)$ breaks the axial symmetry in a frame rotating around the Z-axis[1] (chosen $\parallel B_0$)

$$H_{rot} = -(\omega_{B0} - \omega_{rf})I_z + \omega_{B1} I_x \tag{4.2}$$

with $\omega_{rf} = 2\pi\nu_{rf}$ the frequency of the rf-field,

$$\omega_{B0} = \frac{g\mu_N B_0}{\hbar} = 2\pi\nu_L \tag{4.3}$$

the Larmor angular frequency and $\omega_{B1} = \frac{g\mu_N B_1}{\hbar}$ with g the nuclear g-factor and μ_N the nuclear magneton. The energy levels of the $|m\rangle$ and $|m'\rangle$ states[2] with $\Delta m = 1$ cross when the Larmor precession ν_L of the nuclear spins matches the radio frequency ν_{rf}

$$\nu_L = \frac{g\mu_N B_0}{h} = \nu_{rf} \tag{4.4}$$

When this condition is fulfilled, the levels $|m\rangle$ and $|m'\rangle$ are mixed due to the perturbation term $\omega_{B1} I_x$, similar as the mixing induced by a non-collinear electric quadrupole and magnetic dipole interaction in Level Mixing Resonance (LMR) [Cou01]. The initial polarization is then destroyed. This can be detected by a change of the asymmetry of the nuclear β-decay as a function of the rf-frequency ν_{rf} (keeping the static magnetic field strength B_0 constant) or vice versa. For the measurements in this work, the rf-frequency ν_{rf} is scanned without modulation.

In figure 4.2 an example for an NMR-spectrum in LiF from October 2001 is given. Due to the high production rate of ^{8}Li, the statistical errors are smaller than the dimensions of the points themselves. On the left figure a "hyperfine scan" with a created asymmetry of $A = 6.0(1)\%$ is shown. In this scan the power of the laser light is in saturation. This asymmetry A equals the amplitude of the resonance. On the right figure the acceleration voltage is fixed to resonance, so the β-asymmetry on the baseline is the β-asymmetry a^P_{in} with created polarization. In the NMR resonance condition this polarization will be destroyed and we have the asymmetry a^0_{rf}. When all detected polarization would be destroyed, the level a^0_{rf} would be equal to a^0_{out}. In reality only 90% of the created polarization is destroyed because not all nuclei undergo the same Zeemann-splitting due to defects or small inhomogeneities of the magnetic field

---

[1] The Hamiltonian in the static frame equals

$$H = -\vec{\mu}.\vec{B}_0 + \vec{\mu}.\vec{B}_{rf}(t) \tag{4.1}$$

[2] m is the projection of the nuclear spin I on the quantization axis

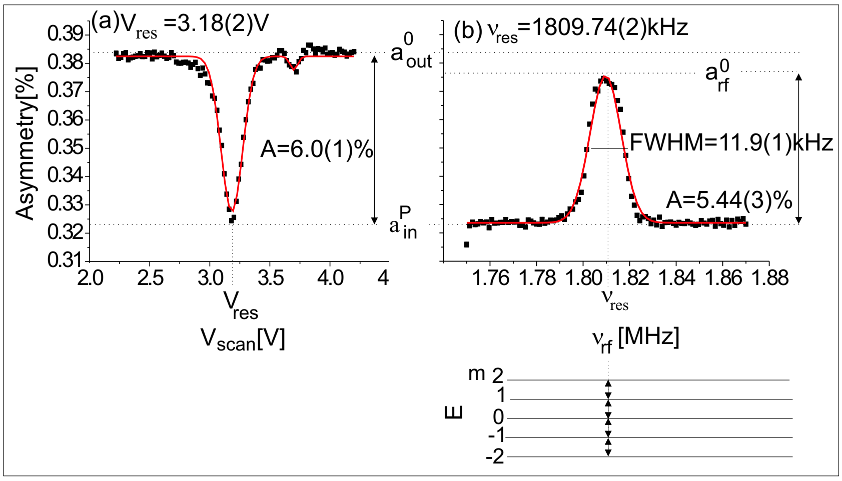

Figure 4.2: *(a) "Hyperfine scan" of* ^{8}Li *in LiF,* $W = 75mW$, $HV_{ISOLDE} = +60007.1\,V$, $V_{fluke} = 500\,V$, $k_D = 14963.536cm^{-1}$. *(b)NMR scan of* ^{8}Li *in LiF with* $B_1 = 0.5G$, *the additional voltage fixed on* $V_{scan} = 3.18\,V$. *The other applied voltages and properties of the laser light are the same as in (a).*

over the crystal. To determine the amplitude, position and linewidth of the peak, the spectra are fitted with a Gaussian curve[3]

$$y = y_0 + Ae^{-2(\frac{x-x_c}{W})^2} \tag{4.6}$$

without conditions. y_0 is the baseline, A the amplitude of the peak, x_c the central position of the peak. The full width half max (FWHM) of the peak is determined by $FWHM = W\sqrt{ln(4)}$.

4.2.2 β-NQR (Nuclear Quadrupole Resonance)

A β-NQR experiment is the same as a β-NMR [Sli78, Mat71] experiment, except that the atoms are implanted in a crystal with a non-cubic lattice symmetry with an axial symmetric electric field gradient. The caused additional quadrupole interaction allows the extraction of the quadrupole frequency $\nu_Q = \frac{4I(2I-1)\omega_Q}{2\pi}$. The Hamiltonian of such experiment equals:

$$H = \frac{\omega_Q}{\hbar}(3I_z^2 - I^2) - (\omega_{B0} - \omega_{rf})I_z + (\omega_{B0}\sin\beta + \omega_{B1})I_x \tag{4.7}$$

---

[3] Attention must be paid to different definitions such as

$$y = y_0 + Ae^{-0.5(\frac{x-x_c}{W'})^2} \tag{4.5}$$

with $W' = 0.5W$, which we don't use.

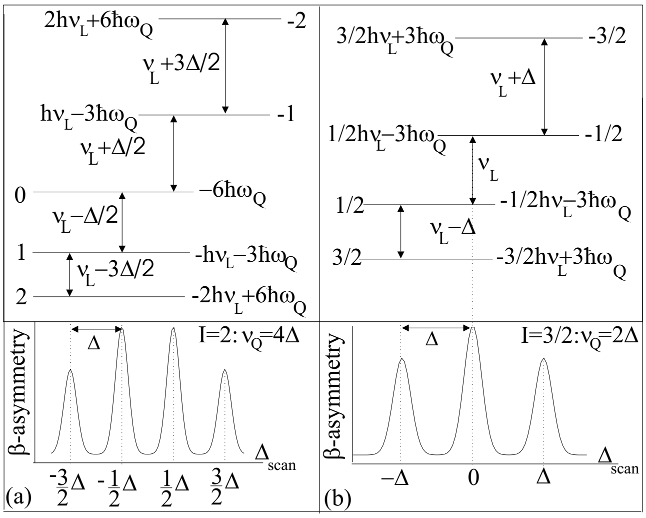

Figure 4.3: *Energy splitting of the* m_I *levels and the* β*-asymmetry as a function of* $\Delta_{scan} = \nu_{rf} - \nu_L$ *for (a)*$I = 2$*, e.g.* ^8Li *and (b)* $I = 3/2$*, e.g.* $^{9,11}Li$

in a frame rotating around the axis of the magnetic field B_0 and with a frequency ω_{rf}.
If the angle β between the static field axis and the symmetry axis of the electric field gradient is small and if $2\pi\nu_L \gg \omega_Q$, the non-equidistant energy levels at a certain magnetic field B_0 of the m-quantum levels are given by

$$E_m = \langle m|H|m\rangle = -mh(\nu_L - \nu_{rf}) + \hbar\omega_Q(3m^2 - I(I+1))\frac{3\cos^2\beta - 1}{2} \qquad (4.8)$$

In our case the angle β between the axis of $\vec{B}_0$ and the axis of the electric field gradient, is put to zero. An error of one degree will give an additional uncertainty in the measured quadrupole frequency $\nu_Q = \frac{4I(2I-1)\omega_Q}{2\pi}$ of 0.05%. An error of five degrees will give an additional uncertainty in the measured quadrupole frequency $\nu_Q = \frac{4I(2I-1)\omega_Q}{2\pi}$ of 1.1%. This should be taken into account as a possible systematic error.
The perturbation Hamiltonian of the rf-photons induces resonant transitions between the m-quantum levels if the energy of the photons matches the energy splitting of two m-quantum levels with $\Delta m = 1$, i.e. if $E_m - E_{m'} = 0$. The β-asymmetry as a function of the rf-frequency ν_{rf} shows $2I$ equidistant resonances at a distance of $\Delta = \frac{6\omega_Q}{2\pi} = \frac{6\nu_Q}{4I(2I-1)}$. In resonance, the initial polarization is partially destroyed by the mixing of two m-quantum levels. The amplitudes of the resonances are much smaller than in NMR because only two quantum levels contribute to the signal.

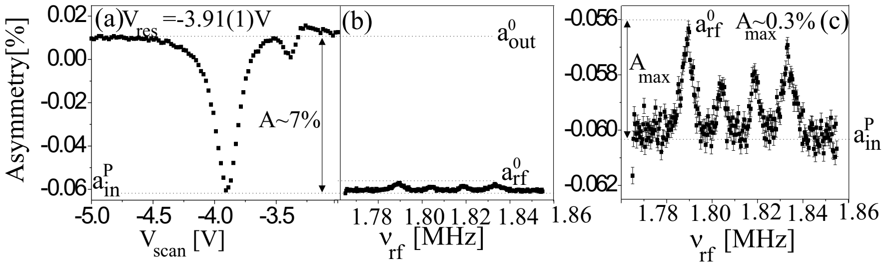

Figure 4.4: *(a) "Hyperfine scan" of* ^{8}*Li in* $LiTaO_3$*,* $W = 100mW$*;* $HV_{ISOLDE} = +60009.3\,V$*,* $V_{fluke} = 400\,V$*,* $k_D = 14963.64cm^{-1}$*. (b-c)Single-rf-NQR scan of* ^{8}*Li in* $LiTaO_3$ *with* $B_1 = 0.94G$ *and the additional voltage fixed on* $V_{scan} = -3.91V$*. The other applied voltages and the properties of the laser light are the same as in (a). (c) is a zoom of (b).*

In figure 4.3 two examples are given. In the first example for ^{8}Li with $I = 2$, we have four resonances as a function of $\Delta_{scan} = \nu_{rf} - \nu_L$. The distance between the peaks is $\Delta = \frac{\nu_Q}{4}$. In the second example for ^{9}Li with $I = 3/2$, we have three resonances at a distance of $\Delta = \frac{\nu_Q}{2}$.
In figure 4.4 is shown that only a small part of the initial polarization is destroyed in a NQR resonance. From the initial asymmetry of 7% in the "hyperfine scan" of ^{8}Li in $LiTaO_3$ (fig. 4.4a) only 0.3% was destroyed for the most intense resonance (fig. 4.4b-c). So only 4.3% of the initial polarization was destroyed for the most intense resonance.

4.2.3 Multiple-rf-NQR

To overcome the problem of small resonances in single-rf-NQR, several rf-frequencies are used simultaneously. By applying more than one resonance frequency at the same time, a resonance with a larger amplitude is obtained. In the next paragraphs some examples are given. To induce all transitions, $2I$ simultaneous rf-frequencies are needed.

- **^{8}Li**
  Due to experimental limitations, only two[4] rf-frequencies were used simultaneously for ^{8}Li with $I = 2$.
  In figure 4.5 an example is given from May 2003. In this example ^{8}Li was implanted into Zn. In the single-rf-NQR scan, 11% of the created polarization is destroyed in resonance. In figure (4.5d), an example of a double-rf-NQR spectrum is shown. The two simultaneously used frequencies are $\nu_{rf,1} = \nu_L + x$ and $\nu_{rf,2} = \nu_L - x$ with x scanned from 0 to y. In this spectrum about 50% of the created polarization (fig. 4.5c) is

---

[4] Instead of $2I = 4$

destroyed. We clearly improved the result compared to the single-rf-NQR spectrum (fig. 4.5b-d). The narrow peaks are two-photon peaks and will be discussed later.

There are two possibilities for a double-rf-NQR scan in ^{8}Li. One can use the frequencies of previous figure or $\nu_{rf,1} = \nu_L + x$ and $\nu_{rf,2} = \nu_L + \frac{x}{3}$ with x scanned from $-y'$ to $+y'$. In figure 4.6 the two manners are compared with examples of June 2002. The spectra in this figure have all an enormous bump-background around $\Delta = 0$. This can be explained by the fact that the beam was hitting the Cu crystal holder. This means that the Zn crystal was not positioned in the center of the beam line. Afterwards this position was optimized (section 5.2.3). Because of this bump and because we don't have enough points in each peak, it is very difficult to fit the single-rf-spectrum in figure 4.6a. Since we know the position of the peaks out of the spectrum of figure 4.5e, we fixed these positions. The baseline shifted for the double-rf-spectra compared to the single-rf one. The same shift is visible in the "hyperfine scans", which are not shown here.
The amplitudes of the largest peaks of the two double-rf-NQR-spectra are similar. Because of the smaller needed scan range in the first manner, we chose for the rest of the experiments for the first manner.

- **^{9,11}Li**
  For ^{9,11}Li with $I = 3/2$, three rf-frequencies are used together. One rf-frequency is fixed at the Larmor frequency $\nu_1 = \nu_{L,fix}$. The two other rf-frequencies are $\nu_{2(3)} = \nu_{L,fix} + (-)\Delta_{scan}$ with Δ_{scan} varying from 0 to y. In figure 4.7 this is illustrated with a measurement from May 2003 of ^{9}Li implanted in Zn.

  The fixed frequency $\nu_{L,fix}$, being present during the whole scan, causes a small shift of the baseline $(a^P_{in} - a^P_{rf})$. When $\Delta_{scan} = \Delta$, all levels are mixed. In the multiple rf-scan 42% of the created polarization is destroyed, while in the single rf-scan this was only 12%. The created polarization is about a factor three smaller than for ^{8}Li due to the smaller asymmetry parameter of ^{9}Li. The difference in linewidth of the peaks of the single-rf scan (W = 3.8kHz) and the multiple-rf-scan (W = 1.2kHz), is mainly due to a different amplitude of the rf-field. In between the single-NQR scan and the multiple-rf-NQR scan, the baseline of the "hyperfine scan" is shifted due to beam fluctuations.

In the two examples the positions of the peaks in the single-rf-NQR and multiple-rf-NQR spectra agree with each other. To proof that they are really the same, the deduced Δ from the fitted positions are plotted for all available single- and multiple rf-NQR scans of ^{8}Li and ^{9}Li (fig. 4.8a(b)). The grey bands indicate the weighted averages with error δ over one time period. The uncertainties in this picture are statistically and are determined by a χ^2 analysis which will be discussed in the chapter about the experimental results (section 6.1). In figure 4.9 an example of a spectrum is shown, together with two simulated Gaussian

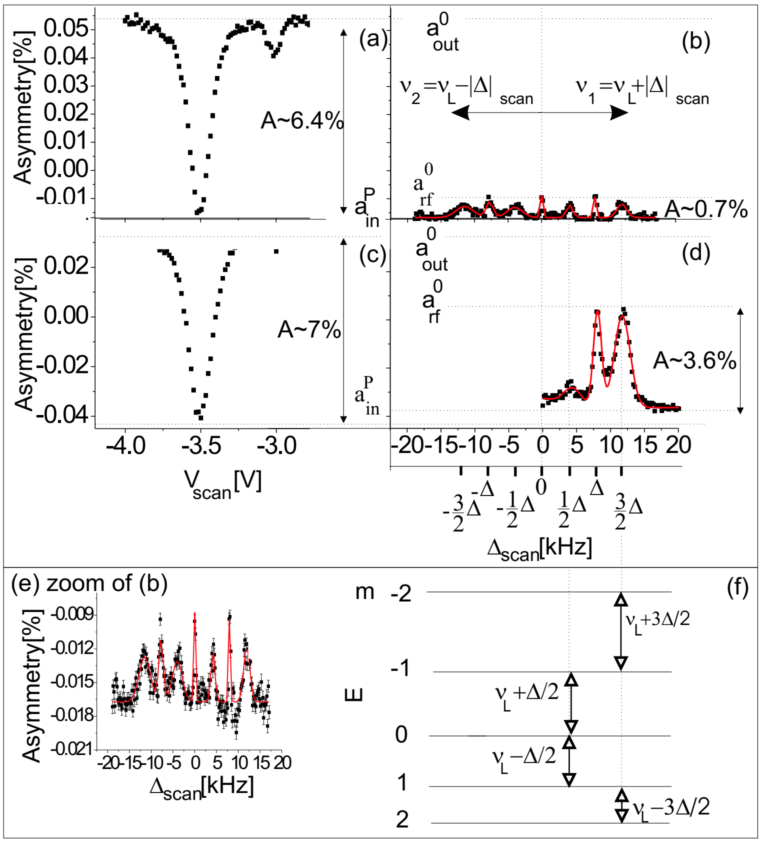

Figure 4.5: *An example from May 2003. (a) "Hyperfine scan" performed closest in time to the NQR measurement of (b).* $W = 130mW$, $HV_{ISOLDE} = +60009.3\,V$, $V_{fluke} = 400\,V$,$k_D = 14963.64cm^{-1}$. *(b) Single NQR-spectrum of* ^8Li *implanted into Zn.* $B_1 = 2.5G$. *The additional voltage is fixed to resonance* $V_{scan} = -3.5\,V$. *The other applied voltages and properties of the laser light are as in (a). (c) "Hyperfine scan" performed closest in time to the NQR measurement of (d). The quantified properties of the laser light and applied voltages are the same than in (a). Nevertheless we see a shift in the baseline. In between the two measurements the Zn crystal was moved to check the position of the laser spot. It is possible that the final position of the Zn crystal after the repositioning is not identical to the position before. This, together with possible beam fluctuations explains the shift. (d) Double-rf-NQR-spectrum of* ^8Li *in Zn.* $B_1 = 3.8G$. *The additional voltage is fixed to resonance* $V_{scan} = -3.5\,V$. *The other applied voltages and properties of the laser light are as in (a). (e)Zoom of (b). (f) Energy splitting of the nuclear m-levels.*

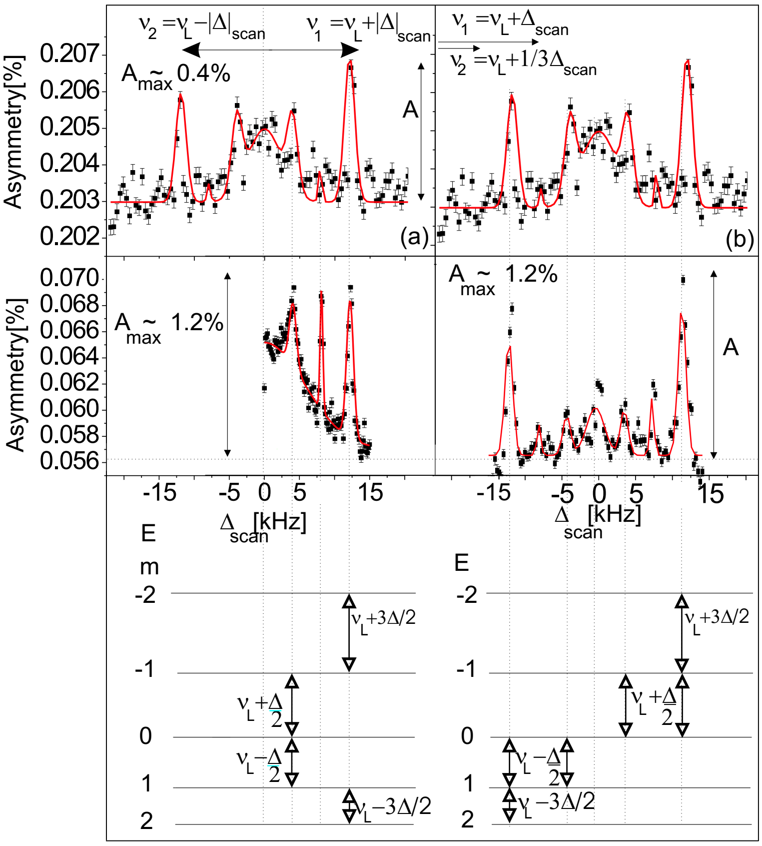

Figure 4.6: *Above: single NQR-scan on* ^8Li *in Zn with the used rf-frequencies in multiple-rf-NQR.* $B_1 = 1.8G$. $A^0_{out} = 0.259$, $A^P_{in} = 0.198$. *Middle: Multiple-rf-NQR scan on* ^8Li *in Zn (a)* $\nu_{rf,1} = \nu_L + x$ *and* $\nu_{rf,2} = \nu_L - x$ *with* x *scanned from* 0 *to* y. $B_1 = 3G$. $A^0_{out} = 0.110$, $A^P_{in} = 0.050$. *(b)*$\nu_{rf,1} = \nu_L + x$ *and* $\nu_{rf,2} = \nu_L + \frac{x}{3}$ *with* x *scanned from* $-y'$ *to* $+y'$. *The non-identified peaks are due to two-photon transitions (section 4.3).*

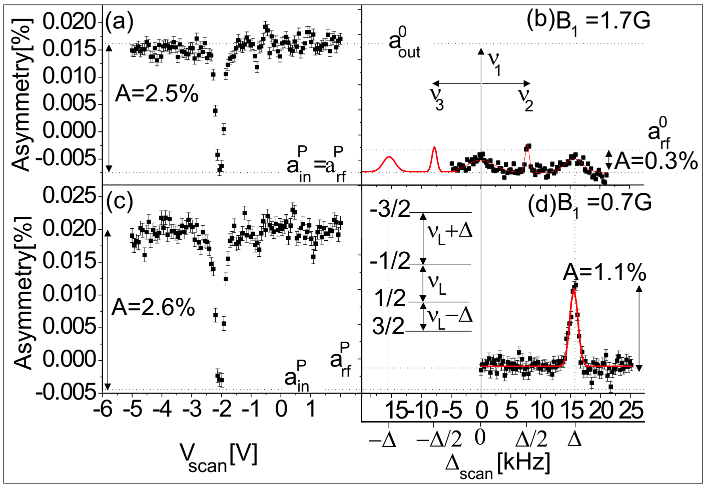

Figure 4.7: *Example of "hyperfinescans" and NQR scans for ^{9}Li in Zn. (a,c) "Hyperfine scan" with $HV_{ISOLDE} = +60009.3\,V$, $V_{fluke} = -6700\,V$, $k_D = 14963.64cm^{-1}$. (b) Single-rf-NQR spectrum. The left part is only a simulation without experimental data. The additional voltage is fixed to resonance $V_{scan} = -2.03\,V$. The other applied voltages and properties of the laser light are identical to those of (a). The narrow two-photon peaks will be discussed later. (d) Multiple-rf-NQR scan.*

curves, one with a central position $xc - \delta$ and the other with a central position $xc + \delta$. δ is the absolute error.

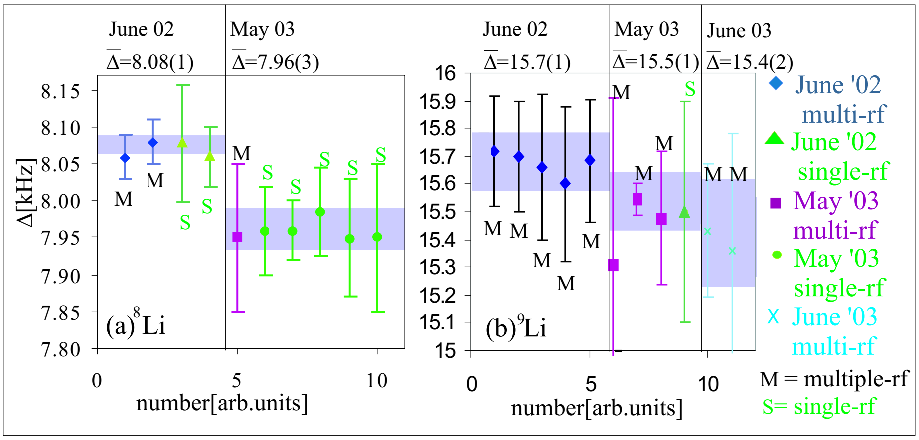

Figure 4.8: *Comparison of the* Δ *in different experiments and for multiple- versus single-rf-NQR scans (a)*^{8}*Li in Zn (b)*^{9}*Li in Zn. The uncertainties are statistical (section 6.1).*

In figure 4.8 several parameters are changed: the time, the measuring procedure and the position of the crystal. The measurements of June 2002 and May 2003 differ in both the parameter of time and that of the crystal position. A different position or orientation of the Zn crystal with respect to the axis of the static field $\vec{B}_0$ can influence the result in several ways. If the crystal is not well centered, the beam can hit the Cu-crystal holder. The interaction of the spin-oriented Li atoms with the cubic structure of Cu in a magnetic field results in a broad resonance around the Larmor frequency (fig. 4.6). Also a misalignment of the electric field gradient and the static magnetic field can cause a shift of the resonance positions (section 4.2.1) and a reduction of the observed Δ with respect to the real Δ. The angle between the axis of the electric field gradient and the static magnetic field is put to 0^o with an error of 5^o. The influence on the measured resonance position due to this uncertainty is around 1.1%. This is exactly the observed shift in figure (4.8a): there is a systematic shift downwards of about 1% for the found resonance positions in May 2003 with respect to those of June 2002. The consistency of the shift for ^{8}Li and ^{9}Li is quantified in table 4.1.

This indicates that we should always compare measurements under the same experimental conditions. And when the crystals are moved within one run one should also take care to remeasure the reference value. In between the measurements in May 2003 and those in June 2003 the crystals were not removed and replaced. However, they were moved up and down in the coil. Here we see that within the error the results are the same: $\frac{\Delta(May03)}{\Delta(June03)}(^9\mathrm{Li}) = 1.006(15)$.

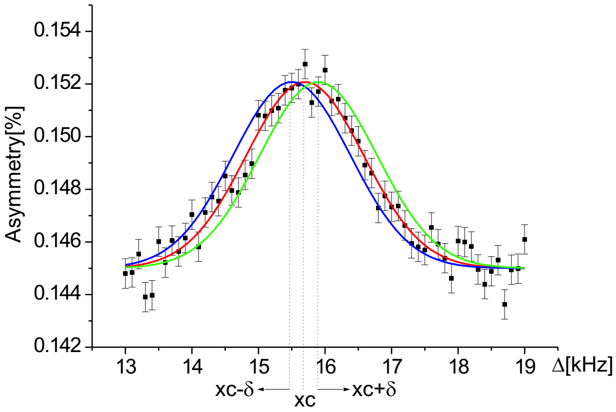

Figure 4.9: *Example of a spectrum for* ^9Li *in Zn, measured in June 2002, used to create figure 4.8. The central curve is the fitted Gaussian function with position xc. The left curve is a simulation of a Gaussian function with the same parameters as the central curve, except for its position, which is* $xc-\delta$ *with* δ *the absolute error. The right curve is made analogously, but with central position* $xc+\delta$*. For more details on error propagation: see section 6.1.*

Table 4.1: *Weighted average of* Δ *for one time period (June 2002, May 2003, June 2003) and one isotope (*^8Li *or* ^9Li*) implanted into a Zn crystal.*

	$\Delta(^8\text{Li})$ [kHz]	$\Delta(^9\text{Li})$ [kHz]	$\frac{\nu_Q(^9Li)}{\nu_Q(^8Li)}$
June 02	8.08(1)	15.7(1)	0.972(6)
May 03	7.96(3)	15.5(1)	0.974(7)
June 03		15.4(2)	

	^{8}Li	^{9}Li	
$\frac{\Delta(June02)}{\Delta(May03)}$	1.015(4)	1.013(11)	
$\frac{\Delta(May03)}{\Delta(June03)}$		1.006(15)	

Within one time period, the results are in agreement with each other. This indicates that the measuring procedure (single-rf-NQR or multiple-rf-NQR) doesn't influence the result.

The ratio of the quadrupole frequencies of ^{8}Li and ^{9}Li stays constant over the different runs (table 4.1). This indicates that this systematic error cancels out in the ratio of the quadrupole frequencies. This means a calibration measurement on an isotope in a crystal with a known quadrupole frequency is always recommended. The systematic error of 1.1% should only be taken into account for the absolute values of the quadrupole moments.

For a complete understanding of a triple-rf-NQR spectum for nuclei with $I = 3/2$, several triple-rf-NQR scans were performed on ^{9}Li in Zn, each with different fixed frequency $\nu_{L,fix}$. For the x-variable of the multiple-rf-NQR spectrum we have two possibilities: one of the two varying frequencies, e.g. $x = \nu_1 = \nu_{L,fix} + \Delta_{scan}$, or $x = \nu_1 - \nu_{L,fix} = \Delta_{scan}$. The position of the resonance as a function of Δ_{scan} equals $\Delta = \frac{\nu_Q}{2}$.

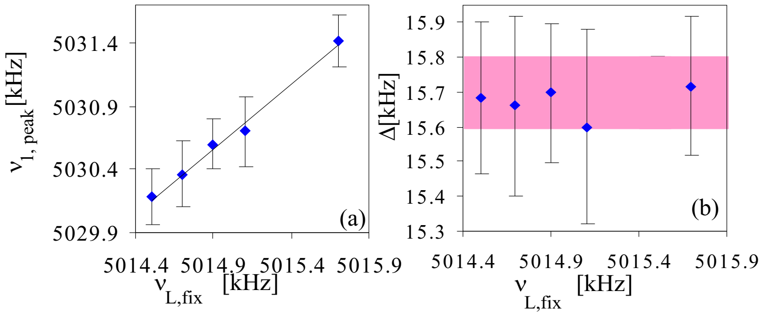

Figure 4.10: *Dependence on the fixed frequency $\nu_{L,fix}$ to the resonance positions in multiple-rf-NQR-scans for ^{9}Li in Zn of June 2002. (a)The position of the NQR-resonance ν_{peak} for one of the two other frequencies. (b) $\Delta = \nu_{peak} - \nu_{L,fix}$ versus $\nu_{L,fix}$. The colored band shows the weighted average with standard deviation. The uncertainties are statistical and determined by a χ^2 analysis as will be discussed in the chapter about experimental results (section 6.1).*

In figure 4.10a is shown that the resonance position $\nu_{1,peak}$ varies linearly as a function of the fixed frequency $\nu_{L,fix}$. The resulting $\Delta = \nu_{1,peak} - \nu_{L,fix}$ is constant as a function of the fixed frequency $\nu_{L,fix}$ (fig. 4.10b). This is important because the fixed frequency $\nu_{L,fix}$ in the triple-rf-NQR scan is the measured Larmor frequency $\nu_{L,meas}$. The Larmor frequency $\nu_{L,meas}$ is measured in a crystal with cubic lattice symmetry. This can slightly differ from the Larmor frequency ν_L of the nuclei in the crystal with non-cubic lattice symmetry: nuclei implanted in different crystals and subjected to the same magnetic field can feel slightly different effective fields due to Knight shifts or inhomogeneities in the crystal (section 5.2.1). On top of this there is always an experimental uncertainty on the measurement. For the multiple-rf-NQR experiments, the output signals of several Rode Schwarz rf-generators are summed with a "resistance sum box" (fig. 4.11).

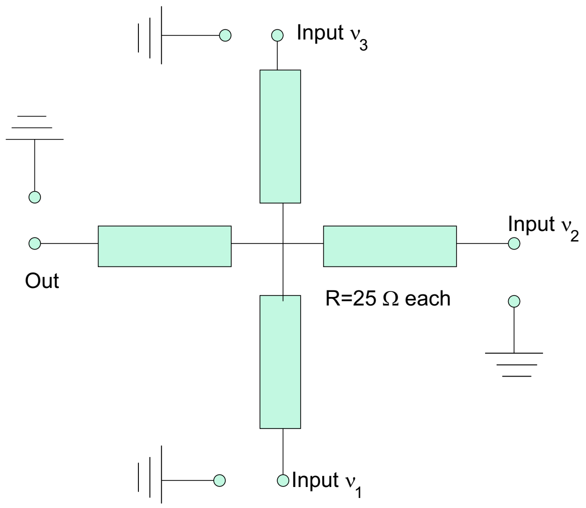

Figure 4.11: *Electric scheme of the "resistance sum box".*

This is a box with three inputs and one output. Inside it consists of some resistances to avoid the reflection of the signal. The summed signal is sent through the LRC circuit.

4.3 Multiphoton transitions

In previous sections, only transitions between adjacent levels, $\Delta m = 1$ transitions, were discussed. If the rf-power is increased, the probability for transitions between levels with $\Delta m = 2$ induced by the simultaneous absorption of two photons, called two-photon transitions, increases. Its probability is proportional to [Ack83, Kei96]

$$W^{\Delta m} \propto \frac{(g\mu_N B_1)^{2\Delta m}}{\hbar^{2\Delta m}\omega_Q^{2\Delta m-2}} \tag{4.9}$$

Looking as a function of Δ_{scan}, the ratio of the resonance positions due to two-photon- and one-photon-transitions is in general given by (using eq. 4.8)

$$\frac{\nu_{2photon} - \nu_L}{\nu_{1photon} - \nu_L} = \frac{0.5(E_m - E_{m-2})}{E_m - E_{m-1}} = \frac{-6+6m}{-3+6m} \tag{4.10}$$

A peak due to a $\Delta m = 2$ transition is narrower than a peak due to a $\Delta m = 1$ transition. The amplitude of a peak due to $\Delta m = 2$ transitions is determined by several parameters: the probability for the transition, the asymmetry parameter of the β-decay and the destroyed polarization. The probability for a $\Delta m = 1$ transition is higher than that for a $\Delta m = 2$ transition. The destroyed polarization is maximal if the most populated m-level is one of the mixing levels.

These $\Delta m = 2$ transitions are only visible as resonances in the β-asymmetry if the inhomogeneous linewidth is small enough. In crystals with a cubic lattice symmetry, $\Delta m = 2$ peaks are situated at the Larmor frequency. In this section we discuss the properties of the resonances due to two-photon transitions in Zn, which has a hexagonal closed packed lattice structure.

4.3.1 Single-rf-NQR

^{8}Li in Zn

In figure 4.12 a NQR spectrum for ^{8}Li in Zn with three possible $\Delta m = 2$ transitions is shown. The spectrum is symmetric around zero. To examine the properties of two-photon transitions, it is sufficient to measure one side of the spectrum.

In figure 4.13 the first part of three single-rf NQR spectra with different rf-powers are shown. The ratio of the position $xc1$ of the one-photon peak and the position $xc2$ of the two-photon peak is as expected 1.5.

Because only the $\Delta m = 1$ transition is saturated, the amplitude of the $\Delta m = 2$ transition increases the most as a function of the rf-power (fig. 4.14b), while the linewidth increases most for the $\Delta m = 1$ transition (fig. 4.14a). The statistical error on the ratio of the linewidths $\frac{FWHM(\Delta m=2)}{FWHM(\Delta m=1)}$ and amplitudes $\frac{A(\Delta m=2)}{A(\Delta m=1)}$ are too large to draw conclusions about a systematic change with the rf-power B_1 (fig. 4.14c). The only constraint we can put in the fits concerning the linewidths, is that $FWHM(\Delta m = 1) > FWHM(\Delta m = 2)$. The ratio of the amplitudes is larger than one in this case because the most populated m-level is one of the mixing levels in the $\Delta m = 2$ transition.

^{9}Li in Zn

In figure 4.15 an example for ^{9}Li in Zn is shown. The amplitudes of the peaks are determined by the probability of the transition, the asymmetry parameter of the β-decay and the amount of destroyed polarization. The destroyed polarization depends on the nuclear spin. Therefore the ratio of the amplitudes $\frac{A(\Delta m=2)}{A(\Delta m=1)}(^{9}Li) = 2.0(2)$ is different from the same ratio for ^{8}Li in Zn: $\frac{A(\Delta m=2)}{A(\Delta m=1)}(^{8}Li) \approx 1 - 1.5$.

4.3.2 Multiple-rf-NQR

Multi-photon transitions can also occur in multiple-rf-NQR.

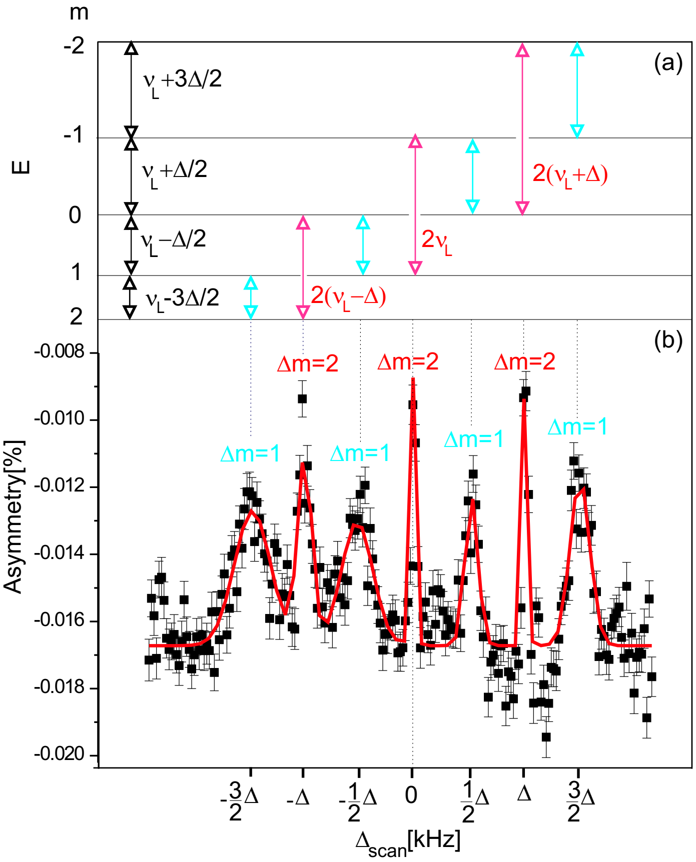

Figure 4.12: *(a) Energy levels of the m-states at a certain magnetic field for* ^{8}Li *(*$I = 2$*) in Zn. (b) Spectrum of the* β*-asymmetry as a function of* $\Delta_{scan} = \nu_{scan} - \nu_L$ *with* $B_1 = 2.6G$ *for* ^{8}Li *in Zn. The resonances due to* $\Delta m = 2$ *transitions are positioned in between the resonances due to* $\Delta m = 1$ *transitions.*

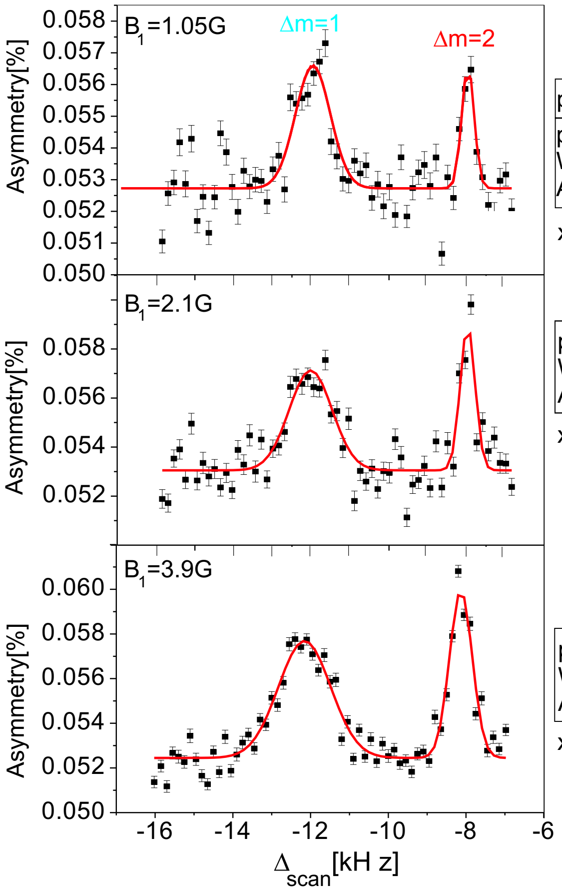

	peak 1	peak2
pos(theo)	$-\frac{3}{2}\Delta$	$-\Delta$
pos[kHz] W[kHz] A[%]	-12.0(1) 0.9(1) 0.38(5)	-7.97(5) 0.3(1) 0.39(7)

xc1/xc2=1.51(1)

	peak 1	peak2
pos[kHz] W[kHz] A[%]	-12.0(2) 1.1(2) 0.43(4)	-7.97(4) 0.38(5) 0.60(8)

xc1/xc2=1.51(2)

	peak 1	peak2
pos[kHz] W[kHz] A[%]	-12.2(2) 1.4(1) 0.52(3)	-8.1(1) 0.58(4) 0.7(1)

xc1/xc2=1.51(3)

Figure 4.13: *β-asymmetry for a single-rf NQR experiment of ^{8}Li in Zn as a function of $\Delta_{scan} = \nu_{scan} - \nu_L$ for negative Δ_{scan}.*

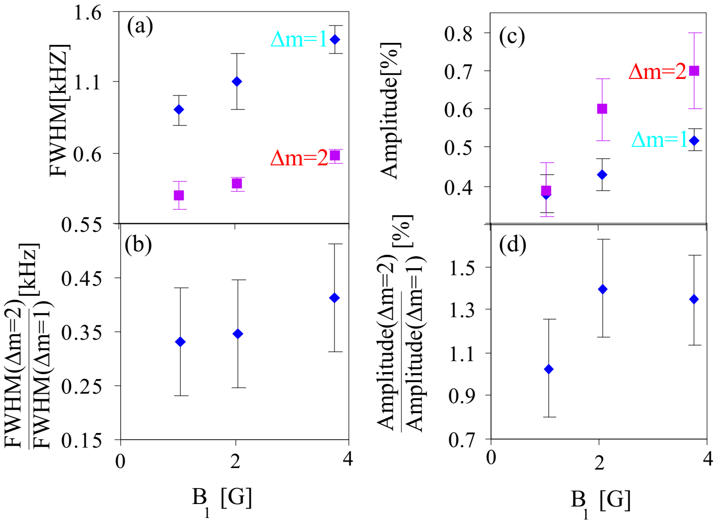

Figure 4.14: *The linewidth and the amplitude of the resonances of figure (4.13). The uncertainties are statistical (section 6.1).*

^{8}Li in Zn

In figure 4.16 two examples of double-rf-NQR spectra for ^{8}Li in Zn are given. In the measured second half of the spectrum with $\Delta_{scan} > 0$ we expect two $\Delta m = 2$ peaks and two $\Delta m = 1$ peaks. The relative positions of the different peaks correspond within the error to the expected values. The ratio of the linewidths $\frac{FWHM(\Delta m=2)}{FWHM(\Delta m=1)}$ is a bit larger than for the single-rf-NQR case for the same rf-power. The ratio of the amplitudes decreased a bit with respect to that for the single-rf-NQR spectra.

^{9}Li in Zn

If the fixed frequency $\nu_{L,fix}$ is chosen properly, we expect one $\Delta m = 1$ resonance and one two-photon peak (fig. 4.17). The small amplitude of the $\Delta m = 1$ peak compared to that for ^{8}Li is reflecting the smaller asymmetry parameter of the β-decay of ^{9}Li. In this peak, all m-levels are mixed, so a maximum of polarization is destroyed. In the $\Delta m = 2$ peak twice two levels are mixed, what destroys only partially the polarization. This explains why the $\Delta m = 2$ peaks in this case are much smaller than the $\Delta m = 1$ peak ($\frac{A(\Delta m=2)}{A(\Delta m=1)}(^9Li) \approx 0.4$). At $\Delta_{scan} = 0$, the rf-power for this frequency is a factor of three larger than in the rest of the scan, what can result in a small peak. The relative positions correspond within the error bar to the expected value. The figure shows that a rf-power of $B_1 = 0.7$G is not enough to produce $\Delta m = 2$ transitions. In the last picture the power is

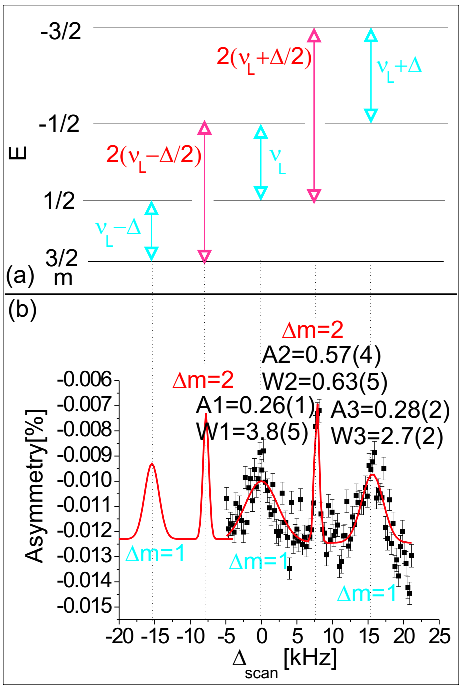

Figure 4.15: *(a) Energy levels for I=3/2. (b)Single-rf-NQR spectrum of* ^{9}*Li in Zn with* $B_1 = 1.7G$*. The ratio of the amplitudes* $\frac{A(\Delta m=2)}{A(\Delta m=1)} = 2.0(2)$*. The ratio of the linewidths* $\frac{FWHM(\Delta m=2)}{FWHM(\Delta m=1)} = 0.24(4)$

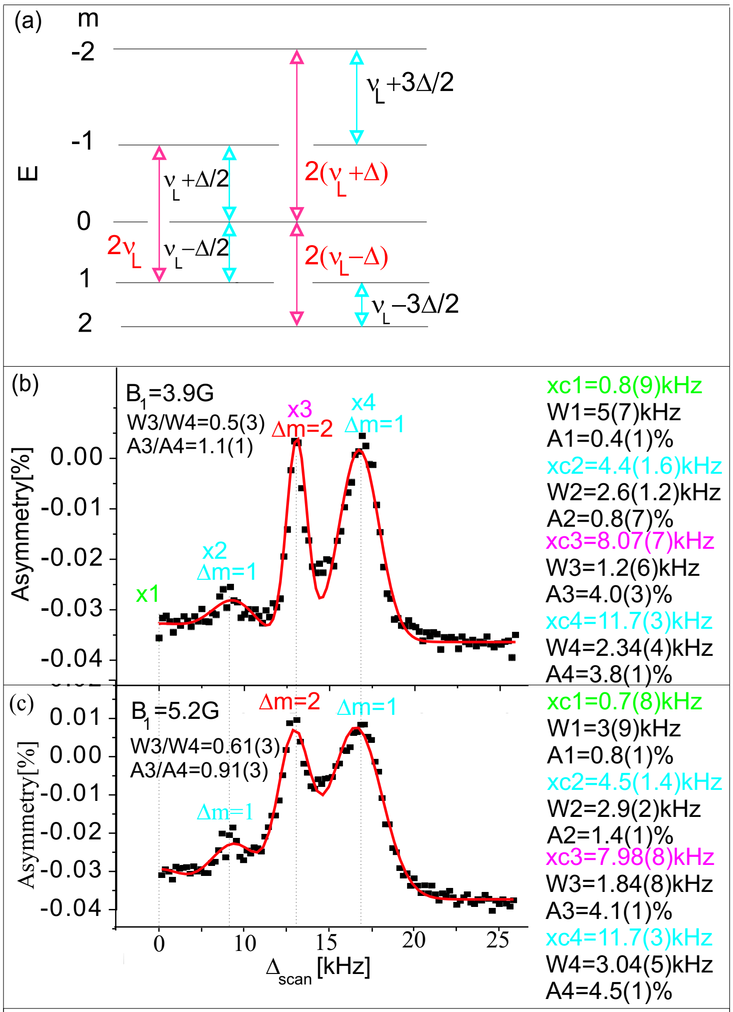

(d)

	expected	(b)	(c)
xc1	0	0.8(9)	0.7(8)
xc4/xc2	3	2.7(9)	2.6(9)
xc4/xc3	1.5	1.45(7)	1.46(8)
xc3/xc2	2	1.8(5)	1.8(5)
xc4-xc2	xc3	7.3(1.6)	7.1(1.6)

Figure 4.16: *(a) Energy level scheme of the m-levels.(b-c) Double-rf NQR spectra of* ^{8}*Li in Zn.(d) Confirmation of the relations between different positions.*

so large that the one-photon peak masks almost the two-photon peak due to its wideness.

The predictability of the relative positions of the different peaks with the assumption that the peaks come from respectively $\Delta m = 2$ and $\Delta m = 1$ transitions is shown once more in figure 4.18, with an overview of all results.

This assures us that the additional resonances belong to $\Delta m = 2$ transitions. From now on we will fit spectra with multi-photon transitions with the necessary constraints about the positions.

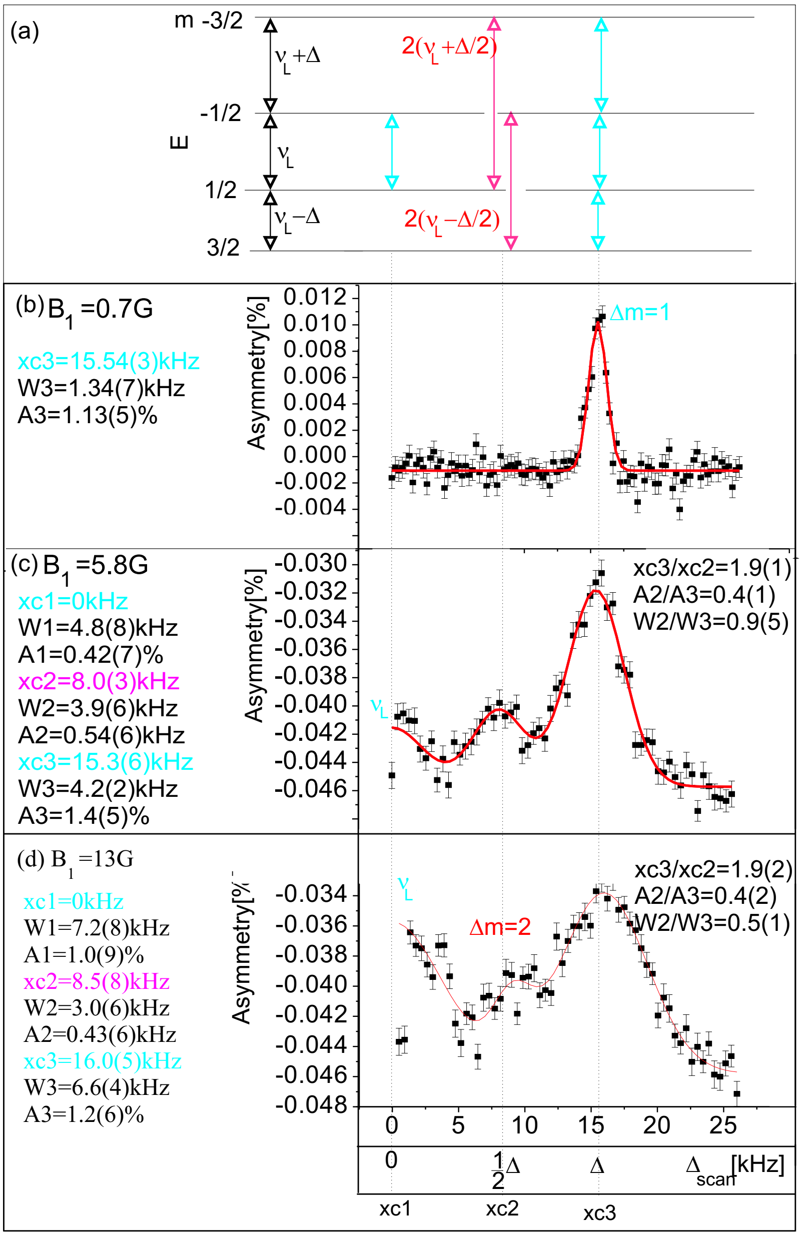

Figure 4.17: *(a) Energy level scheme for ^9Li in a non-cubic crystal. (b-d)Multiple-rf-NQR spectra for ^9Li in Zn. The expected ratio of the position of the one-photon and two-photon peak is 2, as experimentally verified.*

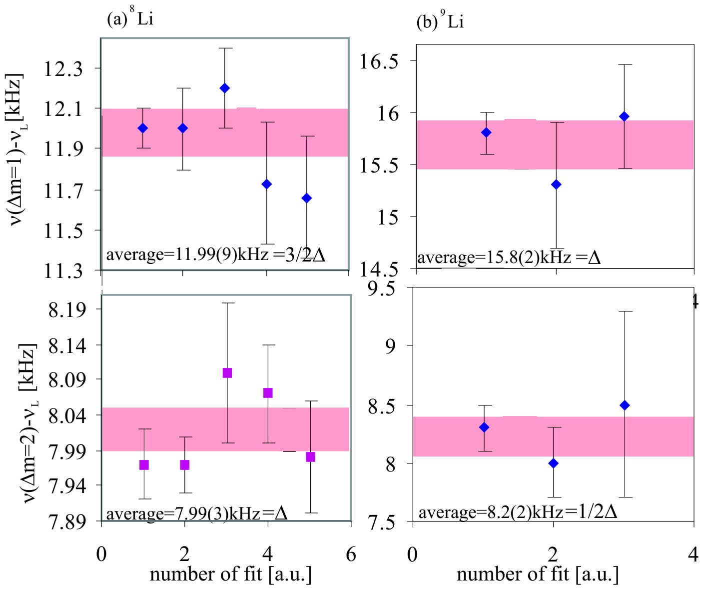

Figure 4.18: *Overview of the fit results for the positions of the* $\Delta m = 1$ *and* $\Delta m = 2$ *peaks. (a)* ^{8}*Li in Zn. The ratio* $\frac{\nu(\Delta m=1)-\nu_L}{\nu(\Delta m=2)-\nu_L} = 1.50(1)$ *is in agreement with the expected* 1.5. *(b)* ^{9}*Li in Zn. The ratio* $\frac{\nu(\Delta m=1)-\nu_L}{\nu(\Delta m=2)-\nu_L} = 1.9(1)$ *is in agreement with the expected* 2. *The uncertainties are determined statistically (section 6.1).*

Chapter 5

Optimizations and calibrations

5.1 Calibrations

5.1.1 Calibration of rf-power B_1

To induce the rf-field $\vec{B}_{rf}$, an AC current was sent through an electric RLC-circuit consisting of a coil, a resistance and a variable capacity (figure 5.1a). The variable capacity is needed to get sufficiently high rf-power. A Rode Schwarz rf-generator produced an AC voltage with the chosen frequency, accurate up to 1Hz. A current probe monitored the current I_{probe} going through the LRC circuit. The relation between the amplitude I_p of the current I_{probe} and the rf-power B_1 is dependent on the inductance L of the circuit, which was not measured in this experiment.

The calibration of the rf-power B_1 versus the amplitude I_p of the current was performed with a Hall probe (figure 5.1b). To perform this calibration, a DC current was sent through the rf-coils. The induced static magnetic field was measured with a Hall probe for different input voltages V_{in}. This gives us the linear relation $B_0 = DI_p$ with D is a constant for one coil. Using an AC current, we get a rf-power

$$B_1 = D\frac{I_p}{\sqrt{2}} \tag{5.1}$$

I_p shows a resonance curve as a function of the frequency for a constant capacity C and constant inductance L [Ser01] with a maximum at $\nu_{rf,max} = \frac{1}{2\pi\sqrt{LC}}$. Therefore the capacities were optimized for the needed frequency ranges. In table 5.1 some rf-powers B_1 for different frequencies are given for one input voltage V_{in} (table 5.1). The rf-power B_1 is proportional to the input voltage V_{in}.

Two different coils were used (fig. 5.2). In October 2001 and in June 2002 a coil with single windings, with a distance of 4mm between the windings was

(a) LRC circuit during experiment

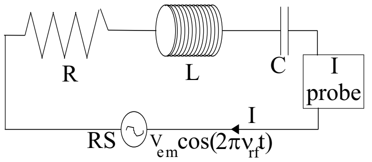

(b) LRC circuit during calibration of rf-field

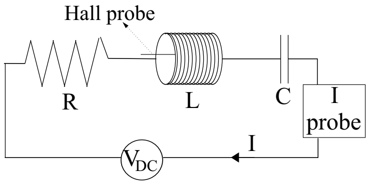

Figure 5.1: *Schematic drawing of an RLC-circuit which consists of a resistance R [Ω], an inductance L[H] and a capacity C[F]. (a) The current probe is used to monitor the amplitude of the AC current through the circuit. (b) During the calibration of the induced magnetic field with a DC-current, a Hall probe was inserted into the coil.*

Table 5.1: *The amplitude I_p of the current I_{probe} through the electric RLC-circuit versus the rf-power B_1 for $V_{in} = 100mV$. The capacities are optimized for a frequency in the region.*

	ν $[kHz]$	I_p $[A]$	B_1 $[G]$
coil 1	1800	0.73(5)	0.94(4)
	5000	1.5(1)	0.38(2)
	5300	2.0(1)	0.34(2)
coil 2	1800	1.12(5)	5.62(46)
	5000	0.45(1)	1.9(1)
	5300	0.42(1)	1.7(1)

used (coil 1). In May 2003 a coil with double windings without spacing and with additional insulation was used (coil 2). In table 5.1 is shown that we get much more power out of the second coil, which is used for the final experiment.

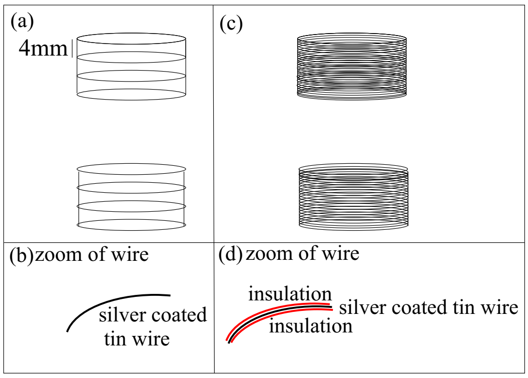

Figure 5.2: *Schematic view of the two used rf-coils. (a) Coil used in October 2001 and June 2002, made of a silver coated tin wire (zoom in (b)). The distance between the windings is about 4mm. (c) Coil used in May and June 2003. The silver coated tin wire is extra insulated (zoom in (d)). Like this the windings can be placed without any spacing.*

In figure 5.3 the rf-power as a function of the rf-frequency is plotted with an input voltage of $V_{in} = 100\text{mV}$. The capacities are optimized for a frequency in the region. The dotted lines indicate the maximum scan range for that isotope. Within this scan range, the amplitude of the rf-field B_1 is varying with more or less 4%. The effect in an NMR/NQR-scan will be negligible.

5.1.2 Homogeneity and stability of static magnetic field

The amplitude of the static magnetic field B_0, felt by the nuclei is calibrated and monitored with a NMR-scan on ^{8}Li, with a known g-factor (section 6.2.1). The drift of the magnetic field was also monitored via the measurement of the current going through the coils. This was measured via the voltage on a resistance of $R = 0.05\Omega$ placed between the magnet power supply and the coils, using a high precision Prema voltage meter (accuracy is 10^{-5}). In the beginning of the first experiment the magnetic field versus the current going through the coils was calibrated roughly with a hall probe.
Figure 5.4b shows that in June 2002 the Larmor frequency stays constant except for the first few hours, in which probably the power supply for the magnet was not yet stabilized. This is not visible on the magnet current (fig. 5.4a)), because the observed drift is of the order of the accuracy of the Prema meter. Figure 5.4 c-e show that the magnetic field was drifting a bit during the last

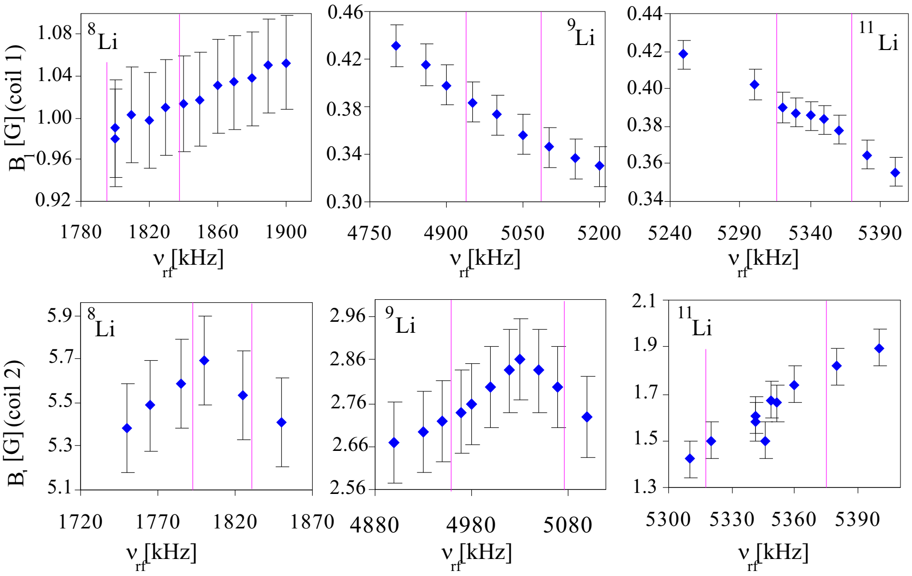

Figure 5.3: *Amplitude* B_1 *of the rf-field as a function of the rf-frequency with capacities, optimized for a frequency in the region and an input voltage of* $V_{in} = 100mV$*. The dotted lines indicate the maximum scan range for that isotope. The uncertainties are determined by the uncertainty on the measured amplitude* I_p *of the current.*

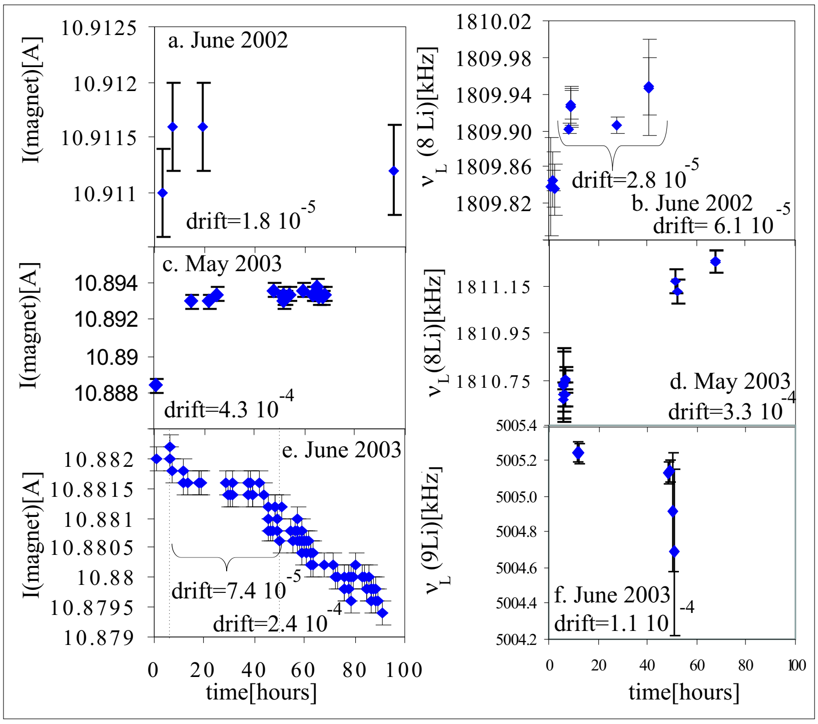

Figure 5.4: *(a-c-e) Current* I_{magnet} *through the coils inducing the static magnetic field* B_0 *as a function of the time. The uncertainty is determined by the accuracy of the read-out of the prema-meter* (10^{-5}) *(b-d) Larmor frequency of* ^{8}*Li in Si as a function of the time for the different experiments. The mentioned drift is the difference between the highest and lowest value, normalized by the average of the two values. (f) Larmor frequency of* ^{9}*Li in Si as a function of the time for the experiment in June 2003. The uncertainties in (b,d,f) are determined statistically (6.1).*

two experiments. The same trend was found in the Larmor frequencies of ^{8}Li or ^{9}Li (fig. 5.4d-f).

In October 2001, the time range in which different NMR measurements in the same crystal with a cubic lattice symmetry were repeated was too short to show instabilities or inhomogeneities.
In order to take into account these drifts in the interpretation of the nuclear moments measurements, we will take as a reference value the weighted average of the frequencies of ^{8}Li (^{9}Li) nearest in time from the frequency measurement of ^{9}Li (^{11}Li).

5.2 Optimizations

The low count rate of ^{11}Li ($< 100\frac{\beta}{s}$) and the high accuracy we are aiming for, make an experimental set-up with optimal conditions necessary. Therefore test measurements were performed on the well produced ^{8}Li ($> 10^{6}\frac{\beta}{s}$) and ^{9}Li ($> 10^{5}\frac{\beta}{s}$) nuclei in October 2001 and June 2002.

5.2.1 Choice of cubic crystal for magnetic moments

We have three candidates as crystals with a cubic lattice symmetry, i.e. LiF, Si and Au. LiF is an insulator with a cubic fcc lattice structure [CRC77]. Si is a semi-conductor with a cubic diamond lattice structure [CRC77]. Au is a metal with a cubic fcc lattice structure [CRC77].

In figure 5.5 an example of a ”hyperfine scan” and NMR-scan for ^{8}Li in these crystals is given. In the spectrum for ^{8}Li in Si from October 2001 (fig. 5.5a) we see a bump with on top a nice peak at the position of the Larmor frequency. This means that the Li-ion beam was probably hitting the Cu crystal holder, as explained in section 5.2.3. The fitted curve is a sum of a Gaussian (bump) and a Lorentzian (peak) curve. This bump is gone in the spectra for ^{8}Li in Si from June 2002 (fig. 5.5b). By eye we see already that the NMR-resonances for ^{8}Li in Si are much narrower than the NMR-resonances for ^{8}Li in the other crystals. The amplitudes of the NMR-resonances for ^{8}Li in Si and in LiF are similar, while those in Au are much smaller. Now we will discuss the amplitude and linewidth more in detail. Therefore the spectra of fig. 5.5b-d were fitted with a Gaussian function.

Asymmetry

The resulting amplitudes for the ”hyperfine scans” are shown in figure 5.6a. The shown detected asymmetry when the power of the laser light is saturated is determined by the created polarization and the nuclear spin-lattice relaxation time. This relaxation has different causes. The main contribution comes from the conduction electrons in metals and semi-conductors, which induce fast changing electro-magnetic fields [Wol79]. Such a time-dependent interaction

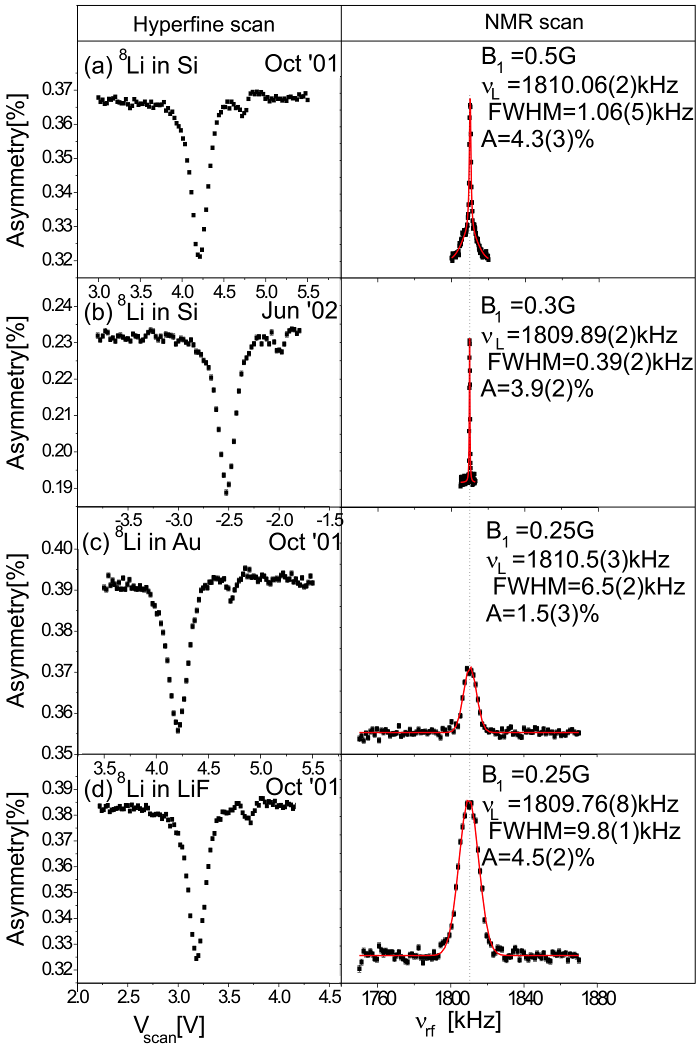

Figure 5.5: *Some examples of "hyperfine scans" (left column) and NMR-scans (right column) for ^{8}Li in Si, Au, LiF. The mentioned uncertainties are determined statistically (section 6.1).*

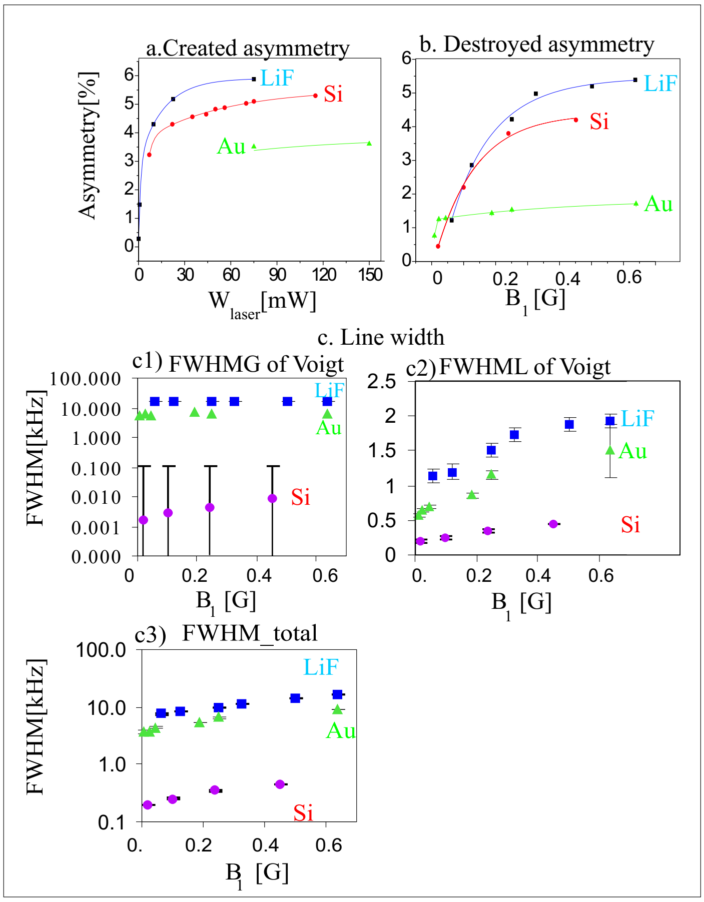

Figure 5.6: *Different properties of the spectra for different crystals. The mentioned uncertainties are determined statistically (section 6.1).*
(a)Created asymmetry as a function of the power of the laser light.
(b)Destroyed asymmetry as a function of the rf-power.
(c)Linewidth as a function of the rf-power. In the two first pictures (c1 and c2) the spectra are fitted with a Voigt curve. The picture which is labeled "c1" shows the width of the Gaussian component of the Voigt curve. The picture which is labeled "c2" shows the width of the Lorentzian component of the Voigt curve. In the last picture (c3) the spectra are fitted with one Gaussian function, giving the total linewidth.

aims for a thermal equilibrium between the nucleus and the surrounding lattice. In thermal equilibrium, the nuclear spins are populated isotropically. A measure of the time scale on which this relaxation occurs is the relaxation time t_{rel}. This t_{rel} can be expressed by

$$t_{rel} = \frac{1}{\frac{64}{9}\pi^2\hbar^3\gamma_e^2\gamma_I^2 < |u_k(0)|^2 >^2_{Ef} \rho(\epsilon_F)^2 kT} \tag{5.2}$$

with γ_e (γ_I) the gyromagnetic ratio $\gamma = \frac{g}{\hbar}$ of the electron (respectively the nucleus) , $< |u_k(0)|^2 >^2_{Ef}$ the electron probability at the site of the nucleus averaged over the Fermi-surface. $\rho(\epsilon_F)$ is the density of electrons at the fermi-surface, k is the Boltzmann constant and T is the temperature. In this expression, only γ_I is isotope dependent, all other parameters are depending on the properties of the implantation host. Its temperature dependence can also be expressed by the Korringa relation [Kor50, Wol79]

$$Tt_{rel} = C_K = \frac{\gamma_e^2}{4\pi\hbar k g_I^2 K^2} \tag{5.3}$$

with C_K the ”Korringa constant” (dependent on the nuclear g-factor), and K the Knight shift (see further) [Ros69, Kor50]. For insulators, the main mechanism of relaxation is caused by the interaction of the fluctuating electric field gradients, caused by the vibrations of the lattice, with the nuclear quadrupole moment, called quadrupolar relaxation [Kra54, Wol79]. This mechanism is in general much slower than the magnetic relaxation. So the relaxation time t_{rel} will be in general much longer for insulators than for metals and semiconductors.
The spin-lattice relaxation time t_{rel} indicates how fast the spin-depolarization occurs:

$$P(t) = P(0)e^{-\frac{t}{t_{rel}}} \tag{5.4}$$

with P(t) the polarization at time t. If this relaxation time t_{rel} is long enough compared to the half life $T_{1/2}$ of the implanted nucleus, almost no polarization is destroyed. This is why most polarization is detected in LiF with the longest relaxation time $t_{rel}(300K) > 15$s [Bul72] amongst the used crystals. It is also the main reason why the detected polarization in Au with t_{rel}(^{8}Li in Au)= 0.6(3)s at room temperature [Has73] is only half that in LiF.

In figure (5.6b) the amplitudes of the NMR peaks are shown as a function of the rf-power. The observed saturation curve can be explained with the same argument as for the saturation curve of the created polarization, since the rf-field consists of a number of photons. The rf-power for which saturation occurs is not the same for all the crystals. For Au and Si, the saturation point is reached quickly, i.e. around $B_1 = 0.3$G, while for LiF it is only reached around $B_1 = 0.5$G. Needing more power for LiF before the maximum polarization is destroyed, means that defects are created or that the total magnetic field in LiF is less homogeneous than in Au and Si. In the latter case, the LiF crystal contains a lot of impurities and induces small additional magnetic fields over the crystal, what will cause a spread on the Larmor frequency ν_L and an inhomogeneous broadening of the resonance. We see that most (least) polarization is destroyed in LiF(Au) with saturated rf-power. The fraction of destroyed polarization with saturated rf-power is determined by the implantation of the isotopes into the crystal and by the relaxation time. The implantation of nuclei into a crystal is complicated. It is important that all nuclei end up in a site without electric field gradient and the same total magnetic field B_0. The fraction of nuclei that are not implanted in the expected site will not undergo the same splitting of their energy levels. This fraction will thus not contribute to resonant destruction of the polarization by NMR. This reduces the amplitude of the NMR/NQR peak. In case the sites show a small spread in the electric and magnetic interaction fields, e.g. due to defects, this causes an increased linewidth of the NMR/NQR peak (inhomogeneous line broadening).

For this implantation, a few rules can be formulated. When the crystal is more compact, the nuclei have less space to implant. So the more compact the crystal, the more nuclei will end up in a perturbed lattice site. If the crystal is a compound of the implanted atom, the nuclei have a large chance to be implanted substitutionally. The more defects, the more nuclei will end up in a perturbed lattice site. In table 5.2 we see that the fraction of destroyed polarization compared to the created one is about 80% for LiF and Si, while it is only about 50% for Au. This leads us to the assumption that the compact structure of Au ($\rho = 19.3\frac{g}{cm^3}$, high Z) forces almost two third of the nuclei into perturbed lattice sites with a non-cubic environment. In LiF ($\rho = 2.635\frac{g}{cm^3}$) and Si ($\rho = 2.321\frac{g}{cm^3}$), about 80% of the nuclei reach an unperturbed lattice site. LiF is a compound of Li. Therefore a substitutional implantation of most Li nuclei is expected. This can explain the large amount of nuclei reaching an unperturbed lattice site.

Table 5.2: *Overview of the maximum created and destroyed polarization for the different cubic crystals. In the last column, the fraction of destroyed polarization compared to the created polarization is given.*

crystal	created polarization PQ_1[%]	destroyed polarization PQ_1[%]	destroyed fraction [%]
LiF	20.2(3)	17.7(1)	88(2)
Si	16.7(1)	12.9(1)	77(1)
Au	12.6(2)	5.9(1)	47(1)

In summary, the created polarization is related to the relaxation time. The destroyed polarization is related to the relaxation time and the implantation into the crystal. The fraction of destroyed polarization with respect to the created polarization is related to the implantation.

Linewidths

In figure (5.6c3) the linewidths of the resonances fitted with a Gaussian curve are shown. It is clear that the spectra for which ^{8}Li was implanted into Si has the smallest linewidth. In general the linewidth of a NMR resonance consists of two parts: a homogeneous and an inhomogeneous part. The homogeneous linewidth is mainly caused by power broadening and is proportional to the rf-power. The inhomogeneous linewidth is caused by inhomogeneities in the magnetic field, electric field gradient and impurities in the crystal. So the extrapolated linewidth at zero rf-power represents the inhomogeneous linewidth. For Si we get a small inhomogeneous line broadening of 0.21(2)kHz. For LiF we get a large inhomogeneous broadening[1] of 6kHz. This confirms what we assumed due to the large saturation point in LiF: small electric field gradients are created by defects or small inhomogeneous magnetic fields are induced over the crystal.

Another way to separate the inhomogeneous and homogeneous part of the total linewidth, is to fit the spectra with a Voigt curve. This is a convolution of a Gaussian and a Lorentzian function[2]. The linewidth of the Voigt curve consists of a Gaussian part (fig. 5.6c1), corresponding to the inhomogeneous linewidth and a Lorentzian part (fig. 5.6c2), corresponding to the homogeneous linewidth. The Gaussian part of the linewidth is shown in figure 5.6c1. Here we find for Si even a smaller value.
Anyway, the inhomogeneous linewidth for Si is found to be small. This means that the static magnetic field is homogeneous over the crystal and that Si itself doesn't induce additional small magnetic fields or electric field gradients due to defects. This will give the small total linewidth in Si we noticed in figure (5.6c3).

The small linewidth and the reasonable amplitudes of the peaks in the spectra for Si make of Si the best candidate to perform an NMR scan on Li-isotopes.

---

[1] Experience learns that NMR/NQR spectra with atoms implanted into ionic crystals contain broader resonances than NMR/NQR spectra with atoms implanted into metals or semiconductors.

[2] A Voigt curve can be expressed by

$$y = A \int_{-\infty}^{\infty} \frac{e^{-p^2} dp}{s^2 + (z-p)^2} \tag{5.5}$$

with

$$\begin{aligned} s &= \sqrt{\frac{3}{2}\frac{FWHML}{FWHMG}} \\ z &= \sqrt{2}\frac{x - x_c}{FWHMG} \end{aligned}$$

$FWHML$ ($FWHMG$) is the width of the Lorentz (Gaussian) function.

Corrections on the position

The Larmor frequency is related to the nuclear g-factor via the relation 4.4. The main contribution to the effective magnetic field B_{eff}, felt by the nuclei, is the external applied magnetic field B_{ext}. But if some electrons of the crystal lattice have a non-zero probability of penetrating the wave function of the nucleus, they also induce an additional magnetic field due to the fermi contact interaction term with as Hamiltonian [Cot02, Wol79, Sli78]

$$H_{fc} = \frac{8\pi}{3} g_e g_N \sum_{j,l} I_{z,j} S_l \delta(r_l - R_j) \tag{5.6}$$

In this equation $g_{e,N}$ are the g-factors of respectively the electrons and the nuclei, $I_{z,j}$ is the nuclear spin, S_l is the electron spin. Due to the Kronicker delta $\delta(r_l - R_j)$ with $r_l(R_j)$ the position vector of the electron (nucleus), only electrons whose wave function is penetrating that of the nucleus are contributing to the interaction. This Hamiltonian can be rewritten as [Sli78]

$$H_{fc} = \frac{8\pi}{3} \langle |u_k(0)| \rangle^2_{Ef} \chi^s_e g_N I_z B_0 \tag{5.7}$$

with $\langle |u_k(0)| \rangle^2_{Ef}$ the electron probability at the place of the nucleus, averaged over the fermi surface. This expression is equivalent to that for a Hamiltonian of the interaction of the nuclei with a magnetic field (section 4.2.1)

$$B_{fc} = \frac{8\pi}{3} \langle |u_k(0)| \rangle^2_{Ef} \chi^s_e B_0 \tag{5.8}$$

This additional magnetic field does not depend on the used Li isotope.

Another correction factor occurs because the external field B_{ext} induces current densities in the closed shells of atomic electrons surrounding the implanted Li ion, which produce a magnetic field B_{ds}, opposite in direction to the applied field [Wol79, Sli78, Cor83]

$$B_{ds} = \frac{-q^2}{3mc^2} B_0 \overline{\frac{1}{r}} \tag{5.9}$$

with q,m the charge and mass of the electrons interacting with B_0. $\overline{\frac{1}{r}}$ is the average of the position vectors of the interacting electrons.
Analogously current densities are induced via the external field and the electrons of the Li atom themselves. These currents will also shield the magnetic field for the nuclei.
The two corrections are called diamagnetic shielding[3]. For neutral Li atoms, the correction factor due to the surrounding electrons is negligible. The correction factor σ due to the electrons of the Li-atom is a property of the element and is isotope independent. For Li this correction factor is $\sigma = 0.000104789$ [Rag89].

---

[3] Sometimes this is called "chemical shift"

The effective field is the sum of all these terms: $B_{eff} = B_{ext} + B_{fc} - B_{ds} = B_{ext}(1+K-\sigma)$ with $K = \frac{B_{fc}-B_0}{B_0}$ the Knight shift and $\sigma = \frac{B_{ds}-B_0}{B_0}$ the diamagnetic shielding correction factor, both indicating a shift of the Larmor frequency compared to the Larmor frequency with B_{ext}. All these corrections should be known or negligible small in order to deduce accurate nuclear g-factors from a single NMR-spectrum.

Table 5.3: *Larmor frequency of* ^8Li *in different crystals with the static magnetic field around* $B_{ext} \simeq 2872G$*.*

crystal	ν_L [kHz]	B_{eff} [G]	sys. error[G]	K	corrected ν_L [kHz]
LiF	1809.85(7)	2872.1(1)	0.08	/	1810.04(7)
Si	1810.05(3)	2872.45(6)	0.08	0.000077(17)	1810.10(5)
Au	1810.1(1)	2872.5(2)	0.08	0.00017(7)	1809.98(10)

In table 5.3 an overview of the measured Larmor frequencies of ^{8}Li in different crystals at the same external static magnetic field B_{ext} is given. The difference in Larmor frequencies can not be explained by instabilities of the external field (section 5.4), which are of the order of $2.8 * 10^{-5}$, leading to the absolute systematic error on the effective field B_{eff} of 0.08 (table 5.3). So the differences are due to the combination of the Knightshift and the diamagnetic shielding. For ^{8}Li implanted in Au, with 1s conduction electrons, the electron density at the place of the nucleus is non-negligible and we will have a measurable Knight shift. This Knight shift is measured to be $K = 0.00017(7)$ [Cor83, Has73]. For LiF, being an insulator, no correction is needed for the Knight shift. Taking into account these corrections, the measurements in LiF and Au are consistent with each other (table 5.3). For Si only the relaxation time of ^{8}Li implanted on the surface of hydrogen covered Si is known $t_{rel} = 3(1)$s. If pure Korringa relaxation is assumed, a Knight shift of $K = 0.000077(17)$ is deduced. If we correct for this Knight shift the result is in agreement with the results for the other crystals. However attention has to be paid because the relaxation time of ^{8}Li in pure Si can be different from the one in hydrogen covered Si.
If we use the measurement of ν_L(^{8}Li in Si) to calculate the Knight shift of Li in Si, we get

$$K(^8Li\,in\,Si) = \frac{\nu_L(Si) - \nu_L(LiF)}{\nu_L(LiF)}(1-\sigma) = 0.00011(4) \tag{5.10}$$

The unknown correction factor for Si is no problem for the measurement of the nuclear moments of the other Li-isotopes. In the ratio of the Larmor frequencies of a nucleus with a known g-factor and one with an unknown g-factor, these systematic errors cancel out if they are isotope independent.

$$\frac{\nu_L(^9Li)}{\nu_L(^8Li)} = \frac{g(^9Li)}{g(^8Li)}\frac{B_{ext}(1+K(^8Li)-\sigma(^8Li))}{B_{ext}(1+K(^9Li)-\sigma(^9Li))} = \frac{g(^9Li)}{g(^8Li)} \tag{5.11}$$

The expression for the Knight shift $K = \frac{B_{fc}-B_0}{B_0}$(eq. 5.8) shows that K is isotope independent. The diamagnetic shielding is also isotope independent.
In figure 5.7 the isotope independency of this correction factor is checked experimentally. The position of the Larmor frequency as a function of time is shown for ^{8,9}Li in different crystals. For the crystals with a non-cubic lattice symmetry (Zn, $LiTaO_3$) the Larmor frequency of ^{8}Li is defined as the average of the positions of the outer (or inner) peaks. The Larmor frequency of ^{9}Li in crystals with non-cubic lattice symmetry is the position of the middle peak of the spectrum. The values for $LiTaO_3$ and Si are equal within the error bar. To determine the correction factor between Si and Zn, we fitted a line through the Larmor frequencies in Si to correct for the drift in the magnet current. We extracted a value for the relative difference between the extrapolated Larmor frequency for ^{8}Li in Si and that in Zn of 7.1(6)10^{-5}. For ^{9}Li this difference equals 7(1)10^{-5}. Within the error this corresponds to the correction factor for ^{8}Li. This is an experimental indication that this correction factor is the same for ^{8}Li and ^{9}Li.

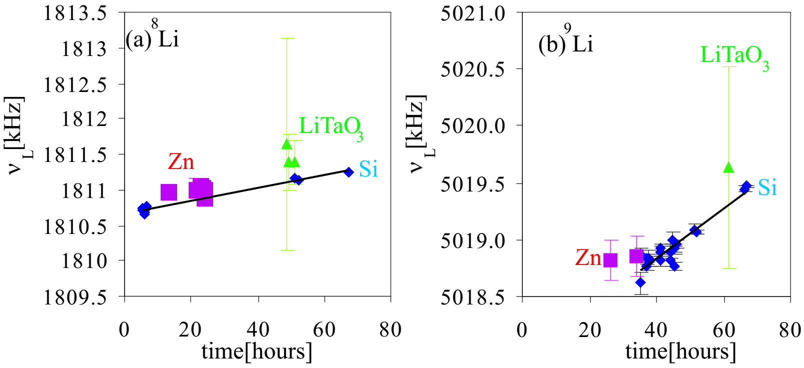

Figure 5.7: *Positions of the Larmor frequency of ^{8,9}Li in Zn, $LiTaO_3$ and Si as a function of time for the experiment in May 2003. The uncertainties are determined statistically (section 6.1).*

A last factor to check is the independence of the Larmor frequency to the rf-power.

In figure 5.8 the found Larmor frequency is shown as a function of the rf-power B_1 for ^{8,9}Li in Si. The used time interval is shown in figure 5.8c-d. In this time interval the current of the magnet can be taken as constant. The found Larmor frequencies are also more or less constant. Nevertheless there is a certain scattering of about 10^{-5} throughout the data. This shows that the statistical errors on the Larmor frequency of ^{8}Li are too small and systematic errors of 10^{-5} will have to be taken into account for the final result of $\nu_L(^8\text{Li})$.

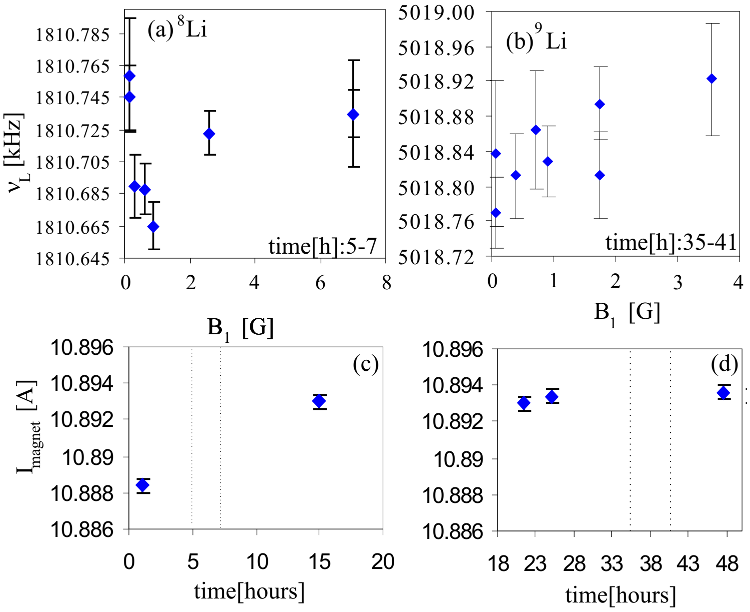

Figure 5.8: *(a-b) Position of the NMR-resonances as a function of the rf-power* B_1 *for the experiment in May 2003. The errors are determined statistically (section 6.1). (a)* ^{8}*Li in Si (b)* ^{9}*Li in Si. (c-d) Current of the magnet for the time interval in which the NMR-resonances out of figure a-b were taken. The errors are determined by the accuracy of the Prema-meter.*

5.2.2 Choice of non-cubic crystal for quadrupole moments

In order to measure the small quadrupole moments of ^{8,9,11}Li, crystals with a relatively large axial symmetric electric field gradient (EFG) are needed. To separate the different peaks of the β-NQR spectrum, the peaks have to be narrow enough. As candidates $LiNbO_3$, $LiTaO_3$ and Zn are chosen. Zn is a metal with a hexagonal closed packed (hcp) lattice structure. The measurement of the quadrupole frequency of ^{8}Li in Zn via multiple rf-NQR by Ohtsubo et al. [Oht93], indicates an interstitial implantation of ^{8}Li nuclei into Zn and a reasonable amplitude of the NQR resonance, despite the large error on the result (6%, table 5.4). This is an indication of a sufficiently long relaxation time t_{rel}.

$LiNbO_3$ and $LiTaO_3$ are both ionic crystals with a rhombohedral lattice structure [CRC77, fer03, Hal70]. We expect a substitutional implantation of the nuclei in these crystals because they are a compound of Li. Of $LiNbO_3$ [Hal70] we used two different samples, one was used in October 2001 and the other in June 2002. The spin-lattice relaxation time t_{rel} is measured at room temperature to be $t_{rel}(300K) = 4.3(12)$s [Ack74]. The quadrupole frequency of ^{7}Li in $LiNbO_3$ was measured with an accuracy of 0.9% [Pet67, Hal70].

$LiTaO_3$ [Abr67, New62] has the largest electric field gradient of the three crystals (table 5.4). The quadrupole frequency ν_Q(^{7}Li in $LiTaO_3$) is known with an accuracy of 0.4% [Cha99]. The relaxation time t_{rel} is measured to be $t_{rel}(300K) > 30$s [Dub77].

Table 5.4: *Some properties of $LiTaO_3$, $LiNbO_3$ and Zn: the quadrupole frequency ν_Q, the distance $\Delta = \frac{\nu_Q}{4}$ between two peaks, the density and the relaxation time T_1. $^{(*)}$The quadrupole frequency of ^{8}Li in $LiTaO_3$ is calculated with ν_Q(^{7}Li in $LiTaO_3$)= $76.4(3)kHz$ [Cha99], Q(^{7}Li)= $40.0(3)mb$ [Voe91, Pyy01] and Q(^{8}Li)= $31.2(5)mb$ [Arn88].*

	$LiTaO_3$	Zn	$LiNbO_3$
lattice structure	rhombohedral	hcp	rhombohedral
ν_Q[kHz] of ^{8}Li in...	$59.4(4)^{(*)}$	33.5(2.0) [Oht93]	42.5(6)[Arn88]
Δ [kHz] of ^{8}Li in...	14.9(1)	8.4(5)	10.6(1)
EFG[$10^{15}\frac{V}{cm^2}$]	7.90(7)	4.24(27)	5.66(5)
density [$\frac{g}{cm^3}$]	7.45	7.14	7.46
t_{rel}[s] of Li in...	> 30	?	4.3(12)

In figure 5.9 an example of single NQR spectra of ^{8}Li implanted into the different crystals is given. Out of the available NQR-spectra for each crystal, the ones with the highest rf-power which still consist of four separated peaks are chosen. For Zn the peaks are still resolvable for $B_1 \approx 5$G. With this high rf-power, additional peaks appear. These additional peaks are caused by $\Delta m = 2$ transitions (section 4.3). Notice that the $LiNbO_3$ sample of October 2001

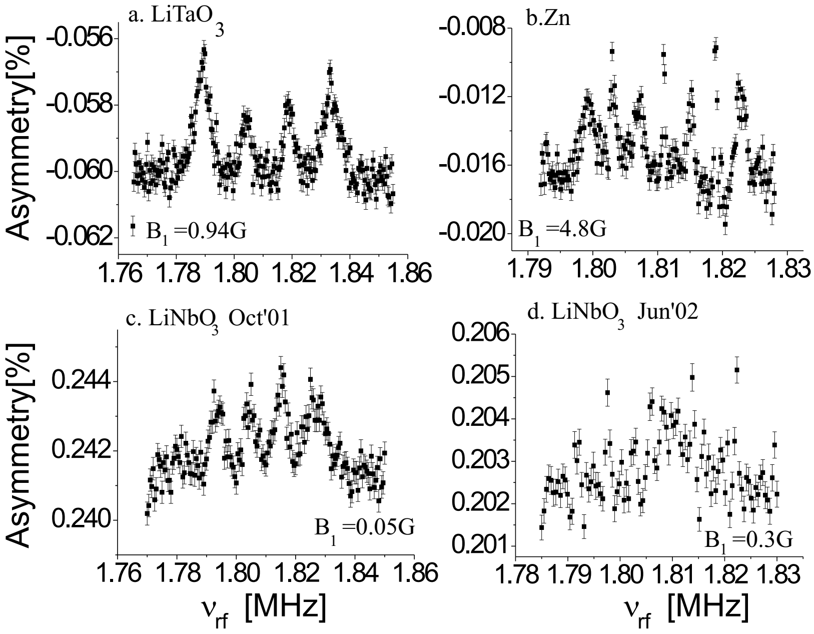

Figure 5.9: *Example of a NQR scan for the different crystals.*

contained less impurities than the one of June 2002.

Linewidth

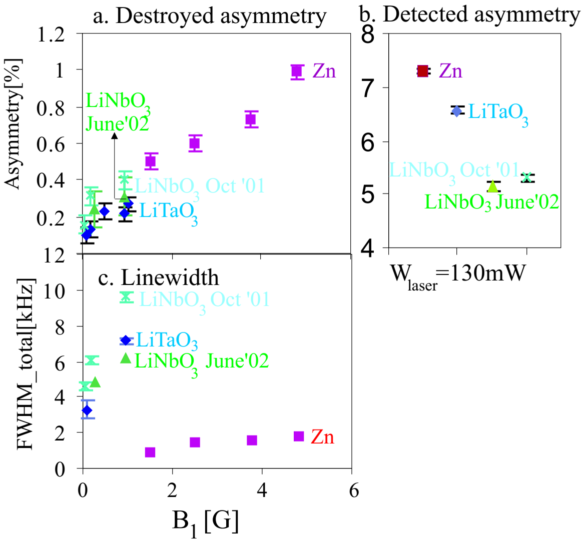

Figure 5.10: *Destroyed polarization (a) and the total linewidth (b) as a function of the rf-power for different crystals. The errors are determined statistically (section 6.1).*

In figure 5.10(b), the FWHM of the NQR resonances, fitted with a Gaussian function, is given for the different crystals as a function of the rf-power. The figure shows a very small linewidth for ^{8}Li in Zn: even at $B_1 = 4.8$G with a linewidth $FWHM < 2$kHz, the peaks are still separated ($\Delta = 8.4(5)$kHz [Oht93]). For LiNbO$_3$, the peaks start to overlap at $B_1 = 0.2$G: the linewidth is $FWHM = 6.1$kHz while $\Delta = 10.6(1)$kHz [Arn88]. For LiTaO$_3$, the peaks start overlapping around one Gauss, with a linewidth $FWHM = 7$kHz and $\Delta = 14.9(1)$kHz [Cha99]. The limit of rf-power for which the peaks are still resolved will give us a limit of amplitude of the NQR resonances. Zn is the best candidate and LiNbO$_3$ is the worst candidate for an NQR measurements on ^{11}Li. Note that this latter was used in the previous measurement of $\frac{Q(^{11}Li)}{Q(^{9}Li)}$ [Arn92].

Asymmetry

The created polarization was measured with a power of the laser light $W = 100$mW. Most created polarization is observed in Zn and LiTaO$_3$ (table 5.5). This means that the unknown relaxation time of Li in Zn is at least larger than three times the half life of ^{8}Li: t_{rel}(Li in Zn)$>$ 2.4s. Why in Zn even more polarization is observed than in LiTaO$_3$ is not clear.

The destroyed polarization was measured as a function of the rf-power B_1. The largest amplitude of the NQR resonances is reached for ^{8}Li in Zn (fig. 5.10a and table 5.5). For similar rf-power[4] similar amplitudes are found for the different crystals. This shows that the fraction of nuclei ending up in a lattice site with a unique EFG will be similar for the three crystals.

Table 5.5: *Overview of the created and destroyed asymmetry A and polarization P. In the last column, the fraction of destroyed polarization compared to the created polarization is given.* $^{(*)}$ *The amplitude A and the polarization P of the rf-scan are the ones with the highest B_1 out of the measured spectra with four separated peaks (figure 5.9). From these spectra the average of the amplitudes of the four peaks is taken.*

crystal	A hyperfine scan [%]	A$^{(*)}$ rf-scan [%]	P created [%]	P$^{(*)}$ destroyed [%]	P$^{(*)}$ fraction [%]	B_1 used [G]
LiNbO$_3$ '01	5.31(7)	0.16(3)	21.9(2)	0.52(4)	2.4(1)	0.05
LiNbO$_3$ '02	5.13(8)	0.24(4)	22.5(2)	0.92(5)	4.1(1)	0.3
LiTaO$_3$ '02	6.57(6)	0.21(2)	26.8(2)	0.63(2)	2.3(1)	0.94
Zn '02	7.29(5)	0.99(1)	28.3(2)	2.9(1)	10.3(1)	4.8

Out of this study we can conclude that Zn is the best candidate to use for NQR measurements on ^{11}Li.

5.2.3 Position of crystal in set-up

The crystals are fixed on a Cu bar. The crystal should be placed such that the ^{8}Li beam doesn't interact with the Cu bar, which has a cubic structure. In addition, some places of the crystals can contain more impurities than other places. The best position of the crystal was experimentally verified by taking spectra at different positions. In figure 5.11 an example is given for ^{8}Li in Zn. In the first two positions the ^{8}Li nuclei were interacting with the Cu bar, resulting in an enormous bump-background at the position of the Larmor frequency of ^{8}Li. This makes a fit of the distance between the other peaks much more difficult.
A similar bump was observed in June 2002 for the spectra of ^{8,9}Li in Zn and in October 2001 for ^{8}Li in Si.

---

[4] Similar rf-power induced by the LRC-circuit. The rf-power which the nuclei feel can be reduced for metals due to the skin-effect [Sli78]. This effect is however minor in this case because of the small implantation depth ($d \approx 0.2\,to\,0.5\mu$m).

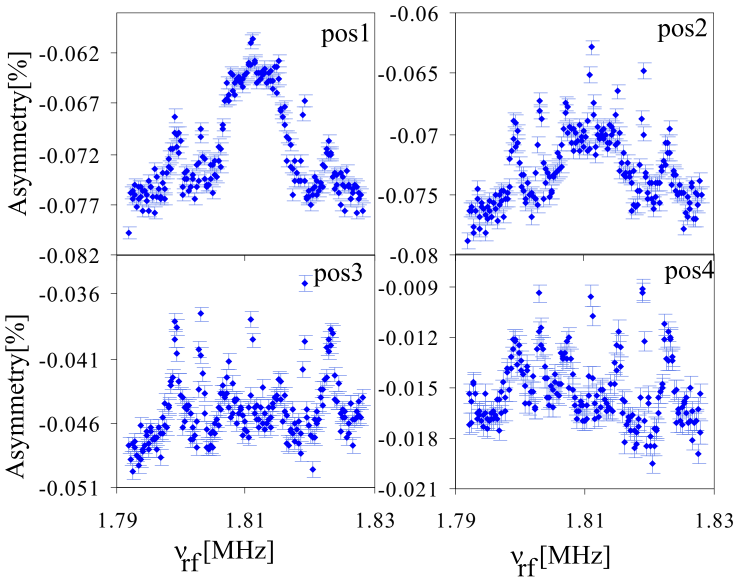

Figure 5.11: *NQR-spectra from May 2003 for ^{8}Li in Zn with different positions of the crystal with respect to the coil with $B_1 = 2.5G$.*

5.2.4 Determination of proper rf-power B_1

A last property to optimize is the rf-power.

Minimum rf-power

The rf-power should be stronger than the minimum rf-power, given by the condition $V\tau > \hbar$ [Sch88, Bor99] with V the interaction strength

$$V = \frac{g\mu_N B_1}{2\hbar}\sqrt{(I-m+1)(I+m)} \tag{5.12}$$

In table 5.6 the resulting minimal rf-power $B_{1,min}$ is given in mG for the three isotopes ^{8,9,11}Li.

Optimum rf-power

With the optimum rf-power, the β-asymmetry is saturated. For the saturation point we take the rf-power for which the asymmetry reaches 80% of its maximum value. For ^{8}Li in Si this corresponds to 0.20(2)G and for ^{9}Li in Si this corresponds to $B_1 = 0.18(1)$G (figure 5.12).

The optimum rf-power for ^{8}Li and ^{9}Li is much higher than the minimum rf-power. This is due to the inhomogeneous line broadening.

Table 5.6: *Minimal rf-power $B_{1,min}$ and the experimental rf-power $B_{1,sat}$ for which the asymmetry of the NMR spectrum is saturated for different isotopes implanted in Si. For the g-factors the values measured by E.Arnold et al. [Arn87, Arn88, Arn92] are taken.*

	$T_{1/2}$ [ms]	g	I [$\hbar$]	$B_{1,min}$ [mG]	$B_{1,sat}$ [G]	$FWHM(B_{rf,sat})$ [kHz]
^{8}Li	838(6)	0.826676(9)	2	0.49	0.20(2)	0.30(1)
^{9}Li	178.3(4)	2.2890(35)	3/2	1.18	0.18(1)	0.90(5)
^{11}Li	8.5(2)	2.445(2)	3/2	23.2		

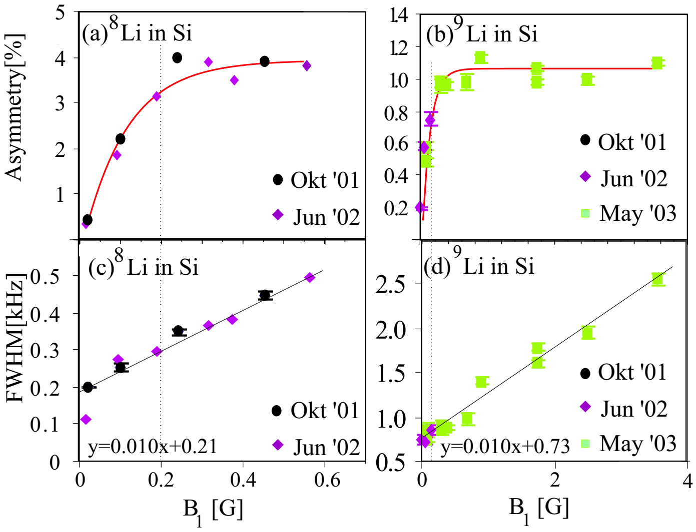

Figure 5.12: *Asymmetry and linewidth for ^{8}Li and ^{9}Li as a function of the rf-power. The errors are determined statistically (section 6.1).*

The optimum rf-power for ^{9}Li, which half life is about five times shorter than that of ^{8}Li, equals more or less that for ^{8}Li. This might suggest that the optimum rf-power is independent of the life time of the nucleus. In that case the optimum rf-power for ^{11}Li in Si will be around 0.20(2)G.

From the figure 5.12d an inhomogeneous linewidth for ^{9}Li in Si of 0.73(4)kHz can be extracted. This is larger than for ^{8}Li ($FWHM = 0.21(2)$kHz). The difference in the two inhomogeneous linewidths is due to the use of a different rf-frequency ν_{rf}. The relative inhomogeneity is the same in the two cases (0.011%), suggesting that it is mainly caused by the inhomogeneity of the local magnetic field.

The measurements of ^{11}Li have been performed with high rf-power (section 6.2.3 and 6.3.5). However, an extrapolation of the above calibrations and optimizations indicate that it would be better to use the same rf-power as for ^{9}Li. In a recent experiment (May 2004) a smaller rf-power of 0.1G has been used.

Chapter 6

Experimental results

In this chapter the experimental results concerning the magnetic (section two) and quadrupole (section three) moments of the Li isotopes are given. In a first section the error propagation is explained.

The NMR spectra are fitted with one Gaussian curve[1] without conditions. The NQR spectra are fitted with a number of equidistant Gaussian curves with common linewidth. This last condition is justified at room temperature for which equal linewidths were found in conventional NMR measurements on ^{7}Li in $LiNbO_3$ [Hal70]. If two-photon peaks are involved, they are also fitted with equidistant Gaussian curves with common linewidth. Additional constraints on the positions are used to connect the peaks due to $\Delta m = 1$ and $\Delta m = 2$ transitions. The only possible additional constraint on the linewidth is that the $\Delta m = 2$ peaks should be narrower than the $\Delta m = 1$ peaks. This condition will be omitted unless explicitly mentioned.

6.1 Error propagation

6.1.1 Statistical errors

Individual spectrum

For the determination of the statistical uncertainty on a single spectrum with j datapoints, each with a β-asymmetry a_j, the spectrum is fitted with a Gaussian function. In this procedure, the reduced χ^2 as a function of the position and

---

[1] The lineshape of a NMR spectrum has a Voigt-profile. However, some single-NQR spectra couldn't be fitted with a Voigt curve. Comparing fits with different lineshapes for ^{8}Li learns that a Gaussian curve is the best approximation of the real lineshape. The fitted positions of the resonances are the same for both lineshapes. Therefore we chose to use for all spectra the same fitprocedure and to fit everything with Gaussian lineshapes.

the linewidth of the resonance is calculated

$$\chi^2_{red} = \frac{1}{N-1}\sum_j (\frac{a_{theo,j} - a_{exp,j}}{\delta_j})^2 \tag{6.1}$$

The optimal parameters are the ones with minimum χ^2_{min}. The interval of parameters with χ^2 between χ^2_{min} and

$$\chi^2_\alpha = \chi^2_{min}(1 + \frac{p}{N-p}F(p, N-p, \alpha)) \tag{6.2}$$

gives the confidence interval of α [Cli70]. $\alpha = 68\%$ corresponds to one standard deviation σ. p is the number of parameters being determined, N is the number of datapoints and F is the F-distribution

$$\begin{aligned} F(m, n, \alpha) &= \frac{\Gamma(\frac{n+m}{2}) n^{\frac{n}{2}} m^{\frac{n}{2}} \alpha^{\frac{n}{2}-1}}{\Gamma(\frac{n}{2})\Gamma(\frac{m}{2})(m+n\alpha)^{\frac{n+m}{2}}} && (6.3) \\ &= \frac{m^{\frac{m}{2}} n^{\frac{n}{2}} \alpha^{\frac{n}{2}-1}}{(m+n\alpha)^{\frac{m+n}{2}} B(\frac{n}{2}, \frac{m}{2})} && (6.4) \end{aligned}$$

with

$$B(p, q) = \frac{(p-1)!(q-1)!}{(p+q-1)!} \tag{6.5}$$

and

$$\Gamma(z) = \int e^{-t} t^{z-1} dt \tag{6.6}$$

the Gamma function.
Taking a confidence level of $\alpha = 68\%$, four parameters to determine (position, width, baseline and amplitude of the peak) and thirty datapoints, we find $\chi^2_{0.683} \approx 1.10\chi^2_{min}$. So a contour of $\chi^2_{min} + 10\%$ will give us in that case an error of 1σ. The more datapoints we have, the smaller the needed interval. However, the datapoints on the baseline contain less information on the peak than the datapoints in the peak. Therefore, we approximated the statistical error by that obtained from the $\chi^2_{min} + 10\%$ contour for all spectra, even those with 100 data points. This approximation gives conservative errors.

In practice, contours of 10% of χ^2 are plotted as a function of the resonance position and the linewidth. An example is given in figure 6.1b. Such a χ^2 plot shows us the correlations between the linewidth and the central position of the resonance. If the contours are circular, both parameters are not correlated. Often a correlation is present.
To define the uncertainty δ, one projects the $\chi^2_{min} + 10\%$ contour on the axis of the rf-frequency (fig. 6.1b). If the $\chi^2_{red} > 1$, the error is corrected by multiplying the error with a factor $\sqrt{\chi^2_{red}}$ [PRD02].

The spectrum is also fitted with a Gaussian function in Origin. The uncertainties which Origin give as fit error are called "fit errors" throughout the

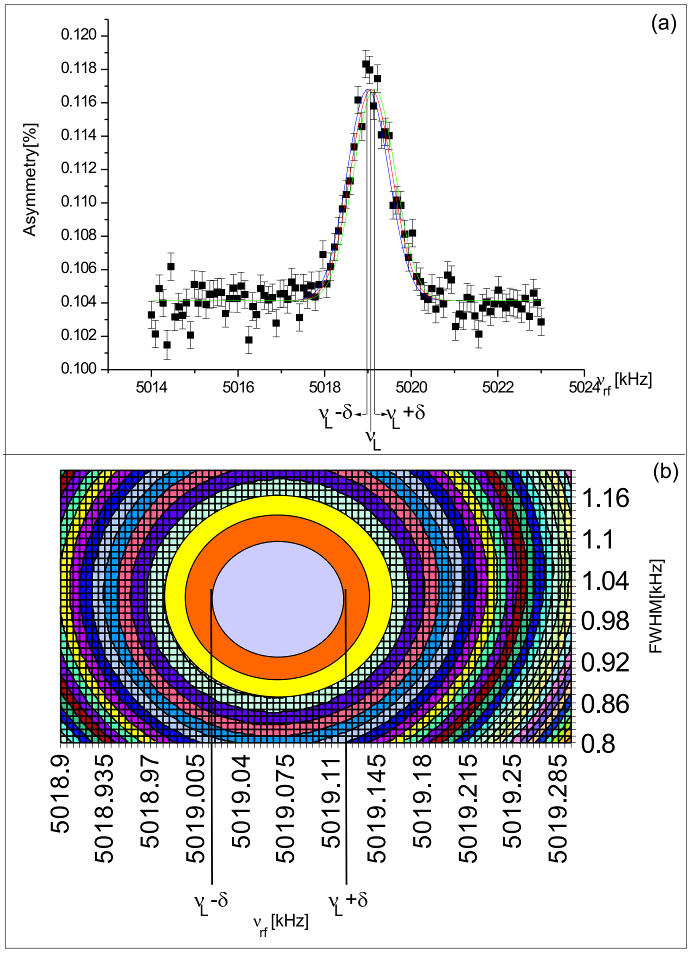

Figure 6.1: *Example of a NMR spectrum for* ^9Li *implanted in Si and a* χ^2 *plot.*

text in this work. These errors are slightly smaller than the errors found in the way described above. But we preferred to be conservative and take the errors as described above. For the amplitudes and linewidths, the χ^2 analysis is not made and the fiterror, given by Origin is taken.

Average of several independent spectra

When we have a set of several independent measurements with resonance positions $\nu_{r,i}$ and individual uncertainty δ_i, the weighted average

$$\nu_{r,average} = \frac{\sum_i \frac{\nu_{r,i}}{\delta_i^2}}{\sum_i \frac{1}{\delta_i^2}} \tag{6.7}$$

is taken as final result. The uncertainty $\delta_{average}$ on this average $\nu_{r,average}$ is determined by both the uncertainty

$$\delta_1 = \frac{1}{\sum_i \frac{1}{\delta_i^2}} \tag{6.8}$$

and the standard deviation

$$\delta_{stdev} = \sqrt{\frac{1}{n-1} \sum_i (\nu_{r,i} - \nu_{r,average})^2} \tag{6.9}$$

and equals

$$\delta_{average} = \sqrt{\delta_1^2 + \delta_{stdev}^2} \tag{6.10}$$

Since the statistical errors are quite conservative, in most cases the standard deviation will be smaller than the statistical error δ_1.

6.1.2 Systematic errors

Besides this statistical uncertainty, some systematical errors may influence the result.

Larmor frequency of ^{8}Li

For the reference measurement of $\nu_L(^8\mathrm{Li})$ there are two systematic errors. The first one is due to the drift of the static magnetic field. Over the range of a full experiment this was varying from 2.10^{-5} up to 4.10^{-4}, depending on the experiment. However, several calibration measurements on ^{8}Li were performed. The error on the weighted average of the results for $\nu_L(^8\mathrm{Li})$ from measurements performed closest in time to the measurement on $\nu_L(^{9,11}\mathrm{Li})$ together with the standard deviation, gives the final systematical error on the reference $\nu_L(^8\mathrm{Li})$ for that measurement. We always took reference values both before and after the measurement on $\nu_L(^{9,11}\mathrm{Li})$.
The used systematic error is thus smaller than the drift over the full experiment.

The used reference value changes for each measurement. The accurate numbers are given in the text together with each separate measurement.

The second systematic error on $\nu_L(^8\text{Li})$ is due to the fact that the pulses are only separated by some seconds while the half life of ^{8}Li is 0.838s. If one assumes that every second pulse was for ISOLDE, like was most of the times the case, the pulses are separated by 2.4s. Assume that from the first pulse a number N_0 Li-isotopes are reaching the stopper crystal. In the first channel counts are added during 2s. With a lifetime $\tau = \frac{T_{1/2}}{ln(2)} = 1.209(9)s$, this gives us

$$N_1(\nu_1) = N_0 \int_0^2 e^{\frac{-t}{\tau}} dt = 0.67 N_0 \tag{6.11}$$

counts in the first channel with an applied rf-frequency ν_1 [Kra88]. In the second channel a rf-frequency ν_2 is applied and a fraction

$$N_2(\nu_1) = N_0 \int_{2.4}^{4.4} e^{\frac{-t}{\tau}} dt = 0.092 N_0 \tag{6.12}$$

of β-particles due to the first pulse is present. This fraction of nuclei interacted with the rf-field with frequency ν_1. The rest of the counts in the second channel is due to the second proton pulse, due to which $N_0{}'$ Li-isotopes are reaching the stopper crystal. This number of counts equals $N_2(\nu_2) = 0.67 N_0{}'$. One can assume that all proton-pulses give more or less the same count rate (i.e. $N_0 \approx N_0{}'$). Therefore we can say that 88% of the β-particles in the second channel has an asymmetry $a(\nu_2)$ corresponding to ν_2 and 12% of them has an asymmetry $a(\nu_1)$ corresponding to ν_1. Analogously, the counts in the third channel consist of 86.5% β-particles with an asymmetry $a(\nu_3)$, 11.8% β-particles with an asymmetry $a(\nu_2)$ and 1.7% β-particles with an asymmetry $a(\nu_1)$.
To calculate the final asymmetry a_i of the i-th channel, we take a weighted average

$$a_i = \frac{\sum_{i-4}^{i} P(\nu_i) a(\nu_i)}{\sum_{i-4}^{i} P(\nu_i)} \tag{6.13}$$

with $P(\nu_i)$ the fraction of nuclei that was interacting with the rf-field with frequency ν_i. The found asymmetry can than be compared with a Gaussian curve, assuming no remaining β-activity from the previous pulses. In figure 6.2 we see that both curves are very similar and almost identical. However, the curve for which the remaining β-activity from the previous pulses is taken into account is shifted slightly to the right compared to the other curve and becomes a bit asymmetric (see zoom in figure 6.2b). The induced error δ_{puls} is of the order of one channel, corresponding to an error of $\delta_{puls} \approx 10^{-5}$. This is of the same order as the systematic error due to the drift in the magnetic field.

As total systematic error on the Larmor frequency of ^{8}Li

$$\delta_{tot,sys} = \sqrt{\delta^2_{Bdrift} + \delta^2_{puls}} \tag{6.14}$$

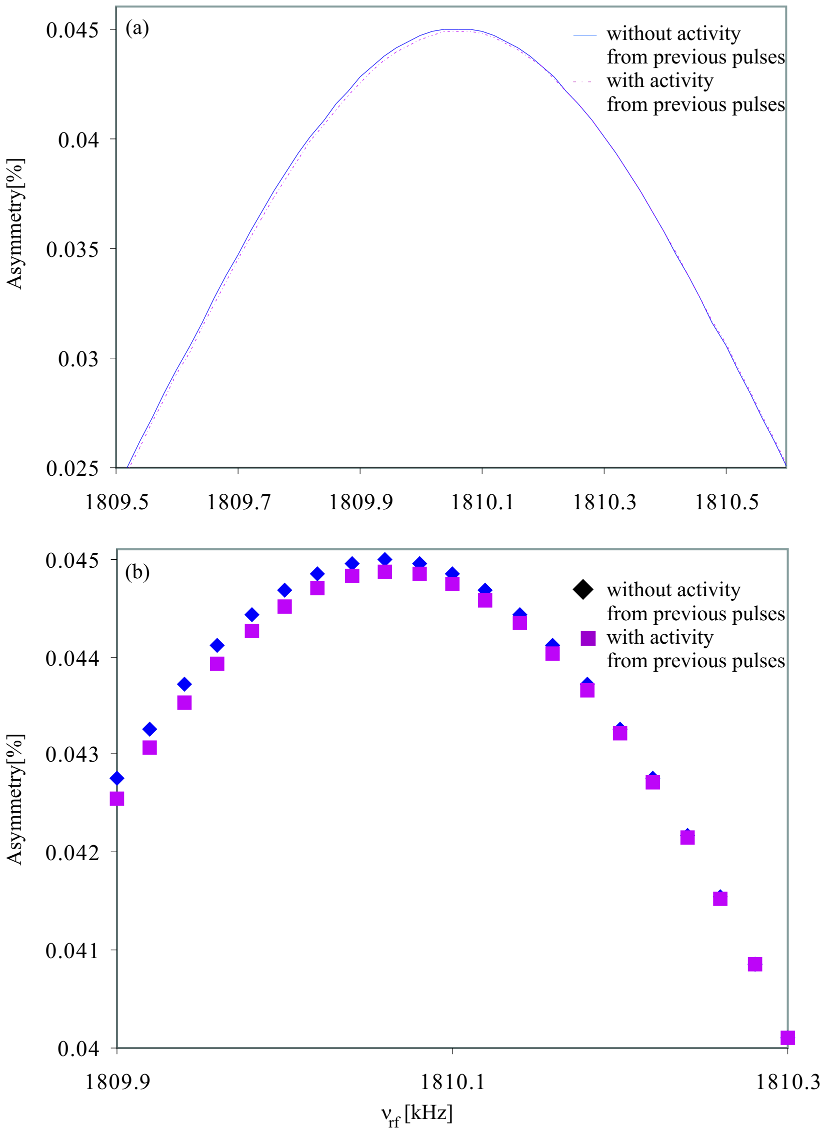

Figure 6.2: *Comparison of the asymmetry with and without remaining β-activity from the previous pulses. (b) is a zoom of (a).*

is taken. This systematic error equals the total error on the Larmor frequency of ^{8}Li, which is used as a reference for $\nu_L(^{9}\mathrm{Li})$ and $\nu_L(^{11}\mathrm{Li})$ measurements, since the statistical error is smaller (typical $5.\,10^{-6}$).

Quadrupole frequencies

For the measurements of the quadrupole frequencies, the uncertainty on the misalignment angle β between the static magnetic field and the electric field gradient is the main cause of a systematic error. This systematic error equals $\frac{3\cos\beta^2-1}{2} \approx 1.1\%$ for $\beta \approx 5°$ and cancels in the ratio of the quadrupole frequencies, when these frequencies are measured in the same crystal which was not taken out of the holder. So for example the measurements from May 2003 and June 2003 may be compared without systematic error.

6.2 Magnetic moments

6.2.1 Reference: $\mu(^{8}\mathrm{Li})$

The Larmor frequency of ^{8}Li in Si is measured each experiment regularly in time (figure 5.4) as a reference. The used reference measurement is the one closest in time to the real measurement, unless explicitly mentioned. Each such measurement takes only about five minutes.

(a) Reference	$g(^{8}\mathrm{Li})[\mu_N]$
[Con59] meas. 1	0.8265(4)
[Has73] meas. 2	0.82668(18)
[Win78] meas. 3a	0.826664(16)
[Win78] meas. 3b	0.826670(16)
[Win78] meas. 3c	0.826687(13)
average	0.826676(9)
average, corr. σ	0.826781(9)
[Rag89]	0.826780(9)

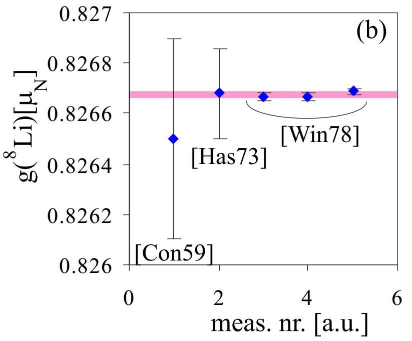

Figure 6.3: *(a) Overview of the different measurements of* $g(^{8}Li)$ *in the past and the tabulated value in the compilation of Raghavan et al. [Rag89]. (b) Graphical overview of the different measured values of* $g(^{8}Li)$*. The colored band shows the weighted average of all measurements, without corrections for diamagnetic shielding.*

The magnetic moment of ^{8}Li was measured several times in the past (fig. 6.3). In the compilation of Raghavan [Rag89], the weighted average of the three last measurements, corrected for the diamagnetic shielding ($\sigma(Li) = 0.000104789$) is given: $\mathbf{g(^8Li)=0.826780(9)}$, giving a magnetic moment $\mu = +1.653560(18)\mu_N$. This is also the value we will adopt in this work.

6.2.2 $\mu(^9$ Li)

The Larmor frequency of ^{9}Li in Si was measured three times independently in June 2002.

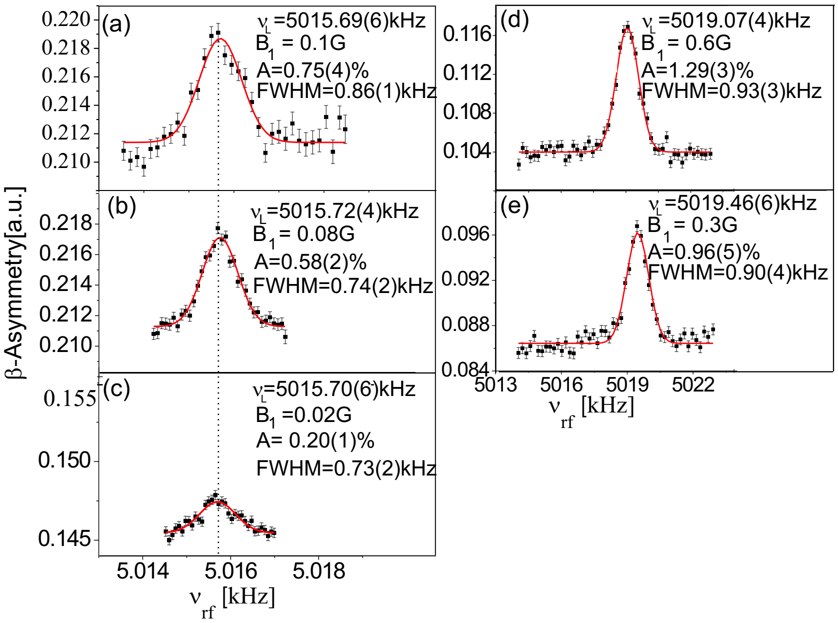

Figure 6.4: *(a-c) Three independent data sets for NMR measurements of* ^9Li *in Si from June 2002. Notice the different amplitudes and linewidths due to different rf-fields. (d-e) Independent data sets for NMR measurements of* ^9Li *in Si from May 2003. The difference in Larmor frequency is explained by the instability of the magnetic field. To deduce the g-factor, a measurement of* $\nu_L(^8Li)$ *just before or after the* $\nu_L(^9Li)$ *measurements is used. The mentioned errors in this figure are statistical errors.*

The raw spectra contain hundred channels with 9s of data taking in sweep mode for each channel. The statistics in three channels was summed to produce the final NMR-spectra (fig. 6.4a-c). All spectra are consistent with each other and have a typical statistical relative error of 4.10^{-6}. These measurements were performed respectively 29, 29.5 and 39 hours after the beginning of the experiment in June 2002, i.e. in the period were the Larmor frequency of ^{8}Li in Si stayed constant within the error (figure 6.5a-b). As reference we take the

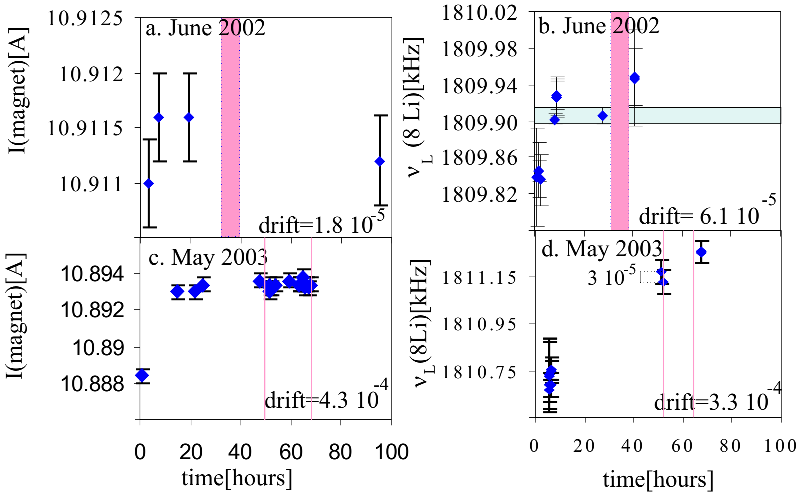

Figure 6.5: *Stability of the current I_{magnet} of the magnet and the Larmor frequency ^8Li as a function of time. The vertical bands indicate the time period in which measurements on $\nu_L(^9Li)$ were performed. The horizontal band indicates the weighted average of all measurements on ^8Li except for the first ones for which the magnet current was not yet stable.*

weighted average, including the standard deviation, of the Larmor frequencies in figure (6.5b), being $\nu_L(^8\mathrm{Li}) = 1809.91(1)$kHz. In this weighted average the first four measurements were not taken into account because for these points the current of the magnet was not yet stable. The standard deviation takes into account possible variations of $\nu_L(^8\mathrm{Li})$ due to fluctuations in the magnet current. Taking into account the systematic error due to the remaining β-particles of the previous pulses one gets $\nu_L(^8\mathrm{Li}) = 1809.91(3)$kHz. This gives us the ratio of the g-factors of ^{9}Li and ^{8}Li, shown in the first part of figure (6.6a). The error is defined by the standard rules for the error on a product [Kno89] and is mainly determined by the systematic error on $\nu_L(^8\mathrm{Li})$.

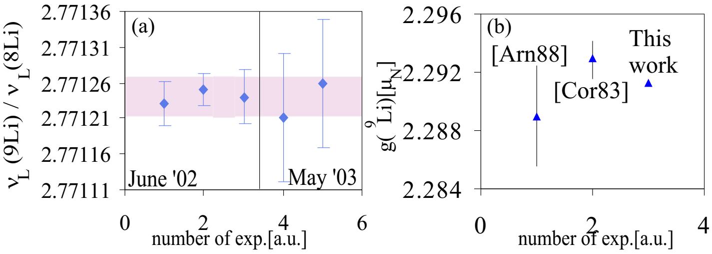

Figure 6.6: *(a) Overview of the different results of this work for the ratio of g-factors for ^{9}Li and ^{8}Li. The colored band is the weighted average of all measurements. (b) Graphical overview of the different measurements of g(^{9}Li) in the past.*

In May 2003 two NMR measurements of ^{9}Li in Si were performed close in time to a reference measurement, respectively at 52 and 67 hours after the beginning of the experiment. As reference we take the Larmor frequency of ^{8}Li in Si measured at respectively 52.2 and 67.2 hours after the beginning of the experiment (fig. 6.5c-d). Taking into account the systematic error of $3.\ 10^{-5}$ due to the drift of the magnetic field in this experiment and the systematic error of $1.5\ 10^{-5}$ due to the restactivity, we get $\nu_L(^8\mathrm{Li}) = 1811.15(6)$kHz for the first measurement and $\nu_L(^8\mathrm{Li}) = 1811.26(6)$kHz for the second measurement. This results in the last part of figure (6.6a) for the ratio of the g-factors $\frac{g(^9Li)}{g(^8Li)}$.
In these measurements, higher rf-fields were used than in June 2002. This increased the amplitude of the resonance, while the linewidth increased only a little bit (figure 6.4d-e), as expected from section (5.2.4). So from these spectra we can deduce the Larmor frequency of ^{9}Li in Si more accurate than for the other spectra of June 2002. However, the instability of the static magnetic field makes the final errors a bit larger than the ones of June 2002.

From figure (6.6a) with the ratio $\frac{g(^9Li)}{g(^8Li)}$ we can conclude that all the measurements of this work are consistent. For the final result we take the weighted

Table 6.1: *Comparison of different measurements of the magnetic moment of* ^{9}Li. *Values labeled with* * *are corrected for the diamagnetic shielding* σ.

	crystal	g	μ $[\mu_N]$	rel. error [%]
E. Arnold et al. [Arn88]	LiF	$2.2890 \cdot (35\cdot)$	$3.4334 \cdot (52\cdot)$	0.15%
Correll et al. [Cor83]*	Au	$2.2929 \cdot (4\cdot)$	$3.4391 \cdot (6\cdot)$	0.017%
Correll. fit this work*	Au	$2.2929 \cdot (12\cdot)$	$3.439 \cdot \cdot (2 \cdot \cdot)$	0.06%
This work *	Si	2.29121(3)	3.43682(5)	0.0013%
[Rag89] *		2.2929(4) 2.2890(35)	3.4391(6) 3.4335(52)	

average of all data points $\frac{g(^{9}Li)}{g(^{8}Li)} = 2.77124(3)$ (colored band in figure 6.6a). Taking the adopted value of [Rag89] for $g(^{8}\text{Li})$, which is corrected for the diamagnetic shielding, this results in a g-factor of **g(^{9}Li)=2.29121(3)**, which has a relative error of 1.3 10^{-5}. With a spin $I = 3/2$ this gives a magnetic moment of $\mu(^{9}\text{Li}) = 3.43682(5)\mu_N$. This is in agreement with the previous measurement of E.Arnold et al. [Arn88], but not with another earlier measurement by F.D.Correl et al. [Cor83] (table 6.1). This NMR-measurement was performed at the Los Alamos National Laboratory Van de Graaf Facility. Polarized ^{9}Li nuclei were produced in a $^{7}\text{Li}(\vec{t}, p)$ reaction, using $5 - 6$MeV polarized tritons. The ^{9}Li nuclei were implanted in a Au single crystal. The Larmor frequency of protons in Au was measured as reference, giving $\nu_H = 4245.8(1.2)$kHz with $g_H = 5.585552(62)$[2]. A new fit of these data (fig. 6.7) showed however that the published error $\nu_L = 1742.8(3)$kHz may have been too small. The newly fitted value is $\nu_L = 1742.9(9)$kHz. This error is corrected for the $\chi^2_{red} = 1.31$ being larger than 1, by the factor [PRD02]

$$\delta = \delta_{fit}\sqrt{\chi^2_{red}} \tag{6.15}$$

With the new error all results are consistent (table 6.1 and figure 6.6b). However it is not clear if the authors showed all their results in the paper [Cor83].

In table 6.1 and figure 6.6b a compilation of all measurements in the past is made. Our measurement improves the uncertainty by two orders of magnitude, what will allow us a more precise fixing of the Larmor frequency in the multi-rf-NQR measurements for the quadrupole moment of ^{9}Li.

6.2.3 $\mu(^{11}$ Li)

For the measurement of its magnetic moment, ^{11}Li was implanted in Si. In June 2002 we performed three independent β-NMR measurements, but all with too

---

[2] In the mean time a more accurate value of $g_H = 5.585694675(57)$ [NIST99] exists, but this doesn't change the final value of $g(^{9}\text{Li})$ within the error.

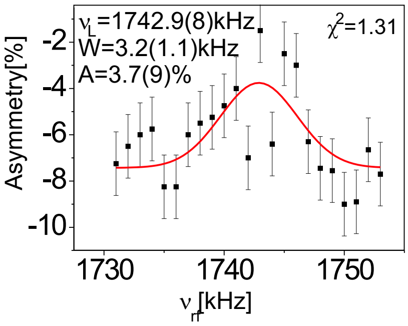

Figure 6.7: *Measurement of the Larmor frequency of* ^9Li *in Au by Correll et al. [Cor83] with a new fit in Origin.*

few statistics (fig. 6.8a-c, measurements of three hours) and too low rf-power. Due to the small rf-power and the rather large scan-range, we only expect one or two points in the resonance according to the linewidths predicted in section 5.2.4. The used rf-powers are not large enough to have the same linewidth for all Li-isotopes. However, as a rough approximation we can still use the predicted linewidths from the linear fit in section 5.2.4 to fix the linewidth in the fit. If we do so, a resonance can be fitted at the same place for the two last spectra (fig. 6.8b-c). This is a first indication that there is a peak.

Although the different spectra are taken with different rf-power, they were added. Adding spectra is done by adding the number of counts in the individual detectors and taking the asymmetry of the resulting summed number of counts. This is shown in figure 6.8d, where we see a clear peak at the same place.

In June 2003 three independent data sets were taken, each during five hours, this time all three with the same large rf-power and a narrower scan-range. The linewidth corresponding to this large rf-power $B_1 = 5$G is $FWHM_{exp} = 3.2$kHz (section 5.2.4), so now there are enough points in resonance. We had hundred channels per spectrum. The statistics of three channels is summed, resulting in the spectra of figure 6.8e-g. In figure 6.8h these spectra are added. This summed spectrum is first fitted with a Gaussian function with all free parameters. This learns us that the linewidth should be 3kHz. Therefore in the individual spectra the linewidth is fixed to 3kHz in the fit. To check the influence of the linewidth on the Larmor frequency, a two-dimensional χ^2-plot is made for the summed spectrum (fig. 6.9). This shows us that for all reasonable linewidths the same Larmor frequency is found. The limits of the first contour of 10% give us $\nu_L = 5346.6(5)$ (fig. 6.10). This corresponds to a relative error of 9.4 10^{-5}, which is slightly higher than the fit error. Since we have in this case no other reliable data to check the scattering of the data points, this highest error is the final error.

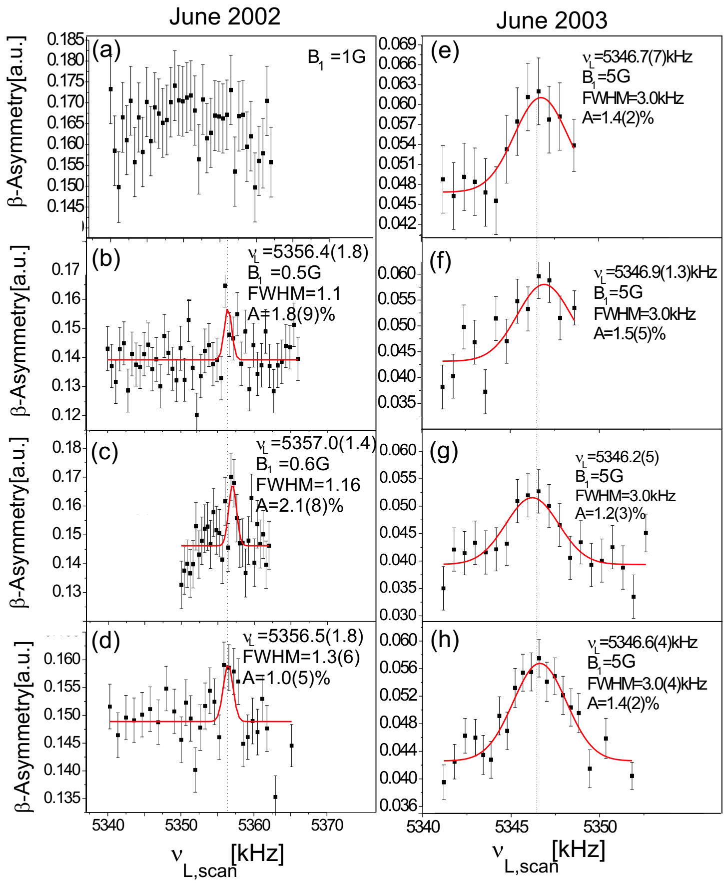

Figure 6.8: *Overview of the different NMR spectra to measure $\nu_L(^{11}Li)$. (a-d) Measurements taken in June 2002. The spectrum in (d) is the sum of the spectra in a-c. (e-h) Measurements performed in June 2003. The spectrum in (h) is the sum of the spectra in e-g. This spectrum will be used for the final result on $g(^{11}Li)$.*

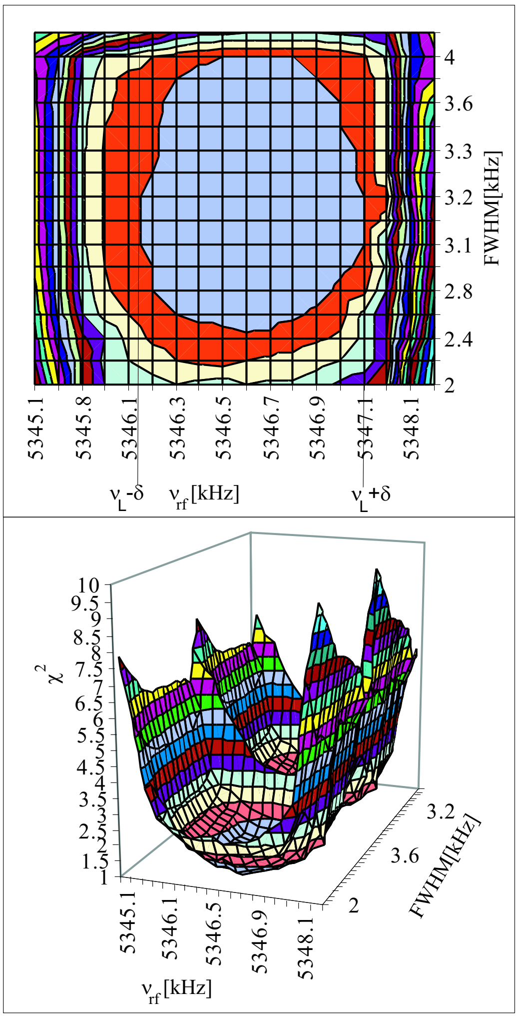

Figure 6.9: *Two-dimensional* χ^2*-plot as a function of the linewidth and the Larmor frequency for the summed spectrum of June 2003. The contours are made in steps of* 10% *of* χ^2*.*

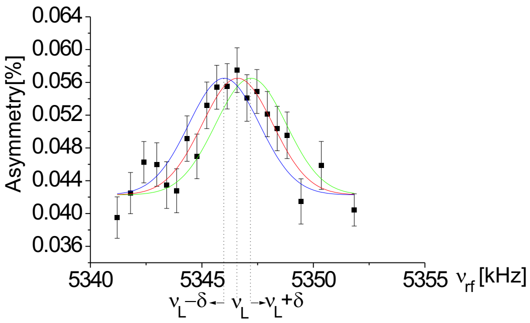

Figure 6.10: *Fit of the summed spectrum of June 2003, which is used for the final result on* $\nu_L(^{11}Li)$*, with on top a simulation for* $\nu_{res} = \nu_L - \delta$ *(left curve) and a simulation for* $\nu_{res} = \nu_L + \delta$ *(right curve).*

To calculate the g-factor of ^{11}Li from this Larmor frequency, we need a reference Larmor frequency. In figure (6.11b) the drift of the magnetic field in time is shown on top of the moment of the other measurements. The Larmor frequency of ^{8}Li was measured only in the very beginning of the experiment. The total drift $2.4 * 10^{-4}$ over the whole experiment should be considered as a systematic error. This systematic error is the final relative error on the Larmor frequency of ^{8}Li, giving $\nu_L(^{8}\mathrm{Li}) = 1806.2(2)$kHz. The Larmor frequency of ^{9}Li was measured in the middle of the measurements of ^{11}Li. As systematic and final error the drift $1.1 * 10^{-4}$ during the period of the ^{11}Li measurements is taken. This gives us $\nu_L(^{9}\mathrm{Li}) = 5005.2(3)$kHz. With an error of 0.001% on the g-factor $g(^{9}\mathrm{Li}) = 2.29121(3)$ measured in May 2003 (corrected for the diamagnetic shielding σ), this reference gives a smaller error on the final result than the reference of ^{8}Li. So as reference the Larmor frequency of ^{9}Li is used, resulting in $\mathbf{g(^{11}Li)=2.4475(3)}$, with a relative error of 0.01% (colored band in figure 6.11a). This gives us a magnetic moment of $\mu(^{11}\mathrm{Li}) = 3.6712(5)\mu_N$. These values are corrected for the diamagnetic shielding σ via the reference measurement. These values are within 2σ in agreement with the measurement of E.Arnold et al. [Arn87] $g(^{11}\mathrm{Li}) = 2.4449(17)$ with an error of 0.07% or $\mu(^{11}\mathrm{Li}) = 3.6673(25)\mu_N$ (table 6.2, figure 6.11a, plotted in red). The values of E.Arnold et al. are not corrected for the diamagnetic shielding σ. The uncertainty is improved by more than a factor of 5. This precision measurement will allow us a more precise fixing of the Larmor frequency in the measurement of the quadrupole moment of ^{11}Li via multiple-rf-NQR.

As a final check we compare the -less reliable- results of June 2002 to those of June 2003. The measurements in June 2002 were performed after the measurements on ^{9}Li, so in the period in which the magnetic field stayed constant

Table 6.2: *Comparison of different measurements on the magnetic moment of* ^{11}*Li. Values labeled with* * *are corrected for the diamagnetic shielding* σ*.*

	crystal	g	μ $[\mu_N]$	rel. error [%]
E. Arnold et al. [Arn87]	LiF	2.4449(17)	3.6673(25)	0.07%
This work *	Si	2.4475(3)	3.6712(5)	0.013%
[Rag89] *		2.4452(17)	3.6678(25)	

(fig. 6.5b). As reference we take the averaged value $\nu_L(^8\mathrm{Li}) = 1809.91(3)\mathrm{kHz}$. This gives us the plotted g-factors at the left side of figure (6.11a). The last one is the g-factor resulting out of the summed spectrum. The data points in the middle of the figure (6.11a) are the g-factors of the individual and summed spectra of June 2003, with as reference nucleus ^{9}Li. All data sets, even those with very few statistics agree with each other.

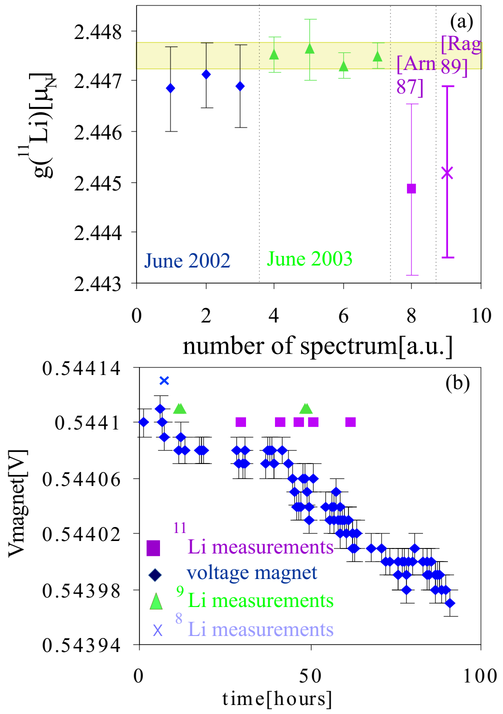

Figure 6.11: *(a) Overview of the different results for the g-factor of* ^{11}*Li, including the measurement of E.Arnold et al [Arn87] and the tabulated value of [Rag89]. The colored band is the final adopted value for g(*^{11}*Li), which is derived from the summed spectrum in figure 6.8h. (b) Time schedule of the experiments in June 2003 on top of the drift of the static magnetic field. The values on the y-axis of the measurements for* ^{9,11}*Li have no meaning.*

6.3 Quadrupole moments

6.3.1 Overview of performed experiments

The measurements of the quadrupole frequencies of the ^{8,9,11}Li isotopes were performed in three experiments, one in June 2002, one in May 2003 and one in June 2003. In each experiment several measurements of the same quadrupole frequency were performed. In table 6.3 the weighted average of the different measurements in one experiment is shown for each experiment. The shown errors are statistical, taking into account the standard deviation (section 4.2.3). Some examples of spectra are shown in the figures 5.12, 5.13, 5.17 and 5.18. The fit results for $^{8}\mathrm{Li}\underline{Zn}$ and $^{9}\mathrm{Li}\underline{Zn}$ from June 2002, May 2003 and June 2003 are summarized in figure 3.8. The fit results for $^{8}\mathrm{Li}\underline{LiTaO_3}$ and $^{9}\mathrm{Li}\underline{LiTaO_3}$ from June 2002 and May 2003 are summarized in the figures 5.13 and 5.19.

Table 6.3: *Overview of the performed experiments and the resulting averaged* Δ *without systematic errors.*

	^{8}Li nr. of scans	$\overline{\Delta}$ [kHz]	^{9}Li nr. of scans	$\overline{\Delta}$ [kHz]	^{11}Li nr. of scans
June 2002					
Zn	4	8.08(1)	5	15.7(1)	
$LiTaO_3$	2	14.81(9)	2	29.12(55)	
May 2003					
Zn	6	7.96(3)	4	15.5(1)	
$LiTaO_3$	5	14.88(6)	3	28.95(36)	
June 2003					
Zn			2	15.4(2)	2

In section 4.2.3 was shown that only quadrupole frequencies which are measured in the same crystal can be compared without introducing a systematic error if this crystal was not removed from its holder. For the measurements on the Li-isotopes this means that the ratio of quadrupole frequencies measured in 2002 and 2003 contains a systematic error of 1.1% due to the uncertainty in the misalignment angle β, while the ratio of quadrupole frequencies measured in May 2003 and June 2003 doesn't contain this systematic error.

To extract the quadrupole moments, the ratio of the quadrupole frequencies measured in the same experiment is used together with a reference quadrupole moment. This will be discussed in detail in next sections.

6.3.2 Quadrupole moment of ^{8}Li

The quadrupole moment of ^{8}Li is known to be positive [Jan94] and is measured already several times in the past [Ack74, Dub77, Arn88, Min92] (table 6.4). In the last measurement of Minamisono et al. [Min92] a slightly higher quadrupole moment than in the previous measurements was found. Therefore a remeasurement was performed. In section (5.2.2) Zn was found to be the best crystal to measure the quadrupole frequency of the Li isotopes. However, the electric field gradient of Li in Zn is not known very precise [Oht93] (next section). Therefore the quadrupole moment of ^{8}Li was measured with a $LiTaO_3$ crystal. A cross-check was made with a $LiNbO_3$ crystal. Afterwards the quadrupole frequency of ^{8}Li in Zn was measured to determine the electric field gradient of ^{8}Li in Zn with higher precision than in [Oht93] (next section). This will be used as a reference measurement for the extraction of the quadrupole moments $Q(^{9,11}\mathrm{Li})$.

^{8}Li in $LiTaO_3$

Seven independent measurements of $\nu_Q(^8\mathrm{Li\ in\ LiTaO_3})$ with statistics of about three hours were performed from which two in June 2002 and five in May 2003.

In figure (6.12) some examples from May 2003 are shown. To determine $\Delta_{scan} = \nu_{rf} - \nu_L$, the Larmor frequency of the last NMR-measurement for ^{8}Li in Si was used. In the double-rf-NQR spectra there are three peaks. The third peak is situated at $\Delta_{scan} = 0$, i.e. where the two sent rf-fields have the same frequency $\nu_L(^8\mathrm{Li\ in\ LiTaO_3})$. This doubles the rf-power, what can be enough to induce two-photon transitions.

In figure 6.13 an overview of the fit results for the different spectra is given. The uncertainties are determined via the χ^2 analysis mentioned in section 6.1, applying also the correction factor for $\chi^2 > 1$. Due to the constraint of equidistant peaks, Δ is a fit parameter. The weighted average from the measurements in June 2002 equals $\Delta = 14.81(9)$kHz (table 6.3). The weighted average from the measurements in May 2003 equals $\Delta = 14.88(6)$kHz (table 6.3). To deduce the quadrupole moment $Q(^8\mathrm{Li})$ from these frequencies, using the known $V_{zz}(Li\underline{LiTaO_3}$, we take the weighted average of these two data: $\Delta = 14.86(5)$kHz. This is a relative error of 0.3%. The fact that the frequencies in both experiments are the same within the error bars, suggests that the crystal was aligned rather well in both cases. However, to exclude any influence due to a misalignment of V_{zz} with respect to B_0 of maximum $< 5°$, we add a systematic error of 1.1%, resulting in $\Delta = 14.86(16)$kHz.

The used reference nucleus to extract the quadrupole moment of ^{8}Li is ^{7}Li. The quadrupole frequency of ^{7}Li in $LiTaO_3$ is measured twice in the past [Pet68, Cha99]. We take the value with the smallest uncertainty, i.e. $\nu_Q = 76.4(3)$kHz [Cha99]. The quadrupole moment of ^{7}Li has recently been revised, based on several different experimental data [Ort75, Wel85, Urb90, Voe91] and is now adopted to be $Q(^7\mathrm{Li}) = 40.0(3)$mb [Pyy01, Voe91]. The ratio of the

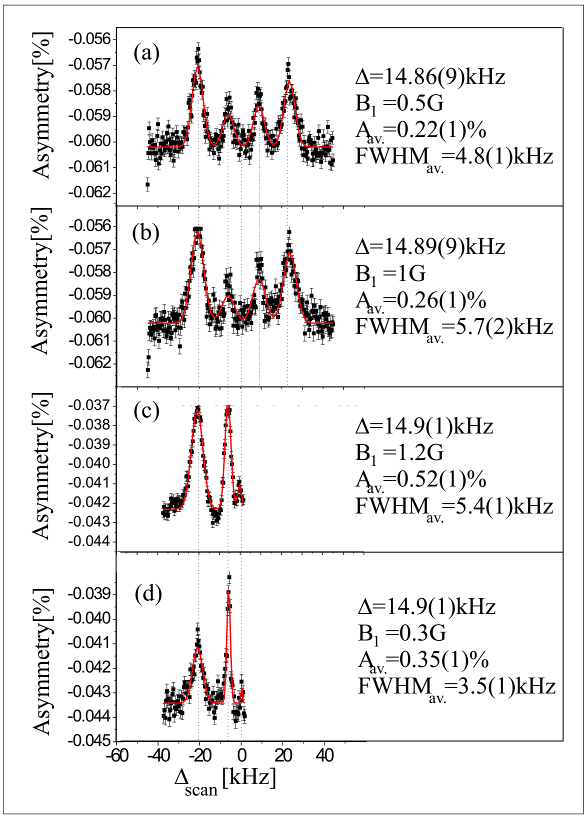

Figure 6.12: *Some examples of NQR spectra for* ^8Li *in* $LiTaO_3$ *from May 2003. On the x-axis* $\Delta_{scan} = \nu_{scan} - \nu_L$ *is plot. (a-b)Single-rf-NQR (c-d) Double-rf-NQR*

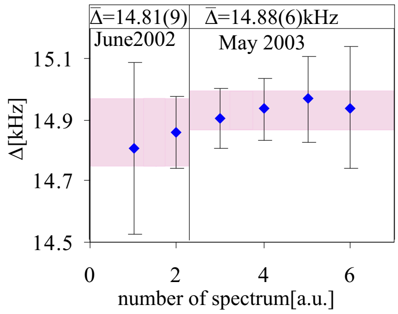

Figure 6.13: *Overview of the results for the different NQR spectra of* ^8Li *in* $LiTaO_3$*. The colored band is the weighted average of the measurements in one experiment. The errors are statistical.*

Table 6.4: *Comparison of the previous measurements of $Q(^8Li)$. (a) The quadrupole moments and quadrupole frequencies are taken directly from the mentioned papers, often with old values for the reference nucleus ^7Li. (b) The quadrupole moments are recalculated, starting from the quadrupole frequencies of ^8Li in the crystal given in the mentioned papers and taking the revised value for $Q(^7Li) = 40.0(3)mb$ [Pyy01, Voe91] and the value with the smallest uncertainty for the quadrupole frequency of ^7Li in that specific crystal. For the values of this work the systematic error is included. (c) The tabulated values for $Q(^8Li)$ in the preliminary compilation of N.Stone [Sto01]. The compilation of Raghavan tabulates the first values of [Sto01].*
[a] *[Pet67, Hal70] ;* [b] *[Cha99];* [c] *[Pet68] ;* [d] *[Wel85] ;* [e] *[Ort75, Doc74];* [f] *[Min92];* [g] *[Urb90].*

	crystal	used $\nu_Q(^7\text{Li})$ [kHz]	used $\lvert Q(^7\text{Li})\rvert$ [mb]	$\Delta(^8\text{Li})$ [kHz]	$\nu_Q(^8\text{Li})$ [kHz]	$\lvert Q(^8\text{Li})\rvert$ [mb]
(a)						
[Arn88]	$LiNbO_3$	54.5(5)[a]	37.0(8)[d]	10.63(15)	42.5(6)	28.7(7)
[Ack74]	$LiNbO_3$	54.5(5)[a]	41(6)[e]	10.8(8)	43(3)	32(6)
[Min92]R	$LiNbO_3$	53.3(11)[f]	40.0(6)[g]	11.2(2)	44.68(88)	33.5(11)
[Min92]R	$LiIO_3$	36.4(5)[f]	40.0(6)[g]	7.31(9)	29.24(36)	32.1(8)
[Min92]R	average					32.7(6)
[Dub77]	$LiTaO_3$	77.6(5)[c]	41(6)[e]	15.1(1)	60.2(3)	32(6)
(b)						
[Arn88]	$LiNbO_3$	54.5(5)[a]	40.0(3)	10.63(15)	42.5(6)	31.2(6)
[Ack74]	$LiNbO_3$	54.5(5)[a]	40.0(3)	10.8(8)	43(3)	31.6(22)
[Min92]	$LiNbO_3$	54.5(5)[a]	40.0(3)	11.2(2)	44.68(88)	32.8(8)
[Min92]	$LiIO_3$	36.4(5)[f]	40.0(3)	7.31(9)	29.24(36)	32.1(5)
[Dub77]	$LiTaO_3$	76.4(3)[b]	40.0(3)	15.1(1)	60.2(3)	31.5(3)
This work	$LiTaO_3$	76.4(3)[b]	40.0(3)	14.86(16)	59.4(7)	31.12(36)
(c)						
[Sto01]	[Dub77]					31.7(4)
[Sto01]	[Arn88]					28.7(7)
[Sto01]	[Min92]					32.7(6)
[Pyy01]			-40.0(3)			

frequencies thus gives a quadrupole moment **Q(^{8}Li)=31.12(36)mb** with a relative error or 1.15%.

For the comparison of this result with earlier measurements, one has to note that the used reference value of $Q(^7\text{Li})$ changed in time. The mentioned revision of this quadrupole moment made a revision of the quadrupole moments for the whole Li-isotope chain necessary. An overview of the non-revised and revised quadrupole moments for ^{8}Li is given in table 6.4. The result of this work is in agreement with the previous measurements of the quadrupole moment of ^{8}Li by E.Arnold et al. [Arn88] and H.Ackermann et al. [Ack74] if we use the same quadrupole moment for the reference nucleus ^{7}Li (table 6.4). However, this value falls out of the 1σ-error bar of the measurement of Minamisono et al [Min92], but it falls within the 2σ-error bar (figure 6.14), which covers 95.5% of the measurements.

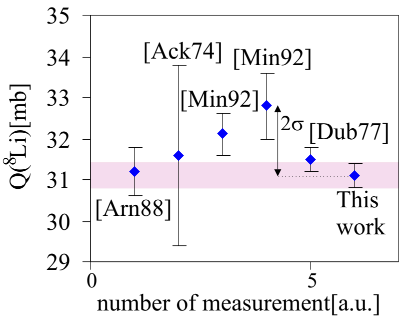

Figure 6.14: *Overview of the results for the quadrupole moment of ^{8}Li in the past. The colored band is the final value of this work.*

The uncertainty on the quadrupole moment of ^{8}Li has two main causes. The largest contribution comes from the systematic error on the misalignment angle. The second but largest error is due to the relative error on the quadrupole moment of ^{7}Li of 0.75%.

^{8}Li in LiNbO$_3$

The NQR measurements for ^{8}Li in LiNbO$_3$ (fig. 6.15) can be used as a cross-check for the found quadrupole moment of ^{8}Li.

As reference nucleus, ^{7}Li is used. With $\nu_Q(^7\text{Li in LiNbO}_3) = 54.5(5)$kHz [Pet67, Hal70] and $Q(^7\text{Li}) = 40.0(3)$mb [Pyy01, Voe91], quadrupole moments of respectively $Q(^8\text{Li}) = 32.0(5)$mb and $Q(^8\text{Li}) = 31.7(4)$mb are found. Here the statistical errors, corrected for the $\chi^2 > 1$, are larger than the systematic error due to the misalignment angle. So the statistical errors equal the final uncertainties. The values are in agreement with the measurements in LiTaO$_3$.

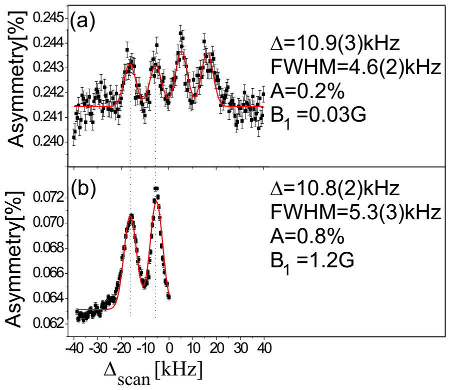

Figure 6.15: *(a) Single NQR-spectrum for* ^{8}*Li in LiNbO*$_3$ *from October 2001 with two hours of statistics. (b) Double-rf-NQR spectrum for* ^{8}*Li in LiNbO*$_3$ *from May 2003 with one hour of statistics.*

6.3.3 Electric field gradient of ^{8}Li in Zn

Ten independent NQR measurements of each about half an hour on ^{8}Li in Zn were performed from which four in June 2002 and six in May 2003. Some examples from May 2003 are shown in figure 6.16.

As final value for Δ, the weighted average of the result from June 2002 ($\overline{\Delta}$ = 8.08(1)kHz) and the result from May 2003 ($\overline{\Delta}$ = 7.96(3)kHz) is taken. The fact that both values do not agree within the error bars, suggests that the Zn crystal was not well aligned in the May 2003 experiment, in which a lower Δ was observed. In the final result Δ = 8.07(8)kHz, the standard deviation is taken into account, which thus accounts for the systematic error. This corresponds to a quadrupole frequency ν_Q(**^{8}Li in Zn)=32.27(32)kHz** with a relative error of 1.05% (indeed of the order of the earlier estimated systematic error). This result is in agreement with the measurement of Ohtsubo et al. [Oht93] ν_Q(^{8}Li in Zn)= 33.5(2.0)kHz and improves the uncertainty by almost a factor of six.

With the new quadrupole moment of $Q(^8\text{Li})$ = 31.12(36)mb, we get an electric field gradient for Li in Zn of V_{zz}(Li in Zn)= 4.29(7) $10^{15}\frac{V}{cm^2}$. The error is mainly determined by the systematic error on the misalignment angle.

6.3.4 Quadrupole moment of ^{9}Li measured in LiTaO$_3$ and Zn

For the measurement of its quadrupole moment, ^{9}Li was implanted in Zn and LiTaO$_3$. We have eleven NQR scans in Zn of each about 1h30min, from which five performed in June 2002, four in May 2003 and two in June 2003. We have five NQR scans in LiTaO$_3$ of each about three hours, from which two performed in June 2002 and three in May 2003. In figure 6.17(6.18) some examples of

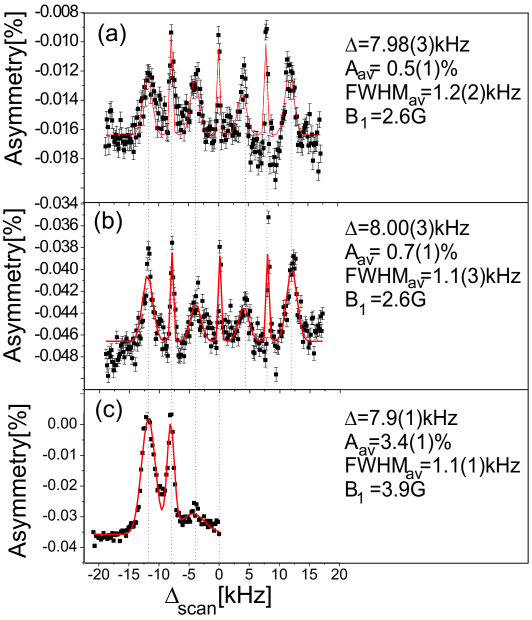

Figure 6.16: *Some examples of NQR spectra for* ^8Li *in Zn measured in May 2003. (a-b) Single-rf-NQR measurements. (c) Double-rf-NQR measurement.*

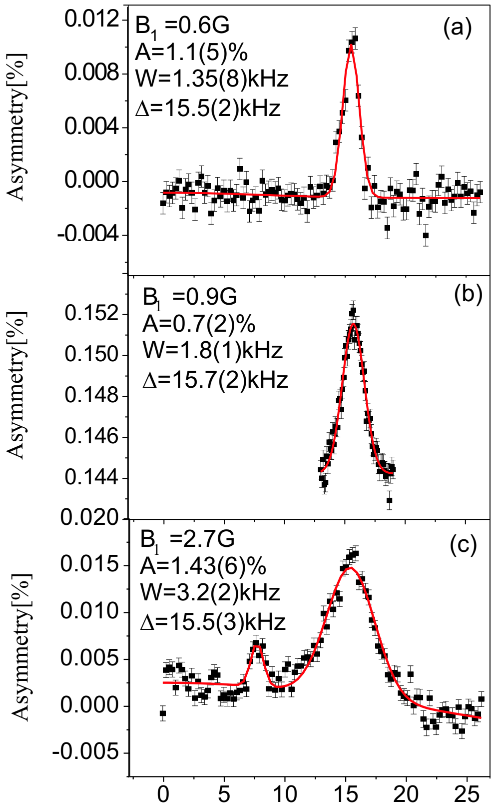

Figure 6.17: *Examples of multiple-rf-NQR scans for* ^{9}*Li in Zn. The indicated linewidths and amplitudes are properties from the* $\Delta m = 1$ *peak at* $\Delta_{scan} = \Delta$.

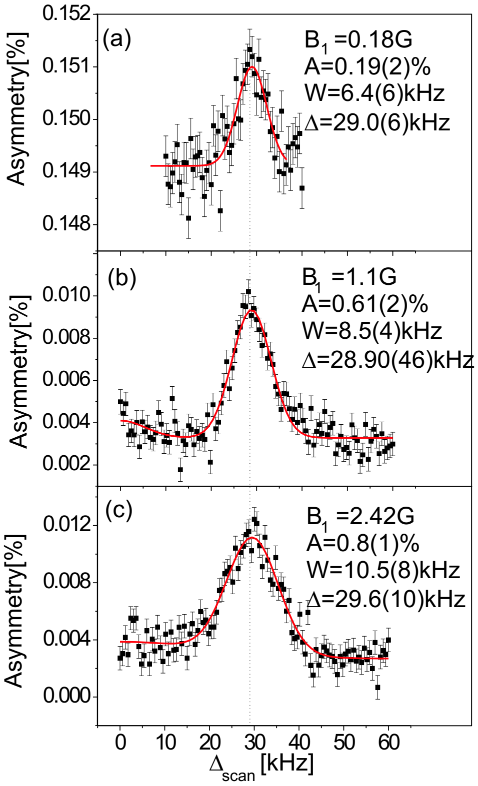

Figure 6.18: *Examples of multiple-rf-NQR scans for* ^9Li *in* $LiTaO_3$. *The indicated linewidths and amplitudes are properties from the* $\Delta m = 1$ *peak at* $\Delta_{scan} = \Delta$.

multiple-rf-NQR scans of ^{9}Li in Zn (LiTaO$_3$) from May 2003 are given. The positions of the peaks are consistent.

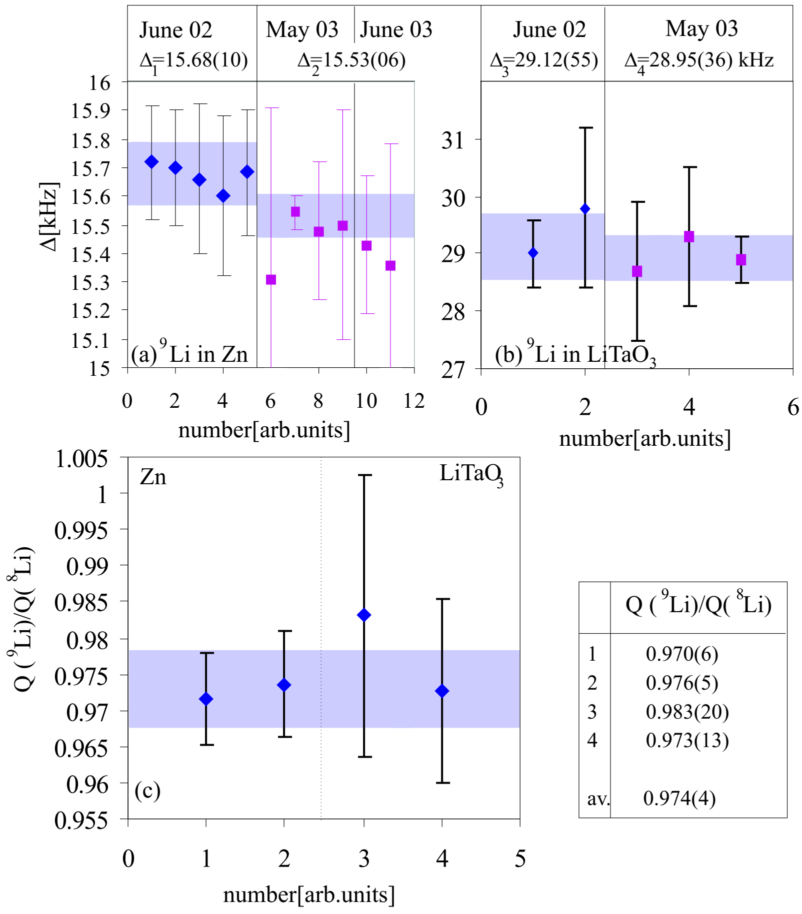

	Q (^{9}Li)/Q(^{8}Li)
1	0.970(6)
2	0.976(5)
3	0.983(20)
4	0.973(13)
av.	0.974(4)

Figure 6.19: *(a-b) Fitted* $\Delta = \frac{\nu_Q}{2}$ *for* ^{9}*Li in Zn and LiTaO*$_3$*. The colored bands indicate the weighted average of the results for the indicated experiment. (c) Ratio of the quadrupole moment of* ^{9}*Li and that of* ^{8}*Li. The colored band indicates the weighted average. All uncertainties are statistical.*

In figure 6.19 the fit results of all available spectra are given. The errors are determined using the χ^2 analysis of section 6.1, applying the correction for $\chi^2 > 1$.

To calculate the quadrupole moment of ^{9}Li, we use the formula

$$Q(^{9}Li) = \frac{\nu_Q(^{9}Li)}{\nu_Q(^{8}Li)} Q(^{8}Li) \tag{6.16}$$

with $\nu_Q(^{8}Li)$ and $\nu_Q(^{9}Li)$ quadrupole frequencies which are measured in the same experiment and in the same crystal. The results for ^{8}Li in Zn are given in figure 4.8, those for ^{8}Li in LiTaO$_3$ in figure 6.13 and those for ^{9}Li in LiTaO$_3$ and Zn in figure 6.19. There are four independent ways to calculate the ratio $\frac{Q(^{9}Li)}{Q(^{8}Li)}$:

- as the ratio of the averaged quadrupole frequencies measured in June 2002 with Zn as implantation crystal: $\frac{\nu_Q(^{9}Li)}{\nu_Q(^{8}Li)} = 0.5\frac{15.68(10)}{8.08(1)} = 0.970(6)$
- as the ratio of the averaged quadrupole frequencies measured in May 2003 and June 2003 with Zn as implantation crystal: $\frac{\nu_Q(^{9}Li)}{\nu_Q(^{8}Li)} = 0.5\frac{15.53(06)}{7.96(3)} = 0.976(5)$
- as the ratio of the averaged quadrupole frequencies measured in June 2002 with LiTaO$_3$ as implantation crystal: $\frac{\nu_Q(^{9}Li)}{\nu_Q(^{8}Li)} = 0.5\frac{29.12(55)}{14.81(9)} = 0.983(20)$
- as the ratio of the averaged quadrupole frequencies measured in May 2003 with LiTaO$_3$ as implantation crystal: $\frac{\nu_Q(^{9}Li)}{\nu_Q(^{8}Li)} = 0.5\frac{28.95(36)}{14.88(6)} = 0.973(13)$

Using the values in table 6.3 and in figure 6.19, with $\nu_Q(^{9}Li) = 2\Delta$ and $\nu_Q(^{8}Li) = 4\Delta$, we obtain the ratios from figure 6.19. As final value for the quadrupole moment $Q(^{9}\mathrm{Li})$ we take the weighted average of these four values, taking into account the standard deviation. This gives $\frac{Q(^{9}Li)}{Q(^{8}Li)} = 0.974(4)$. With a reference quadrupole moment $Q(^{8}\mathrm{Li}) = 31.12(36)$mb, this results in a quadrupole moment **Q(^{9}Li)=30.31(39)mb** with a relative error of 1.3%.

In table 6.5 an overview of the revised and non-revised quadrupole moments of ^{9}Li of earlier measurements is given. The measurement of this work is in agreement with the measurement of Correl et al.[Cor83]. The result of E.Arnold et al.[Arn88] differs by 2σ from the result of this work.

With the measured quadrupole moment $Q(^{9}\mathrm{Li}) = 30.31(39)$mb the uncertainty is improved by a factor of two.

6.3.5 Quadrupole moment of ^{11}Li measured in Zn

For the measurement of its quadrupole moment, ^{11}Li was implanted in Zn. Two measurements were performed in June 2003, one at $B_1 = 3$G (set 1) during six hours and one at $B_1 = 1.4$G (set 2) during ten hours. In the first data set (set 1) only two frequencies were sent simultaneously, i.e. $\nu_{L,fix} - \Delta_{scan}$ and $\nu_{L,fix} + \Delta_{scan}$ without the fixed frequency $\nu_{L,fix} = 5346.200(1)$kHz itself. In the second data set (set 2), all three frequencies were sent simultaneously through the coil with $\nu_{L,fix} = 5346.100(1)$kHz. So all polarization will be destroyed

Table 6.5: *Comparison of the different measurements of* $Q(^9Li)$ *in the past. (a) The quadrupole moments are taken directly from the mentioned papers, often with old values for the reference nucleus* ^7Li. *(b) The quadrupole moments are recalculated, starting from the quadrupole frequencies of* ^9Li *in the crystal given in the mentioned papers and taking the revised values for* $Q(^7Li) = 40.0(3)mb$ *[Pyy01, Voe91] and* $\nu_Q(^7Li$ *in* $LiNbO_3)= 54.5(5)kHz$ *[Pet67, Hal70]. (c) The tabulated values for the quadrupole moment of* ^9Li *in the preliminary compilation of N. Stone [Sto01] and the compilation of P. Raghavan [Rag89]. (d) The quadrupole moments and frequencies measured in this work with as reference nucleus* ^8Li.

	crystal	used ν_Q(ref) [kHz]	used $\lvert Q(\mathrm{ref})\rvert$ [mb]	$\Delta(^9\mathrm{Li})$ [kHz]	$\nu_Q(^9\mathrm{Li})$ [kHz]	$\lvert Q(^9\mathrm{Li})\rvert$ [mb]
(a)						
[Arn88]	$LiNbO_3$	54.5(5)	37.0(8)	18.7(5)	37.4(11)	25.3(9)
[Cor83]	$LiNbO_3$	54.5(5)	36.6(3)	24.2(15)	48.4(30)	32.2(66)
(b)						
[Arn88]	$LiNbO_3$	54.5(5)	40.0(3)	18.7(5)	37.4(11)	27.4(9)
[Cor83]	$LiNbO_3$	54.5(5)	40.0(3)	24.2(15)	48.4(30)	35.5(66)
(c)						
[Sto01]	[Arn88]					25.3(9)
[Sto01]	[Cor83]					36(7)
[Rag89]	[Arn88]					27.8(8)
[Rag89]	[Cor83]					36(7)
(d)This work						
	$LiTaO_3$			29.0(3)	58.0(6)	
	Zn			15.58(17)	31.16(34)	
			31.12(36)			30.31(39)

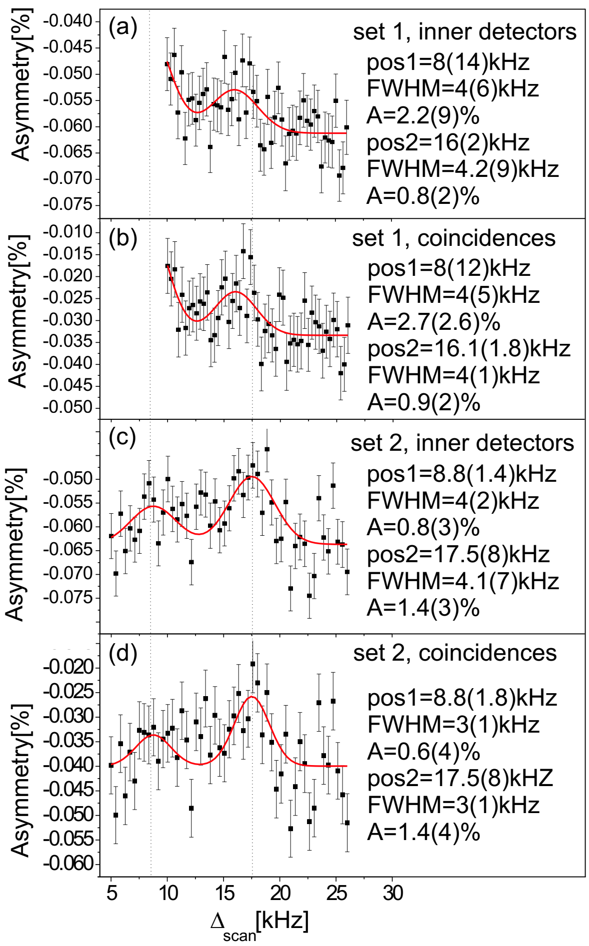

Figure 6.20: *(a-b) First data set with* $B_1 = 3G$.
(c-d) Second data set with $B_1 = 1.4G$.
In (a-c) the asymmetry of the counts in the inner detectors is shown. In (b-d) the asymmetry of the coincidence counts is shown.

in resonance. Out of resonance already a part of the polarization is destroyed because of the present $\nu_{L,fix}$, what causes a higher baseline. In set 1 we have a low baseline with an asymmetry a_{in}, but in resonance not all polarization is destroyed because only twice two levels are mixed, what causes a reduction of the amplitude.

The fixed frequency $\nu_{L,fix}$ is smaller than the found Larmor frequency $\nu_L = 5346.6(5)$kHz in section 6.2.3 because of the decreasing magnet current. The effect of the decreasing magnet current on the Larmor frequency was monitored with ^{9}Li.

In figure 6.20 the multiple-rf-NQR spectra are shown with both the β-asymmetry from the coincidence counts and that from the counts of the inner detectors. These spectra are fitted with two Gaussian curves and the condition that the first, $\Delta m = 2$-peak, is narrower than the second $\Delta m = 1$-peak, which position is twice that of the $\Delta m = 2$ peak. A third Gaussian at $\Delta_{scan} = 0$, is not added in the fit because it is situated too far from the scan-range to fit it properly.
In the first data set (fig. 6.20a-b), the scan begins at larger Δ_{scan} than the top of the two-photon peak. This causes large fit-errors and a shift of the one-photon peak to the left. When fitting the spectra of set one with only one peak a broad peak over the whole spectrum is fitted. So that's also not a good fit. Therefore and because we see on the figure that both the $\Delta m = 1$ and the $\Delta m = 2$ peak of the two data sets are consistent, only the second data set will be considered in the rest of the section.

Once two channels (figure 6.21a,c) and once three channels are taken together (figure 6.21b,d) in each spectrum. All spectra give consistent results (fig. 6.22). The uncertainties on these fitresults are determined by the "fit error".

In all these spectra the condition $FWHM(\Delta m = 1) > FWHM(\Delta m = 2)$ results in peaks with equal linewidths, what is not the aim. Therefore we will artificially vary the ratio of both linewidths for the raw dataset 2 of the inner detectors.

In figure 6.23 the fit results for different conditions on this ratio are shown. All fits give consistent results with as uncertainties the "fit errors". Increasing the ratio $\frac{FWHM(\Delta m=2)}{FWHM(\Delta m=1)}$ from 0.1 to 0.5 results in an increasing linewidth of the one-photon peak. When the linewidths of the one-photon peak and the two-photon peak are taken equal, the linewidth of the one-photon peak decreases again to 2.55kHz.

Finally a correlation test of the parameters of position and linewidth is performed. This is done via a two-dimensional χ^2-plot (fig. 6.24). The contours are not completely circular. This indicates that there is a correlation between

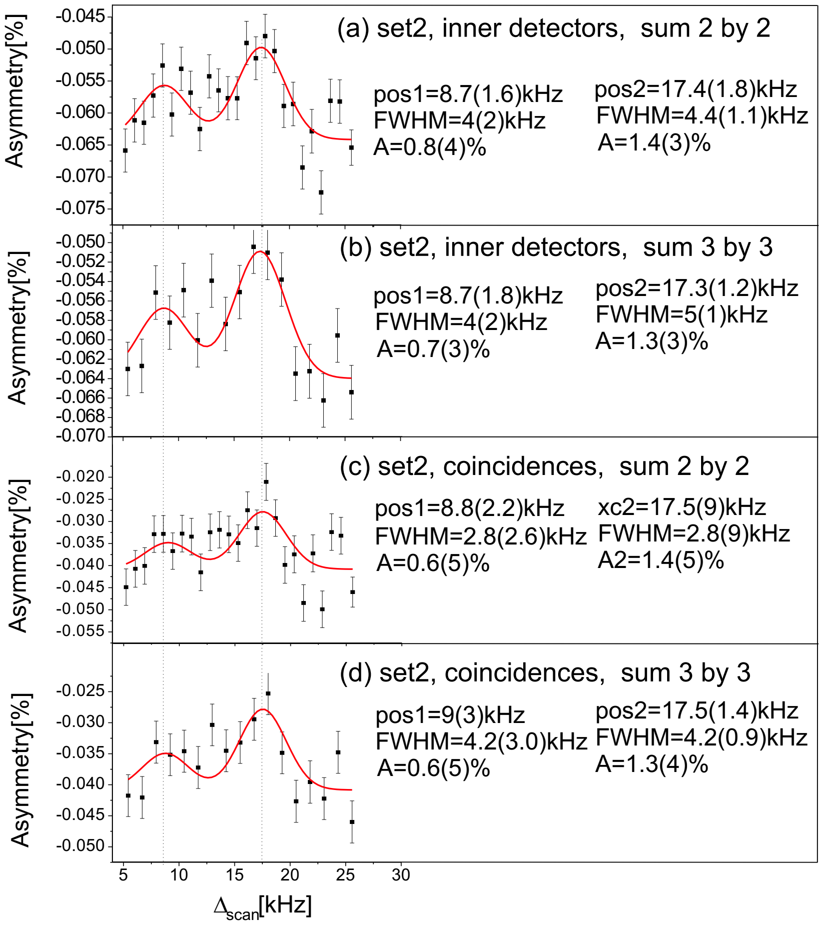

Figure 6.21: *Second data set with* $B_1 = 1.4G$. *(a-b)* β*-asymmetry coming from the counts in the inner detectors.*
(c-d) β*-asymmetry coming from the coincidence counts. In (a-c) the statistics of two channels is summed. In (b-d) the statistics of three channels is summed.*

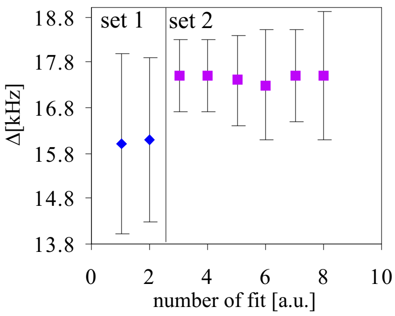

Figure 6.22: *The different fit results for the two sets (inner detectors, coincidences, non summed and summed) with the condition that the two-photon peak should be narrower than the one-photon peak. Since these are different fit results from the same data set, it is normal that we don't have a statistical distribution.*

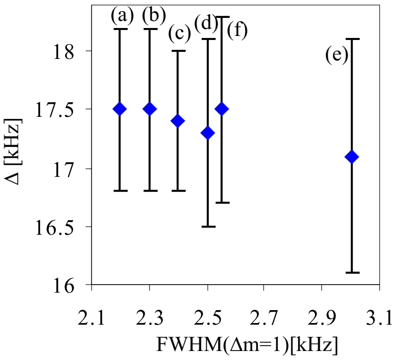

Figure 6.23: *The different fit results for the raw spectrum of the inner detectors from the second data set with different conditions on the linewidth:*
(a) No two-photon peak
(b) $FWHM(\Delta m = 2) = 0.1 FWHM(\Delta m = 1)$
(c) $FWHM(\Delta m = 2) = 0.24 FWHM(\Delta m = 1)$
(d) $FWHM(\Delta m = 2) = 0.3 FWHM(\Delta m = 1)$
(e) $FWHM(\Delta m = 2) = 0.5 FWHM(\Delta m = 1)$
(f) $FWHM(\Delta m = 2) = FWHM(\Delta m = 1)$

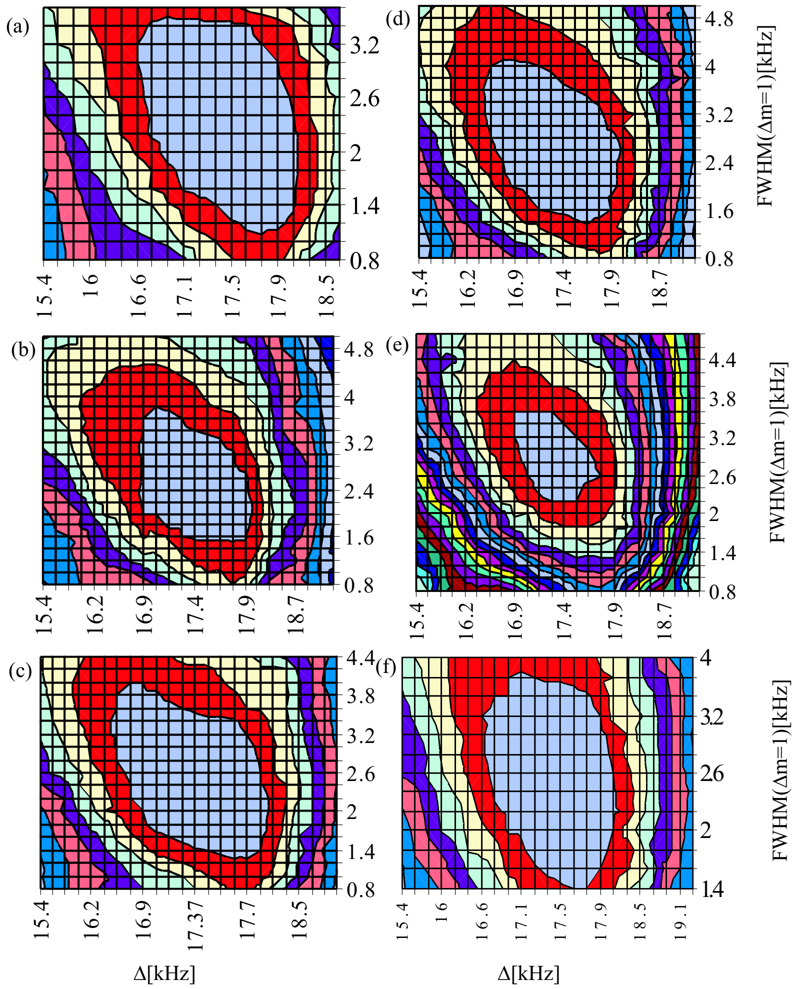

Figure 6.24: *Two-dimensional* χ^2*-plots for different conditions on the ratio* $\frac{FWHM(\Delta m=2)}{FWHM(\Delta m=1)}$*, labeled as in figure 6.23. The shown contours are contours of* 10% *of* χ^2.

the linewidth and the position of the one-photon peak. On the other hand, if we take the first contour of an increase of 10% of χ^2 as error on the result, for all conditions consistent results are found as is shown in figure 6.25.

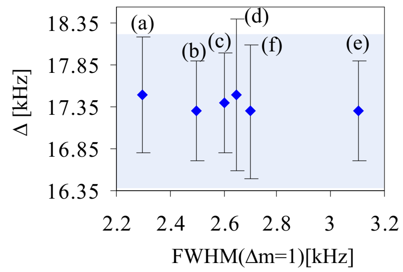

Figure 6.25: *Positions of the one-photon peak with the errors determined by the* χ^2 *plots. The labels are as in figure 6.23.*

As final value, we take an averaged value with the largest error determined by the χ^2, resulting in $\Delta = 17.3(9)$kHz (colored band in figure 6.25). This corresponds to a quadrupole frequency ν_Q(^{11}**Li in Zn)=34.6(18)kHz**, which is a relative error of 5%. This is larger than the systematic error of 1.1% due to the misalignment angle.

For the calculation of the quadrupole moment $Q(^{11}\mathrm{Li})$, we used the quadrupole moment $Q(^{8}\mathrm{Li}) = 31.12(36)$, measured in this work. For the quadrupole frequency ν_Q(^{8}Li in Zn), we used the weighted average from May 2003: ν_Q(^{8}Li in Zn) = 31.84(12)kHz. This gives a quadrupole moment $\mathbf{Q(^{11}Li)=33.8(18)mb}$. This is in agreement with the measurement of E. Arnold [Arn92] (table 6.6) The uncertainty improved by more than a factor of two.

Table 6.6: *Comparison of the different measurements of* $Q(^{11}Li)$ *in the past.*

	crystal	$\Delta(^{11}\mathrm{Li})$ [kHz]	$\nu_Q(^{11}\mathrm{Li})$ [kHz]	$Q(^{11}\mathrm{Li})$ [mb]
[Arn92]R	LiNbO$_3$	22(3)	44(6)	31.2(45)
This work	Zn	17.3(9)	34.6(18)	33.8(18)
[Sto01]	[Arn92]			31(5)

In figure 6.26 the NQR spectra of ^{9}Li and ^{11}Li are compared. The colored bands indicate the final result for the two nuclei. The figure shows that there is no overlap between the two quadrupole frequencies, i.e. the quadrupole moments of ^{9}Li and ^{11}Li are different.

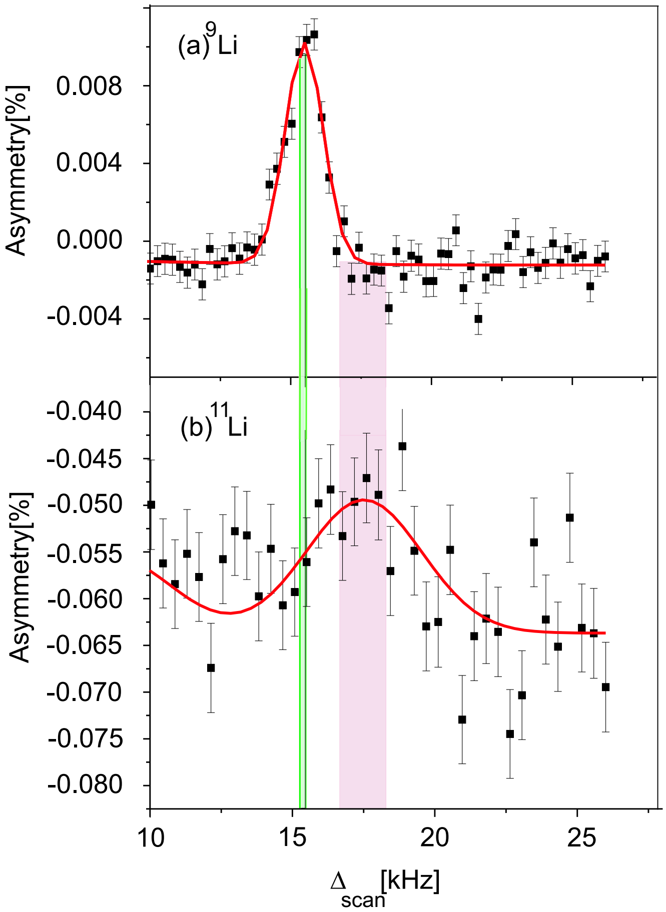

Figure 6.26: *(a)The best multiple-rf-NQR spectrum for* ^{9}Li.
(b) The best multiple-rf-NQR spectrum for ^{11}Li. *The narrow band at the left of the picture indicates the final* Δ *for* ^{9}Li *in Zn. The other band indicates the final* Δ *for* ^{11}Li *in Zn.*

To specify the difference, the ratio of the two measured quadrupole frequencies is taken. The used quadrupole frequency for ^{9}Li is the weighted average of the values from May 2003 and June 2003 (fig. 5.19, $2\Delta_2$), because between these two experiments the crystal was not removed from its crystal holder. This gives[3]

$$\frac{\nu_Q(^{11}Li)}{\nu_Q(^{9}Li)} = \frac{34.6(18)}{31.06(12)} = 1.114(59) \tag{6.17}$$

This ratio is in agreement with the ratio $\frac{\nu_Q(^{11}Li)}{\nu_Q(^{9}Li)} = 1.14(16)$ measured by E.Arnold et al.[Arn92]. The uncertainty is improved by almost a factor of three. The found ratio **1.11(6)** differs from one by almost 2σ. So, the chance that the two extra, loosely bound, neutrons in ^{11}Li influence the quadrupole moment is about 95%. The consequences of this result will be discussed extensively in next chapter.

6.4 Overview table

In table 6.7 an overview of all experimental results is given.

Table 6.7: *Overview of the different properties for the Li isotopes, without the stable ^{6}Li isotope with $g(^6Li) = 0.82204728(55)$, $I^\pi = 1^+$, $Q(^6Li) = -0.83(8)mb$ [Rag89].*
*[a] [Rag89];[b] [Voe91]; [c] [Pet67], [d] [Cha99]; [e] [Fir96]; [f] [Arn92]; * means that the value is corrected for the diamagnetic shielding.*

	^{7}Li	^{8}Li	^{9}Li	^{11}Li
I$^\pi$ [$\hbar$]	$3/2^{-\ a}$	$2^{+\ a}$	$3/2^{-\ a}$	$3/2^{-\ a}$
g*	$+2.1709750(27)^a$	+0.826780(9)	2.29121(3)	2.4475(3)
μ^* [μ_N]	$+3.25646253(40)^a$	+1.653560(18)	3.43682(5)	3.6712(5)
Q [mb]	$-40.0(3)^b$	+31.12(36)	30.31(39)	33.8(18)
ν_Q[kHz] in				
Zn		32.27(32)	31.16(34)	34.6(18)
LiTaO$_3$		59.4(6)	58.0(6)	
$T_{1/2}$ [ms]	stable	$838(6)^e$	$178.3(4)^e$	$8.5(2)^e$
Q_β [MeV]		$16.004(1)^e$	$13.606(1)^e$	$20.610(2^e)$
A_1		0.24^e	0.08^e	0.24^f

The g-factors and magnetic moments are corrected for the diamagnetic shielding. The uncertainty on the g-factors of ^{9,11}Li are mainly determined

---

[3] From this ratio we can calculate as a cross-check the quadrupole moment of ^{11}Li, using the quadrupole moment of ^{9}Li: $Q(^9\text{Li}) = 30.31(39)$mb. This gives us $Q(^{11}\text{Li}) = 33.8(18)$mb, like expected.

by the systematic error on $\nu_L(^8\mathrm{Li})$ due to the drift of the current for the magnetic field and due to the restactivity.

For the quadrupole moments a systematic error of 1.1% is taken into account, which is the largest contribution on the final error of $Q(^{8,9}\mathrm{Li})$. For $\mathrm{Q}(^{11}\mathrm{Li})$, this systematic error is negligible compared to the statistical error of 5%.

Chapter 7

Interpretation of the results

The experimental results of previous chapter are summarized in figure 7.1 together with the nuclear moments of the odd-even B-isotopes. Without any calculation we can already see that the nuclear moments are all close to their single-particle value[1]. This indicates that all shown Li- and B-isotopes have a rather pure proton $\pi 0p_{3/2}$ configuration and that the nuclear moments are mainly determined by the proton in the $0p_{3/2}$ state. The variations of the nuclear moments for the different isotopes are small due to small admixtures of other configurations and due to the interaction of the neutrons and the protons in these other configurations. For isotopes with an even number of neutrons, the magnetic moment is much less sensitive to the configuration of the neutrons than

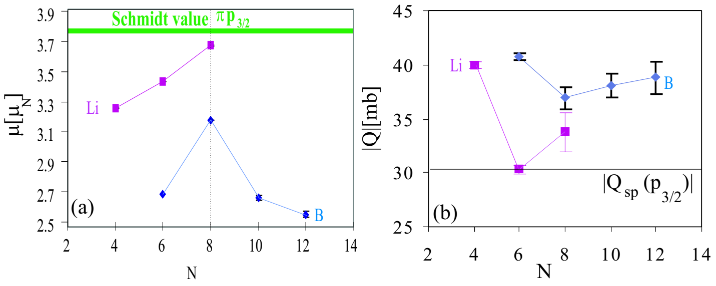

Figure 7.1: *Overview of the present (a)magnetic and (b) quadrupole moments of the odd-even Li and B isotopes.*

---

[1] For the magnetic moments the single-particle value is the Schmidt-value. For an odd proton in an orbital with $j = l + 1/2$, this is $\mu_{sp} = j - 1/2 + 2.793$. For $j = 3/2$ we find $\mu_{sp} = 3.793$. The single particle value for the quadrupole moment $|Q_{sp}(0p_{3/2})| = \frac{2j-1}{2j+2}\langle r^2\rangle e = \frac{2}{5}\langle r^2\rangle e \approx 30.4$mb. In this calculation $\langle r^2\rangle = \int_0^\infty r^4 R_{nlj}^2 dr \approx 7.6\text{fm}^2$ with R_{nlj} the radial wave function, is used [Boh69].

the quadrupole moment. Therefore the quadrupole moment is better suited to investigate the presence of different neutron configurations and correlations in the ^{11}Li wave functions.

The quadrupole moments of the Li isotopes show that the two loosely bound neutrons in ^{11}Li polarize the ^{9}Li core, resulting in a higher quadrupole moment. The quadrupole moments of the odd Li-isotopes reach a minimum at ^{9}Li, which has six neutrons. This minimum is more pronounced than the minimum at $N = 8$ for the B-isotopes. On the other hand, the magnetic moments are closest to the Schmidt line when the neutron number is approaching $N = 8$.

In this chapter these experimental results will be compared with several theoretical model predictions. First shell model calculations performed with the ANTOINE code [Cau99] are discussed. It can be questioned whether the shell-model assumption that all nuclei feel a mean field from the other nuclei, is still valid for these light nuclei. The validity of this assumption is particularly doubtful for the extra neutrons in ^{11}Li . However, the shell model calculations can give an idea about the influence of the different orbitals on the quadrupole moments. In the subsequent sections an overview of the present status of more accurate models is given.

7.1 Shell model

The full Hamiltonian of a free nucleus is

$$H = \sum_{i=1}^{A} E_{k,i} + \sum_{i<j=1}^{A} W(i,j) \tag{7.1}$$

with $E_{k,i}$ the single nucleon kinetic energies and $W(i,j)$ two-body interactions. In the shell model the two-body interactions are approximated by one-body potentials $U(i)$:

$$H = \sum_{i=1}^{A}(E_{k,i} + U(i)) + (\sum_{i<j=1}^{A} W(i,j) - \sum_{i=1}^{A} U(i)) = H_0 + H_{res} \tag{7.2}$$

The one-body potential $U(i)$ represents the mean potential that the ith nucleon feels in the presence of all other nucleons. Often an harmonic oscillator potential or Wood-Saxon potential is used for this potential. The eigenvalues of H_0 give the bare single particle energies. This gives a good idea of the energies of nuclei consisting of an inert core plus or minus one nucleon. The residual interaction H_{res} contains all two-body interactions. Necessary ingredients for this interaction are the spin-orbit coupling and pairing. The dimensions of the diagonalization matrices rapidly become very large when going to heavier nuclei. Therefore restricted model spaces are chosen in which the calculations are performed. The nuclear orbitals are divided into a core space and a valence space. The core space is completely filled and frozen as a vacuum. For the p-shell nuclei the ^{4}He nucleus is taken as core. The valence space is only partially filled. It is usually one major shell on top of the core part. One generates all possible Slater determinants in the valence shell. The number of Slater determinants determines the dimension of the calculation. Cutting a model space introduces errors in the calculations. Therefore the residual interactions need to be modified to effective interactions. The two-body matrix elements and the single particle energies are taken as free parameters and are fitted to describe the experimental nuclear excited states. Another way of obtaining effective interactions is to start from the free nucleon-nucleon interaction and to incorporate the necessary modifications to obtain the appropriate nuclear two-body interaction matrix elements. These interactions are called "realistic interactions".

Due to the use of restricted model spaces, not only the residual interaction has to be adapted. Also the use of effective operators and charges is necessary. For the p-sd shell model space, these effective parameters are well known [Bro88]. For the effective g-factors one can use the free ones: $g_l^\pi = 1.0$, $g_s^\pi = 5.58$, $g_l^\nu = 0$, $g_s^\nu = -3.826$ [Bro88]. For the effective charges one uses $e_\nu = 0.5$ and $e_\pi = 1.3$ [Bro88].

7.2 Overview shell model calculations with ANTOINE

Shell model calculations were performed with the latest version of the ANTOINE code [Cau99]. In this code one starts from a Wood-Saxon one body potential U(i). The validity of this mean potential can be questioned for these light nuclei. The model space and effective interaction can be chosen as an input. The code uses the Lanczos diagonalization algorithm [Cau99] in which only the lowest eigenvalues are calculated. The number of desired energy levels can be chosen as an input parameter.

7.2.1 Effective interactions

Examples of effective interactions

- **CKI (p-shell)**
  This first effective interaction was developed by Cohen and Kurath in 1965 [Coh65, Coh67]. The model valence space is the 0p-shell. As core the doubly magic ^{4}He nucleus, with two protons and two neutrons in the 0s-orbital, is taken. This interaction was built by adapting the two-body matrix elements to fit the calculation with experimental binding energies and energy levels of stable nuclei in the p-shell (A=8-16). Tests of this interaction with other experimental quantities such as nuclear moments and transition strengths revealed its strengths and limits. This interaction works in general quite well in the beginning of the shell. But for the upper

end of the shell, an admixture of the sd-shell is necessary, as was already suggested by Cohen and Kurath themselves [Coh65].

- **PSDMK (p-sd shell)**
  For this effective interaction the same ^{4}He nucleus is used as core. For the valence space the 0p-1s0d-shell is used. The two-body matrix elements for the 0p-shell are the same as in the CKI interaction. Those of the pure 1s0d-shell are the Preedom-Wildenthal matrix elements [Pre72]. These matrix elements were established fitting the calculations to experimental binding- and excitation energies. The mixing matrix elements between the two shells come from Millener and Kurath [Mil75, Kuo67].
  This PSDMK-interaction is an available interaction in OXBASH [Oxb84, Smi04]. From there it was converted to a readable format for ANTOINE.

- **MK3W (s-p-sd shell, cross-shell modified)**
  For this effective interaction no core is used. As model space the 0s-0p-1s0d-1p0f-shell is used. The two-body matrix elements for the 0p-shell are the same as in the CKI interaction. Those of the pure 1s0d-shell are the same as in the PSDMK interaction. The mixing matrix elements between the 0p and 1s0d shell come from E.K. Warburton and D.J. Millener [War89], who modified the Millener-Kurath matrix elements [Mil75] to fit the ^{16}N spectrum exactly. So it was modified for light neutron-rich nuclei. The modified matrix elements are called the MKIII matrix elements [War89]. The matrix elements concerning the 1p0f-shell are taken from Millener and Kurath [Mil75]. Since we deal only with light elements in this work, no nucleons will be allowed in the 1p0f-shell. In this case, the MK3W interaction has a model space $s - p - sd$. It can be seen as the PSDMK for which the cross-shell two body matrix elements are modified for neutron-rich nuclei.
  This MK3W-interaction is an available interaction in OXBASH [Oxb84, Smi04]. From there it was converted to a readable format for ANTOINE.

Magnetic moments

In figure 7.2 the calculations of the magnetic moments with the ANTOINE code [Cau99] are compared with the experimental results for the odd-even Li and B-isotopes.

- **Li-isotopes**
  The calculations with the effective CKI interactions, allowing valence neutrons only in the p-shell, are reproducing the magnetic moments quite well (fig. 7.2 filled squares), although it overestimates the magnetic moment of ^{11}Li.

  When we allow two nucleons to be excited into the sd-shell, using the PSDMK interaction ("PSDMK, max. 2"), the magnetic moment of ^{11}Li

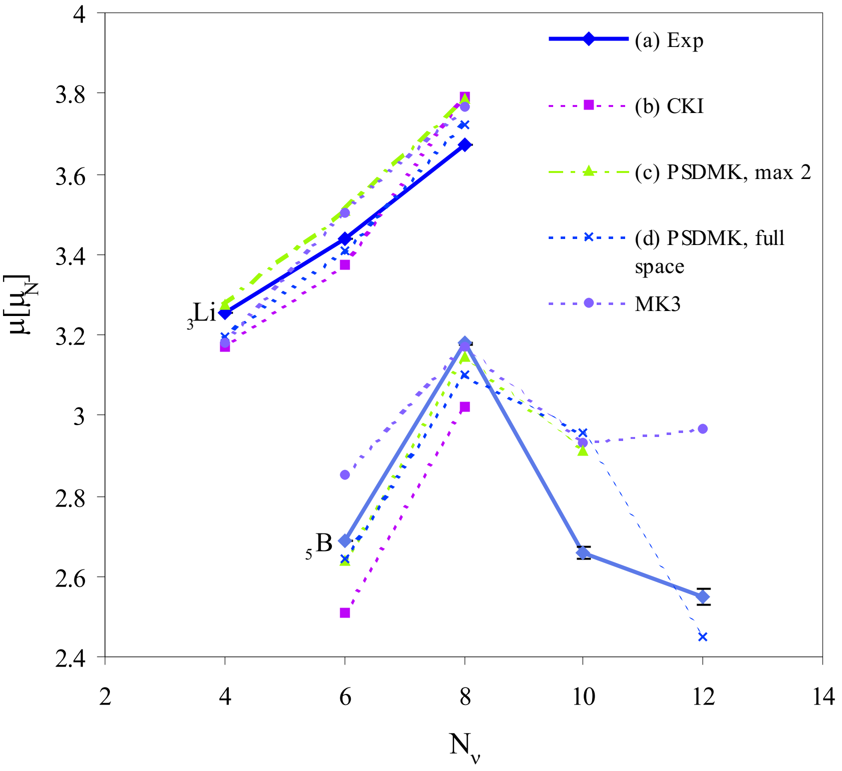

Figure 7.2: *Comparison of (b-d) calculated and (a) experimental magnetic moments of the odd-even Li and B-isotopes. (c) PSDMK interaction with maximum two nucleons in the sd-shell. (d) PSDMK interaction without restrictions. (e) MK3W interactions with maximum two nucleons in the sd-shell for the Li-isotopes. For the* $^{11-15}B$ *(*^{17}B*) isotopes four (six) neutrons and one proton are allowed in the sd-shell.*

is still a bit overestimated (fig. 7.2 filled triangles).
When we take the full p-sd-shell without restrictions ("PSDMK, full space"), the magnetic moments of all Li isotopes are very well reproduced, even that of ^{11}Li (fig. 7.2, crosses). This is a first indication that excitations of the halo-neutrons in the sd-shell are needed to reproduce the ^{11}Li magnetic moment. Even for ^{7}Li and ^{9}Li a better agreement is found by allowing some $2p-2h$ excitations of neutrons from the p-shell to the sd-shell. The calculated wave function of the ground state of ^{11}Li is in this case 84% of the normal $\nu(p^2_{1/2}p^4_{3/2})\pi(p^1_{3/2})$ configuration for the valence particles (appendix A). 15% of the wave function covers all intruder configurations with the two last neutrons coupled in pairs in the sd-shell. The last 1% is the intruder configuration $\nu(0p^4_{3/2}1s^1_{1/2}0d^1_{5/2})\pi(0p^1_{3/2})$ in which two neutrons are decoupled, reducing the magnetic moment. When we allow maximal two nucleons in the sd-shell, the neutrons are coupled in pairs in all configurations. This explains the influence of the model space on the magnetic moments of the Li-isotopes. However, the effect is small because the magnetic moments are mainly determined by the unpaired proton in $\pi p_{3/2}$.

The MK3W interaction has cross-shell matrix elements which are specially modified for neutron-rich nuclei. Therefore we performed the calculation also with this interaction. In this calculation, maximum two nucleons were allowed in the sd-shell. This calculation gives a similar result for ^{11}Li, but less good agreement for ^{7,9}Li, nuclei closer to stability. In this calculation 8% of the ^{11}Li wave function contains a configuration with at least one unpaired neutron in an orbital of the sd-shell.

- **B-isotopes**
  The magnetic moments for ^{11}B and ^{13}B are underestimated in the CKI interaction and well reproduced in the PSDMK interaction, even when not taking the full model space ("PSDMK, max 2", filled triangles). The MK3W interaction doesn't reproduce the magnetic moment of the stable ^{11}B. This is not surprising, since this interaction was developed for neutron-rich nuclei.

  For the heavier ^{15}B and ^{17}B the CKI interaction can not be used anymore, since the sd-shell is necessary. For ^{17}B we have to assume more than two nucleons in the sd-shell. The predictions of the magnetic moments by the PSDMK and MK3W interactions deviate from the experimental values for ^{15}B and ^{17}B.
  The deviation of the magnetic moments from the Schmidt value has two origins. One is the first order proton core polarization and the other is due to those configurations in which two neutrons in the sd-shell couple to form $J^\pi = 2^+$. The former mechanism gives almost full account of the

quenching at $A = 13$ and the size of the effect stays quite stable for $11 \leq A \leq 17$. In contrast, the effect of the latter mechanism rapidly varies as the neutron number changes [Oku95]. Okuno et al. explained the deviation from the PSDMK calculations for ^{15}B [Oku95] by the underestimation of the neutron 2^+ configurations. This is confirmed here, by a better agreement of the full calculation with the experimental value. The same explanation was given by Ueno et al. for ^{17}B [Uen96].

Quadrupole moments

In figure 7.3 the calculations of the quadrupole moments with the ANTOINE code are compared with the experimental results for the odd-even Li and B-isotopes. For the Li-isotopes, the difference between the calculations in the p-shell (CKI) and in the p-sd shell (PSDMK) is minimal, irrespective of the number of allowed p-h excitations. However, with the MK3 interaction, modified to better describe the neutron- rich ^{16}N (N=9), the quadrupole moment of

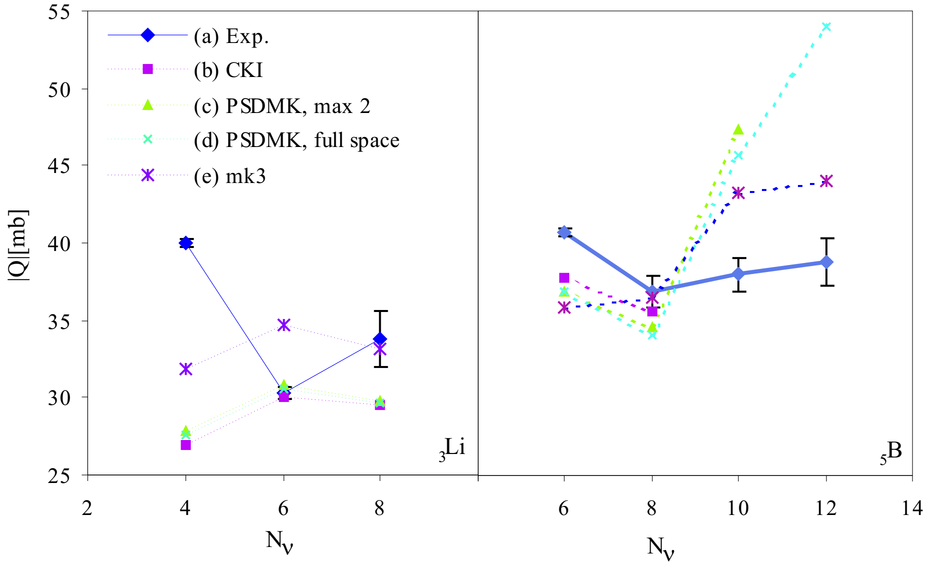

Figure 7.3: *Comparison of (a) experimental and (b-e) calculated quadrupole moments of the odd-even Li (left) and B-isotopes (right). In the calculations the effective charges* $e_n = 0.5$ *and* $e_p = 1.3$ *[Bro88] were used. For the calculation (c) maximum two neutrons were allowed in the sd-shell. For the calculation (d) no restrictions were put on the p-sd model space. In the figure the used effective interaction is mentioned. For the calculation (e) maximum two neutrons were allowed in the sd-shell for the Li-isotopes. For the* $^{11-15}$*B (*^{17}*B) isotopes four (six) neutrons and one proton are allowed in the sd-shell.*

^{11}Li (N=8) is better reproduced. In the latter calculation about 8% of the calculated ^{11}Li wave function has an unpaired neutron in the sd-shell (table A.10), while it is only 1% in the calculation with the PSDMK interaction. On the other hand, this MK3 interaction doesn't reproduce the quadrupole moments of the less neutron-rich nuclei ^{7,9}Li. The quadrupole moment of ^{9}Li is best reproduced with the PSDMK interaction.
The calculated trend of the quadrupole moment as a function of the neutron number is the opposite from what we observe for all used interactions.
Remarkable is the large underestimation of the quadrupole moment of ^{7}Li with all used interactions. This was interpreted as a cluster phenomenon by Kanada-En'yo et al. [Kan01] (section 7.6).

The quadrupole moments of ^{15}B and ^{17}B are largely overestimated with the PSDMK effective interaction. The MK3 gives a better agreement although the quadrupole moments are still slightly overestimated. Ogawa et al. explained this discrepancy with the quenching of the effective charges [Oga03] for isotopes with large $\frac{N-Z}{A}$ ratios. The varying effective charges were calculated using particle-vibration coupling models [Sag01, Boh75]. In this model the effective charges are a function of the parameter $x = \frac{N-Z}{A}$.

$$\begin{aligned} e_\nu(j,j') &= \quad \frac{1}{2}\alpha_{j,j'}(1-x)[(1-0.65x)\chi_{\tau=0} - \chi_{\tau=1}] \\ e_\pi(j,j') &= 1+ \frac{1}{2}\alpha_{j,j'}(1-x)[(1+0.65x)\chi_{\tau=0} + (1+x)\chi_{\tau=1}] \end{aligned}$$

with $\alpha_{j,j'}$ orbital dependent factors, j, j' the involved orbitals, τ the isospin and $\chi_{\tau=0(1)}$ the polarizability coefficients. In [Oga03] it is shown that best results are obtained for $\chi_{\tau=0} = 1.0$ and $\chi_{\tau=1} = -0.33$. The effective charges are reduced with increasing isospin by the parameter x. This reduction is more pronounced for light nuclei. In addition, the polarization charges can be affected by the radial distributions of single-particle wave functions. In particular the effective charges can be quenched for loosely bound single particles. This decoupling effect is incorporated by the orbital dependent factor $\alpha_{jj'}$. We used the $\alpha_{jj'}$ of [Oga03] for the particles in the last filled orbitals. The obtained effective charges are given in table 7.1.

As Ogawa et al. [Oga03] showed, the calculations with the PSDMK interaction and these quenched effective charges reproduce the trend in the quadrupole moments of the odd-even B-isotopes (fig. 7.4). However, this calculation systematically underestimates the quadrupole moments of the Li-isotopes, even worse than the other calculations. The given formula for the effective charges was based on the assumption that the local $\frac{N-Z}{A}$ ratio as well as the total density are preserved in any point of the nucleus. This is clearly not the case for ^{11}Li with a long density tail (=halo). This can explain why the quenching doesn't work here. To reproduce the quadrupole moment of ^{11}Li with the PSDMK interaction by changing the effective charges, one needs in fact an enhanced neutron effective charge $e_\nu = 1.0$ and a slightly higher proton effective charge $e_\pi = 1.44$. These are unrealistic values (fig. 7.5). With these high effective charges the

Table 7.1: *Used parameters for the calculation of the quenched effective charges as explained in [Oga03] with* $\chi_{\tau=0} = 1.$ *and* $\chi_{\tau=1} = -0.33$.

nucleus	x	e_π	e_ν
^{11}B	0.09	1.29	0.52
^{13}B	0.23	1.26	0.41
^{15}B	0.33	1.23	0.19
^{17}B	0.41	1.21	0.17
^{7}Li	0.14	1.28	0.48
^{9}Li	0.33	1.23	0.33
^{11}Li	0.45	1.20	0.14

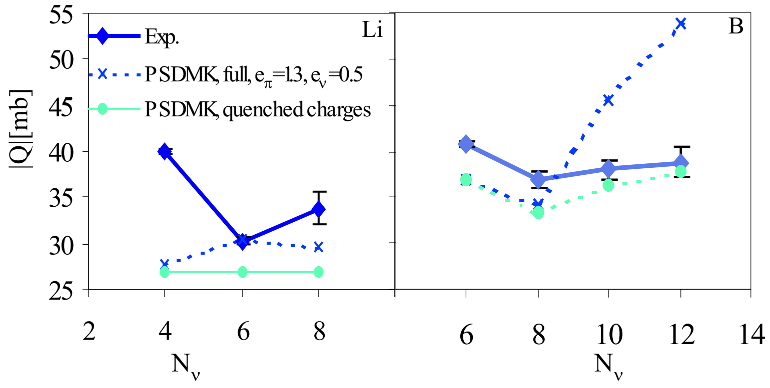

Figure 7.4: *Comparison of experimental and calculated quadrupole moments of the odd-even Li (left) and B-isotopes (right) with quenched effective charges (table 7.1) and the PSDMK interaction.*

quadrupole moment of ^{7}Li is also surprisingly well reproduced, while that of ^{9}Li is largely overestimated.

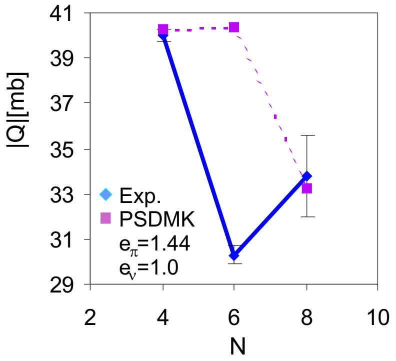

Figure 7.5: *Experimental quadrupole moments of* ^{7,9,11}*Li compared with ANTOINE calculations with the PSDMK effective interactions with unrealistic high effective charges* $e_\pi = 1.44$ *and* $e_\nu = 1.0$.

Polarizability of the ^{9}Li core

In this paragraph we discuss the question how the halo neutrons polarize the ^{9}Li core when their configuration is respectively $s^2_{1/2}$, $p^2_{1/2}$ or $d^2_{5/2}$. Therefore different ANTOINE calculations were performed using the PSDMK interaction, blocking the halo neutron respectively in the $0p_{1/2}$, $1s_{1/2}$ or $0d_{5/2}$ orbitals. The result is shown in figure 7.6.

The neutrons in both $(\nu 0p_{1/2})^2$ and $(\nu 1s_{1/2})^2$ configurations will couple to 0^+. In a simple single particle picture the quadrupole moment of the two configurations is equal and determined only by the proton configuration $\pi 0p_{3/2}$. In the calculations a small difference of about 5% is found due to the proton-neutron interactions. The experimental value for the quadrupole moment of ^{9}Li lies in between the two values.

The two neutrons in the $(\nu 0d5/2)^2$ configuration can couple to 0^+ and to 2^+. The part of the neutrons that couple to 2^+ will enhance the quadrupole moment via the coupling with the protons to a total spin $3/2^-$. The calculations show an enhancement of about 27%.

The experimental value $|Q| = 33.8(1.8)$mb lies in between the values for the 0^+ configurations $\nu(0p_{1/2})^2$, $\nu(1s_{1/2})^2$ and the value for the $\nu(0d_{5/2})^2$ configuration. This is an indication that an admixture of configurations with the two neutrons coupled to 2^+ is necessary. The contribution of these configurations are underestimated in the PSDMK calculations performed without restriction on the number of neutrons in the sd-orbits. The calculated wave function for

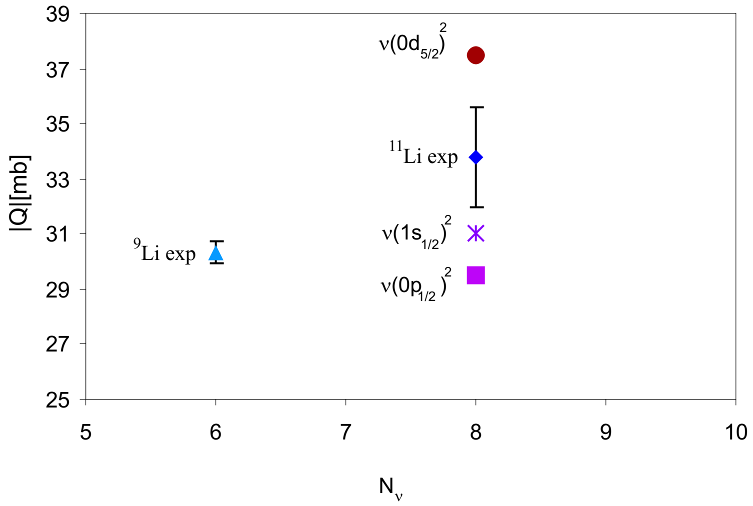

Figure 7.6: *ANTOINE calculations for* $Q(^{11}Li)$ *with the effective PSDMK interaction, assuming different pure neutron configurations for the halo neutrons, compared to the experimental values for* ^{11}Li *and* ^{9}Li *(0p-0h).*

^{11}Li results in a large probability of normal, non intruder states ($P = 84\%$) and only 6% of the intruder $0d^2_{5/2}$ or $1s_{1/2}0d_{5/2}$ configurations (appendix A).

By mixing two wave functions, one can calculate the quadrupole moment of the mixed wave function as a function of the mixing probability a^2. The comparison of this to the the experimental quadrupole moment, gives an estimate of the mixing probability a^2.
We define a mixed wave function

$$|\psi\rangle = a|\phi_1\rangle + b|\phi_2\rangle \tag{7.3}$$

with $|\phi_1\rangle$ a linear combination of all wave functions with neutron configurations coupled to 0^+.

$$\begin{aligned} |\phi_1\rangle \quad = \quad & c|(\nu(0p^2_{1/2})_{0+} \otimes \pi(p^1_{3/2})_{3/2-})_{3/2-}\rangle \\ & +d|(\nu(1s^2_{1/2})_{0+} \otimes \pi(p^1_{3/2})_{3/2-})_{3/2-}\rangle \\ & +e|(\nu(0d^2_{5/2})_{0+} \otimes \pi(p^1_{3/2})_{3/2-})_{3/2-}\rangle \end{aligned}$$

and $|\phi_2\rangle$ the wave function with a neutron configuration coupled to 2^+.

$$|\phi_2\rangle = |(\nu(0d^2_{5/2})_{2+} \otimes \pi(p^1_{3/2})_{3/2-})_{3/2-}\rangle \tag{7.4}$$

We neglect here the $|(\nu(1s_{1/2}0d_{5/2})_{2+} \otimes \pi(p^1_{3/2})_{3/2-})_{3/2-}\rangle$ for simplicity.

The spectroscopic quadrupole moment of the mixed wave function equals [Hey94]

$$\begin{aligned} eQ_s(|\psi\rangle) &= \langle 3/2, m=3/2|eQ_{s.p.}+eQ_{coll}|3/2, m=3/2\rangle \\ &= \sqrt{\frac{16\pi}{5}}\begin{pmatrix} 3/2 & 2 & 3/2 \\ -3/2 & 0 & 3/2 \end{pmatrix}\langle 3/2||eQ_{s.p.}+eQ_{coll}||3/2\rangle \end{aligned}$$

with $Q_{s.p.}$ the single particle quadrupole moment and

$$Q_{coll} = \sqrt{\frac{B(E2,0^+\rightarrow 2^+)}{5}}[(b_{20}^{\dagger}+b_{20})\otimes 1] \tag{7.5}$$

the quadrupole moment due to collective vibrations [Hey94, Vyv01]. The creation (annihilation) operators $b_{20}^{\dagger}$ (b_{20}) create (annihilate) a boson with spin 2. This gives us

$$\begin{aligned} eQ_s(|\psi\rangle) &= a^2Q_s(|\phi_1\rangle)+(1-a^2)Q_s(|\phi_2\rangle) \\ &\quad +2\sqrt{\frac{16\pi B(E2)}{500}}a\sqrt{1-a^2}\langle\phi_1||(b_{20}^{\dagger}+b_{20})\otimes 1||\phi_2\rangle) \end{aligned}$$

Using the Wigner-Eckart theorem to split the collective operator for the protons and the neutrons gives [Hey94]

$$\begin{aligned} eQ_s(|\psi\rangle) &= a^2Q_s(|\phi_1\rangle)+(1-a^2)Q_s(|\phi_2\rangle)-4\begin{Bmatrix} 0 & \frac{3}{2} & \frac{3}{2} \\ \frac{3}{2} & 2 & 2 \end{Bmatrix}\langle 0^+||b_{20}||2^+\rangle \\ &= a^2Q_s(|\phi_1\rangle)+(1-a^2)Q_s(|\phi_2\rangle)+1.12\sqrt{B(E2)}a\sqrt{1-a^2} \end{aligned}$$

Using this formula, we can determine the needed amount of mixing to reproduce the experimental quadrupole moment. This formula contains four unknown parameters: $Q_s(|\psi\rangle)$, $Q_s(|\phi_1\rangle)$, $Q_s(|\phi_2\rangle)$ and $B(E2,|\phi_1(0^+)\rangle\rightarrow|\phi_2(2^+)\rangle)$.

- For $Q_s(|\psi\rangle)$ we use the experimental value $|Q(^{11}\mathrm{Li})| = 33.8(18)$mb.

- $Q_s(|\phi_1\rangle)$ is the quadrupole moment of ^{11}Li with all neutrons coupled to 0^+. In figure 7.6 is shown that this is well approximated by the observed quadrupole moment of ^{9}Li. Therefore we use as an approximation $Q_s(|\phi_1\rangle) = 30.31$mb.

- $Q_s(|\phi_2\rangle)$ is the quadrupole moment of ^{11}Li with all neutrons coupled to 2^+. The calculated quadrupole moment for the configuration $0d^2_{5/2}$, is an admixture of a configuration with the two neutrons coupled to 2^+ and a configuration with the two neutrons coupled to 0^+. In the configurations $0p^2_{1/2}$ and $1s^2_{1/2}$, the two neutrons are coupled to 0^+. Therefore we use as an approximation the calculated quadrupole moment for the configuration $0d^2_{5/2}$ for $Q_s(|\phi_2\rangle)$. This gives $Q_s(|\phi_2\rangle) = -37.5$mb.

- Also for the reduced electromagnetic transition strength $B(E2, |\phi_1(0^+)\rangle \rightarrow |\phi_2(2^+)\rangle)$ some assumptions are necessary. For ^{11}Li nothing about this transition strength is known. Therefore we look to isotones, such as ^{12}Be. For ^{12}Be the nuclear deformation length δ is measured [Iwa00b], wile the electro-magnetic deformation length $\delta_{e.m.} = \beta_2 R$ is needed to determine $B(E2)$ [Ram01, Nun02]

  $$B(E2) = (\frac{3ZR\delta_{e.m.}}{4\pi})^2 \tag{7.6}$$

  However, from the comparison of the experimental nuclear deformation length δ with shell model calculations one could deduce $B(E2)$ indirectly as $B(E2,^{12}\text{Be}) = 52(6)e^2fm^4$ [Iwa00b].
  Nunes et al. [Nun02] calculated the transition strengths for ^{12}Be, but different parametrizations of the model give very different results varying from $B(E2) = 5\text{e}^2\text{fm}^4$ to $B(E2) = 50\text{e}^2\text{fm}^4$.

To calculate the needed amount of mixing, we assume that the transition strength $B(E2)$ is similar for ^{12}Be as for ^{11}Li. Using the extreme values of the calculations of Nunes et al. [Nun02] for $B(E2)$, one can deduce the limits of mixing of $(2p-2h)_{2+}$ intruder components into the ^{11}Li wavefunction.
The minimum transition strength $B(E2) = 5\text{e}^2\text{fm}^4$ gives $a^2 = 0.937$. This means an admixture of 6.3% of the $\nu(0d_{5/2})^2_{2+}$ configuration to the wave function of the ^{11}Li ground state. The maximum transition strength $B(E2) = 50\text{e}^2\text{fm}^4$ gives an admixture of 0.8% of the $\nu(0d_{5/2})^2_{2+}$ configuration to the wave function of the ^{11}Li ground state.

So a small, but present, admixture of 2^+ neutron configurations can explain the observed ^{11}Li quadrupole moment. The fact that such a small admixture leads to an enhancement of the quadrupole moment with about 10% shows the sensitivity of the quadrupole moment to the admixture of 2^+ neutron configurations. However, due to the unknown $B(E2)$ one can not fix the amount of mixing.
Johannsen et al. [Joh90] predicted that this admixture is less than 1%. These calculations are based on a three-body model in which two neutrons form a spatially extended halo around an inert ^{9}Li core. In this model the motion of these neutrons relative to the core is predicted to have total angular momentum $L = 0$ with less than 1% admixture of $L = 2$. Our result confirms these calculations if we use the values for $B(E2)$ deduced from the combination of the experimental result and shell model calculations.

In this argumentation it was assumed that the two loosely bound neutrons are in the same orbital. This leads with the effective PSDMK interaction to a small admixture of $L = 2$ neutron configurations. With the MK3 effective interaction, ANTOINE calculates a wave function with also a small contribution of a configuration with only one neutron in the $0d_{5/2}$ orbital (table A.10). With this wave function the observed quadrupole moment of ^{11}Li is reproduced. So in the two cases a contribution of the $0d_{5/2}$ orbital to the total wave function of the ^{11}Li ground state is necessary. **This is the first experimental indication that one or both halo neutrons of ^{11}Li have a non-zero probability to occur in the $0d_{5/2}$ orbital.**

7.2.2 Realistic interaction leading to the shell evolution paradigm

Realistic interactions are obtained by fitting the calculated values for the free nucleon-nucleon scattering observables, such as phase shifts in all possible reaction channels and polarization data [Hey94]. Based on the general invariance principles [Rin80] a central part V_C, a tensor part V_T and a spin-orbit term V_{LS} contribute to a total realistic force between two nucleons 1 and 2 [Hey94]

$$\begin{aligned} V &= V_C(1,2) + V_T(1,2) + V_{LS} \\ &= V_0(r) + V_\sigma(r)\sigma_1.\sigma_2 + V_\tau(r)\tau_1.\tau_2 + V_{\sigma\tau}(r)\sigma_1\sigma_2\tau_1\tau_2 \\ &\quad +(V_{T0}(r) + V_{T\tau}(r)\tau_1\tau_2)S_{12} \\ &\quad +V_{LS}(r)l.S \end{aligned}$$

with σ, τ the spin- and isospin operator, r the distance between the two nucleons and $S_{12} = \frac{3}{r^2}(\sigma_1.r)(\sigma_2.r) - \sigma_1.\sigma_2$.
The spin-isospin dependent part $V_{\sigma\tau}$ of the central force is attractive and is acting on spin-orbit pairs $j = l \pm 1/2$ with different isospin and same orbital angular momentum l [Fed79, Des63]. The strength of this force increases with the number of nucleons filling the involved orbits. Around stability with $N \approx Z$ and ample occupancy of the $j = l + 1/2$ orbit in the valence shell, the proton (neutron) $j = l - 1/2$ orbit is lowered by neutrons (protons) in the $j = l + 1/2$ orbit. In exotic nuclei, this lowering can be absent and the $j = l + 1/2$ orbit can be located rather high, not far from the upper shell. This can lead to a weakening of the shell closure. Since the weakening of shell closures were only observed since the experimental availability of exotic radioactive beams, this phenomenon got only recently extra attention. Otsuka et al. [Ots01, Ots02, Ots03] reminded that the evolution of the relative distance of the orbits over the nuclear chart can be explained by the varying strength of the spin-isospin dependent term of the residual nucleon nucleon interaction. To know $V_{\sigma\tau}$ as a function of the isospin, one needs to fit experimental data to $V_{\sigma\tau}$. For the region around the Island of Inversion of ^{32}Mg shell model calculations, using the adapted isospin dependent $V_{\sigma\tau}$ term, explained the new magic number $N = 16$ for ^{24}O [Ots01]. Experimental indications for this "new" magic number $N = 16$ were found by a systematic study of the single-neutron- [Oza00] and two-neutron separation energy [Dlo02] in neutron rich nuclei. At the other side of the stability line, $Z = 16$ was found to be a magic number for neutron deficient $N = 13 - 15$ nuclei by the study of Q_{β^-} and the single-proton separation energy [Kan02].

Also for light nuclei the term $V_{\sigma\tau}$ is isospin dependent. In the effective in-

teraction[2] PSDMK2, the attractive $V_{\sigma\tau}$ part of the interaction is too weak as compared to the realistic G-matrix interaction [Sag93]. Therefore this effective interaction was modified by adapting artificially the two-body matrix elements [Ots01].
Around $N = 8$ the energy levels of the $N = 7$ isotones ^{13}C,^{11}Be and ^{9}He are reproduced quite well by ANTOINE calculations using this modified PSDMK2 interaction [Ots01].

With this modified PSDMK2 interaction, Suzuki et al. [Suz03] found recently admixtures of 50% for the $0p^2_{1/2}$ configuration and 25% for each of the two intruder configuration $(1s^2_{1/2})$ and $(0d^2_{5/2})$ for the last two neutrons in ^{11}Li [Suz03]. This was achieved by fitting the calculations to the observed Gamow-Teller transitions $B(GT)$ and magnetic moments.
For the quadrupole moments of the Li-isotopes no calculation was performed with this adapted interaction.

In the qualitative overview of the experimental data around $N = 8$, it can be seen that $V_{\sigma\tau}$ plays an important role to determine the shell closures (fig. 7.7 and 2.7).

For stable nuclei, such as $^{13}_{6}\mathrm{C}^{7}$, the filled proton-orbit $j_{>} = 0p_{3/2}$ lowers the neutron-orbit $j_{<} = 0p_{1/2}$ due to the attractive coupling $V_{\sigma\tau}$ of the two orbits. This causes a shell gap at $N = 8$, what is experimentally indicated by the high first excitation level and the normal spin/parity of ^{13}C (fig. 7.7). When removing one proton of the $j_{>}$-orbit, this attraction becomes weaker. The observed trend line for the quadrupole moments of the B isotopes, which shows the presence of a weak shell closure at $N = 8$, confirms this. When removing one more proton the attractive $V_{\sigma\tau}$ term becomes so weak that the $\nu p_{1/2}$ orbit is hardly lowered. Like this a level of the sd-shell might become lower in energy than the $0p_{1/2}$ level. The $1s_{1/2}$ level has an energy lower than the $0d_{5/2}$ level in this case. This is because the $0d_{5/2}$ nucleon interacts more strongly with the $0p_{1/2}$ nucleon, which is not low anymore, while the $1s_{1/2}$ nucleon interacts more strongly with the $0s_{1/2}$ nucleons. The well-known inverse parity of ^{11}Be indicates that the attraction of the spin-orbit pair $p_{1/2} - p_{3/2}$ is not strong enough anymore to keep the shell gap at $N = 8$. When we remove one more proton, the proton orbit $j_{>}$ is almost empty and the attraction $V_{\sigma\tau}$ term becomes even weaker. This might give rise to a new shell gap at $N = 6$. The decreasing quadrupole moments of the Li-isotopes when approaching $^{9}_{3}\mathrm{Li}_{6}$, might be an indication for such a new magic number.

In this picture of the shell-evolution a possible new magic number $N = 6$ is suggested. This magic number was also suggested by the cluster core model of R.K. Gupta et al. [Gup00, Gup02]. In this model the halo structure is investigated in terms of potential energy surfaces (PES). These PES are calculated

---

[2] This interaction is very similar to the PSDMK effective interaction.

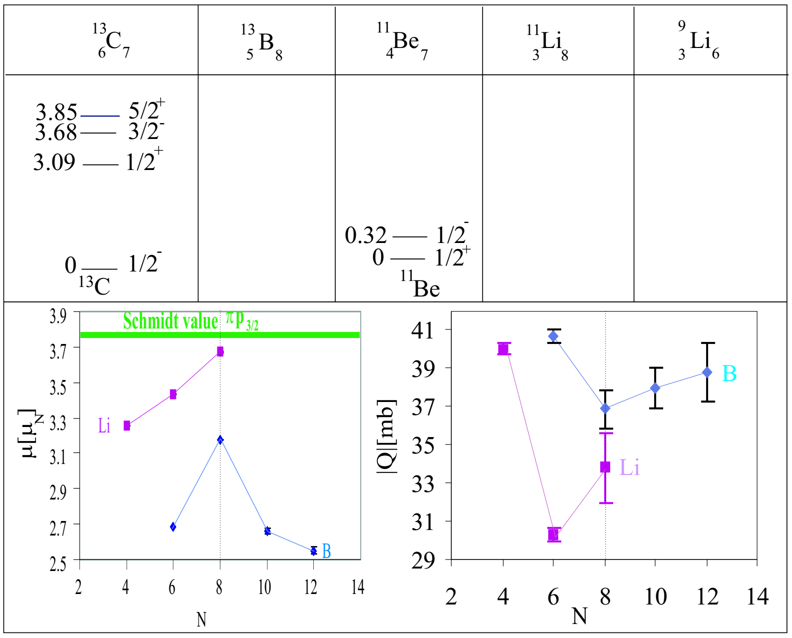

Figure 7.7: *Schematic view of the shell evolution paradigm test.*

as the sum of binding energies $B(A, Z)$, Coulomb repulsion, nuclear proximity attraction V_p [Blo77] and the centrifugal potential V_l [Sar85] for all the possible cluster and core configurations of a nucleus:

$$V(A_1, A_2, R, l) = -\sum_{i=1}^{2} B(A_i, Z_i) + \frac{Z_1 Z_2 e^2}{R} + V_p + V_l \qquad (7.7)$$

In these calculations the nuclei with mass number A are split in a core with mass number A_1 and a cluster with mass number $A_2 = A - A_1$. The deformation effects are neglected in both the Coulomb and proximity energies, for reasons of simplicity. The radius is calculated as $R_i = 1.15 fm A_i^{1/3}$. The PES are calculated as a function of the possible cluster-core configurations, i.e. as a function of A_2. A minimum potential energy means a configuration formed with the largest quantum mechanical probability. A minimum potential energy also indicates that one of the contributing nuclei (the core of one of the clusters) is a magic or nearly magic nucleus [Gup02]. In figure 7.8 some examples are given from [Gup00, Gup02]. The different curves correspond to different angular momenta l. Four minima are visible in the picture for ^{20}Mg [Gup02]. These correspond to the magicity of the neutron deficient $^{16}_{10}\mathrm{Ne}_6$, $^{14}_{8}\mathrm{O}_6$, $^{18}_{10}\mathrm{Ne}_8$. This indicates a magic number $N = 6$ far from stability and $N = 8$ close to stability. The potential energy as a function of A_2 for ^{11}Li shows only one minimum, i.e. for a two-neutron cluster and a $^{9}_{3}\mathrm{Li}_6$ core. This might indicate a magic number

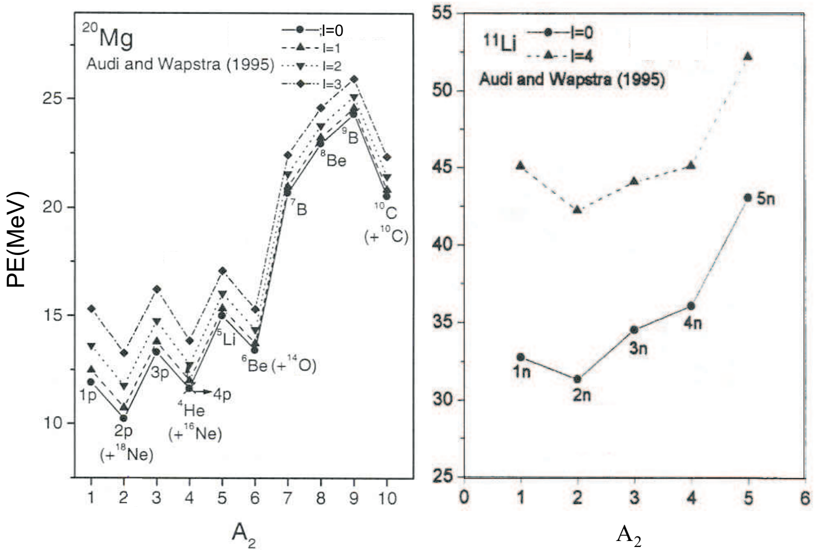

Figure 7.8: *Potential energy as a function of the mass number A_2 of the cluster contributing to the nuclei ^{20}Mg and ^{11}Li. Picture taken from [Gup00, Gup02].*

$N = 6$ for nuclei with $Z = 3$.

7.3 Large basis no-core shell model (NCSM)

For light nuclei, the capacities of the computers allow larger model spaces. This is used in large-basis no-core shell model calculations. In such calculations all nucleons are active without a fixed core. In addition, the model space up to $N\hbar\omega$ is taken into account. This larger model space diminishes the errors induced by approximating the A-body effective interaction by a two-body effective interaction. Such calculations are performed for $A = 7 - 11$ by P. Navratil et al.[Nav98] with $N = 6$ for $A = 7$ and $N = 4$ for the other nuclei. The used effective interaction is based on the modern nucleon-nucleon Reid93 potential [Rei93] together with the Coulomb potential. Also isospin-breaking elements are considered, such as the different $T = 1$ channels for proton-neutron, proton-proton and neutron-neutron systems.

In table 7.2 an overview of the calculations for the nuclear moments of the odd-even Li isotopes is given. Both the magnetic and the quadrupole moments are systematically underestimated, but the trend line is reproduced: the smallest quadrupole moment is that of ^{9}Li. In these calculations free g-factors and bare charges are used. The experimental values can be reproduced by taking effective charges according to Navratil et al.[Nav98], but no numbers on the nu-

Table 7.2: *Nuclear moments calculated in a large-basis no-core shell model [Nav98]. Free g-factors and bare charges are used.*

		$\mu[\mu_N]$	$\|Q\|$[mb]
^{7}Li	exp.	3.25646253(40)	40.0(3)
	model	2.994	27.10
^{9}Li	exp.	3.43682(5)	30.31(39)
	model	2.940	20.85
^{11}Li	exp.	3.6712(5)	33.8(1.8)
	model	3.601	23.01

clear moments are given in that article. The claimed needed effective charges are close to the common used ones in the shell model: $e_\pi(^7\text{Li}) = 1.18$, $e_\nu(^7\text{Li}) = 0.18$, $e_\pi(^9\text{Li}) = 1.25$, $e_\nu(^9\text{Li}) = 0.25$, $e_\pi(^{11}\text{Li}) = 1.27$, $e_\nu(^{11}\text{Li}) = 0.27$. So even in this almost unlimited model space effective charges are needed to correct for approximations in the effective interaction.

In the mean time it is possible to use a three-body effective interaction without any adjustable parameter. This is called "ab initio large basis no-core shell model". It is tested for the ^{3}He and ^{4}He isotopes in the large $18\hbar\omega$ space, for which well converged results are found [Bar02, Nav03]. Also for some Be, B,N and C isotopes good agreement for the low-lying spectra were found. Up to now no nuclear moments for the Li-isotopes were reported.

7.4 Monte Carlo Shell model

The Monte Carlo Shell Model [Ots01b, Ots99, Ots01c] has been developed to overcome the problem of too large dimensions in conventional shell model calculations. In this model a basis $\chi_i, i = 1...n$ is constructed with a variational method such that each χ_i has maximal relevance for the final eigenstates. The dimension n of this basis is much smaller than for arbitrary bases. This makes it possible to diagonalize the full matrix. This diagonalization method is called quantum monte carlo diagonalization. This model has been applied to midshell nuclei such as ^{48}Cr, ^{56}Ni and the Ba isotopes. Good agreement with experimental level schemes was found.

In the $N \approx 20$ region of neutron rich unstable nuclei, the mixing between the $0p0h$ and $2p2h$ configurations in low lying states due to a varying shell gap is reproduced quite well [Uts01].

Until now no calculations were performed for the Li isotopes. It would be interesting to compare future calculations for Li with the calculations presented in this work.

7.5 Cluster models

In cluster models the nucleus is not divided into a core and a valence part as in conventional shell model calculations. The nucleus is described as an interacting system of two-, three- or more clusters of nucleons. Recently different cluster calculations were performed. Below an overview is given.

7.5.1 Microscopic multicluster model with a stochastical variational method [Var95, Var02]

In this model ^{7}Li is described as a two-cluster system ^{7}Li= $\alpha + t$. For the other Li-isotopes, neutrons are added: ^{8}Li= $\alpha + t + n$, ^{9}Li= $\alpha + t + n + n$, ^{11}Li= $\alpha + t + n + n + n + n$. The wave function is an anti-symmetrized product of the internal states of the clusters and the functions of the relative motions. The internal structure of the clusters (α, t, n) is approximated by a Slater determinant of 0s harmonic oscillator wave functions [Bra00]

$$\psi_0(x) = \sqrt{\frac{\beta}{\pi}} \exp\left(-\beta x^2\right) \tag{7.8}$$

of a common width parameter $\beta = \frac{m\omega}{\hbar}$. Such wave functions have a Gaussian form with a full width half maximum of $FWHM = ln(2)\sqrt{\frac{2}{\beta}}$. The width parameter is adjusted to get nearly correct values for the sum of the radii of the free α plus t clusters and to minimize its energy. This gives $\beta = 0.52\mathrm{fm}^{-2}$. The function of relative motion is approximated by a linear combination of nodeless harmonic-oscillator functions of different width parameters, which are relatively unsensitive to the results. Various cluster arrangements are combined to include the different correlations between the clusters. A cluster arrangement is indicating the priority of coupling of the clusters. In the example of ^{8}Li we have the arrangements $(\alpha, t)n$, $\alpha(t, n)$, $(\alpha, n)t$.

To keep the dimension of the basis low, a stochastic variational method [Var94] is applied. Here the important basis states are selected using an admittance test. A candidate is admitted if it, together with the previous selected basis states, lowers the energy more than a preset value ϵ. If k successive candidates fail to fulfill the condition, ϵ is divided by two and the search is continued.

The Minnesota effective nucleon-nucleon interaction [Tho77], consisting of a central part, a spin-orbit part and a Coulomb part without effective charges is used. The strength of the spin-orbit force was set to give the correct spacing between the $3/2^-$ and $1/2^-$ states of the ^{7}Li and ^{7}Be subsystems. The parameter u of the central part was set to get overall agreement between experimental and model energies of the states of ^{7}Be, ^{8}B, ^{7}Li and ^{8}Li (u=1). With these parameters fixed, the model contains no free parameters.

Before applying this model to the Li-isotopes [Var95, Var02] this procedure was successfully tested on the neutron rich He isotopes [Var94].

The results of Varga et al.[Var95, Var02] for the nuclear moments of the odd-even Li-isotopes are shown in table 7.3.

Table 7.3: *Nuclear moments calculated in a multicluster model with a stochastic variational method [Var95, Var02].*

		$\mu[\mu_N]$	$\lvert Q\rvert$[mb]
^{7}Li	exp.	3.25646253(40)	40.0(3)
	model	3.15	36.5
^{9}Li	exp.	3.43682(5)	30.31(39)
	model	3.43	27.4
^{11}Li	exp.	3.6712(5)	33.8(1.8)
	model	3.23	37.1

The model predicts the smallest quadrupole moment for ^{9}Li, as it is experimentally observed. However, the ^{11}Li quadrupole moment is largely overestimated, while the ^{7}Li quadrupole moment is underestimated.

7.5.2 Microscopic cluster model [Des97]

P. Descouvement described ^{11}Li in a three cluster model as ^{9}Li$+n+n$ [Des97]. The ^{9}Li nucleus is described in the shell model with all p-shell wave functions allowed by the Pauli principle. This procedure yields many ^{9}Li states, defined by a flexible mixing of shell model basis states. In this way core excitations, expected to be important in halo nuclei [Nun96], are consistently introduced. The parameter u of the Minnesota force [Tho77] and the strength of the spin-orbit term was adapted to the binding energy of ^{11}Li and the excitation energy of ^{9}Li. The results are shown in table 7.4. The quadrupole moment of ^{9}Li is strongly underestimated. The quadrupole moment of ^{11}Li is reproduced more or less.

Table 7.4: *Absolute values for the quadrupole moments calculated in a multicluster model [Des97].*

	Exp.[mb]	Model[mb]
^{9}Li	30.31(39)	22.5
^{11}Li	33.8(1.8)	31.3

7.5.3 Hyperspherical functions method [Tim02]

In this model, hyperspherical coordinates r,θ,ϕ_1,... are used instead of the distances between the clusters. The energy is split in a hyperradial and a hyperangular part. The eigenfunctions of the hyperangular part are called hyperspherical functions. The eigenfunctions of the hyperradial part are called the

hyperradial functions. The wave function is then expanded in the hyperspherical functions basis; it is represented as a sum of products of the hyperradial and the hyperspherical functions.
Such an expansion has been shown to converge for three-four-nucleon bound systems providing comparable results for binding energies and root mean square radii to other few-body methods [Bal82]. For $A > 4$ the number of hyperspherical harmonics becomes very large and no studies of convergence have been done with the traditional formulation of the hyperspherical functions method. Recently a modified version was proposed with an adapted effective interaction [Tim02]. At the moment only binding energies of the H and He isotopes are calculated. The experimental data are reproduced quite well. It would be very interesting to compare future calculations with the experimental data presented in this work.

7.6 Antisymmetrized molecular dynamics

The microscopic method of antisymmetrized molecular dynamics (AMD) [Kan01] is free from assumptions of inert core or existence of clusters. The wave function of the system is written as a linear combination of AMD basis wave functions ϕ_{AMD}. An AMD basis wave function ϕ_{AMD} is a Slater determinant of Gaussian wave packets

$$\phi_{AMD} = \frac{1}{\sqrt{A!}} AS(\phi_1, \phi_2, ..., \phi_A) \tag{7.9}$$

with $\phi_i = \phi_{Xi}(r_j)\chi_i\tau_i$, AS the anti-symmetrization and

$$\phi_{Xi}(r_j) \propto exp[-\nu(r_j - \frac{X_i}{\sqrt{\nu}})^2] \tag{7.10}$$

with χ_i is the intrinsic spin function

$$\chi_i = \begin{pmatrix} 1/2 + \xi_i \\ 1/2 - \xi_i \end{pmatrix} \tag{7.11}$$

parameterized by ξ_i and τ_i is the isospin function which is up (proton) or down (neutron). After the projection onto a parity eigenstate, variational calculations are performed to find the state which minimizes the energy of the system. Afterwards a projection on the angular momentum is performed. In the simplest version of the model the directions of intrinsic spins of single particle wave functions are fixed via fixed $\xi_i = \pm 1/2$.
As effective interaction the Case(1) of MV1 [And80] force is adopted for the central part of the effective force. This contains a zero-range three-body force

$$V^{(3)} = v^{(3)}\delta(r_1 - r_2)\delta(r_1 - r_3) \tag{7.12}$$

in addition to the Volkov1 two-body interaction [Vol65]

$$V^{(2)} = (1 - m + bP_\sigma - hP_\tau - mP_{\sigma\tau})(V_A exp[-(\frac{r}{r_A})^2] + V_R exp[-(\frac{r}{r_R})^2]) \tag{7.13}$$

for the density dependent terms. For the parameters following values are used: $v^{(3)} = 4000\text{MeV fm}^6$, $b = h = 0$, $V_A = -83.34\text{MeV}$, $r_A = 1.60$ fm, $V_R = 104.86$ MeV, and $r_R = 0.82$ fm. P_σ and P_τ stand for spin- and isospin exchange operators, respectively and r denotes $|r_1 - r_2|$. The free parameter m is the majorana parameter. In addition to the central force, a spin-orbit and Coulomb term are adopted. The Coulomb interaction is approximated by a sum of seven Gaussians. For the spin-orbit interaction the two-body G3RS force [Yam79] is taken

$$V_{LS} = (u_I exp(-\kappa_I r^2) + u_{II} exp(-\kappa_{II} r^2)) P(^3O) L.(S_1 + S_2) \tag{7.14}$$

with $\kappa_I = 5.0\text{fm}^{-2}$ and $k_{II} = 2.778\text{fm}^{-2}$ and u_I, u_{II} free parameters.

To find the appropriate values for the free parameters (m, u_I and u_{II}) the binding energies of Li, B, Be and C isotopes were calculated with different parameters. Best agreement was found for $m = 0.576$, $u_I = -u_{II} = 900\text{MeV}$ [Kan01]. To look at the influence of different interactions, also the Volkov1 interaction [Vol65] with $m = 0.56$ and $u_I = -u_{II} = 900\text{MeV}$ was used as central force for this calculation. This Volkov1 interaction contains only two-body forces. The results without the three-body force overestimate the excitation energies of non-normal parity states in most nuclei. So a three-body force term is necessary to reproduce the data.

With the optimum parameters for the binding energies the nuclear moments of these isotopes are calculated. In table 7.5 and figures 7.9 and 7.10 an overview of the results with free charges and g-factors is given.

Table 7.5: *Nuclear moments in the pure AMD model (AMD) of Y. Kanada-En'yo et al. [Kan01] and its Shell Model Limit (SML). Values are taken from [Kan01]. For Q(^{7}Li) an extra value is given with an adapted wave function in the pure AMD model (AMD $\phi_{ad.}$).*

		$\mu[\mu_N]$	$\|Q\|$[mb]
^{7}Li	Exp.	3.25646253(40)	40.0(3)
	AMD	3.15	27.6
	SML	3.14	15.1
	AMD $\phi_{ad.}$		46.1
^{9}Li	Exp.	3.43682(5)	30.31(39)
	AMD	3.42	27.0
	SML	3.44	23.2
^{11}Li	Exp.	3.6712(5)	33.8(1.8)
	AMD	3.79	29.4
	SML	3.79	29.4

When we compare the AMD results with the experimental results, we see that the trend line of the nuclear moments as a function of the neutron number is reproduced for both Li and B isotopes. On the other hand all quadrupole moments are a bit underestimated.

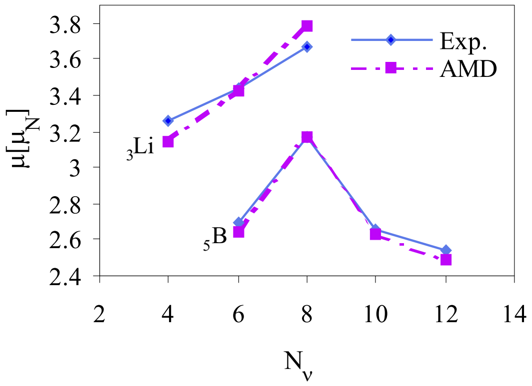

Figure 7.9: *Magnetic moments of the odd-even Li and B isotopes calculated in the AMD model [Kan01].*

For ^{7}Li, which quadrupole moment is largely underestimated (also in the shell model) this can be corrected by adapting the wave function of relative motion. When the clustering is well developed, the relative wave function between clusters spreads out toward the outer spatial region resulting in a long tail. However, since the single nucleon wave function of AMD is a Gaussian wave packet, the relative wave function between clusters is also necessarily a Gaussian wave packet. The adaption of the wave function is done by superposing several AMD wave functions which are written as $\alpha + t$ clustering states with different distances between the centers of two clusters. The obtained quadrupole moment of ^{7}Li with the adapted wave function reproduces better the experimental value, but now it overestimates it (fig. 7.10(AMD ϕ_{ad}) and table 7.5). This confirms the strongly developed cluster in ^{7}Li, while the clustering effects of ^{9}Li and ^{11}Li are much less pronounced.

Roughly speaking the electromagnetic properties of the odd-even nucleus reflect the orbit of the last valence proton. However, the nuclear moments shift as a function of the neutron number. This can be explained in relation to the drastic change between cluster and shell-model-like structures. There are two fundamental effects of the cluster structures on the nuclear moments. One is caused by the spatial relative distance between the clusters (spatial clustering effects). The other is concerned with the angular momentum coupling correlation of nucleons. In order to extract the effect of the cluster coupling of angular momenta from the AMD wave functions, the inter-cluster relative distances in the AMD wave functions are made artificially very small. In the obtained shell-model limit (SML) states, the spatial cluster is not recognizable anymore but

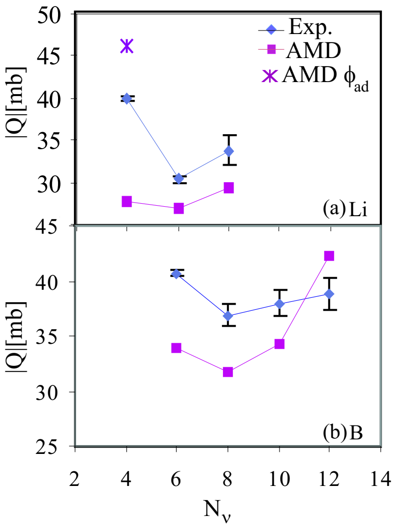

Figure 7.10: *Quadrupole moments of the odd-even (a) Li and (b) B isotopes calculated in the AMD model [Kan01]. The label AMD ϕ_{ad} means that the wave function is corrected for the strong clustering effect.*

only effects of the cluster coupling of angular momenta persist. The magnetic moments in the shell-model limit are found to be almost the same as those of the original AMD (table 7.5). This means the magnetic dipole moments don't depend on the spatial clustering but are effected only by the cluster coupling of angular momenta. This is easily understood because the expectation values of linear terms of operators J, L, S are mainly determined by the cluster coupling of angular momenta. This coupling lowers the magnetic moment compared to the free Schmidt-value. The cluster effect is the strongest for ^{7}Li which is shown to consist of $\alpha + t$ [Ike80].

The quadrupole moments are effected most by the spatial clustering. The amount of spatial clustering is determined by the difference of the full AMD calculation and the shell model limit of the AMD calculation, in which the spatial clustering has been removed (table 7.5). The spatial clustering is the largest in ^{7}Li and decreases for the other Li isotopes as the cluster structure weakens.

This model describes the experimental nuclear moments the best amongst the other models. Let's therefore look to the prediction of another property, such as the radii. The AMD calculations with the three-body force seem to qualitatively agree with the observed radii, except for very neutron rich nuclei. It underestimates the large radii of the halo nuclei ^{11}Li, ^{11}Be, ^{14}Be [Kan01].

7.7 Overview

In table 7.6 an overview of the presented calculations for the magnetic moments is given. These are predicted quite well by all models. This is due to the fact that the valence proton has the expected $p_{3/2}$ configuration and the neutrons are mainly paired for the Li-isotopes with an even neutron number.

Table 7.6: *Overview of the calculated magnetic moments* $[\mu_N]$ *compared with the experimental ones.*

	^{7}Li	^{9}Li	^{11}Li
Exp.	3.25646253(40)	3.43682(5)	3.6712(5)
Shell model			
CKI	3.17	3.38	3.79
PSDMK-full space	3.20	3.41	3.72
PSDMK-max. 2part.	3.28	3.51	3.79
MK3W-max. 2part.	3.18	3.50	3.77
no-core [Nav98]	2.994	2.940	3.601
Cluster models			
[Var02]	3.15	3.43	3.23
AMD [Kan01]	3.15	3.42	3.79

In table 7.7 and figure 7.11 an overview of the calculated quadrupole moments is given.

Table 7.7: *Overview of the experimental and calculated absolute values of the quadrupole moments* [*mb*]. ** The calculation of the quadrupole moment for* ^{7}*Li is with an adapted wave function (see section 7.6).*

	^{7}Li	^{9}Li	^{11}Li
Exp.	40.0(3)	30.31(39)	33.8(1.8)
Shell model			
CKI	27.20	29.99	29.5
PSDMK-full space	27.6	30.52	29.6
PSDMK-max. 2part.	27.9	30.78	29.75
MK3W-max. 2part.	31.9	34.7	33.17
no-core [Nav98]	27.10	20.85	23.01
Cluster models			
[Var02]	36.5	27.4	37.1
[Des97]		22.5	31.3
AMD [Kan01]	46.1*	27.0	29.4

With the shell model even the qualitative trend line as a function of the neutron number is not reproduced. The CKI and the PSDMK effective interactions give similar results. While in CKI only neutrons in the p-shell are considered,

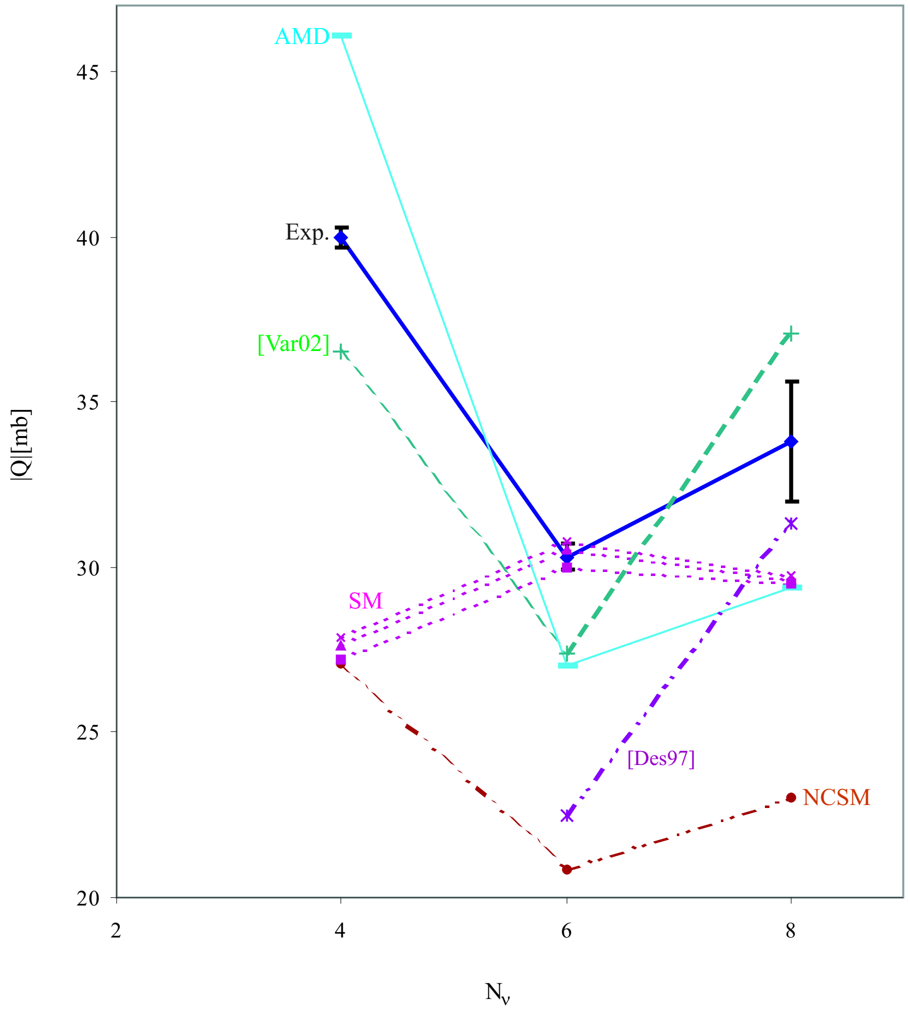

Figure 7.11: *Overview of the calculated quadrupole moments in the different models.*

the PSDMK interaction has been used to allow also np-nh excitations from the νp- to the νsd-shell. However, it turns out that the contribution of such configuration is calculated to be very small, thus giving similar quadrupole moments for both interactions. For ^{9}Li the two interactions are in agreement with the experiment.

The quadrupole moment of ^{11}Li can only be reproduced if p-h neutron excitations are allowed and if the p-sd cross-shell interaction is modified to better reproduce the spectrum of neutron-rich light nuclei (the MK3W interaction was fitted to better reproduce the spectrum of ^{16}N). Thus shell model calculations are unable to reproduce the trend in the Li-quadrupole moments using the same effective interaction. This is an indication that the assumption of a mean field is not valid for these light nuclei. However, in this region of light nuclei, shell model calculations can still be used to check the influence of the different configurations.

The no-core shell model with a realistic two-body nucleon-nucleon interaction does reproduce the trend of the quadrupole moments, but underestimates the absolute values. In this model free charges have been used.

The Cluster models of Varga et al. [Var02] and Descouvement et al. [Des97] predict a too large polarization of the core by the two halo neutrons. The quadrupole moment of ^{9}Li is underestimated in the two models. The experimental quadrupole moment of ^{11}Li lies in between the two predicted values.

The AMD-model of Kanada-En'yo reproduces the trend of the quadrupole moments quite well, but underestimates slightly the quadrupole moments of ^{9,11}Li. In this model the importance of clustering effects is shown. For ^{7}Li the wave function has to be adapted to correct for the long tail in the relative motion caused by the well developed clusters. For the other Li isotopes with weaker cluster structures, this correction is not needed.

Since none of these models are working perfectly, improvement of these models and/or calculations of nuclear moments with the models in development will be necessary in future.

Chapter 8

Conclusions

The nuclear moments of ^{8,9,11}Li were measured very precisely via β-NMR. Nuclear spin-orientation was obtained via the technique of optical pumping. The set-up was optimized, mainly by testing different crystals.

The implantation of the Li isotopes into Si allowed a determination of the magnetic moment of ^{9}Li with a factor hundred better accuracy: $\mu(^{9}\mathrm{Li}) = 3.43682(5)\mu_N$. For ^{11}Li the uncertainty on the magnetic moment is improved by a factor of seven: $\mu(^{11}\mathrm{Li}) = 3.6712(5)\mu_N$.

Both shell model calculations and more sophisticated models reproduce these magnetic moments quite well. The magnetic moments approximate the free Schmidt value at $N = 8$, indicating that the odd proton occupies mainly the $\pi p_{3/2}$ orbit and neutron excitations are mainly of E2-character. Such excitations only slightly influence the magnetic moment.

The implantation of the Li isotopes into $LiTaO_3$ and Zn allowed a determination of the quadrupole moments of ^{9,11}Li with a twice better accuracy: Q(^{9}Li)= 30.31(39)mb and Q(^{11}Li)= 33.8(1.8)mb. The ratio of the moments was deduced from the ratio of the quadrupole frequencies measured for ^{9,11}Li in Zn, giving: $\frac{Q(^{11}Li)}{Q(^{9}Li)} = 1.11(6)$.

The improvement of the accuracy on the ratio and absolute values of $Q(^{9}\mathrm{Li})$ and $Q(^{11}\mathrm{Li})$ is mainly due to the implantation in a Zn crystal, which provides a nearly perturbation-free environment for the Li-probes such that the rf-induced resonance are very narrow. The production rate of ^{11}Li however was much less than predicted because of the sintering of the target. Therefore additional beam time was asked to reduce the uncertainty with an additional factor of two. It was accepted and the experiment has been performed in May/June 2004.

The consistency of the quadrupole moment of ^{9}Li was checked by the implantation of ^{9}Li into $LiTaO_3$, Zn and $LiNbO_3$. The absolute value of the adopted quadrupole moments relies on the adopted value for $Q(^{7}\mathrm{Li})$. This reference value has changed since the first measurements on $Q(^{8,9}\mathrm{Li})$. Therefore all measured values were revised. For the measurement of the quadrupole moment of

^{11}Li, only two data sets were available. Therefore different ways of analysis were performed to check the consistency of this result.

The accuracy of the electric field gradient of Li implanted in Zn was improved by a factor of six $V_{zz} = 4.29(7)\ 10^{15}\frac{V}{cm^2}$.

The observed trend in the quadrupole moments might suggest that $N = 6$ becomes a magic number in these $Z = 3$ nuclei: the quadrupole moments of the unpair Li isotopes decrease towards ^{9}Li with six neutrons. The trend in the magnetic moments is not suggesting this. The g-factor is usually less sensitive to admixture of quadrupole correlations, which might indicate that $N = 6$ is not a new magic number, but rather the two halo neutrons polarize the core. The fact that the quadrupole moment of ^{11}Li is larger within 2σ than that of ^{9}Li also gives an indication that the two loosely bound neutrons of ^{11}Li polarize the protons in the core, i.e. that one of the halo-neutrons is situated in the $0d_{5/2}$-orbital.

None of the presented models predicts the values of the measured quadrupole moments. Nevertheless the qualitative trend as a function of the neutron number is reproduced more or less by all models except for the shell model (the no-core shell model, the cluster models and the AMD model). The fact that the trend line is not reproduced by the shell model is not surprising because it can be questioned if the assumption of a mean field is still valid for these light nuclei. The trend line is the best reproduced in the no-core shell model [Nav98]. The cluster model of Varga et al. [Var95] and the AMD model [Kan01] approximate the experimental data the best. In the AMD model the importance of clustering effects is shown. For ^{7}Li the wave function has to be adapted to correct for the long tail in the relative motion caused by the well developed clusters. For the other Li isotopes with weaker cluster structures, this correction is not needed. To explain the experimental data within the frame of shell model calculations with the PSDMK interaction, a small admixture of the $\nu(0d_{5/2})^2_{2+}$ configuration to the total wave function of the ^{11}Li ground state is necessary if one assumes that the two halo-neutrons are situated in the same orbital. This is the first experimental indication of a contribution of the $0d_{5/2}$ orbital to the wave function of the ^{11}Li ground state.

These new precise experimental data invite theoreticians to test and improve their models.

Appendix A

Calculated wave functions of ^{7,9,11}Li

In tables A.1 - A.10 an overview of the wave functions for the different shell-model calculations performed with ANTOINE [Cau99] is given. Here a ^{4}He core with 2 protons and 2 neutrons in the $0s_{1/2}$ orbital is assumed.

- **"CKI"** means that the effective CKI interaction [Coh65, Coh67] with the p-shell model space is used.
- **"PSDMK"** means that the effective PSDMK interaction with a larger p-sd shell model space is used [Pre72, Mil75, Kuo67].
- **MK3** means that the effective MK3W interaction with a coreless 0s-0p-1s0d-1p0f shell model space is used [War89, Mil75].
- **"max2"** means that only two nucleons are allowed in the sd-shell.
- **"full"** means that no restrictions are put on the number of particles in the sd-shell.
- **"2 fix"** means that 2 neutrons are blocked somewhere in the sd-shell.
- **"0 fix"** means that all neutrons are blocked in the p-shell.
- **"2 fix 1s$_{1/2}$"** means that two neutrons are blocked in the $1s_{1/2}$ orbital and the other neutrons in the p-shell.
- **"2 fix 0d$_{5/2}$"** means that two neutrons are blocked in the 0d$_{5/2}$ orbital and the other neutrons in the p-shell.
- **"2 fix 0d$_{3/2}$"** means that two neutrons are blocked in the 0d$_{3/2}$ orbital and the other neutrons in the p-shell.

The wave functions with a probability smaller than 1% are not shown.

A.1 ^{7}Li

The most probable configuration for the wave function of the ^{7}Li ground state is one with two neutrons in the $p_{3/2}$ orbital as expected. Blocking two neutrons in a specific orbital takes away all degrees of freedom.

A.2 ^{9}Li

For ^{9}Li the wave function has the largest probability to have a configuration with all neutrons in the p-shell for all calculations, except when a number of particles are blocked in the sd-shell (table A.4).

The wave function for ”PSDMK,2max” and ”PSDMK,full” doesn’t differ a lot.

A.3 ^{11}Li

For ^{11}Li the wave function has the largest probability to have a configuration with all neutrons in the p-shell for all calculations, except when a number of particles are blocked in the sd-shell (table A.8). On the other hand the wave function for ”PSDMK, 2max” and ”PSDMK, full” differ in that sense that without restrictions for 1.3% of the wave function a pair of neutrons is broken.

Table A.1: *Wave functions of* ^{7}Li *calculated with the PSDMK and CKI interactions.*

	ν					π	
P[%]	$0p_{3/2}$	$0p_{1/2}$	$0d_{5/2}$	$1s_{1/2}$	$0d_{3/2}$	$0p_{3/2}$	$0p_{1/2}$
CKI							
53.8	2	0				1	0
15.5	0	2				1	0
13.3	1	1				1	0
10.1	1	1				0	1
8.4	2	0				0	1
PSDMK, 2 max							
63.9	2	0	0	0	0	1	0
13.1	0	2	0	0	0	1	0
8.7	1	1	0	0	0	0	1
8.4	1	1	0	0	0	1	0
4.9	2	0	0	0	0	0	1
PSDMK, full							
55.4	2	0	0	0	0	1	0
12.5	0	2	0	0	0	1	0
9.7	1	1	0	0	0	1	0
8.8	1	1	0	0	0	0	1
5.7	2	0	0	0	0	0	1
1.1	1	0	1	0	0	0	1
1.0	1	0	0	0	1	1	0
PSDMK,0fix							
64.4	2	0	0	0	0	1	0
12.9	0	2	0	0	0	1	0
8.9	1	1	0	0	0	0	1
8.7	1	1	0	0	0	1	0
5.1	2	0	0	0	0	0	1
PSDMK,2fix							
85.3	0	0	0	2	0	1	0
4.2	0	0	2	0	0	1	0
3.7	0	0	1	1	0	0	1
3.6	0	0	1	1	0	1	0
1.3	0	0	0	0	2	1	0
PSDMK, 2 fix $1s_{1/2}$							
100	0	0	0	2	0	1	0
PSDMK, 2 fix $0d_{5/2}$							
100	0	0	2	0	0	1	0
PSDMK, 2 fix $0d_{3/2}$							
100	0	0	0	0	2	1	0

Table A.2: *Wave functions of* ^{7}Li *calculated with the MK3W interaction, allowing maximum two neutrons in the sd-shell and no in the pf-shell. In the unmentioned orbitals of the sd-shell no nucleons are present.*

	ν				π		
P[%]	$0s_{1/2}$	$0p_{3/2}$	$0p_{1/2}$	$1s_{1/2}$	$0s_{1/2}$	$0p_{3/2}$	$0p_{1/2}$
43	2	2	0	0	2	1	0
15.3	2	0	2	0	2	1	0
10.6	2	1	1	0	2	0	1
9.8	2	1	1	0	2	1	0
5.5	2	2	0	0	2	0	1
4.3	1	2	0	1	2	1	0
1.2	1	0	2	1	2	1	0

Table A.3: *Wave function of* ^{9}Li *calculated with the CKI interaction.*

	ν		π	
P[%]	$0p_{3/2}$	$0p_{1/2}$	$0p_{3/2}$	$0p_{1/2}$
58.6	4	0	1	0
27	2	2	1	0
11.5	3	1	1	0
2.6	3	1	0	1

Table A.4: *Wave functions of* ^{9}*Li calculated with the PSDMK interaction.*

	ν					π	
P[%]	$0p_{3/2}$	$0p_{1/2}$	$0d_{5/2}$	$1s_{1/2}$	$0d_{3/2}$	$0p_{3/2}$	$0p_{1/2}$
PSDMK, 2 max							
49.7	4	0	0	0	0	1	0
36.3	2	2	0	0	0	1	0
7.3	3	1	0	0	0	1	0
2.8	3	1	0	0	0	0	1
1.6	2	0	2	0	0	1	0
PSDMK, full							
43.9	4	0	0	0	0	1	0
34.4	2	2	0	0	0	1	0
8.2	3	1	0	0	0	1	0
2.8	3	1	0	0	0	0	1
2.0	2	0	2	0	0	1	0
PSDMK,0fix							
52.2	4	0	0	0	0	1	0
36.5	2	2	0	0	0	1	0
8	3	1	0	0	0	1	0
2.9	3	1	0	0	0	0	1
PSDMK,2fix							
52.9	2	0	0	2	0	1	0
8.7	0	2	0	2	0	1	0
6.4	1	1	0	2	0	1	0
6.2	1	1	0	2	0	0	1
4.9	2	0	1	1	0	1	0
4.1	2	0	2	0	0	1	0
3.9	2	0	0	2	0	0	1
2.7	1	1	1	1	0	1	0
2.4	2	0	1	1	0	0	1

Table A.5: *Wave functions of* ^{9}Li *calculated with the PSDMK interaction and two neutrons fixed in a specific orbital of the sd-shell.*

P[%]	ν					π	
	$0p_{3/2}$	$0p_{1/2}$	$0d_{5/2}$	$1s_{1/2}$	$0d_{3/2}$	$0p_{3/2}$	$0p_{1/2}$
PSDMK, 2 fix $1s_{1/2}$							
68	2	0	0	2	0	1	0
11	0	2	0	2	0	1	0
8	1	1	0	2	0	1	0
8	1	1	0	2	0	0	1
5	2	0	0	2	0	0	1
PSDMK, 2 fix $0d_{5/2}$							
57	2	0	2	0	0	1	0
12	0	2	2	0	0	1	0
12	1	1	2	0	0	1	0
8.7	1	1	2	0	0	0	1
8	2	0	2	0	0	0	1
1.3	0	2	2	0	0	0	1
PSDMK, 2 fix $0d_{3/2}$							
65	2	0	0	2	0	1	0
11	0	2	0	2	0	1	0
9	1	1	0	2	0	1	0
7.7	1	1	0	2	0	0	1
6.3	2	0	0	2	0	0	1

Table A.6: *Wave functions of* ^{9}Li *calculated with the MK3W interaction, allowing maximum two neutrons in the sd-shell and no in the pf-shell. In the unmentioned orbitals of the sd-shell no nucleons are present.*

P[%]	ν				π		
	$0s_{1/2}$	$0p_{3/2}$	$0p_{1/2}$	$1s_{1/2}$	$0s_{1/2}$	$0p_{3/2}$	$0p_{1/2}$
40.7	2	2	2	0	2	1	0
33.6	2	4	0	0	2	1	0
7	2	3	1	0	2	1	0
3.2	1	4	0	1	2	1	0
3	1	2	2	1	2	1	0
2.5	2	3	1	0	2	0	1

Table A.7: *Wave function of* ^{11}Li *calculated with the CKI interaction.*

P[%]	ν		π	
	$0p_{3/2}$	$0p_{1/2}$	$0p_{3/2}$	$0p_{1/2}$
100	4	2	1	0

Table A.8: *Wave functions of ^{11}Li calculated with the PSDMK interaction.*

P[%]	ν $0p_{3/2}$	$0p_{1/2}$	$0d_{5/2}$	$1s_{1/2}$	$0d_{3/2}$	π $0p_{3/2}$	$0p_{1/2}$	$0d_{5/2}$
PSDMK, 2 max								
91.8	4	2	0	0	0	1	0	0
2.2	4	0	2	0	0	1	0	0
2.1	2	2	2	0	0	1	0	0
PSDMK, full								
83.8	4	2	0	0	0	1	0	0
2.4	2	2	2	0	0	1	0	0
2.3	4	0	2	0	0	1	0	0
1.0	2	2	0	0	2	1	0	0
1.3	4	0	1	1	0	1	0	0
PSDMK,0fix								
100	4	2	0	0	0	1	0	0
PSDMK,2fix								
47.6	4	0	0	2	0	1	0	0
24.8	2	2	0	2	0	1	0	0
6.8	3	1	0	2	0	1	0	0
2.4	3	1	0	2	0	0	1	0
3.4	4	0	2	0	0	1	0	0
2.9	4	0	1	1	0	1	0	0
2.2	2	2	2	0	0	1	0	0
2	3	1	1	1	0	1	0	0
1.8	2	2	1	1	0	1	0	0
1.3	4	0	1	1	0	0	1	0

Table A.9: *Wavefunctions of ^{11}Li calculated with the PSDMK interaction and two neutrons fixed in a specific orbital of the sd-shell.*

P[%]	ν $0p_{3/2}$	$0p_{1/2}$	$0d_{5/2}$	$1s_{1/2}$	$0d_{3/2}$	π $0p_{3/2}$	$0p_{1/2}$
PSDMK, 2 fix 1s$_{1/2}$							
58.3	4	0	0	2	0	1	0
30.6	2	2	0	2	0	1	0
8	3	1	0	2	0	1	0
2.9	3	1	0	2	0	0	1
PSDMK, 2 fix 0d$_{5/2}$							
46	4	0	2	0	0	1	0
35	2	2	2	0	0	1	0
13	3	1	2	0	0	1	0
2.4	3	1	2	0	0	0	1
1.4	2	2	2	0	0	0	1
1.4	4	0	2	0	0	0	1
PSDMK, 2 fix 0d$_{3/2}$							
56.2	4	0	0	0	2	1	0
30.8	2	2	0	0	2	1	0
8	3	1	0	0	2	1	0
3	3	1	0	0	2	0	1

Table A.10: *Wave functions of ^{11}Li calculated with the MK3W interaction, allowing maximum two neutrons in the sd-shell and no in the pf-shell. In the unmentioned orbitals of the sd-shell no nucleons are present.*

	ν					π		
P[%]	$0s_{1/2}$	$0p_{3/2}$	$0p_{1/2}$	$0d_{5/2}$	$1s_{1/2}$	$0s_{1/2}$	$0p_{3/2}$	$0p_{1/2}$
81.5	2	4	2	0	0	2	1	0
6	1	4	2	0	1	2	1	0
1.5	2	3	2	1	0	1	1	1
1.1	2	3	2	1	0	1	2	0

Appendix B

Nederlandse samenvatting

Eén van de sleutelactiviteiten in de hedendaagse kernfysica is de studie van exotische kernen. Dit zijn kernen met extreme eigenschappen zoals een extreme verhouding van het aantal neutronen tot het aantal protonen, extreme excitatie-energie of extreme totale spin. De studie van neutronrijke[1] kernen onthulde onverwachte fenomenen zoals de vorming van neutronhalos[2] en de geleidelijke verdwijning van schillensluitingen[3]. Deze verschijnselen tonen dat de kracht tussen de nucleonen - de sterke kracht - nog niet voldoende begrepen is. In het bijzonder is de invloed van de extreme voorwaarden op de spinbaankoppelingsterm onvoldoende begrepen. Dankzij deze term zijn de magische getallen tot stand gekomen in het schillenmodel [May49]. De parametrizaties van de bestaande kernmodellen zoals het schillenmodel [May49] moesten dus worden aangepast en nieuwe modellen werden ontwikkeld.

Het magnetische en het quadrupoolmoment van exotische kernen zijn grondige tests voor de nieuwe kernmodellen. Bovendien bevatten ze veel informatie over de structuur van deze kernen: het magnetische dipoolmoment is gevoelig aan de orbitalen van de ongepaarde nucleonen. Het elektrische quadrupoolmoment bevat informatie over de vervorming van de ladingsverdeling van de kern.

Deze verhandeling beschrijft een precisiemeting van de kernmomenten van de grondtoestanden van de neutronrijke ^{9}Li en ^{11}Li kernen. Deze kernen zijn om twee redenen interessant:

- ^{11}Li is een van de meest bestudeerde voorbeelden van een neutronhalo

---

[1] Neutronrijke kernen zijn kernen waarbij de verhouding van het aantal neutronen tot het aantal protonen veel groter is dan bij stabiele kernen.

[2] Een neutronhalokern is een kern met enkele zeer zwak gebonden neutronen. Dit zorgt voor een zeer uitgestrekte massastraal.

[3] Kernen waarvan de nucleonen een volledige schil vullen zijn veel stabieler dan andere kernen. Althans, dit is het geval voor kernen dicht bij de stabiliteitslijn. Wanneer men verder van deze stabiliteitslijn gaat, blijkt dit niet altijd het geval meer te zijn. Het aantal nucleonen nodig om een volledige schil te vullen wordt een "magisch getal"genoemd.

kern, bestaande uit een ^{9}Li pit (Eng.: core) met twee zeer zwakgebonden neutronen. Nochtans blijven er heel wat vragen onopgelost, zoals de invloed van de twee zwakgebonden neutronen op de ladingsverdeling van de pit. De bestaande experimentele gegevens duiden op een ontkoppelde pit en twee neutronen. Een voorbeeld van zulke experimentele gegevens bestaat uit de bijna constante werkzame doorsnedes (Eng.: cross sections) van ^{7}Li tot ^{11}Li voor ladingsveranderende processen [Bla92, Tan96]. Dit zijn processen die een verandering van het aantal protonen van het projectiel tot gevolg heeft. Deze werkzame doorsnede is een maat voor de protonstraal. Het feit dat deze werkzame doorsneden ongeveer constant blijven voor de Li-isotopen, wijst op een bijna constante protonstraal in functie van het aantal neutronen. Dit wijst op een quasi afwezige invloed van de extra neutronen op de protonverdeling. Binnen de foutenmarge is er echter wel een toename van de protonstraal mogelijk. Anderzijds voorpelde T. Misu et al. [Mis97] dat voor bindingsenergieën gaande naar 0 en voor een tweedelige halo de vervorming van een systeem bepaald kan worden door de valentiedeeltjes, onafhankelijk van de deformatie van de pit. Als dit doorgetrokken kan worden naar een driedelige halo zoals ^{11}Li, zal het quadrupoolmoment van ^{11}Li verschillen van dat van ^{9}Li. Een nauwkeurige bepaling van de verhouding van beide quadrupoolmomenten $\frac{Q(^{11}Li)}{Q(^{9}Li)}$ zal een verduidelijking brengen in de polarizatie van de ^{9}Li romp die de halo-neutronen teweeg brengen.

- ^{11}Li heeft juist acht neutronen, wat een magisch getal is. Kort bij de stabiliteitslijn zou dit een gevulde schil van neutronen betekenen. De vraag is of deze schillensluiting behouden blijft zo dicht bij de neutrondruppellijn[4]. Voor de $_{4}$Be-isotopen met vier protonen zijn aanwijzingen gevonden dat deze schillensluiting verdwijnt. Zo werd er voor de spin en pariteit van de grondtoestand van $^{11}_{4}$Be$_{7}$ $I^{\pi} = \frac{1}{2}^{+}$ gevonden in plaats van de verwachte $I^{\pi} = \frac{1}{2}^{-}$ [Mil83] met het ongepaarde neutron in het $0p_{1/2}$-orbitaal. Er zijn twee mogelijke configuraties voor deze spin en pariteit: een ongepaard neutron in het $1s_{1/2}$-orbitaal of een ongepaard neutron in het $0d_{5/2}$-orbitaal dat koppelt met een aangeslagen $(^{10}\mathrm{Be})^{2+}$ pit (Eng.:core) (fig. 2.5). Beide mogelijkheden wijzen echter op een configuratie waarbij het ongepaarde neutron zich in de $1s0d$-schil bevindt in plaats van in de $0p$-schil. Dit is een indicatie dat de energiekloof (Eng.: energy gap) tussen beide schillen afneemt voor neutronrijke kernen voor $Z = 4$. In $^{12}_{4}$Be$_{8}$ werden laagliggende aangeslagen toestanden met $I^{\pi} = 0^{+}$ en $I^{\pi} = 1^{-}$ gevonden [Shi03, Iwa00]. Normaal verwacht men dat de aangeslagen toestanden voor een kern met een magisch aantal neutronen allen zeer hoog in energie liggen. Laagliggende toestanden wijzen dus op iets onverwacht. Dit geval werd verklaard door het verdwijnen van de energiekloof tussen de $0p_{1/2}$ en de $1s_{1/2}$-orbitalen [Shi03].

  In het β-verval van ^{11}Li [Suz94, Bor97, Aoi97, Ots95] werden er onver-

---

[4] De druppellijn is de grens van gebonden kernen op de kernkaart.

wacht grote logft-waarden[5] gevonden. Dit kan enkel worden verklaard als de sd-schil ook bijdraagt tot de golffunctie van ^{11}Li [Ots95]. Recent werd er ook een directe experimentele aanwijzing gevonden voor een bijdrage van configuraties met nucleonen in de sd-schil tot de totale golffunctie van de grondtoestand van ^{11}Li. De longitudinale momentumverdeling van ^{10}Li fragmenten, gevormd uit de fragmentatie van ^{11}Li en een koolstoftrefschijf, werd opgemeten [Sim99]. Uit de vorm van de verdeling werd bepaald dat de bijdrage van $\nu 1s^2_{1/2}$ component in de golffunctie van de grondtoestand $45 \pm 10\%$ is. Hierin werd enkel de $\nu 1s_{1/2}$ en $\nu 0p_{1/2}$ orbitalen in rekening gebracht. Het $0d_{5/2}$ orbitaal werd buiten beschouwing gelaten.

Wanneer de $N = 8$ schillensluiting behouden blijft voor de neutronrijke kern $^{11}_{3}$Li$_8$, zal zijn quadrupoolmoment kleiner zijn dan dat van ^{9}Li. Wanneer er een opmenging van indringtoestanden (Eng.:intruder states)[6] optreedt in de grondtoestand van ^{11}Li, is dit niet noodzakelijk meer. Wanneer een van de opmengende indringtoestanden minstens een neutron in het $0d_{5/2}$- orbitaal heeft, kan het quadrupoolmoment van ^{11}Li groter zijn dan dat van ^{9}Li. Een precieze meting van het quadrupoolmoment van ^{11}Li kan een indicatie geven over de eventuele menging van indringtoestanden met een halo neutron in het $0d_{5/2}$-orbitaal en normale toestanden in de golffunctie van de ^{11}Li-grondtoestand.

De kernmomenten van ^{9,11}Li werden opgemeten met de β-NMR/NQR (Nucleaire Magnetische Resonantie/ Nucleaire Quadrupool Resonantie) techniek [Mat71] aan de ISOLDE faciliteiten in CERN[7]. De vereiste initiële spinoriëntatie werd geproduceerd met de techniek van optisch pompen[8] [Coh66]. Deze techniek is uiterst geschikt voor alkalimetalen zoals Li. Deze kernmomenten werden opgemeten in samenwerking met de COLLAPS-groep van Mainz (Duitsland), geleid door Prof. Dr. R. Neugart. Deze groep had de kernmomenten van ^{9,11}Li al opgemeten, gebruikmakend van de ISOLDE-faciliteiten in CERN en de techniek van optisch pompen. De nauwkeurigheid was echter niet goed genoeg om iets te besluiten over de invloed van de twee zwakgebonden neutronen op de pit van de kern. Daarom werd nu een precisiemeting uitgevoerd met een geoptimaliseerde versie van diezelfde set-up. Dit garandeerde het optimaal gebruik van de bestaande expertise.

Het nauwkeurig opmeten van quadrupoolmomenten met de multiple-rf-NQR-techniek [Arn92] vereist een nauwkeurige kennis van de magnetische momenten. Daarom werden ook de magnetische momenten heropgemeten.

---

[5] De logft waarde is een maat voor de sterkte van de overgang. Kleine logft-waarden wijzen op een sterke overgang. Grote logft-waarden wijzen op vertraagd verval waarbij de matrixelementen voor de overgang klein zijn.

[6] Voor kernen met $N < 8$ zijn indringtoestanden configuraties met neutronen in een van de orbitalen uit de sd-schil.

[7] Conseil Européen pour la Recherche Nucléaire [CERN].

[8] Bij de techniek van optisch pompen, maakt men gebruik van atomaire overgangen, geïnduceerd door circulair gepolariseerd laserlicht om de atomaire spins te polarizeren. Deze oriëntatie wordt overgebracht naar de kernspins via de hyperfijnkrachten.

Het optimaliseren van de experimentele opstelling gebeurde voornamelijk door het testen van verschillende implantatiekristallen. Deze testen gebeurde met ^{8}Li kernen die veelvuldig aangemaakt worden. Ook de calibratie van het magneetveld gebeurde met ^{8}Li kernen waarvan de g-factor bekend is.

De implantatie van de Li-isotopen in Si maakte een honderd keer nauwkeurigere bepaling van het magnetisch moment van ^{9}Li mogelijk: $\mu(^{9}\mathrm{Li}) = 3.43682(5)\mu_N$. Voor $\mu(^{11}\mathrm{Li})$ werd de foutenmarge met een factor zeven gereduceerd: $\mu(^{11}\mathrm{Li}) = 3.6712(5)\mu_N$. Deze magnetische momenten zijn gecorrigeerd voor de diamagnetische afscherming (Eng.: diamagnetic shielding). Zowel schillenmodelberekeningen als meer gesofisticeerde modellen voorspellen deze magnetische momenten vrij goed. De magnetische momenten van de Li-isotopen gaan naar de Schmidt-waarde toe wanneer het aantal neutronen het magisch getal acht benadert. Dit duidt aan dat het oneven proton hoofdzakelijk het $\pi 0p_{3/2}$ orbitaal bevolkt en dat de neutron excitaties hoofzakelijk een E2 karakter hebben, aangezien deze het magnetisch moment nauwelijks beïnvloeden.

De implantatie van de Li-isotopen in LiTaO$_3$ en Zn zorgde voor quadrupoolmomenten van ^{9,11}Li met een twee keer kleinere foutenmarge: $Q(^{9}\mathrm{Li}) = 30.31(39)$mb en $Q(^{11}\mathrm{Li}) = 33.8(1.8)$mb. Dit geeft een verhouding $\frac{Q(^{9}Li)}{Q(^{11}Li)} = 1.11(6)$.

De consistentie van het quadrupoolmoment van ^{9}Li werd nagegaan door verschillende metingen met implantatie in verschillende kristallen LiTaO$_3$, Zn en LiNbO$_3$. De absolute waarde van de aangenomen quadrupoolmomenten steunt op de aangenomen waarde van $Q(^{7}\mathrm{Li})$. Deze referentiewaarde is veranderd sinds de eerste metingen van de quadrupoolmomenten $Q(^{8,9}\mathrm{Li})$ [Pyy01]. Daarom werden alle vroeger gemeten waarden aangepast.
Er werden slechts twee metingen uitgevoerd voor het quadrupoolmoment van ^{11}Li. Daarom werden er verschillende analyses uitgevoerd om de consistentie van het resultaat na te gaan.

Verder werd de foutenmarge van de elektrische veldgradiënt van Li geïmplanteerd in Zn, gereduceerd met een factor zes: $V_{zz} = 4.29(7)10^{15}\frac{V}{cm^2}$.

De experimentele gegevens zouden een aanwijzing kunnen geven dat $N = 6$ een magische schillensluiting is. De quadrupoolmomenten van de oneven Li-isotopen verkleinen immers bij het naderen van ^{9}Li met zes neutronen, zowel gaande van ^{7}Li naar ^{9}Li als van ^{11}Li naar ^{9}Li (dit laatste is wel slechts een 2σ-effect). Aan de andere kant suggereert de trend in de magnetische momenten dit helemaal niet.
De verhouding $\frac{Q(^{9}Li)}{Q(^{11}Li)} = 1.11(6)$ geeft aan dat met ongeveer 95% kans de twee zwak gebonden neutronen van ^{11}Li de protonen in de pit beïnvloeden, en dus dat minstens één van de haloneutronen zich in het $0d_{5/2}$ orbitaal bevindt. Dit is de eerste experimentele aanwijzing voor een bijdrage van het $0d_{5/2}$ orbitaal

aan de golffunctie van de ^{11}Li grondtoestand.

Geen van de huidige modellen voorspelt de quadrupoolmomenten correct. Toch wordt de kwalitatieve trend in functie van het neutronenaantal vrij goed voorspeld door de meeste modellen. Het schillenmodel is hierin de grote uitzondering. Dit is geen verrassing, aangezien de geldigheid van de aanname van een gemiddeld interactieveld (Eng.: mean field) dat alle kernen voelen voor zulke lichte kernen in vraag gesteld kan worden. De trendlijn wordt het beste voorspeld door een uitbreiding van het schillenmodel waarin alle nucleonen in rekening gebracht worden zonder een deel van de nucleonen te bevriezen (Eng.: no-core shell model) [Nav98]. Het clustermodel van Varga et al. [Var95] en het geantisymmetriseerde moleculaire dynamica (Eng.: Antisymmetrized Molecular Dynamics) AMD-model [Kan01] benaderen de experimentele gegevens het best. In een clustermodel worden de ^{7}Li kernen aanzien als bestaande uit twee subdelen, clusters, een α (twee neutronen en twee protonen) en een triton ^{3}H. Voor ^{9}Li en ^{11}Li zijn de bijkomende neutronen allemaal extra afzonderlijke subdelen. In het AMD-model worden er geen veronderstellingen over een bevroren pit (zoals in het schillenmodel) of over subdelen gemaakt. Alle configuraties toegelaten door het Pauli-principe worden in rekening gebracht. Voor het reproduceren van het quadrupoolmoment van ^{7}Li bleek het echter noodzakelijk om in de golffuctie correcties aan te brengen voor de bestaande clustereffecten. Voor de andere Li isotopen bleek deze correctie niet nodig.
Om het geobserveerde quadrupoolmoment van ^{11}Li te verklaren met behulp van het schillenmodel met de effectieve PSDMK-interactie, is een bijdrage van de $\nu(0d_{5/2})^2_{2+}$ configuratie in de gemengde totale golffunctie van de ^{11}Li grondtoestand noodzakelijk wanneer we veronderstellen dat beide haloneutronen zich in hetzelfde orbitaal bevinden.

Bibliography

[Abr67] S.C. Abrahams, W.C. Hamilton, A. Sequeira, J. Phys. Chem. Solids **28** (1967) 1693.

[Ack74] H. Ackermann, D. Dubbers, M. Grupp, P. Heitjans, H.-J. Stöckmann, Phys. Lett. **B52** (1974) 54.

[Ack83] H. Ackermann, P. Heitjans, H.-J. Stöckmann in Hyperfine Interactions of Radioactive Nuclei, Topics in Current Physics 31, Edt. J. Christiansen, Springer-Verlag, Berlin, Heidelberg, New York, Tokyo (1983).

[Ajz88] F. Ajzenberg-Selove, Nucl. Phys. **A490** (1988) 1.

[And80] T. Ando, K. Ikeda, A. Toshaki, Prog. Theor. Phys. **64** (1980) 1608.

[Ann90] R. Anne, S.E. Arnell, R. Bimbot, H. Emling, D. Guillemaud-Mueller, P.G. Hansen, L. Johannsen, B. Jonson, M. Lewitowicz, S. Mattson, A.C. Mueller, R. Neugart, G. Nyman, F. Pougheon, A. Richter, K. Riisager, M.G. Sain-Laurent, G. Schrieder, O. Sorlin, K. Wilhelmsen, Phys. Lett. **B250**(1990) 19.

[Aoi97] N. Aoi, K. Yoneda, H. Miyatake, H. Ogawa, Y. Yamamoto, E. Ideguchi, T. Kishida, T. Nakamura, M. Notani, H. Sakurai, T. Teranishi, H. Wu, S.S. Yamamoto, Y. Watanabe, A. Yoshida, M. Ishihara, Nucl. Phys. **A616** (1997) 181.

[Arn86] E. Arnold, ”Experimmente an on-line polarisierten kurzlebigen Lithium Isotopen”, PhD. thesis, Johannes Gutenber-Universität, Mainz (1986), unpublished, p. 56.

[Arn87] E. Arnold, J. Bonn, R. Gegenwart, W. Neu, R. Neugart, E.-W. Otten, G. Ulm, K. Wendt, Phys. Lett. **B197** (1987) 311.

[Arn88] E. Arnold, J. Bonn, W. Neu, R. Neugart, E.W. Otten, ISOLDE collaboration, Z. Phys. **A331** (1988) 295.

[Arn92] E. Arnold, J. Bonn, A. Klein, R. Neugart, M. Neuroth, E.W. Otten, P. Lievens, H. Reich, W. Widdra, Phys. Lett. **B281** (1992) 16.

[Aud95] G. Audi, A.H. Wapstra, Nucl. Phys. **A595** (1995) 409-480.

[Aum00] T. Aumann, A. Navin, D.P. Balamuth, D. Bazin, B. Blank, B.A. Brown, J.E. Bush, J.A. Caggiano, B. Davids, T. Glasmacher, V. Guimaraes, P.G. Hansen, R.W. Ibbotson, D. Karnes, J.J. Kolata, V. Maddalena, B. Pritychenko, H. Scheit, B.M. Sherrill, J.A. Tostevin, Phys. Rev. Lett. **84** (2000) 35.

[Bal82] J.L. Ballot, M. Fabre de la Ripelle, J.S. Levinger, Phys. Rev. **C26** (1982) 2301.

[Bar77] F.C. Barker, G.T. Hickey, J. Phys. **G3** (1977) L23.

[Bar02] B.R. Barrett, P. Navratil, J.P. Vary, Nucl. Phys. **A704** (2002) 254c.

[Ben02] J.R.J. Bennett, U.C. Bergmann, P.V. Drumm, J. Lettry, T. Nilsson, R. Catheral, O.C. Johnson, H.L. Ravn, H. Simon, Isolde collaboration, Nucl. Phys. **A701** (2002) 327c.

[Ber65] R. Bernheim, "Optical pumping: an introduction", Benjamin New York (1965).

[Bjo81] T. Björnstad, H.A. Gustafsson, P.G. Hansen, B. Jonson, V. Lindfors, S. Mattsson, A.M. Poskanzer, H.L. Ravn, Nucl. Phys. **A359** (1984) 1.

[Bla92] B. Blank, J.-J. Gaimard, H. Geissel, K.H. Schmidt, H. Stelzer, K. Sümmerer, D. Bazin, R. Del Moral, J.P. Dufour, S. Fleury, F. Hubert, H.G. Clerc, M. Steiner, Z. Phys. **A343** (1992) 375.

[Blo77] J. Blocki, J. Randrup, W.J. Swiatecki, C.F. Tsang, Ann. Phys. **105** (1977) 427.

[bnl] http://www2.bnl.gov/ton/

[Boh69] A. Bohr, B.R. Mottelson, "Nuclear Structure" Volume 1 (Benjamin New York, 1969)

[Boh75] A. Bohr, B.R. Mottelson, "Nuclear Deformation" (Benjamin New York, 1975)

[Boh93] H.G. Bohlen, B. Gebauer, M. von Lucke-Petsch, W. von Oertzen, A.N. Ostrowski, M. Wilpert, H. Lenske, D.V. Alexandrov, A.S. Demyanova, E. Nikolskii, A.A. Korsheninnikov, A.A. Ogloblin, R. Kalpakchieva, Y.E. Penionzhkevich, S. Piskor, Z. Phys. **A344** (1993) 381.

[Bor97] M.J.G. Borge, L. Grigorenko, D. Guillemaud-Mueller, P. Hornshoj, F. Humbert, B. Jonson, T.E. Leth, G. Martinez Pinedo, I. Mukha, T. Nilsson, G. Nyman, K. Riisager, G. Schrieder, M.H. Smedberg, O. Tengblad, M.V. Zhukov, ISOLDE collaboration, Nucl. Phys. **A613** (1997) 199.

[Bor99] D. Borremans, ”Fotonaangeklede kerntoestanden in een toestandsmengingsinteractie”, diploma thesis KULeuven (1999), unpublished

[Bra00] B.H. Bransden, C.J. Joachain, ”Quantum Mechanics”, Second edition, Pearson Education, Prentice Hall, London (2000) p. 170-182.

[Bro88] B.A. Brown, Ann. Rev. Nucl. Part. Sci **38** (1988) 29.

[Bul72] M.I. Bulgakov, A.D. Gul’ko, Yu.A. Oratovskii, B.B. Trostin, Sov. Phys. JETP **34** (1972) 356.

[Cau99] E. Caurier, F. Nowacki, Acta Physica Polonica **30** (1999) 705.

[CERN] http://user.web.cern.ch/user/cern.html

[Cha90] S.K. Charagi, S.K. Gupta, Phys. Rev. **C41** (1990) 1610.

[Cha99] E.V. Charnaya, V.S. Kasperovich, M.N. Palatnikov, M.G. Shelyapina, C. Tien, C.S. Wur, Ferrorelectrics **234** (1999) 223.

[Chu00] L.V. Chulkov, O.V. Bochkarev, D. Cortina-Gil, H. Geissel, M. Hellström, M. Ivanov, R. Janik, K. Kimura, T. Kobayashi, A.A. Korsheninnikov, G. Münzenberg, F. Nickel, A.A. Ogloblin, A. Ozawa, M. Pfützner, V.N. Pribora, M.V. Rozhkov, H. Simon, B. Sitar, P. Strömen, K. Sümmerer, T. Suzuki, I. Tanihata, M. Winkler, K. Yoshida, Nucl. Phys. **A674** (2000) 330.

[Cit77] M.L. Citron, H.R. Gray, W. Gabel, C.R. Stroud Jr., Phys. Rev. **A16** (1977) 1507.

[Cli70] D. Cline, P.M.S. Lesser, Nucl. Instr. Meth. **82** (1970) 291.

[Coh66] C. Cohen-Tannoudji, A. Kastler, ”Optical Pumping” in ”Progress in Optics” (North-Holland), ed. by E. Wolf, Vol. V (1966) 1.

[Coh57] M.H. Cohen, F. Reif, Sol. Stat. Phys. **5** (1957) 321.

[Coh65] S. Cohen, D. Kurath, Nucl. Phys. **A73** (1965) 1.

[Coh67] S. Cohen, D. Kurath, Nucl. Phys. **A101**(1967) 1.

[Collaps] http://is389-proj-collaps.web.cern.ch/is389-proj-collaps/

[Con59] D. Connor, Phys. Rev. Lett. **3** (1959) 429.

[Con62] D. Connor, T. Tsang, Phys. Rev. **126** (1962) 1506.

[Cor78] F.D. Correll, Hyp. Int. **4** (1978) 544 +[Has73a, Tan77].

[Cor83] F.D. Correll, L. Madansky, R.A. Hardekopf, J.W. Sunier, Phys. Rev. **C 28** (1983) 862.

[Cot02] S. Cottenier, Hyperfine Interactions, course 2^nd licentie, not published.

[CRC77] CRC Handbook of Chemistry and Physics, "A ready-reference book of chemical and physical data", 58th edition (1977-1978), edited by R.C. Weast

[Cou01] N. Coulier, G. Neyens, D.L. Balabanski, D. Borremans, R. Coussement, J.M. Daugas, G. Georgiev, S. Teughels, K. Vyvey, Phys. Rev.**C 63** (2001) 054605.

[Cug97] J. Cugnon, C. Volant, S. Vuillier, Nucl. Phys. **A620** (1997) 475.

[Des63] A. Deshalit, I. Talmi, "Nuclear Shell Theory" (1963)Academic, New York

[Des97] P. Descouvement, Nucl. Phys. **A626** (1997) 647.

[Dlo02] Z. Dlouhy, J.C. Angelique, R. Anne, G. Auger, D. Baiborodin, C. Borcea, E. Caurier, A. Gillibert, S. Grevy, D. Guillemaud-Mueller, A.S. Lalleman, M. Lewitowicz, S.M. Lukyanov, W. Mittig, J. Mrazek, A.C. Mueller, F. Nowacki, F. de Oliveira, N. Orr, R.D. Page, Yu.E. Penionzhkevich, F. Pougheon, A.T. Reed, Z. Ren, D. Ridikas, P. Roussel-Chomaz, M.G. Saint-Laurent, H. Sakurai, F. Sarazin, H. Savajols, O. Sorlin, O. Tarasov, A. de Vismes, J. Winfield, Nucl. Phys. **A701** (2002) 189c.

[Doc74] K.K. Docken, R.R. Freeman, J. Chem. Phys. **61** (1974) 4217.

[Dub77] D. Dubbers, K. Dörr, H. Ackermann, F. Fujara, H. Grupp, M. Grupp, P. Heitjans, A. Körblein, H.-J. Stöckmann, Z. Physik **A282** (1977) 243.

[End90] P.M. Endt, Nucl. Phys **A521** (1990) 1.

[Ewa04] G. Ewald, W. Nörtershauser, A. Dax, S. Götte, R. Kirchner, H.-J. Kluge, Th. Kühl, R. Sanchez, A. Wojtaszek, B.A. Bushaw, G.W.F. Drake, Z.-C. Yan, C. Zimmermann, submitted to PRL (2004)

[Fed79] P. Federman, S. Pittel, R. Campos, Phys. Lett. **B82** (1979) 9.

[Fei69] F.D. Feiock, W.R. Johnson, Phys. Rev. **187** (1969) 39.

[fer03] http://cst-www.nrl.navy.mil/lattice/struk/LiNbO3f.html

[Fir96] R.B. Firestone, "Table of Isotopes", volume eight edition, John Wiley and Sons, New York, Eds:V.S.Shirley, (1996)

[Fis63] T.R. Fisher, Phys. Rev. **130** (1963) 2388.

[For99] S. Fortier, S. Pita, J.S. Winfield, W.N. Catford, N.A. Orr, J. Van de Wiele, Y. Blumenfeld, R. Chapman, S.P.G. Chappell, N.M. Clarke, N. Curtis, M. Freer, S. Galès, K.L. Jones, H. Langevin-Joliot, H. Laurent, I. Lhenry, J.M. Maison, P. Roussel-Chomaz, M. Shawcross, M. Smith, K. Spohr, T. Suomijarvi, A. de Vismes, Phys. Lett. **B461** (1999) 22.

[geant] GEANT Detector Description and Simulation Tool, http://wwwinfo.cern.ch/asdoc/ geantold/geantmain.html.

[Gei99] W. Geithner, S. Kappertz, M. Keim, P. Lievens, R. Neugart, L. Vermeeren, S. Wilbert, V.N. Fedoseyev, U. Köster, V.I. Mishin, V. Sebastian, Phys. Rev. Lett. **83** (1999) 3792.

[Gei02] W. Geithner, "Nuclear Moments and Differences in Mean Square Charge Radii of Short-Lived Neon Isotopes by Collinear Laser Spectroscopy", PhD thesis Johannes Gutenberg Institut, Mainz (2002), unpublished.

[Gup99] R.K. Gupta, W. Greiner, Heavy Elements and Related New Phenomena, Singapore: World Scinetific, (1999) 397.

[Gup00] R.K. Gupta, M. Balasubramaniam, R.K. Puri, W. Scheid, J. Phys. **G26** (2000) L23.

[Gup02] R.K. Gupta, S. Kumar, M. Balasubramaniam, G. Münzenberg, W. Scheid, J. Phys. **G28** (2002) 699.

[Hal70] T.K. Halstead, The Journal of Chemical Physics **53**,9 (1970) 3427.

[Han87] P.G. Hansen, B. Jonson, Europhys. Lett. **4** (1987) 409.

[Has73] R.C. Haskell, L. Madansky, Phys. Rev. **C7** (1973) 1277.

[Has73a] R.C. Haskell, L. Madansky, J. Phys. Soc. Japan, **34, suppl.** (1973) 167.

[Hey94] K.L.G. Heyde, "The Nuclear Shell Model", Springer-Verlag, Berlin, Second Edition.

[Ike80] K. Ikeda, H. Horiuchi, S. Saito, Y. Fjuiwara, M. Kamimura, K. Kato, Y. Suzuki, E. Uegaki, H. Furutani, H. Kanada, T. Kaneko, S. Nagata, H. Nishioka, S. Okabe, T. Sakuda, M. Seya, Y. Abe, Y. Kondo, T. Matsuse, A. Tohsaki-Suzuki, Prog. Theor. Phys. Suppl. **68** (1980) 21.

[Isolde] http://isolde.web.cern.ch/ISOLDE/

[iso] http://isolde.web.cern.ch/ISOLDE/normal/prodintr.html;
http://isolde.web.cern.ch/ISOLDE/normal/isoprodsc.html;
http://isolde.web.cern.ch/ISOLDE/normal/isoprodpsb.html

[Iwa00] H. Iwasaka, T. Motobayashi, H. Akiyoshi, Y. Ando, N. Fukuda, H. Fujiwara, Zs. Fülöp, K.I. Hahn, Y. Higurashi, M. Hirai, I. Hisanaga, N. Iwasa, T. Kijima, A. Mengoni, T. Minemura, T. Nakamura, M. Notani, S. Ozawa, H. Sagawa, H. Sakurai, S. Shimoura, S. Takeuchi, T. Teranishi, Y. Yanagisawa, M. Ishihara, Phys. Lett. **B491** (2000) 8.

[Iwa00b] H. Iwasaka, T. Motobayashi, H. Akiyoshi, Y. Ando, N. Fukuda, H. Fujiwara, Zs. Fülöp, K.I. Hahn, Y. Higurashi, M. Hirai, I. Hisanaga, N. Iwasa, T. Kijima, T. Minemura, T. Nakamura, M. Notani, S. Ozawa, H. Sakurai, S. Shimoura, S. Takeuchi, T. Teranishi, Y. Yanagisawa, M. Ishihara, Phys. Lett. **B481** (2000) 7.

[Izu96] H. Izumi, K. Asahi, H. Ueno, H. Okuno, H. Sato, K. Nagata, Y. Hori, M. Adachi, N. Aoi, A. Yoshida, G. Liu, N. Fukunishi, M. Ishihara, Phys. Lett. **B336** (1996) 51.

[Jac57] J.D. Jackson, S.B. Treiman, H.W. Wyld, Phys. Rev. **106** (1957) 517.

[Jan94] H.J. Jänsch, M. Detje, H.D. Ebinger, W. Preyss, H. Reich, R. Veith, W. Widdra, D. Fick, M. Röckelein, H.G. Völk, Nucl. Phys. **A568** (1994) 544.

[Joh90] L. Johannsen, A.S. Jensen, P.G. Hansen, Phys. Lett. **B244** (1990) 357.

[Kan01] Y. Kanada-En'yo, H. Horiuchi, Prog. Theor. Phys. Suppl. **142** (2001) 205.

[Kan02] R. Kanungo, I. Tanihata, A. Ozawa, Phys. Lett. **B528** (2002) 58.

[Kap97] D.B. Kaplan, A.V. Manohar, Phys. Rev. **C56** (1997) 76.

[Kas50] A. Kastler, J. de Physique 11 (1950) 255.

[Kas57] A. Kastler, J. Opt. Soc. Am. 47 (1957) 460.

[Kei96] M. Keim, "Messung der Kernquadrupolmomente neutronenreicher Natriumisootpe", PhD. thesis Johannes Gutenberg-Universität, Mainz (1996), unpublished.

[Kin84] W. King, "Isotope Shifts in Atomic Spectra", Plenum Press - New York and London (1984).

[Kit90] A. Kitagawa, K. Matsuta, Y. Nojiri, T. Minamisono, Hyp. Int. **60** (1990) 869.

[Kno89] G.F. Knoll, "Radiation Detection and Measurement", second edition, John Wiley and Sons, New York, chapter 3.

[Kop58] H. Kopferman, E. Schneider, "Nuclear Moments", Academic Press Inc New York (1958).

[Kop69] U. Kopf, H.J. Besch, E.W. Otten, C. platen, Z. Phys. **226** (1969) 297.

[Kor50] J. Korringa, Physica **XVI** (1950) 601.

[Kos00] U. Köster, "Ausbeuten und Spektroskopie radioaktiver Isotope bei Lohengrin und ISOLDE", PhD thesis , Technischen Universität München (2000), unpublished.

[Kra54] J.v. Kranendonk, Physica **XX** (1954) 781.

[Kra86] K.S. Krane, "Nuclear Oriëntation Formalism", in 'Low-Temperature Nuclear Oriëntation', p.31, red. N.J. Stone en H.Postma, North Holland, Amsterdam,(1986).

[Kra88] K.S. Krane, "Introductory Nuclear Physics", John Wiley and Sons (1988)

[Kry93] R.A. Kryger, A. Azhari, A. Galonsky, J.H. Kelley, R. Pfaff, E. Ramakrishnan, D. Sackett, B.M. Sherrill, M. Thoennessen, J.A. Winger, S. Yokoyama, Phys. Rev. **C47** (1993) R2439.

[Kug93] E. Kugler, Nucl. Instr. Meth. **B79** (1993) 322.

[Kug00] E. Kugler, Hyp. Int. **129** (2000) 23.

[Kuo67] T.T.S Kuo, Nucl. Phys. **A103** (1967) 71.

[Lab01] M. Labiche, N.A. Orr, F.M. Marquès, J.C. Angélique, L. Axelsson, B. Benoit, U.C. Bergmann, M.J.G. Borge, W.N. Catford, S.P.G. Chapell, N.M. Clarke, G. Costq, N. Curtis, Q. D'Arrigo, E. de Goés Brennand, O. Dorvaux, G. Fazio, M. Freer, B.R. Fulton, G. Giardina, S. Grévy, D. Guillemaud-Mueller, F. Hanappe, B. Heusch, K.L. Jones, B. Jonson, C. Le Brun, S. Leenhardt, M. Lewitowicz, M.J. Lopez, K. Markenroth, A.C. Mueller, T. Nilsson, A. Ninane, G. Nyman, F. de Oliveira, I. Piqueras, K. Riisager, M.G. Sint Laurent, F. Sarazin, S.M. Singer, O. Sorlin, L. Stuttgé, Phys. Rev. **86** (2001) 600.

[Let97] J. Lettry, R. Catherall, P. Drumm, P. Van Duppen, A.H.M. Evensen, G.J. Focker, A. Jokinen, O.C. Jonsson, E. Kugler, H. Ravn and the ISOLDE Collaboration, Nucl. Instr. Meth. **B126** (1997) 130.

[Lie91] P. Lievens, "Laserspektroskopische studie van nukleaire grondtoestandseigenschappen van strontiumiosotopen", PhD. thesis KULeuven, unpublished (1991).

[Lin95] M. Lindroos, C. Broude, G. Goldring, H. Haas, M. Hass, P. Richards, L. Weissmann, Nucl. Instr. Meth. **A361** (1995) 53.

[Mat71] E. Matthias, B. Olson, D.A. Shirley, J.E. Templeton, Phys. Rev. **A4** (1971) 1626.

[Mat99] K. Matsuta, T. Onishi, M. Fukuda, T. Minamisono, M. Mihara, M. Sasaki, T. Yamaguchi, T. Miyake, K. Sato, K. Minamisono, F. Ohsumi, Y. Muramoto, S. Oui, C. Ha, K. Tanaka, K. Kidera, A. Morishita, T. Tsubota, T. Sumikama, A. Kitagawa, M. Torikoshi, M. Kanazawa, T. Nishio, S. Koda, T. Ohtsubo, S. Fukuda, Y. Nojiri, S. Momota, A. Ozawa, K. Yoshida, T. Suzuki, T. Kobayashi,

I. Tanihata, S.S. Hanna, J.R. Alonso, G.F. Krebs, T.J.M. Symons, Hyp. Int. **120/121** (1999) 713.

[May49] M.G. Mayer, Phys. Rev. **75** (1949) 1969.

[Met58] N. Metropolis, R. Bivins, M. Storm, A. Turkevich, J.M. Miller, G. Friedlander, Phys. Rev. **110** (1958) 185.

[Mil75] D.J. Millener, D. Kurath, Nucl. Phys. **A255** (1975) 315.

[Mil83] D.J. Millener, J.W. Olness, E.K. Warburton, S.S. Hanna, Phys. Rev. **C28** (1983) 497.

[Min75] T. Minamisono, J.W. Hugg, D.G. Mavis, T.K. Saylor, S.M. Lazarus, H.F. Glavish, S.S. Hanna, Phys. Rev. Lett. **34** (1975) 1465.

[Min92] T. Minamisono, T. Ohtsuto, I. Minami, S. Fukuda, A. Kitagawa, M. Fukuda, K. Matsuta, Y. Nojiri, S. Takeda, H. Sagawa, H. Kitagawa, Phys. Rev. Lett. **69** (1992) 2058.

[Min93] T. Minamisono, T. Ohtsubo, Y. Nakayama, S. Fukuda, T. Izumikawa, M. Tanigaki, M. Matsui, S. Takeda, N. Nakamura, M. Fukuda, K. Matsuta, Y. Nojiri, Hyp. Int. **78** (1993) 159.

[Mis97] T. Misu, W. Nazarewicz, S. Åberg, Nucl. Phys. **A614** (1997) 44.

[Nav98] P. Navratil, B.R. Barrett, Phys. Rev. **C57** (1998) 3119.

[Nav00] A. Navin, D.W. Anthony, T. Aumann,T. Baumann, D. Bazin, Y. Blumenfeld, B.A. Brown, T. Glasmacher, P.G. Hansen, R.W. Ibbotson, P.A. Lofy, V. Maddalena, K. Miller, T. Nakamura, B.V. Pritychenko, B.M. Sherrill, E. Spears, M. Steiner, J.A. Tostevin, J. Yurkon, A. Wagner, Phys. Rev. Lett. **85** (2000) 266.

[Nav03] P. Navratil, W.E. Ormand, Phys. Rev. **C68** (2003) 034305.

[Neu73] R. Neugart, Z.Physik **261** (1973) 237.

[Neu00] R. Neugart, Hyp. Int. **127** (2000) 101.

[New62] R.E. Newnham, Y.M. de Haan, Z. Krist. **117** (1962) 235.

[Ney93b] G. Neyens, "De normale wederkerige relatie tussen de emissie- en absorptie-waarschijnlijkheid van atomaire fotonen kan verbroken worden door het aanleggen van een statisch elektrisch veld loodrecht op een statisch magnetisch veld." , bijstelling PhD thesis, KULeuven, unpublished (1993)

[Ney03] G. Neyens, Rep. Prog. Phys. **66** (2003) 633.

[NIST99] http://physics.nist.gov/cuu/Constants/ copy from Journ. Phys. and Chem. Reference Data, Vol. **28** (1999) 6.

[Nun96] F.M. Nunes, I.J. Thompson, R.C. Johnson, Nucl. Phys. **A596** (1996) 171.

[Nun02] F.M. Nunes, I.J. Thompson, J.A. Tostevin, Nucl. Phys. **A703** (2002) 593.

[Oga03] H. Ogawa, K. Asahi, T. Suzuki, H. Izumi, H. Miyoshi, M. Nagakura, K. Yogo, A. Goto, T. Suga, T. Honda, H. Ueno, Y.X. Watanabe, K. Yoneda, A. Yoshimi, N. Fukuda, Y. Kobayashi, A. Yoshida, T. Kubo, M. Ishihara, N. Imai, N. Aoi, W.-D. Schmidt-Ott, G. Neyens, S. Teughels, Phys. Rev. **C67**(2003) 064308.

[Oht93] T. Ohtsubo, Y. Nakayama, I. Minami, M. Tanigaki, S. Fukuda, A. Kitagawa, M. Fukuda, K. Matsuta, Y. Nojiri, H. Akai, T. Minamisono, Hyp. Int. **80** (1993) 1051.

[Oku95] H. Okuno, K. Asahi, H. Ueno, H. Izumi, H. Sato, M. Adachi, T. Nakamura, T. Kubo, N. Inabe, A. Yoshida, N. Fukunishi, T. Shimoda, H. Miyatake, N. Takahashi, W.D. Schmidt-Ott, M. Ishihara, Phys. Lett. **B354** (1995) 41.

[Ort75] H. Orth, H. Ackermann, E.W. Otten, Z. Phys. **A273** (1975), 221.

[Ots95] T. Otsuka, A. Muta, M. Yokoyama, N. Fukunishi, T. Suzuki, Nucl. Phys. **A588** (1995) 113c.

[Ots99] T. Otsuka, T. Mizusaki, M. Honma, J. Phys. **G25** (1999) 699.

[Ots01] T. Otsuka, R. Fujimoto, Y. Utsuno, A. Brown, M. Honma, T. Mizusaki, Phys. Rev. Lett. **87** (2001) 082502.

[Ots01b] T. Otsuka, Nucl. Phys. **A693** (2001) 383.

[Ots01c] T. Otsuka, Y. Utsuno, M. Honma, T. Mizusaki, Progr. Part. Nucl. Phys. **46** (2001) 155.

[Ots02] T. Otsuka, Prog. Theor. Phys. Suppl. **146** (2002) 6.

[Ots03] T. Otsuka, Nucl. Phys. **A722** (2003) 347c.

[Ott89] E.W. Otten, "Nuclear Radii and Moments of Unstable Isotopes", in Treatise on heavy-ion science, Edited by D. Bromley, volume 8, Plenum Publishing Corporation (1989) 517-638.

[Oxb84] B. A. Brown et al, The computer code Oxbash, MSU-NSCL Report No. 524 (1984).

[Oza00] A. Ozawa, T. Kobayashi, T. Suzuki, K. Yoshida, I. Tanihata, Phys. Rev. Lett. **84** (2000) 5493.

[Pet67] G.E. Peterson, P.M. Bridenbaugh, P. Green, J. Chem. Phys. **46** (1967) 4009.

[Pet68] G.E. Peterson, P.M. Bridenbaugh, J. Chem. Phys. **48** (1968) 3492.

[Pos86] *Low Temperature Nuclear Orientation*, Eds. H. Postma and N. Stone (North-Holland, Amsterdam, 1986).

[PRD02] Phys. Rev. **D66**, "Introduction, Procedures" (2002).

[Pre72] B.M. Preedom, B.H. Wildenthal, Phys. Rev. **C6** (1972) 1633.

[Pre97] W. Preyss, M. Detje, H.D. Ebinger, H.J. Jansch, C. Polenz, B. Polivka, R. Veith, D. Fick, Hyp. Int. **110** (1997) 295.

[PSB] http://ab-div-op-ps.web.cern.ch/ab-div-op-ps/

[Pyy01] P. Pyykkö, Molecular Physics **99** (2001) 1617.

[Rag89] P. Raghavan, At.Data Nucl. Data Tables **42** (1989) 189.

[Ram01] S. Raman, C.W. Nestor, P. Tikkanen, At. Data Nucl. Data Tables **78** (2001) 1.

[Rei93] V.G.J. Stoks, R. Klomp, CPF. Terhegen, J.J. Deswart, Phys. Rev. **C49** (1994) 2950.

[Rii92] K. Riisager, R. Anne, S.E. Arnell, R. Bimbot, H.Emling, D. Guillemaud-Mueller, P.G. Hansen, L. Johannsen, B.Jonson, A. Latimier, M. Lewitowicz, S. Mattson, A.C. Mueler, R. Neugart, G. Nyman, F. Pougheon, A. Richard, A. Richter, M.G. Sain-Laurent, G. Schrieder, O. Sorlin, K. Wilhelmsen, Nucl. Phys. **A540** (1992) 365.

[Rin80] P. Ring, P. Schuck, "The Nuclear Many-Body Problem", Springer, Berlin-Heidelberg (1980).

[Roe74] E. Roeckl, PF. Dittner, C. Detraz, R. Klapisch, C. Thibault, C. Rigaud, Phys. Rev. **C10** (1974) 1181.

[Ros69] F.A. Rossini, W.D. Knight, Phys. Rev. **178** (1969) 641.

[Sag93] H. Sagawa, B.A. Brown, H. Esbensen, Phys. Lett. **B309** (1993) 1.

[Sag01] H. Sagawa, K. Asahi, Phys. Rev. **C63** (2001) 064310.

[Sal90] K.E. Sale, T.F. Wang, R.N. Boyd, G.J. Mathews, D.W. Heikkinen, M.L. Roberts, M.S. Islam, P.B. Corn, Phys. Rev. **C41**(1990) 2418.

[Sar85] D.R. Saroha, N. Malhotra, R.K. Gupta, J. Phys. G **11** (1985) L27.

[Sch88] G. Scheveneels, "Toestandsmengingsspektroskopie voor in-bundel quadrupoolinteractiemetingen", PhD. thesis KULeuven (1988), unpublished

[Sch00] F. Schmitt, A. Dax, R. Kirchner, H.-J. Kluge, T. Kühl, I. Tanihata, M. Wakasugi, H. Wang, C. Zimmermann, Hyp. Int. **127** (2000) 111.

[Ser01] R.A. Serway, R.J. Beichner, ”Physics for Scientists and Engineers with modern physics”, 5th edition, Saunders College Publishing.

[Sev89] N. Severijns, J. Wouters, J. Vanhaverbeke, L. Vanneste, Phys. Rev. Lett. **63** (1989) 1050.

[Shi03] S. Shimoura, A. Saito, T. Minemura, Y.U. Matsuyama, H. Baba, H. Akiyoshi, N. Aoi, T. Gomi, Y. Higurashi, K. Ieki, N. Imai, N. Iwasa, H. Iwasaka, S. Kanno, S. Kubono, M. Kunibo, S. Michimasa, T. Motobayashi, T. Nakamura, H. Sakurai, M. Serata, E. Takeshita, S. Takeuchi, T. Teranishi, K. Ue, K. Yamada, Y. Yanagisawa, M. Ishihara, N. Itagaki, Phys. Lett. **B560** (2003) 31.

[Sil87] R.E. Silverans, P. Lievens, L. Vermeeren, Nucl. Instr. Meth. **B26** (1987) 591.

[Sim99] H. Simon, D. Aleksandrov, T. Aumann, L. Axelsson, T. Baumann, M.J.G. Borge, L.V. Chulkov, R. Collatz, J. Cub, W. Dostal, B. Eberlein, T.W. Elze, H. Emling, H. Geissel, A. Grunschloss, M. Hellström, J. Holeczek, R. Holzmann, B. Jonson, J.V. Kratz, G. Kraus, R. Kulessa, Y. Leifels, A. Leistenschneider, T. Leth, I. Mukha, G. Munzenberg, F. Nickel, T. Nilsson, G. Nyman, B. Petersen, M. Pfützner, A. Richter, K. Riisager, C. Scheidenberger, G. Schrieder, W. Schwab, M.H. Smedberg, J. Stroth, A. Surowiec, O. Tengblad, M.V. Zhukov, Phys. Rev. Lett. **83** (1999) 496.

[Sli78] C.P. Slichter, ”Principles of Magnetic Resonance”, Eds: M.Cardona, P.Fulde, H.-J. Queisser, Springer-Verlag, Berlin, Heidelberg, New York, (1978).

[Smi04] N.A. Smirnova, private communication (2004).

[Sob79] I.I. Sobelman, ”Atomic spectra and Radiative Interactions”, Springer Verlag, Berlin, Heidelberg, New York (1979).

[Stef75] R.M. Steffen and K. Alder in ”The electromagnetic interaction in nuclear spectroscopy” (North Holland, Amsterdam, 1975).

[Sto01] http://www.nndc.bnl.gov/nndc/stone_moments/nuclear-moments.pdf, table of recommended nuclear moments, preprint 2001

[Suz94] T. Suzuki, T. Otsuka, Phys. Rev. **C50** (1994) R555.

[Suz97] T. Suzuki, T. Otsuka, Phys.Rev. **C56** (1997) 847.

[Suz03] T. Suzuki, R. Fujimoto, T. Otsuka, Phys. Rev. **C67** (2003) 044302.

[Tal60] I. Talmi, I. Unna, Phys. Rev. Lett **4** (1960) 469.

[Tan77] I. Tanihata, S. Kogo, K. Sugimoto, Phys. Lett. **B67** (1977) 392.

[Tan85] I. Tanihata, H. Hamagaki, O. Hashimoto, Y. Shida, N. Yoshikawa, K. Sugimoto, O. Yamakawa, T. Kobayashi, N. Takahashi, Phys. Rev. Lett. **55** (1985) 2676.

[Tan96] I. Tanihata, J. Phys. **G22** (1996) 157.

[Tan03] I. Tanihata, R. Kanungo, C.R. Physique **4**(2003) 437.

[Teu01] S. Teughels, "Exploring the limits of the Island of Inversion with the Level Mixing and Nuclear Magnetic Resonance techniques", PhD thesis, KULeuven, unpublished.

[Thi75] C. Thibault, R. Klapisch, C. Rigaud, A.M. Poskanzer, R. Prieels, L. Lessard, W. Reisdorf, Phys. Rev. **C12** (1975) 644.

[Tho77] D.R. Thomson, M. Lemere, Y.C. Tang, Nucl. Phys. **A286** (1977) 53.

[Tho94] I.J. Thompson, M.V. Zhukov, Phys. Rev. **C49** (1994) 1904.

[Tho96] I.J. Thompson, M.V. Zhukov, Phys. Rev. **C53** (1996) 708.

[Tim02] N.K. Timofeyuk, Phys. Rev. **C65** (2002) 064306.

[ton] http://atom.kaeri.re.kr/ton/

[Uen96] H. Ueno, K. Asahi, H. Izumi, K. Nagata, H. Ogawa, A. Yoshimi, H. Sato, M. Adachi, Y. Hori, K. Mochinaga, H. Okuno, N. Aoi, M. Ishihara, A. Yoshida, G. Liu, T. Kubo, N. Fukunishi, T. Shimoda, H. Miyatake, M. Sasaki, T. Shirakura, N. Takahashi, S. Mitsuoka, W.-D. Schmidt-Ott, Phys. Rev. **C53** (1996) 2142.

[Urb90] M. Urban, A.J. Sandlej, Chem.Phys. Lett.**173** (1990) 157.

[Uts01] Y. Utsuno, T. Otsuka, T. Mizusaki, M. Honma, Phys. Rev. **C60** (1999) 054315.

[Van86] L. Vanneste, in Low Temperature Nuclear Orientation, eds. H. Postma and N.J. Stone (North-Holland, Amsterdam, 1986), chapter 3 .

[Var94] K. Varga, Y. Suzuki, R.G. Lovas, Nucl. Phys. **A571** (1994) 447.

[Var95] K. Varga, Y. Suzuki, I. Tanihata, Phys. Rev. **C52**(1995) 3013.

[Var02] K. Varga, Y. Suzuki, R.G. Lovas, Phys. Rev. **C66** (2002) 041302(R).

[Vee03] Veeco Applied EPI, Vapor Pressure Data, http://www.veeco.com/learning/ learning_vaporelements.asp

[Voe91] H.G. Voelk, D. Fick, Nucl.Phys. **A530** (1991) 475.

[Vol65] A.B. Volkov, Nucl. Phys. **74** (1965) 33.

[Vyv01] K. Vyvey, " Testing Nuclear Models By Measuring Quadrupole Moments of High Spin Isomers in Spherical and Deformed Nuclei", Phd. thesis, KULeuven, unpublished

[Vyv02] K. Vyvey, A.M. Oros-Peusquens, G. Neyens, D.L. Balabanski, D. Borremans, S. Chmel, N. Coulier, R. Coussement, G. Georgiev, H. Hübel, N. Nenoff, D. Rossbach, S. Teughels, K. Heyde, Phys. Lett. **B538** (2002) 33.

[War89] E.K. Warburton, D.J. Millener, Phys. Rev. **C39** (1989) 1120.

[Wel85] A. Weller, P. Egelhof, R. Caplar, O. Karban, D. Krämer, K.H. Möbius, Z. Moroz, K. Rusek, E. Steffens, G. Tungate, Phys. Rev. Lett. **55** (1985) 480.

[Wil70] R.L. Williams Jr., L. Pfeiffer, J.C. Wells Jr., L. Madansky, Phys. Rev. **C2** (1970) 1219.

[Wil71] R.L. Williams Jr., L. Madansky, Phys. Rev. **C 3** (1971) 2149.

[Win78] A. Winnacker,D. Dubbers, F. Fujara, K. Dörr, H. Ackermann, H. Grupp, P. Heitjans, A. Körblein, H.-J. Stöckmann, Phys. Lett. **A67**(1978) 423.

[Win01] J.S. Winfield, S. Fortier, W.N. Catford, S. Pita, N.A. Orr, J. Van de Wiele, Y. Blumenfeld, R. Chapman, S.P.G. Chappell, N.M. Clarke, N. Curtis, M. Freer, S. Galès, H. Langevin-Joliot, H. Laurent, I. Lhenry, J. M. Maison, P. Roussel-Chomaz, M. Shawcross, K. Spohr, T. Suomijärvi, A. de Vismes, Nucl. Phys. **A683** (2001) 48.

[Wol79] D. Wolf, "Spin-Temperature and Nuclear-Spin Relaxation in Matter: basic principles and applications", Clarendon Press, Oxford, 1979.

[Yam79] N. Yamaguchi, T. Kasahara, S. Nagata, Y. Akaishi, Prog. Theor. Phys. **62** (1979) 1018.

[Yan00] Z.C. Yan, G.W.F Drake, Phys. Rev. **A61** (2000) 022504.

[You94] B.M. Young, W. Benenson, J.H. Kelley, R. Pfaff, B.M. Sherrill, M. Steiner, M. Thoennessen, J. S. Winfield, N.A. Orr, J.A. Winger, J.S. Yennello, A. Zeller, Phys. Rev. **C49** (1994) 279.

[Zhuk93] M.V. Zhukov, B.V. Danilin, D.V. Fedorov, J.M. Bang, I.J. Thompson, J.S. Vaagen, Phys. Rep. (Review Section of Phys. Lett.) **231** (1993) 151.

[Zin95] M. Zinser, F. Humbert, T. Nillson, W. Scwab, Th. Blaich, M.J.G. Borge, L.V. Chulkov, H. Eickhoff, Th. E. Elze, H. Emling, B. Franzke, H. Freiesleben, H. Geissel, K. Grimm, D. Guillemaud-Mueller, P.G. Hansen, R. Holzmann, H. Irnich, B. Jonson, J.G. Keller, O. Klepper, H. Klingler, J.V. Kratz, R. Kulessa, D. Lambrecht, Y. Leifels, A. Magel, M. Mohar, A.C. Mueller, G. Münzenberg, F. Nickel, G. Nyman, A. Richter, K. Riisager, C. Scheidenberger, G. Schrieder, B.M. Sherrill, H. Simon, K. Stelzer, J. Stroth, O. Tengblad, W. Trautmann, E. Wajda, E. Zude, Phys. Rev. Lett. **75** (1995) 1719.

[Zwie79] B. Zwieglinski, W. Benenson, R.G.H. Robertson, Nucl. Phys. **A315** (1979) 124.